Lecture Notes in Electrical Engineering 409

Alessandro De Gloria
Editor

Applications in Electronics Pervading Industry, Environment and Society

APPLEPIES 2015

Springer

Lecture Notes in Electrical Engineering

Volume 409

About this Series

"Lecture Notes in Electrical Engineering (LNEE)" is a book series which reports the latest research and developments in Electrical Engineering, namely:

- Communication, Networks, and Information Theory
- Computer Engineering
- Signal, Image, Speech and Information Processing
- Circuits and Systems
- Bioengineering

LNEE publishes authored monographs and contributed volumes which present cutting edge research information as well as new perspectives on classical fields, while maintaining Springer's high standards of academic excellence. Also considered for publication are lecture materials, proceedings, and other related materials of exceptionally high quality and interest. The subject matter should be original and timely, reporting the latest research and developments in all areas of electrical engineering.

The audience for the books in LNEE consists of advanced level students, researchers, and industry professionals working at the forefront of their fields. Much like Springer's other Lecture Notes series, LNEE will be distributed through Springer's print and electronic publishing channels.

More information about this series at http://www.springer.com/series/7818

Alessandro De Gloria
Editor

Applications in Electronics Pervading Industry, Environment and Society

APPLEPIES 2015

Springer

Editor
Alessandro De Gloria
DITEN
University of Genoa
Genoa
Italy

ISSN 1876-1100 ISSN 1876-1119 (electronic)
Lecture Notes in Electrical Engineering
ISBN 978-3-319-47912-5 ISBN 978-3-319-47913-2 (eBook)
DOI 10.1007/978-3-319-47913-2

Library of Congress Control Number: 2016955429

Printed on acid-free paper

This Springer imprint is published by Springer Nature
The registered company is Springer International Publishing AG
The registered company address is: Gewerbestrasse 11, 6330 Cham, Switzerland

Preface

This is the third edition of the Applepies proceedings published by Springer, with the conference that is ever increasing its reach and impact, also at international level. This confirms our initial intuition, that applications of electronic systems are a focal point at the intersection of technology and requirements, users and developers, business and academy.

The papers of this edition represent a mix that clearly reflects the perspectives and the potential of the field, with particular reference to the Internet of the Things (IoT). We can identify three main areas: sensors, embedded architectures, and applications.

The health domain has a great relevance, implying the development of wearable systems that monitor a person's status in a variety of activities, while both healthy or ill.

Another significant and pervasive domain is represented by intelligent transportation systems, where IoT and, more in general, electronic technologies are a major factor towards autonomous driving by significantly increasing the context awareness.

Also the methodologies and tools for embedded system development and life-cycle management are accurately covered, stressing the importance of an approach that combines the centrality of the user needs with the importance of market efficiency and effectiveness.

Achieving good cost/performance ratios requires deep knowledge both of the system's target application and domain, and of the technologies that are potentially able to fulfill the expected goals.

This calls for the importance of the role of the university as a place where teachers and students, in their different roles, work together to study, share, develop, and transmit knowledge and ideas. The business world can benefit through technology transfer and by getting valuable students, able to face the challenges of the real world, in a variety of domains such as healthcare, transportation, agriculture, education, tourism, entertainment, cultural heritage, energy, construction, etc.

By reporting original research works and discussing several examples, this book will hopefully help the readers to get significant insights into this direction.

Genoa, Italy Alessandro De Gloria

Contents

A Wireless Personal Sensor Node for Real Time Dosimetry of Interventional Radiology Operators 1
Daniel Magalotti, Pisana Placidi, Stefania Fabiani, Lucia Bissi, Massimiliano Paolucci, Andrea Scorzoni, Andrea Calandra, Giovanni Verzellesi and Leonello Servoli

A New FPGA-Based Architecture for Iterative and Space-Variant Image Processing. 9
Stefano Marsi, Sergio Carrato and Giovanni Ramponi

Embedded Electronic Systems for Tactile Data Processing 17
Ali Ibrahim, Luca Noli, Hussein Chible and Maurizio Valle

Microwave Imaging for Breast Cancer Detection: A COTS-Based Prototype. 25
Azzurra Pulimeno, Marco Vacca, Mario R. Casu, Jorge A. Tobon, Francesca Vipiana, Daniele Jahier Pagliari, Raffaele Solimene and Luca P. Carloni

A SystemVerilog-UVM Methodology for the Design, Simulation and Verification of Complex Readout Chips in High Energy Physics Applications 35
Sara Marconi, Elia Conti, Pisana Placidi, Andrea Scorzoni, Jorgen Christiansen and Tomasz Hemperek

Embedded System for In-Line Characterization of Industrial Fluids 43
Stefano Ricci, Valentino Meacci, Beat Birkhofer and Johan Wiklund

A Low Cost, Portable Device for Breath Analysis and Self-monitoring, the Wize Sniffer 51
Danila Germanese, Marco Righi, Antonio Benassi, Mario D'Acunto, Riccardo Leone, Massimo Magrini, Paolo Paradisi, Dario Puppi and Ovidio Salvetti

A Short Term Simulator for Vessel Manoeuvres Prediction 59
Paolo Neri and Bruno Neri

A Portable System for the Monitoring of Dissolved Oxygen in Aquatic Environment 67
Luca Lombardo, Jiaran Zhang, Salvatore Gianluca Leonardi, Davide Aloisio, Giovanni Neri, Daoliang Li and Nicola Donato

Sensormind: Virtual Sensing and Complex Event Detection for Internet of Things 75
Davide Brunelli, Gianluca Gallo and Luca Benini

RF-Powered HF-RFID Analog Sensors Platform 85
Demetrio Iero, Corrado Felini, Massimo Merenda and Francesco Giuseppe Della Corte

Enabling Technologies for the In-house Monitoring of Vital Signs in Chronic Patients 93
Massimiliano Donati, Alessio Celli, Alessandro Benini, Luca Fanucci and Sergio Saponara

Measuring Tissue Compression: A Circuit for Sensing and Signal Conditioning 101
Sonja Hermann, Patrick Thomas, Richard B. Reilly and Martin J. Burke

Narrowband Delay Tolerant Protocols for WSN Applications: Characterization and Selection Guide 109
Claudio S. Malavenda, Francesco Menichelli and Mauro Olivieri

New X-Ray Radiation Sensor for Dosimetry Imaging 123
Calogero Pace, Evgeny Pikhay, Anna Santaniello, Yael Nemirovsky and Yakov Roizin

A Novel Instrumentation for an Advanced High Temperature Reverse Bias (HTRB) Testing on Power Transistors 133
Calogero Pace, Jorge Hernandez Ambato and Carlo Giordano

A Wireless Sensor Node Based on Microbial Fuel Cell 143
Simone Acciarito, Gian Carlo Cardarilli, Luca Di Nunzio, Rocco Fazzolari and Marco Re

Autonomous Wireless Sensor Network for Structural Health Monitoring of Aerostructures.......... 151
Andrea Corniani, Simone Faccini, Enrico Turri, Nicola Testoni and Luca De Marchi

Wearable Speech Enhancement System for Motor Impaired People 159
Alessandro Palla, Luca Fanucci, Roberto Sannino and Mattia Settin

System-Level Analysis for Integrated Power Amplifier Design in mmWave Consumer Wireless Communications 167
Sergio Saponara and Bruno Neri

UDOO-Based Environmental Monitoring System 175
Giulio Borrello, Erica Salvato, Giovanni Gugliandolo, Zlatica Marinkovic and Nicola Donato

A Smart LED Light Control System for Environmentally Friendly Buildings 181
Michele Magno, Tommaso Polonelli and Luca Benini

A Low-Cost, Open-Source Cyber Physical System for Automated, Remotely Controlled Precision Agriculture 191
Davide Cimino, Alberto Ferrero, Leonardo Queirolo, Francesco Bellotti, Riccardo Berta and Alessandro De Gloria

Assessment of Driver Behavior Based on Machine Learning Approaches in a Social Gaming Scenario 205
Gautam R. Dange, Pratheep K. Paranthaman, Francesco Bellotti, Marco Samaritani, Riccardo Berta and Alessandro De Gloria

A Novel Technique for the CMRR Improvement in a Portable ECG System 219
Pietro Di Buono, Leonardo Mistretta and G. Costantino Giaconia

An Optimization Device for Series Parallel Connected PV Plants 227
Eleonora Riva Sanseverino, G. Costantino Giaconia, Vincenzo Li Vigni, Pietro Di Buono, Pietro Romano, Marco Iannello and Vincenzo Tirrasi

A Wireless Personal Sensor Node for Real Time Dosimetry of Interventional Radiology Operators

Daniel Magalotti, Pisana Placidi, Stefania Fabiani, Lucia Bissi, Massimiliano Paolucci, Andrea Scorzoni, Andrea Calandra, Giovanni Verzellesi and Leonello Servoli

Abstract Wireless Sensor Networks (WSN) featuring portable devices are widely used for healthcare applications such as real time patient monitoring. In this paper the attention has been focused on dose monitoring of Interventional Radiology operators by describing the design of a dedicated WSN for real time monitoring. The performances of the network have been evaluated inside the operating room showing that it is possible to achieve data delivery in clinical environments. Data have been acquired during medical Interventional Radiology procedures making use of a final prototype ("Prototype2"), a non-miniaturized prototype (Prototype1) and a reference acquisition system ("Demo2") with the aim to compare their performance and to show the correct functionality of the prototypes during operating conditions.

1 Introduction

Recent advances in Micro-Electro-Mechanical Systems (MEMSs) technology, wireless communications, embedded systems and digital circuit electronics have stimulated the condition to develop low-cost, low-power, multifunctional portable sensor devices which can be used to observe and monitor physical phenomena [1].

D. Magalotti · G. Verzellesi
University of Modena and Reggio Emilia, Reggio Emilia, Italy

D. Magalotti (✉) · P. Placidi · S. Fabiani · L. Bissi · M. Paolucci · A. Scorzoni · L. Servoli
Istituto Nazionale di Fisica Nucleare, Perugia, Italy
e-mail: daniel.magalotti@pg.infn.it

P. Placidi · L. Bissi · A. Scorzoni · A. Calandra
University of Perugia, Perugia, Italy

S. Fabiani
University of Aquila, Scuola di Specializzazione in Fisica Medica, L'Aquila, Italy

M. Paolucci
AUSL Umbria 2, Servizio di Fisica Sanitaria, Perugia, Italy

A. De Gloria (ed.), *Applications in Electronics Pervading Industry, Environment and Society*, Lecture Notes in Electrical Engineering 409,
DOI 10.1007/978-3-319-47913-2_1

These sensors can cooperate to create Wireless Sensor Networks (WSNs) that are widely used in healthcare applications [2]. In this context, new wireless technologies open up possibilities for providing real time feedback information about the health status condition, both to the patient himself and to a medical center that will be able to detect an emergency condition [3] and to generate an alert in case of possible health threatening conditions [4].

This paper focuses on the field of Interventional Radiology (IRad), where radiological devices provide guidance for minimally invasive diagnostic and therapeutic procedures. As the benefits for patients increase, the use of radiation in medicine exposes not only the patient but also the medical staff to health risks during the working activity. While the development of modern health technology makes new applications safer, their inappropriate use can lead to unnecessary radiation exposition, thus causing potential health hazards for both patients and staff [5]. In [6], we have presented and characterized the first prototype of a wireless dosimetric system based on a commercial CMOS image sensor. In this system a data processing and reduction algorithm has been developed, with the goals of retrieving two different observables from a subset of collected data while being compatible with real time requirements.

The present paper describes the architecture and the communication test of the final version of the wireless sensor network. The network and the correct functionality of the wireless protocol have been tested inside an operating room in order to evaluate the Packet Error Rate (PER) of the sensor node. Then the data acquisition performance of the system during medical IRad medical procedures is discussed.

2 System Architecture and Network

The monitoring network in operating room is shown in Fig. 1. The medical operator wears one or more Personal Sensor Nodes, PSNs, (e.g. on head or hands), each of which working as a transmitter unit. The receiver unit is located in a fixed position of the operating room and connected to a remote station which merges and stores all the received data for off line data processing.

The transmitter unit [6] consists of: (i) a commercial CMOS image sensor used as X-ray radiation detector [7], (ii) a digital signal processing unit (DSPU) and (iii) a wireless interface/control unit. The DSPU consists of a Complex Programmable Logic Device (Xilinx XC2C512 CPLD) implementing a one threshold data reduction algorithm yielding two system observables: the number N of pixels over threshold in a sensor frame and the sum E of the energies of the pixels over threshold in a sensor frame (ADC counts). The two observables are then correlated with the dosimetric quantities by using a calibration factor obtained in a certified calibration center [8].

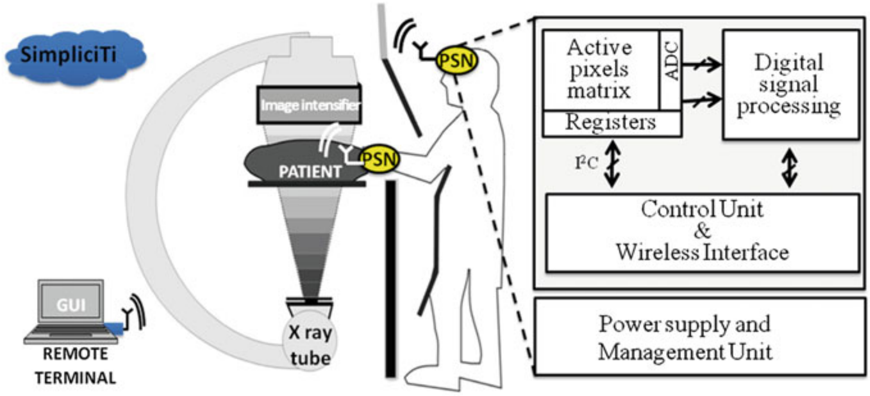

Fig. 1 Monitoring system scenario and block diagram of the PSN architecture

The System on Chip (CC430F6137 from Texas Instruments), which combines a MSP430 core and a RF module together, provides the control unit and the wireless interface. The adopted wireless protocol is Texas Instruments' SimpliciTI, operating in the Industrial/Scientific/Medical (ISM) radio band at 868 MHz carrier frequency. The power consumption is about 200 mW with a 3.6 V external power supply in order to be compatible with the typical voltage of a mobile phone battery.

3 Performance of the Network Inside the Operating Room

The wireless losses of the network have been evaluated inside the operating room during several IRad procedures in order to estimate and to test the capability of the system to manage more than one dosimeter Prototype2 working simultaneously in the network while the operator was performing actual procedures.

The experimental setup is shown in Fig. 2a, consisting of (A) four Prototypes2 hosted in garments worn by the operator and (B) a receiver unit placed inside the operating room. The operator wears a garment hosting two Prototypes2 ($P2_A$ and $P2_B$), at the level of the chest and two wrist garments for the left and right arm hosting respectively the $P2_C$ and $P2_D$ prototypes. Each Prototype2 has an additional TLD (ThermoLuminescent Dosimeter) used as reference dosimetric system (Fig. 2b).

The network performances have been evaluated by measuring the PER of the acquisitions performed by all the Prototypes2. The distribution of the PER is shown in Fig. 3 and the values are always below 2.5 % while the average value is about 0.83 % and the RMS is 0.51 %. The losses and the PER value are dependent on the actions of the operator during the IRad procedures. A method has been used at the end of the acquisition to recover the procedure losses even if the packets have been lost randomly both with X-ray signal and no signal during the IRad procedures.

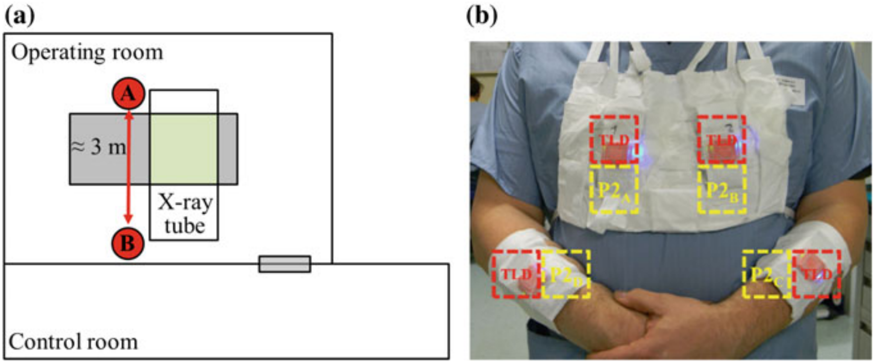

Fig. 2 **a** Experimental set-up inside the operating room during several Interventional Radiology procedures: A = operator; B = receiver unit. **b** Measurement setup in operating room during IRad procedures. The operator wear a garment at level of chest with the Prototypes2 and two wrist garments for the left and right arm

Fig. 3 Distribution of the PER for the four Prototypes2 for all medical procedures

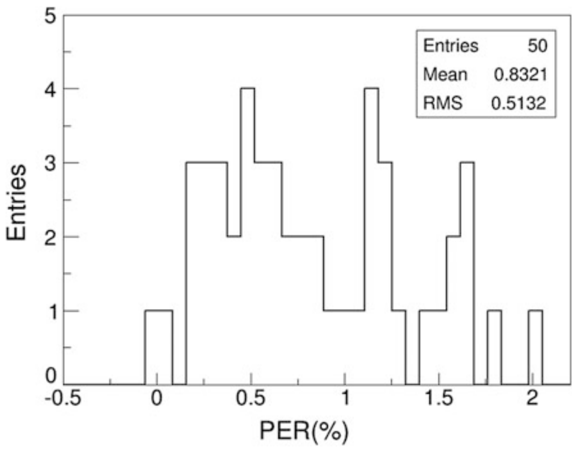

4 System Performance During Medical Procedures

In this section, we report about the analysis of the network during several IRad medical procedures in order to compare the performances of the network.

The first purpose is to evaluate the synchronization among the *N* observables acquired from all Prototypes2 of the network (Fig. 4). All Prototypes2 are correlated with respect to each other and with respect to the X-ray burst. The different amplitudes of the *N* observables is due to the different position of the Prototype2 in the operator garment.

The signal contribution has been extracted for all the IRad procedures (about seventy) by considering only the contribution of the X-ray signal in the evaluation

Fig. 4 *N* observable acquired by the four Prototypes2 during a time interval of a medical procedure

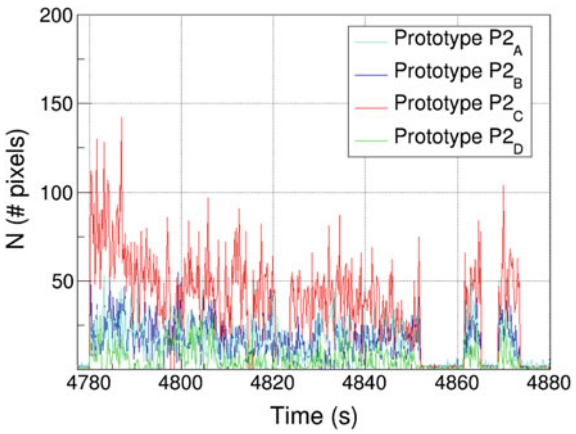

Fig. 5 Correlation between the *E* and *N* observables for all the procedures considering both the Prototypes1 (*red points*) and Prototypes2 (*blue points*)

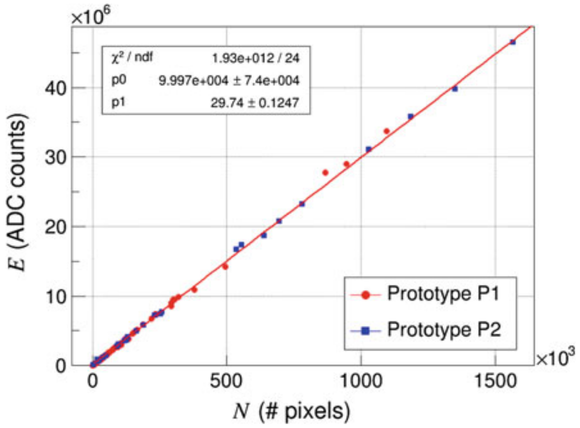

of the observables. The correlation between the integral value of the observables is plotted in Fig. 5 considering both the Prototype1 (red points) and Prototype2 (blue points) and a good linearity can be observed for all the operating conditions.

Moreover to compare the performance of all the Prototypes we apply the calibration constants found for each sensors by exposing them to a known X-ray source and correlating the deposited energy with the sensor signal expressed in terms of ADC counts. Then we evaluate the mean value of the Gaussian distribution of the ratio between the *E* and *N* observables for all the operating conditions.

Figure 6 shows the ratio E/N as measured by a reference acquisition system (the Demo2 system), the Prototype1 and the Prototype2 for all the medical procedures. The mean value of the ratio is essentially constant with an average collected energy of 4.26 ± 0.03 keV. The results show that the average pixel response does not depend on the procedure, hence it does not depend on the different spectra of the diffused radiation. Moreover the average pixel response does not depend on the different acquisition systems.

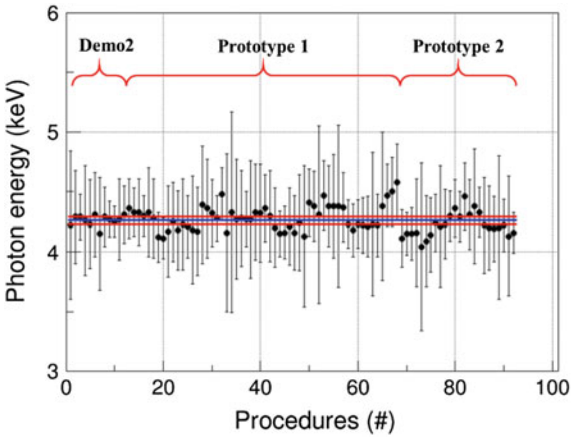

Fig. 6 Photon energy obtained as mean value of the Gaussian distribution as a function of all the procedures by highlighting the results for the different acquisition systems. The blue line and the red lines are the mean value and the uncertainty calculated by considering all the points

5 Conclusion

A wireless sensor network for the dosimetry of IRad operators, based on a commercial CMOS image sensor, has been described.

The performances of the network have been evaluated inside the operating room showing that it is possible to achieve data delivery in clinical environments. Data have been acquired during medical Interventional Radiology procedures making use of two prototypes and a reference acquisition system with the aim to compare their performance and to show the correct functionality of the prototypes during operating conditions. Finally, the system shows a good synchronization between the observables and the X-ray tube and the average pixel response does not depend on the procedure, hence it does not depend on the different spectra of the diffused radiation.

Acknowledgments This work was supported in part by Italian Istituto Nazionale di Fisica Nucleare in the framework of the “Real time Active PIxel Dosimetry” project and in part by Dipartimento di Ingegneria Elettronica within the framework of the “Mecca-Bio-Tronica: Un nuovo approccio integrato e multidisciplinare per lo studio, la gestione e la progettazioni di impianti biologici per l’energia e l’ambiente project”.

References

1. Yick, J., Mukherjee, B., Ghosal, D.: Wireless sensor network survey. Comput. Netw. **52**(12), 2292–2330 (2008)
2. Dolgov, A.B., Zane, R.: Low-power wireless medical sensor platform, 28th Annual International Conference of the IEEE Engineering in Medicine and Biology 2006. 3 Sept 2006
3. Gao, T., Pesto, C., Selavo, L., Yin, C.: Wireless medical sensor networks in emergency response: implementation and pilot results. IEEE Conference on Technologies for Homeland Security, pp. 187–192. Waltham, USA, 12–13 May 2008

4. Hao, Y., Foster, R.: Wireless body sensor networks for health monitoring applications. Physiol Measur **29(**11), R27 Nov 2008
5. Vañó, E., González, L., Guibelalde, E., Fernández, J.M., Ten, J.I.: Radiation exposure to medical staff in interventional and cardiac radiology, an international journal of radiology, radiation oncology and all related science, The British Institute of Radiology, vol. 71, no. 849 (2014)
6. Conti, E., et al.: A portable dosimetric system based on a CMOS image sensor for radiation protection in interventional radiology. IEEE International Instrumentation and Measurement Technology Conference (I2MTC), pp. 288–292. Montevideo, Uruguay, 12–15 May 2014
7. Magalotti, D., et al.: Performance of CMOS imager as sensing element for a real-time active pixel dosimeter for interventional radiology procedures. J. Instrum. **9**(1), C01036 (2014)
8. Magalotti, D., et al.: Experimental characterization of a wireless personal sensor node for the dosimetry during interventional radiology procedures. IEEE Trans. Instrum. Meas. doi:10.1109/TIM.2015.2476279

A New FPGA-Based Architecture for Iterative and Space-Variant Image Processing

Stefano Marsi, Sergio Carrato and Giovanni Ramponi

Abstract We propose a strategy to realize an innovative FPGA-based architecture able to speed up the Lucy-Richardson algorithm (LRA) for space-variant image deconvolution. The architecture exploits the possibility to distribute data into different memory blocks in the FPGA. In such a way, the algorithm execution is split into several channels operating in parallel. Since the LRA is implemented via an iterative and space-variant convolution, the approach adopted in this paper can be exploited in other similar image processing algorithms.

1 Introduction

In many practical situations, digital images or video frames undergo distortions that can be modelled as the convolution of an ideal image with a linear operator described by a given Point Spread Function (PSF). The Lucy-Richardson algorithm (LRA) [1, 2] is a classic and widely used tool for the restoration of these images. It performs an iterative deconvolution that can be formulated as follows:

$$D_k = \sum_i S_{i,k} W_{i,r} \tag{1}$$

$$W_{i,r+1} = W_{i,r} \sum_k S_{i,k} \frac{H_k}{D_k} \tag{2}$$

S. Marsi (✉) · S. Carrato · G. Ramponi
DIA—University of Trieste, via A.Valerio 10, Trieste, Italy
e-mail: marsi@units.it

S. Carrato
e-mail: carrato@units.it

G. Ramponi
e-mail: ramponi@units.it

A. De Gloria (ed.), *Applications in Electronics Pervading Industry, Environment and Society*, Lecture Notes in Electrical Engineering 409,
DOI 10.1007/978-3-319-47913-2_2

where W_i is the i-th pixel of the original, raster-scanned image W that we want to recover, S is the PSF of the distortion, $H = W * S$ is the degraded image, and r represents the iteration index.

If the PSF is stationary, the equation can be simplified and the result can be obtained using Fourier techniques [1, 2]. If the PSF is space-variant instead, such as for cases of lens distortions and aberrations or in the shake effect present in long-exposure photographs [3–6], the LRA becomes in practice extremely demanding. Assuming for instance to process a 640 × 480 image, both summations in Eqs. (1) and (2) extend to about 3.10^5 elements at each iteration. Moreover, the variables W, H and D require approximately 2.5 Mb each of storage space, while the 8-bit coefficients $S_{i,j}$ require approximately 94 GB.

In this paper we present an implementation of the LRA that exploits the sparsity of the deconvolution matrix and the computing power of modern FPGAs, and is able to process 640 × 480 frames at the estimated rate of 5 frame/s.

2 The Proposed Architecture

We start by observing that the matrix of the coefficients $S_{i,j}$ is not a generic matrix but a convolution matrix that models the different PSFs of each pixel in the image. It is reasonable to assume that each PSF affects only a rather limited number of pixels. Taking advantage of the theory of sparse matrices, a significant reduction both in computational effort and in memory requirements can then be obtained. Many strategies and architectures exist that are suitable to compute the product of a sparse matrix with a vector (SpMV product) [7, 8]. Such solutions however are highly resource-consuming and they apply to generic sparse matrices, whose nonzero values may occupy any position in a row, and are highly resource-consuming. Furthermore, it should be noted that in Eqs. (1, 2) the SpMV products must be performed twice and in two different manners: in Eq. (1) it can be directly realized via a SpMV product between S and W, while Eq. (2) requires a product with the transposed matrix S^T (SpMTV product). Sparse matrices are typically coded by rows; this permits to access sequentially the matrix data when the SpMV product is performed. However, this code is not compatible with the execution of the SpMTV product: the latter requires indeed a prior transposition operation, which is quite complex to realize [8] for sparse matrix representations.

In our implementation we exploit the specific structure of the matrix S, which manifests itself if the information content of the matrix is analyzed with some care. Indeed, scanning the images in lexicographical order and considering the i-th pixel, S_{ij} represents the value taken by the PSF associated with pixel “i” in position “j”. Thus, the i-th row of matrix S contains the PSF associated with pixel i: the positions of the non-zero values in the row correspond to the positions of the pixels involved in the PSF, and their values are the values assumed by the PSF. Conversely, the j-th column takes non-zero values only in correspondence of those pixels whose PSF passes through the pixels “j”, and the associated value is actually the PSF of the pixel “*i*” in position “*j*”. These considerations will be very useful in the simplification of the SpMV and SpMTV products explained below.

The PSFs that the LRA uses obviously depend on the kind of distortion we want to correct. For instance, in the case of images degraded by motion blurring the PSFs typically take the form of a path of contiguous pixels. For images degraded by lens blurring or aberration, instead, the PSFs are typically composed by a set of contiguous pixels grouped in an ellipsoid-like shape. The PSFs have to be previously estimated knowing the lens characteristics or the movement of the camera, and can be compactly stored using a chain code. Furthermore, we have experimentally verified that even quite a severe quantization of the values of the PSFs produces small degradations in the restored output: using more than five bits per coefficient does not lead to a significant improvement in the final result. Finally, thanks to the previously described structure of the S matrix, the same coding strategy can be adopted to represent both its rows and its columns; in such a way the calculation of the SpMV and SpMTV products is respectively simplified.

The architecture we propose to realize Eqs. (1, 2) is depicted in Fig. 1. The blocks H, W and T are memories that contain the values of the original image to be processed (H), the deblurred image (W) at a given iteration step, and some temporary values (T) obtained through a point-by-point division between the values of H and the result of Eq. (1). The block “SpMV/SpMTV” is used to perform both the summations. The block “1/x” performs the reciprocal operation; it is realized with a lookup table. A suitable timing system, not shown in the figure, controls the read/write memories and switches the multiplexer to build the correct path during the different phases of the algorithm.

Each iteration of the algorithm requires two loops through the proposed circuit. In the first loop the values contained in the matrix W are convoluted with the coefficients S_{ij} to realize Eq. (1). These values are sequentially divided by the H values and stored in a temporary memory T. In the second loop, the values in T are convoluted with the transposed matrix S^T. The results, multiplied by W, are

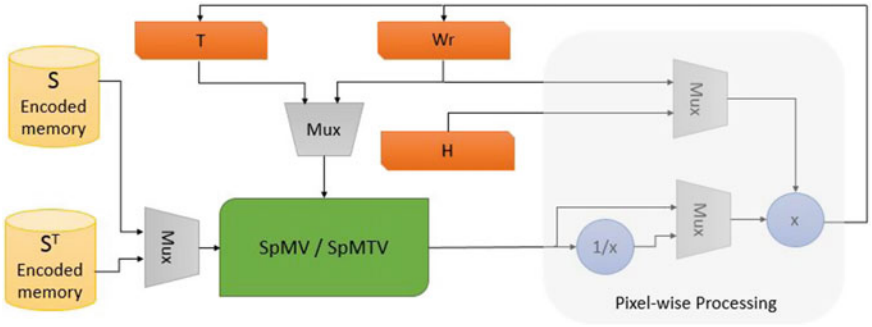

Fig. 1 The architecture proposed to simplify the realization of the iterative convolution process addressed in the Lucy-Richardson algorithm

overwritten on the same *W* value. The process is iterated until the result converges to a stable solution. The entire process typically takes a few tens iterations.

The core of the architecture is the SpMV/SpMTV block. Figure 2 shows its internal structure, and the way it connects to the adjacent blocks and to the memory. A memory contains all the PSFs associated with the various pixels, sorted in a lexicographic order and chain-coded. The system sequentially accesses these data and, through an appropriate decoder, extracts both the weights and the positions of the pixels composing each PSF. By means of the position information, the image pixels that are involved in the convolution process are downloaded from a dedicated memory. These values are multiplied by the proper weights of the PSF and are accumulated in a register (MAC). A control system, not shown in the figure, handles the synchronized access to the memory and resets the MAC when the summation is accomplished. Finally, a pipeline structure permits to perform both the MAC process and the decoding of the PSF in parallel.

When the system is implemented in an FPGA, the memories that contain the image data should be split in a series of separate blocks. The FPGA we chose is an Altera Stratix V, with “M20K” embedded memory blocks. Exploiting the fact that the accesses to these blocks can be accomplished independently each from the other ones, the SpMV product can be performed through a number of parallel channels. While a channel evaluates the convolution related to one pixel position, other channels can perform the same operation for pixels located elsewhere. The only constraint is that different channels should not access the same memory block at the same time, i.e., the pixels processed by every channel must belong to rows that are suitably distant one from each other.

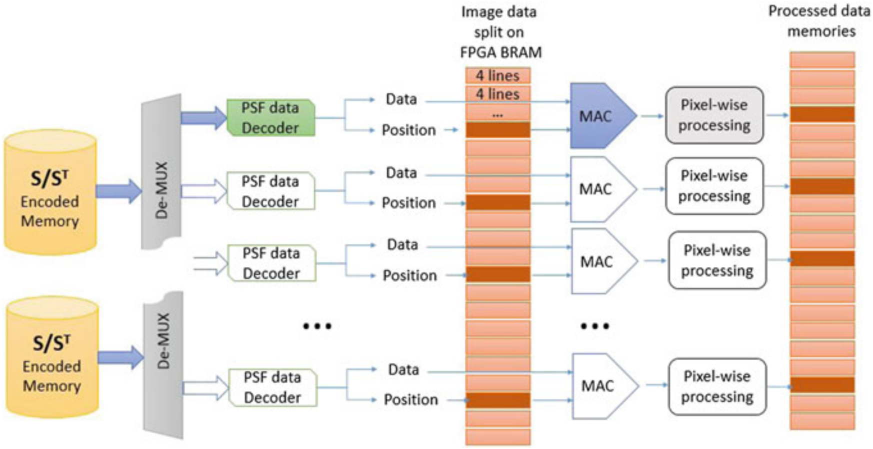

Fig. 2 The structure of the proposed architecture, designed to speed up the space-variant convolution process using several channels working in parallel. The architecture is suitable to perform both the SpMV and SpMTV products

For instance, considering that each M20K block of the FPGA can contain four rows of a 640 × 480 image and supposing that the PSFs do not extend to more than ten contiguous rows, the convolution can be performed without accessing more than five contiguous M20K blocks. Consequently, the convolution related to the pixels of a given row is calculated in parallel with those associated to pixels located at a distance of 20 rows. Exploiting this strategy, the convolution process is replicated into 24 channels operating in parallel, reducing the processing time by the same factor.

The internal FPGA memory stores the image data. The PSFs are in general more resource-consuming, and require an external memory chip. Although this chip cannot provide the data for the channels in a parallel way, the architecture can still take advantage of the parallelism between the channels: it is sufficient to appropriately vary the phase of the external memory access among the various processing channels. For example, suppose the first channel accesses the memory containing the PSF, then collects the needed data, stores them into a local resource, releases the access to external memory, and finally begins the processing. The second channel can now access the memory, store locally the data and begin its processing. This procedure is repeated until all the channels have completed their accesses to the PSF memory. At this time the first channel has presumably completed the convolution calculation related to the first pixel, it can then proceed loading the PSF data related to the second pixel and so on.

The proposed architecture can perform the SpVM product very quickly. Let us suppose we need to process 640 × 480 images. Assume a 100 MHz clock and consider that each MAC can be performed in one clock cycle. Assume also that each PSF be coded using approximately 50 bytes, and that 24 parallel channels are used. Then, the whole SpMV product can be completed in around 6.4 ms. This time is shorter than the one needed to access the external memory. Indeed, the PSF must be read for each pixel, totalling 15×10^6 memory accesses per frame; with a DDR3 memory having a transfer rate of 800 MT/s, the SpMV product then requires about 20 ms. It should be mentioned that this time could easily be halved, by storing the PSFs in two memories that operate in parallel.

Since the LR algorithm can converge in about ten iterations, and since the SpVM product must be repeated twice in each cycle, the entire de-blurring operation can be completed in about 0.2 s. It is also noteworthy that the architecture proposed in this paper is easily scalable: it can be used for larger images, or for larger and much more complex PSFs, if sufficient resources are available. The technological bottleneck is currently the internal memory of the FPGA, which today reaches a maximum of 50 Mb in the Stratix V FPGAs.

The required memory resources grow linearly with the size of the images to be processed. The processing time, instead, is substantially independent of the image size while it mainly depends on the size of the PSFs. A strategy to reduce the computation time and to increase the frame rate could be to split the entire MAC operation, performed in each channel, into several partial MAC blocks, operating in parallel. In such a case, however, a suitable arbitration system should be introduced to control the access to the memory to feed the partial MAC operators. At the same time, to reduce the access time to the external memory, the PSFs information should be partitioned into several memories operating in parallel.

3 Simulation Results

We propose a de-blurring experiment based on the described algorithm. We corrupt the frames of a video surveillance sequence, through a non-uniform spatial convolution that emulates a lens distortion. We then estimate the original data using the LRA. The PSF matrix that distorts the image is slightly different from the one used for the restoration process; this permits to verify the robustness of the method when the distortion process is not known exactly.

The space-variant PSF we use to model the frame distortion is a two-dimensional asymmetric Gaussian function with a superimposed central impulse [6]. The variance along one axis is quite small, while it is larger along the orthogonal axis. Moreover, it increases moving from the center toward the edges of the image. The orientation of the PSFs is also space-variant. A graphical representation of this matrix is shown in Fig. 3a. Note that even if the PSFs are shown only on a coarse grid of points, every pixel of the image is associated to a PSF.

The matrices used for the convolution and for the de-convolution processes differ for the presence of speckle noise with variance 0.04. The noise-corrupted matrix is used in the convolution process, while the clean one is used in the deconvolution; in this way we can simulate e.g. the presence of local irregularities in the lens, which cannot be modeled by the Gaussian PSF. Speckle noise has been selected in order to modify the values of the PSF without affecting the sparsity of the matrix or the main direction of each PSF. In Fig. 3b the obtained result is shown, together with the original and the corrupted data. It can be noted that, except for a slight distortion due to the border effect, the quality of the restored image has significantly improved.

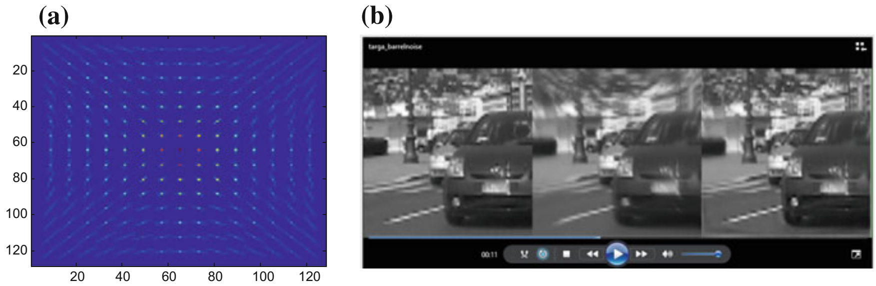

Fig. 3 **a** Representation of the PSFs matrix. **b** Simulated results: an original frame (*left*), its corrupted version (*center*), the restored frame (*right*)

4 A Comparison of Methods

A method similar to the one proposed in this article has been published in [9]: the Authors make combined use of a DSP to control the dataflow and of an FPGA as a coprocessor to speed up repetitive tasks, and they achieve real-time operation. It should be underlined, however, that the Authors have adopted in their study the simplified algorithm proposed by Richardson, where the original image is blurred by a shift-invariant point spread function. A similar simplification has also been addressed in [10], where the de-blurring of an image acquired by a robot is performed with a frame rate of tens of frames per second.

A common approach to deal with space variant PSF consists in segmenting the image into overlapped patches, each of which is processed with a spatially invariant deconvolution operator; this has been done e.g. by Weddell and Webb [11] and Rerabek [12]. However, all these methods have been devised to operate off-line. To the best of our knowledge, the strategy proposed in this paper is the only one which combines a space-variant PSFs deconvolution process and an architecture suitable to operate in real-time.

5 Conclusions

In this paper we have proposed a strategy to realize an architecture performing an iterative space-variant convolution. The suggested architecture is particularly suited for the implementation of the LRA. By exploiting the FPGA structure and in particular the possibility to store image data in different memory blocks, a strategy for fast processing has also been suggested. The proposed system is able to operate in real time on a video surveillance system having 640 × 480 resolution. The proposed architecture is scalable and can be easily applied to larger images or with different kinds of PSF.

References

1. Richardson, W.H.: Bayesian-based iterative method of image restoration. J. Opt. Soc. Am. **62**, 55–59 (1972)
2. Lucy, L.B.: An iterative technique for the rectification of observed distributions. Astron. J. **70**, 745–754 (1974)
3. Harmeling, S., Hirsch, M., Schölkopf, B.: Space-variant single-image blind deconvolution for removing camera shake. In: NIPS 2010, Vancouver, Canada (2010)
4. Joshi, N., Kang, S.B., Zitnick, C., Szeliski, R.: Image deblurring using inertial measurement sensors. In: SIGGRAPH ‘10, New York, NY, USA (2010)
5. Sindelar, O., Scoubek, F., Milanfar, P.: Space-variant image deblurring on smartphones using inertial sensors. In: Proceedings of IEEE Computer Vision and Pattern Recognition Workshops (CVPRW), pp. 191–192 (2014)

6. Wei, J., Bouman, C.A., Allebach, I.P.: Fast space-varying convolution using matrix source coding with applications to camera stray light reduction. IEEE Trans. Image Process **23**(5) (2014)
7. Fowers, J., Ovtcharov, K., Strauss, K., Chung, E.S., Stitt, G.: A high memory bandwidth FPGA accelerator for sparse matrix-vector multiplication. In: 22nd IEEE Annual Symposium on Field-Programmable Custom Computing Machines (FCCM), pp. 36–43 (2014)
8. Aktulga, H.M., Buluc, A., Williams, S., Chao, Y.: Optimizing sparse matrix-multiple vectors multiplication for nuclear configuration interaction calculations. In: IEEE 28th International Symposium on Parallel and Distributed Processing, pp. 1213–1222 (2014)
9. Wang, Z., Weng, K., Cheng, Z., Yan, L., Guan, J.: A co-design method for parallel image processing accelerator based on DSP and FPGA. In: Proceedings of SPIE, vol. 8005 (2011)
10. Kim, M.D., Ueda, J.: Real-time image de-blurring and image processing for a robotic vision system. 2015 IEEE International Conference on Robotics and Automation (ICRA), Seattle, Washington, 26–30 May 2015
11. Weddell, S.J., Webb, R.Y.: The restoration of extended astronomical images using the spatially-variant point spread function. In: 23rd International Conference Image and Vision Computing, New Zealand (2008)
12. Rerabek, M.: Space variant PSF—Deconvolution of wide-eld astronomical images. Acta Polytech. **48**(3) (2008)

Embedded Electronic Systems for Tactile Data Processing

Ali Ibrahim, Luca Noli, Hussein Chible and Maurizio Valle

Abstract The development of embedded electronic systems for tactile data processing is increasingly demanded for many application domains e.g. robotics, prosthetics, industrials automation etc. In this paper we present the requirements for the embedded electronic system implementation of real time tactile data processing based on Tensorial Kernel approach. The paper provides the performance analysis of the FPGA implementation methods of the singular value decomposition as a result on the way to achieve the desired system.

1 Introduction

Embedded electronic systems are applied extensively in industry and in almost all spheres of human life. These systems are usually designed for specific and dedicated functions, and interact with their external environment through sensors and actuators. Each embedded electronic system has specific design constraints. However, there are some common features which are expected from these systems, namely high computing performance, real time operation, low power consumption and small size. However, the computation complexity of the processing algorithms poses a tough challenge in the development of the embedded electronic systems particularly when dealing with huge amount of data to be processed in real time.

Machine learning (ML) methods have been increasingly used for the data analysis in many domains, such as neural/medical data [1] and tactile sensors data [2], and have emphasized the need to take the structure of the original data into consideration. A pattern recognition framework based on Tensorial Kernel

---

A. Ibrahim (✉) · L. Noli · M. Valle
Department of Electrical, Electronic and Telecommunication Engineering and Naval Architecture (DITEN), University of Genoa, via Opera Pia 11, 16145 Genoa, Italy
e-mail: ali.ibrahim@edu.unige.it

A. Ibrahim · H. Chible
Microelectronics Lab, PhD School for Sciences and Technology (EDST)-Lebanese University, AL Hadath, Lebanon

A. De Gloria (ed.), *Applications in Electronics Pervading Industry, Environment and Society*, Lecture Notes in Electrical Engineering 409,
DOI 10.1007/978-3-319-47913-2_3

approach has been presented in [2]. It has proved its effectiveness in processing tactile data when dealing with input tensors. In this perspective, our main goal is to develop a real time embedded electronic system for tactile data processing based on Tensorial Kernel approach. In this paper, we present the system requirements and the performance analysis of the FPGA implementation methods as the results on the way to develop the desired embedded electronic system.

2 Embedded Electronic System Requirements

A general block diagram of the electronic system is shown in Fig. 1. Three basic tasks are handled by the Signal Processing block, namely decimation, setting of data resolution to the Effective Number of Bits (ENOB) and arranging of the serial bit stream into a matrix stream. Decimation implies low pass filtering and down-sampling the input signal, it is the process of reducing the sampling rate down to the Nyquist rate (2 kSamples/s per sensor).

The effective number of bits is given by the following equation: $\mathrm{ENOB} = (\mathrm{SNR} - 1.76)/6.02$, where SNR is the Signal to Noise Ratio. In [3], experimental results reporting SNR values for different values of the contact force at 1 kHz are presented and the ENOB resulted equal to 8. In the present setup ENOB has been set to 8.

Then, samples have to be arranged as a time stream of arrays A(8, 8), i.e. as a third order tensor $\mathbf{S}_1$ where time defines the third tensor dimension (the first two being defined by the generic matrix A corresponding to the geometric arrangement of the input sensor array). If the time window (i.e. the input touch duration t) is set for instance to $t = 0.75$ s, the dimension of the tensor $\mathbf{S}_1$ is (8, 8, 1500). To reduce the huge amount of samples due to the third component of the tensor $\mathbf{S}_1$ an additional factor has been added to the down-sampling ratio to reach (Nyquist rate/D)/s per sensor where D is the sub-sampling factor; sub-sampling is the process of extracting one matrix each group of the input matrix stream. The group size is

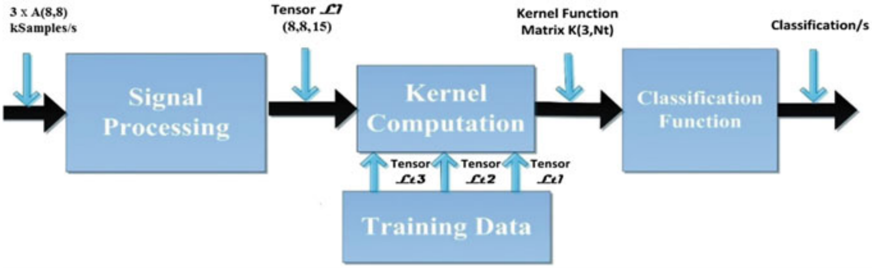

Fig. 1 General block diagram of the digital embedded electronic system

defined by the sub-sampling factor D [4]. Setting D to 100, the Signal Processing block output data rate is equal to $\mathbf{L}_1$ (8, 8, 15)/t with 8 bit data resolution.

The Kernel Computation block unfolds the input tensor, computes the singular value decomposition of the unfolded matrices, then evaluates the kernel functions. Figure 2 illustrates the different steps of the kernel computation method proposed in [1].

The tensor unfolding is a matrix representation where all the column (row) vectors are stacked one after the other [5]. As $\mathbf{L}_1$ is third order tensor, three matrices ($X_{(1)}$, $X_{(2)}$, $X_{(3)}$) are obtained by unfolding applying. The output data stream is made of 3 matrices [$X_{(1)}$(8120), $X_{(2)}$(8120), $X_{(3)}$(15,64)]/t. The kernel computation block computes the singular value decomposition (SVD) of the unfolded matrices ($X_{(1)}$, $X_{(2)}$, $X_{(3)}$) as sketched in Fig. 2. SVD transforms a matrix into the product of three matrices e.g. $X_{(3)} = USV^T$ where U(15,15) is an orthogonal matrix containing the 15 Eigen vectors of $X_{(3)}$ (15,64) $X^T_{(3)}$(64,15), and V(64,64) is an orthogonal matrix containing the 64 Eigen vectors of $X^T_{(3)}$(64,15) $X_{(3)}$(15,64). The S(15,15) matrix is a diagonal matrix diag ($\sigma_0,\ldots\ldots,\sigma_{14}$), where the σ_i are the singular values of $X_{(3)}$ (i.e. the square roots of the Eigenvalues), being arranged in descending order. Once the SVD of the unfolded matrices ($X_{(1)}$, $X_{(2)}$, $X_{(3)}$) is computed, the elaboration of the kernel factor could be addressed. The detailed computation process is presented in [2].

The training data consists of three different tensors $\mathbf{L}_{t1}$, $\mathbf{L}_{t2}$, and $\mathbf{L}_{t3}$ corresponding to three different classes.

The Kernel Computation for $\mathbf{L}_1$ is repeated for the N_t tensors corresponding to each class stored in the Training Data block. Classification function block computes the function presented in [2] using the matrix K(N_t, 3) output of the Kernel computation block. Thus, the classification function block figure out one classification each input touch duration t.

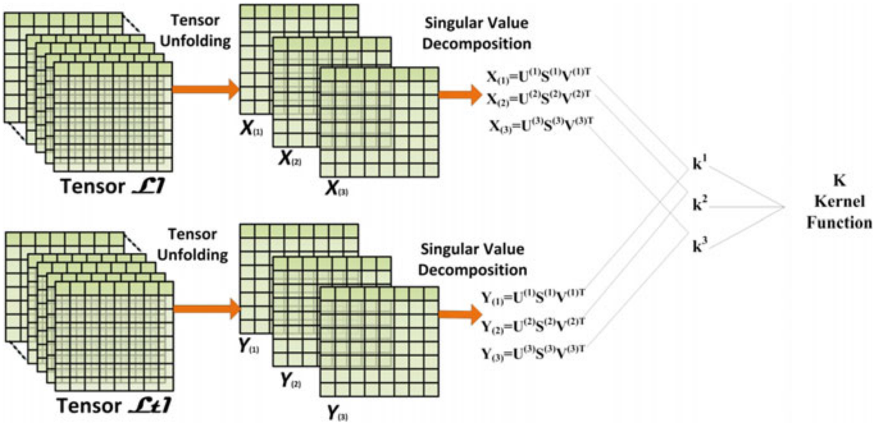

Fig. 2 An illustration of the different steps of the kernel-based tensor computation. k^n represent the kernel factor

3 FPGA Implementations Methods

The SVD is the most computational expensive algorithm of the Tensorial Kernel approach [6]. One sided Jacobi algorithm is used to compute the SVD as it provides high accuracy and fast convergence [7].

The one sided Jacobi computes the SVD through a pre- and post-rotation of the input matrix by the Jacobi rotation. For that, the complexity of this algorithm lies in the computation of the angle of rotation (or cosine and sine functions), and in the management of the rotations. Different methods could be used to compute the angle of rotation and to manage the rotations for the one sided Jacobi algorithm; we have done three different implementations: (1) *Implementation 1*: uses CORDIC method in vectoring mode and one sided Jacobi rotation [8], (2) *Implementation 2*: uses Jacobi method and one sided Jacobi rotation, and (3) *Implementation 3*: uses CORDIC method in vectoring mode and CORDIC method in its rotation mode [9].

3.1 Jacobi Method

Jacobi method is defined by the following equations:

$$\begin{aligned} \alpha = \frac{y-x}{2w} \quad & tg\theta = \frac{sign(\alpha)}{|\alpha| + \sqrt{1+\alpha^2}} \\ \cos\theta = \frac{1}{\sqrt{1+tg^2}} \quad & \sin\theta = tg\theta \times \cos\theta \end{aligned} \tag{1}$$

where x, y, and w are the elements of the input matrix. These equations are used to compute the sine and cosine functions without calculating the angle of rotation. They are introduced as the most accurate since they diminish the accumulation of the rounding errors. The implementation uses four adders and one subtracter, three dividers, three multipliers, and two square roots.

3.2 CORDIC Method

The Coordinate Rotation Digital Computer (CORDIC) is an iterative algorithm and extremely hardware friendly. It involves a set of Shift-Add operations for computing a very rich set of functions from the one basic set of equations [10]. CORDIC can be either operated in vectoring mode or in rotation mode. In the vectoring mode, CORDIC rotates the input vector through whatever angle is necessary to align the resultant vector with the horizontal axis. The result of the vectoring operation is a rotation angle and the scaled magnitude of the original vector. In rotation mode, the angle accumulator is initialized with the desired rotation angle.

3.3 One Sided Jacobi Rotation

This method is based on the traditional one sided Jacobi rotation. It updates the row/column of the input matrix after each pre/post-rotation by applying a row column multiplication to achieve the rotation. The implementation uses four multipliers, one adder and one subtracter.

4 Performance Analysis

Regarding the complexity of the approach, and in order to comply with the constraints imposed by the application, implementation methods have to be well assessed to achieve satisfied results in terms of silicon area, time delay, and power consumption. Hence, this section addresses the assessment of the FPGA implementation methods of the one sided Jacobi algorithm in terms of percentage occupied area, time delay and estimated power consumption;

The design has been implemented for a Xilinx SPARTAN-6 XC6slx16 FPGA device. Table 1 shows the implementation results for a matrix size 4 × 4. The latency has been calculated using the following formula:

$$Elapsed\ time = N \times \frac{1}{f_{\max}} \tag{2}$$

where N is the number of clock cycles needed to compute the SVD, and f_{max} is the maximum frequency. Moreover, the power consumption has been estimated using XPower Analyzer provided by Xilinx tool.

Table 1 shows that *Implementation 3* has the lowest power consumption over the other implementations. Nonetheless, the difference in the estimated power is so tiny. It is clearly seen that the time needed to compute the SVD using *Implementation 2* is acceptable but the occupied area is very high. For that, using this implementation is very expensive and will limit the SVD to the small matrices only. In the other hand, *Implementation 3* provides the best results in terms of occupied area but it possesses the highest latency. So, using *Implementation 3* is suitable for applications which intend to diminish the silicon area with acceptable time response. Finally, *Implementation 1* provides the best results in terms of latency with a satisfied occupied area. For our goal, a tradeoff between the occupied

Table 1 Implementation results for a Xilinx SPARTAN-6 XC6slx16 FPGA

	Occupied area (%)	Latency (us)	Power consumption (W)
Implementation 1	21	26.2	4.05
Implementation 2	51	65.6	4.16
Implementation 3	15	57.5	3.84

Table 2 SVD results using Virtex-5 XC5VLX330T FPGA

	SVD for $X_{(1)}(8,120)$ [%]	SVD for $X_{(2)}(8,120)$ [%]	SVD for $X_{(3)}(15,64)$ [%]
Implementation 1	17	17	31

area and latency is needed. Hence, we can conclude that the *Implementation 1* represents the tradeoff for the hardware implementation of the SVD based on one sided Jacobi algorithm.

Furthermore, Table 2 shows the results of occupied area for the matrices $X_{(1)}(8,120)$, $X_{(2)}(8,120)$, $X_{(3)}(15,64)$ (see Sect. 2) using *Implementation 1* for an FPGA Virtex-5 XC5VLX330T. So, the SVD implementations occupy about 65 % of this FPGA device. Moreover, the computation of the SVD represents 70 % of complexity of the overall system [6]. To this end, a Virtex-5 XC5VLX330T could be an estimation of the hardware requirements for the Tensorial Kernel approach implementation.

5 Conclusion and Future Perspectives

Embedded electronic system is an essential need for tactile sensor systems. In this paper we presented the embedded electronic system requirements to implement the machine learning based Tensorial Kernel approach for tactile data processing. The work provides the performance analysis for the FPGA implementation methods of the SVD which represents the bottleneck of the presented approach. This analysis figure out an implementation suitable with real time embedded systems by providing efficient results in terms of silicon area and time latency. Moreover, the hardware requirements for the overall approach have been estimated according to the selected implementation. The presented work is a part of the hardware implementation of real time embedded processing for tactile sensors data. Next step will consist on finalizing the other blocks of the machine learning based on Tensorial Kernel approach.

References

1. Signoretto, M., De Lathauwerb, L., Suykens, J.A.K.: A kernel-based framework to tensorial. Networks. **24**, 861–874 (2011)
2. Gastaldo, P., Pinna, L., Seminara, L., Valle, M., Zunino, R.: A tensor-based pattern-recognition framework for the interpretation of touch modality in artificial skin systems. IEEE Sens. J. **14**(7) (2014)
3. Pinna, L., Valle, M.: Charge amplifier design methodology for PVDF based tactile sensors. J. Circ. Syst. Comput. (JCSC), **22**(8) (2013)

4. Gastaldo, P., Pinna, L., Seminara, L., Valle, M., Zunino, R.: A tensor-based approach to touch modality classification by using Machine Learning. Robot. Auton. Syst. **63**, 268–278 (2015)
5. De Lathauwer, L., De Moor, B., Vandewalle, J.: A multilinear singular value decomposition. SIAM J. Matrix Anal. Appl. **21**(4), 1253–1278 (2006)
6. Seminara, L., Pinna, L., Ibrahim, A., Noli, L., Caviglia, S., Gastaldo, P., Valle, M.: Towards integrating intelligence in electronic skin. Elsevier Mechatronics. doi:10.1016/j.mechatronics.2015.04.001
7. Wang, X., Zambreno, J.: An FPGA implementation of the hestenes-jacobi algorithm for singular value decomposition. In: IEEE 28th International Parallel & Distributed Processing Symposium Workshops (2014)
8. Ibrahim, A., Valle, M., Noli, L., Chible, H.: Singular value decomposition FPGA implementation for tactile data processing. IEEE NEWCAS 2015. doi:10.1109/NEWCAS.2015.7182094 (2015)
9. Ibrahim, A., Valle, M., Noli, L., Chible, H.: FPGA implementation of fixed point CORDIC-SVD for E-skin systems. IEEE PRIME 2015. doi:10.1109/PRIME.2015.7251399
10. Andraka, R.: A survey of CORDIC algorithms for FPGA based computers. In: Proceedings of 1998 ACM/SIGDA 6th International Symposium on FPGA, pp. 191–200

Microwave Imaging for Breast Cancer Detection: A COTS-Based Prototype

**Azzurra Pulimeno, Marco Vacca, Mario R. Casu, Jorge A. Tobon,
Francesca Vipiana, Daniele Jahier Pagliari, Raffaele Solimene
and Luca P. Carloni**

Abstract Microwave Imaging (MI) for breast cancer detection is a safe diagnostic method that can be used repeatedly in screening campaigns because it does not use ionizing radiations. So far it has been proven in labs and clinics with the aid of costly and bulky instrumentation tools such as a vector network analyzer. In this paper we show that it is possible to build a low-cost system using off-the-shelf components, custom-made antennas, and a Zynq programmable SoC for accelerating the image reconstruction algorithm. We prove the detection capability of our MI system with two 2D tumor phantoms with different dielectric properties. In

---

Work partly supported by the Italian MIUR under FIRB project MICENEA (Microwave Imaging for Combined Early Diagnostics of Breast Cancer).

A. Pulimeno · M. Vacca · M.R. Casu (✉) · J.A. Tobon · F. Vipiana
Department of Electronics and Telecommunications, Politecnico Di Torino, Turin, Italy
e-mail: mario.casu@polito.it

A. Pulimeno
e-mail: azzurra.pulimeno@polito.it

M. Vacca
e-mail: marco.vacca@polito.it

J.A. Tobon
e-mail: jorge.tobonvasquez@polito.it

F. Vipiana
e-mail: francesca.vipiana@polito.it

D.J. Pagliari
Department of Control and Computer Engineering, Politecnico Di Torino, Turin, Italy
e-mail: daniele.jahier@polito.it

R. Solimene
Department of Industrial and Information Engineering, Second University of Naples, Caserta, Italy

L.P. Carloni
Department of Computer Science, Columbia University, New York City, NY, USA

A. De Gloria (ed.), *Applications in Electronics Pervading Industry, Environment and Society*, Lecture Notes in Electrical Engineering 409,
DOI 10.1007/978-3-319-47913-2_4

terms of execution speed of the imaging algorithm, we obtain a speed-up of more than 30× with respect to an execution on a high-end desktop processor.

1 Introduction

Breast carcinoma is the most common cancer in women worldwide. According to the American Cancer Society, it is the second leading cause of cancer deaths among women in the US [1]. Screening campaigns are fundamental because early detection is effective in improving the prognosis of patients, yet conventional diagnostic methods used in screening have significant drawbacks. X-ray mammography, for instance, despite being the gold standard among the breast cancer diagnostic methods, is not very effective in young women with dense breasts. Moreover, it cannot be repeated too frequently because it uses ionizing radiations. It also requires breast compression, which makes it uncomfortable for the patient, if not painful. Ultrasound capability is limited in that it can only distinguish liquid-filled cysts from tumors. Contrast-enhanced magnetic resonance imaging (MRI) is also used to diagnose breast cancer. MRI is highly sensitive but it has a very high false positive rate. Moreover, it is by far the most expensive among the methods in use, which is a significant drawback in an era in which national health services are struggling against financial issues.

Microwave Imaging (MI) emerged lately as an alternative diagnostic method for breast cancer. The principle upon which this technique is based is the significant dielectric contrast that exists between tumor cells and the surrounding fat and fibro-glandular tissue [12]. By illuminating the breast with signals in the microwave spectrum and by acquiring and processing the scattered response, it is possible to reconstruct breast maps under two possible modalities. In the first modality, a map of the complex permittivity (i.e. dielectric constant and conductivity) inside the breast is reconstructed. In the second one, the positions of the points that reflect the most the incident electromagnetic field are highlighted in the reconstructed breast map. If the goal is only the detection and the localization of a tumor, the second modality is sufficient.

MI has been proven effective with numerical and physical phantoms and with preliminary clinical studies [9]. Even though MI is still lagging behind mammography in terms of resolution and accuracy, the lack of risk for the patient due to the absence of ionizing radiations, and the better response for younger women with denser breast tissues, suggest its adoption in screening campaigns. Finally, the cost of the MI medical equipment will be significantly less than the cost of a current digital mammography system.

In this paper we illustrate our MI prototype for breast-cancer detection based on off-the-shelf components (COTS). Our aim is to replace a Vector Network Analyzer (VNA) typically used in MI with COTS components, to use custom-made antennas matched to the coupling medium, and to elaborate the acquired data in a low-cost programmable SoC with FPGA hardware accelerators that replace high-end

CPU/GPU. Since our goal is to detect a tumor, and not to reconstruct the entire map of permittivity, our method belongs to the second of the two classes outlined above.

This paper is organized as follows. We review the most important literature about MI systems in Sect. 2. In Sect. 3 we present the microwave front-end, the designed monopole ultra-wide band antenna, and the tank in which we conduct our experiments. We discuss the MI reconstruction algorithm and its hardware implementation in Sect. 4. We illustrate the results obtained in our experiments in Sect. 5. Conclusions are drawn in Sect. 6.

2 State of the Art of Microwave Imaging Systems

Ultra Wide-Band (UWB) Radar and Tomography are the most common approaches to microwave imaging.

In the radar approach, an array of antennas in different positions irradiates the breast with UWB pulses; the echoes are acquired and processed to reconstruct an image in which the scatterers are highlighted [8]. The tumor will scatter the incoming UWB pulses given its strong dielectric contrast with the normal breast tissue. The radar approach permits only the detection and localization of the tumor in the reconstructed breast image, hence it belongs to the second modality outlined in Sect. 1.

Although it is possible to implement the UWB radar approach to MI in the time-domain [16], a frequency-domain approach that reconstructs the pulses via FFT in a post-processing phase is more common [4]. In this way it is possible to exploit the higher signal-to-noise ratio offered by narrow-band receivers. Usually, a VNA is used to generate and acquire microwave signals, and the multiple antennas are connected to the VNA ports by means of power splitters and a complex array of switches [10]. The acquired signals undergo a processing phase that in the majority of the cases consists of a more or less sophisticated version of the beamforming algorithm. This algorithm is amenable to an efficient parallelization on a dedicated FPGA-based processing system [5]. Even though operations in the frequency domain simplify signals generation and acquisition with respect to the time domain, the UWB approach implies that all the parts involved, including the antennas, are designed to handle signals with a very large bandwidth. The consequence of the large bandwidth and the small frequency step needed to obtain a good resolution is a large acquisition time [7].

In the tomographic approach, the objective is to image the dielectric profile of the breast. This is obtained by irradiating the breast with continuous waves at a single frequency or at a few selected frequencies, by acquiring the scattered electromagnetic field, and by solving a problem of non-linear inversion aimed at determining the complex permittivity of each point in the breast [11]. Therefore, the tomographic approach belongs to the first of the two modalities described in Sect. 1.

The same configuration used for the UWB radar approach working in the frequency domain—multiple antennas, VNA, power splitters, and switches—can also be used in the tomography approach. There have been successful attempts, however, to replace the VNA with dedicated transceivers [11, 17]. Still, there are two main concerns with the implementation of the tomographic approach. First of all, since the non-linear inversion requires the solution of an ill-posed minimization problem, reliability issues may arise due to the possible occurrence of false solutions, let alone the problems of convergence and stability [14]. Second, the computationally-intensive iterative schemes for the solution of the problem may run for days even on a powerful CPU [6].

With our MI system, we address the problems of the two main approaches outlined above. We use the I-MUSIC imaging algorithm illustrated in [13], which does not require generating and acquiring signals over a large bandwidth and it efficiently uses only a few different frequencies in a relatively small bandwidth. Therefore, the design of our system is simplified with respect to previous approaches, which makes it possible to use low-cost off-the shelf components. Moreover, the execution of the I-MUSIC imaging algorithm can be accelerated by means of an FPGA working in tandem with a small embedded CPU, which reduces the execution time to a matter of seconds rather than hours or days.

3 Front-End, Antennas, and Measurement Tank

3.1 Front-End

In a typical MI setting, two antennas are connected to the two ports of a VNA and the transmission coefficient S_{21} is measured in magnitude and phase. To replace the VNA, we devised a system mainly composed of a frequency synthesizer (a transmitter, TX) and a Direct Conversion (DC) receiver (RX). We chose a DC receiver because of its robustness to phase mismatches [3]. Moreover, this choice is also supported by the availability of low-cost and small form-factor COTS that match the performance requirements defined by the system-level analysis performed in [7].

As shown in Fig. 1, the TX branch uses a Linear Technology LTC6946 chip, an ultra-low noise and spurious 0.37–5.7 GHz Integer-N synthesizer with integrated VCO. The TX frequency is currently manually controlled from a PC via a USB-interface board. The reference frequency is provided by a 10-MHz oven-controlled crystal oscillator. The generated RF signal is forwarded to a voltage-controlled variable-gain amplifier by Analog Devices. Then, the *RF out* signal in Fig. 1 is sent to the transmitting antenna.

The receiving antenna provides the *RF in* signal in Fig. 1 and is connected to the DC receiver through a high-performance Low Noise Amplifier (LNA) and a band-pass filter from 700 MHz to 2950 MHz, both by Mini-Circuits. The RX uses the Linear Technology LTM9004 chip, a 14-Bit Direct-Conversion receiver with SNR 80 dB/MHz, typical noise floor −148.3 dBm/Hz, dynamic range 86 dB, minimum detectable signal due to quantization −90 dBm (extended to −110 dBm with the LNA). The Local Oscillator input signal of the RX is provided by the TX

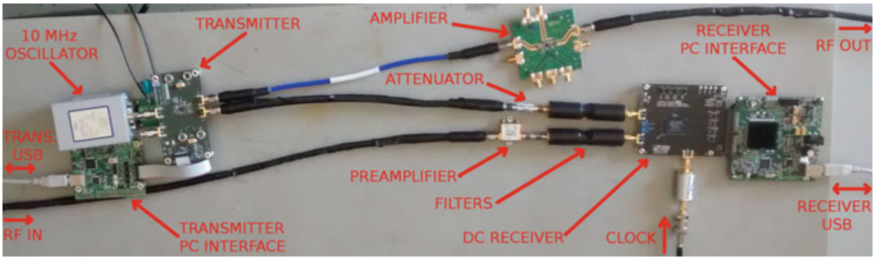

Fig. 1 Front-end system developed with low-cost, small-size off-the-shelf components

with a direct connection and an attenuation to avoid saturation. Finally, the digital values of the acquired signals are sent first to a PC through a USB-interface board and then to the programmable SoC for being processed.

Preliminary experimental results prove that this front-end architecture can replace a bulky vector network analyzer (VNA) [15].

3.2 *UWB Antenna*

We designed an Ultra-Wide Band (UWB) antenna with a good matching in the whole 0.5–3 GHz band when immersed in the coupling liquid, a lossy mixture of glycerin (80 %) and water (20 %) that reduces the mismatch caused by the background/skin interface. The front profile is optimized for 50 Ω matching while maximizing the radiated near field. We used the FEM method proposed in [2] to characterize and analyze the antenna scattering parameters during design. The antenna is printed in standard FR4 dielectric substrate. Figure 2 shows the antenna and its measured S_{11} scattering parameter.

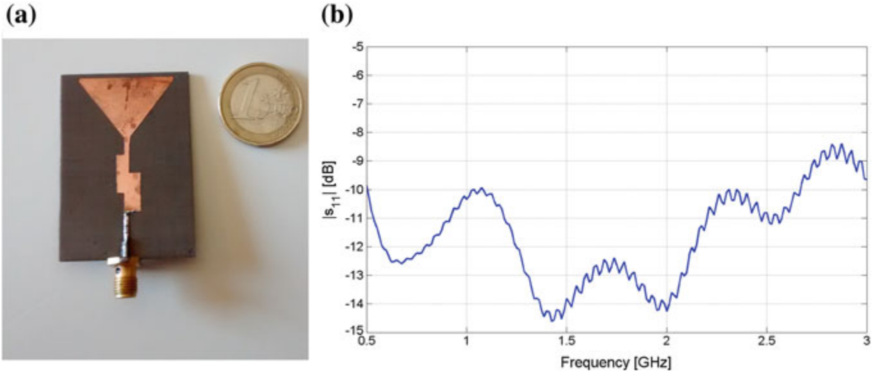

Fig. 2 **a** UWB Monopole and **b** S_{11} measured in 80–20 % glycerin-water mixture

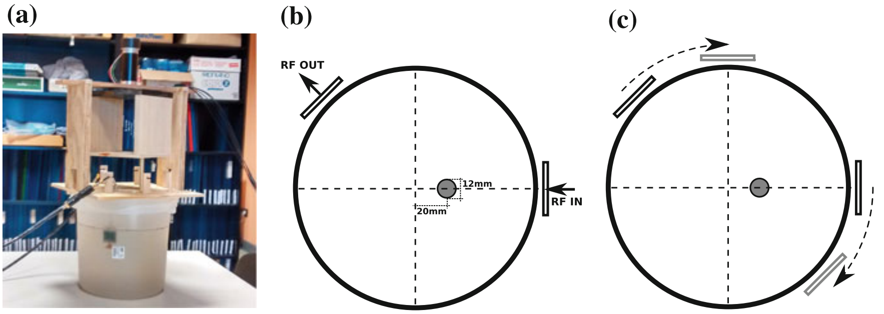

Fig. 3 Tank filled with glycerin-water mixture and the antennas **a**. Multiple antenna pairs are emulated via antennas rotation **b–c**

3.3 Measurement Tank

The TX and RX antennas are immersed in the cylindrical tank of Fig. 3(a) and are connected to the other RF parts via SMA connectors. The target is a tumor phantom represented by cylinders of different materials immersed in the tank. At the present stage we emulate multiple antennas by rotating a single pair of transmitting and receiving antennas that keeps a fixed angle between them that can be any multiple of 45 degrees. In the example in Fig. 3b–c, the angle is 135°. For simplicity, in this preliminary setting we actually rotate the phantom in 20-degree steps using a PC-controlled motor placed on top the tank. In a later stage we will have multiple fixed antennas and switches for connecting to the other RF parts.

For each position we acquire N different signals at N frequencies, which are inputs to the image reconstruction algorithm.

4 I-MUSIC Reconstruction Algorithm on a Xilinx Zynq

To generate the breast image, we adopted the MUltiple SIgnal Classification-inspired (I-MUSIC) algorithm [13]. I-MUSIC processes the N frequency samples in two phases: clutter removal and reflected-energy map generation.

The clutter component is due to a large background-skin scattering and is removed with a subspace-projection method based on singular value decomposition.

A map at frequency f_n is obtained by first computing the dominant eigenvector of the correlation matrix $\mathbf{R} = S_d^n \cdot (S_d^n)^H$, where S_d^n is the nth row of the matrix of decluttered samples, and its elements correspond to the different antenna positions. This eigenvector is then multiplied via Hermitian Product with Green functions that model the propagation between each antenna position and a given location in the scanned surface.

This computation is repeated for all possible locations and all N frequencies. The obtained maps at different frequencies are combined through a *detection function* that shows a peak only in correspondence of real tumors, rejecting single-frequency image artifacts. For a detailed description of I-MUSIC see [13].

I-MUSIC needs hardware acceleration to be performed in an acceptable time. A small 200 × 200 pixels image obtained with 18 antenna positions and 20 frequencies takes approximately 20 s with Matlab on a high-end desktop processor.

Execution time is dominated by the computation of Green functions and Hermitian Product. Therefore, we designed an accelerator for that algorithm section, targeting the Xilinx Zynq System-on-Chip (SoC). The Zynq allows to easily integrate the accelerated part, implemented in the SoC's programmable logic, with the rest of I-MUSIC implemented in software in the SoC's ARM processor.

We modeled the accelerator with behavioral SystemC, and used state of the art High Level Synthesis (HLS) tools to generate the corresponding Register Transfer Level (RTL) description. The adoption of HLS allowed us to greatly reduce the design time and to perform a thorough design space exploration.

The accelerator exploits the task pixel-level parallelism. Since every point of the scanned surface is processed independently, identical processing elements (PE) operate in parallel each on a *row* of the breast map. We chose an image row as atomic processing unit because it is a good balance between internal scratchpad memory size of the accelerator and communication overhead.

The computation in each PE involves complex operations such as division, square root, trigonometric function evaluation, etc. For each of these we devised a high-performance, pipelined implementation.

Processor-Accelerator communication is also optimized. The accelerator has a system-bus slave interface for commands and status information, and a master interface for DMA data transfers. Figure 4 shows the architecture of the developed I-MUSIC computing platform.

We implemented a version of the accelerator that includes the maximum number of processing elements that fit in the Programmable Logic of the Zynq XC7Z702 SoC. The accelerated part of the algorithm takes only 0.55 s to complete for the same input data of the MATLAB example above, which corresponds to a speed-up greater than 30×.

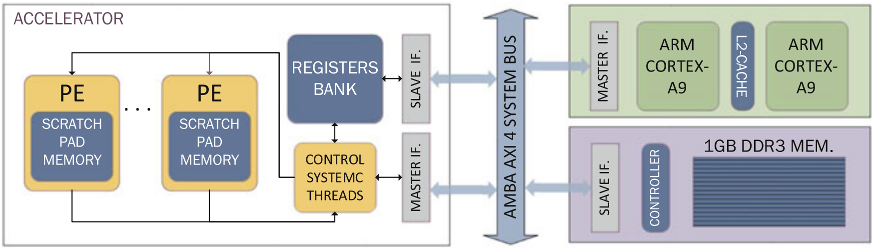

Fig. 4 I-MUSIC computing architecture on a Xilinx Zynq SoC

5 Experimental Results

We initially placed a metallic phantom rod with a 12-mm diameter in front of the transmitter antenna at a 20-mm distance from the tank center. Then we obtained 18 measurements rotating the rod counterclockwise in 20° steps, which emulates 18 antenna pairs. Measurements were taken at 10 different frequencies in 1.4–1.6 GHz range, which is where the receiver is best matched.

Figure 5 shows the results obtained with I-MUSIC. The yellow circle identifies the target, i.e. the metallic cylinder in this first experiment, while the colored shades highlight the scattering points detected by the algorithm. Figure 5a map is reconstructed starting from 5 frequency samples in the 1.4–1.6 GHz band. The target is clearly detected, albeit slightly shifted from its ideal position. The anomalous shadow is eliminated and the focus increased when we pick 10 frequencies in the same band, as shown in Fig. 5b.

In the first experiment, the use of a metallic tumor phantom can be considered a "best case" in terms of reflectivity. The second experiment that we report was obtained with a phantom that presents a much lower contrast with the background, which results in less scattering. We placed in the tank a 20-mm plastic dielectric cylinder filled with a 40–60 % glycerin-water mixture, which offers a dielectric contrast with the background comparable to the contrast of a real tumor with a fatty breast tissue. The imaging result is shown in Fig. 6. Also in this case, the tumor phantom is correctly detected.

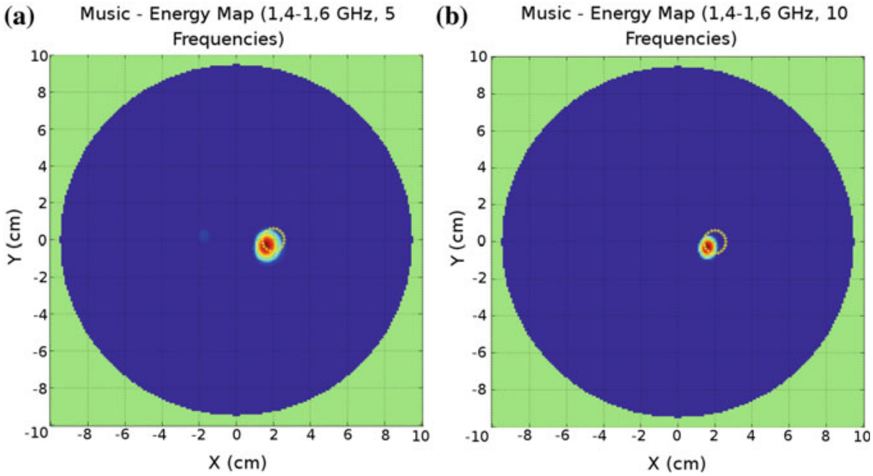

Fig. 5 Energy map reconstructed by I-MUSIC. The circle identifies the rod. Detection considering 5 frequency values **a** and 10 frequency values **b** in the 1.4–1.6 GHz band

Fig. 6 Energy map reconstructed by I-MUSIC. The circle identifies the target, a dielectric cylinder filled with a 40–60 % glycerin-water mixture

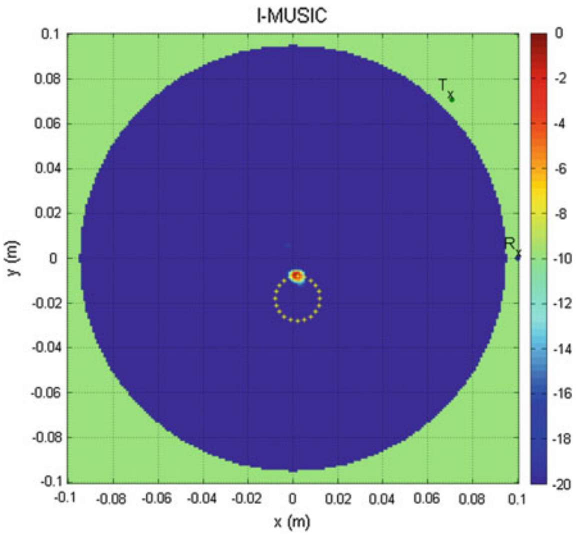

6 Conclusions

We have shown that an MI system for breast-cancer detection based on COTS can be built. Our experimental results show that our system can detect small tumor phantoms, both metallic and dielectric. Moreover, the execution time on the Xilinx Zynq SoC is accelerated by more than 30x compared to the execution time on a desktop processor.

We are still progressing in building our prototype. In the future we will automate the measurements by remotely controlling the frequency sweeping and the transfer of the acquired data from the receiver board to the processing board. We also plan to carry out measurements with more complex and realistic phantoms.

References

1. American Cancer Society: What are the key statistics about breast cancer? http://www.cancer.org/cancer/breastcancer/detailedguide/breast-cancer-key-statistics (2015)
2. Attardo, E., Borsic, A., Vecchi, G., Meaney, P.M.: Whole-system electromagnetic modeling for microwave tomography. IEEE Antennas Wirel. Propag. Lett. **11**, 1618–1621 (2012)
3. Bassi, M., Bevilacqua, A., Gerosa, A., Neviani, A.: Integrated SFCW transceivers for UWB breast cancer imaging: Architectures and circuit constraints. IEEE Trans. Circ. Syst.—I **59**(6), 1228–1241 (2012)
4. Bond, E.J., Li, X., Hagness, S.C., Van Veen, B.D.: Microwave imaging via space-time beamforming for early detection of breast cancer. IEEE Trans. Antennas Propag. **51**(8), 1690–1705 (2003)

5. Casu, M.R., Colonna, F., Crepaldi, M., Demarchi, D., Graziano, M., Zamboni, M.: UWB microwave imaging for breast cancer detection: Many-core, GPU, or FPGA? ACM Trans. Embedded Comput. Syst. **13**(3), 109:1–109:22 (2014)
6. Grzegorczyk, T.M., Meaney, P.M., Kaufman, P.A., di Florio-Alexander, R.M., Paulsen, K.D.: Fast 3-D tomographic microwave imaging for breast cancer detection. IEEE Trans. Med. Imaging **31**(8), 1584–1592 (2012)
7. Guo, X., Casu, M.R., Graziano, M., Zamboni, M.: UWB receiver for breast cancer detection: Comparison between two different approaches. In: 2013 IEEE 26th International SOC Conference (SOCC). pp. 55–60. IEEE (2013)
8. Hagness, S.C., Taflove, A., Bridges, J.E.: Two-dimensional FDTD analysis of a pulsed microwave confocal system for breast cancer detection: fixed-focus and antenna-array sensors. IEEE Trans. Biomed. Eng. **45**(12), 1470–1479 (1998)
9. Hassan, A.M., El-Shenawee, M.: Review of electromagnetic techniques for breast cancer detection. IEEE Rev. Biomed. Eng. **4**, 103–118 (2011)
10. Klemm, M., Leendertz, J., Gibbins, D., Craddock, I.J., Preece, A., Benjamin, R.: Microwave radar-based differential breast cancer imaging: imaging in homogeneous breast phantoms and low contrast scenarios. IEEE Trans. Antennas Propag. **58**(7), 2337–2344 (2010)
11. Meaney, P.M., Fanning, M.W., Li, D., Poplack, S.P., Paulsen, K.D.: A clinical prototype for active microwave imaging of the breast. IEEE J. Microwave Theor. Tech. **48**(11), 1841–1853 (2000)
12. Poplack, S.P., Tosteson, T.D., Wells, W.A., Pogue, B.W., Meaney, P.M., Hartov, A., Kogel, C.A., Soho, S.K., Gibson, J.J., Paulsen, K.D.: Electromagnetic breast imaging: results of a pilot study in women with abnormal mammograms. Radiology **243**(2), 350–359 (2007)
13. Ruvio, G., Solimene, R., Cuccaro, A., Ammann, M.J.: Comparison of noncoherent linear breast cancer detection algorithms applied to a 2-D numerical model. IEEE Antennas Wirel. Propag. Lett. **12**, 853–856 (2013)
14. Ruvio, G., Solimene, R., Cuccaro, A., Gaetano, D., Browne, J.E., Ammann, M.J.: Breast cancer detection using interferometric music: experimental and numerical assessment. Med. Phys. **41**(10), 103101 (2014)
15. Tobon Vasquez, J.A., Attardo, E., Dassano, G., Vipiana, F., Casu, M.R., Vacca, M., Pulimeno, A., Vecchi, G.: Design and modeling of a microwave imaging system for breast cancer detection. In: 9th European Conference on Antennas and Propagation (2015)
16. Zeng, X., Fhager, A., He, Z., Persson, M., Linner, P., Zirath, H.: Development of a time domain microwave system for medical diagnostics. Instrum. Meas. IEEE Trans. **63**(12), 2931–2939 (2014)
17. Zhurbenko, V., RubÃ¦k, T., Krozer, V., Meincke, P.: Design and realisation of a microwave three-dimensional imaging system with application to breast-cancer detection. IET Microwaves Antennas Propag. **4**(12), 2200–2211 (2010)

A SystemVerilog-UVM Methodology for the Design, Simulation and Verification of Complex Readout Chips in High Energy Physics Applications

Sara Marconi, Elia Conti, Pisana Placidi, Andrea Scorzoni, Jorgen Christiansen and Tomasz Hemperek

Abstract The adoption of a system-level simulation environment based on standard methodologies is a valuable solution to handle system complexity and achieve best design optimization. This work is focused on the implementation of such a platform for High Energy Physics (HEP) applications, i.e. for next generation pixel detector readout chips in the framework of the RD53 collaboration. The generic and re-usable environment is capable of verifying different designs in an automated fashion under a wide and flexible stimuli space; it can also be used at different stages of the design process, from initial architecture optimization to final design verification.

1 Introduction

New design and verification challenges are rising in electronic design industry due to the growing complexity of System-On-Chips (SOCs) on multiple aspects: number of transistor, chip size, system functionality, storage resources and limits on sustainable power consumption. Classical methodologies based on a directed testing approach, where ad hoc inputs are provided and the conformity of the output is manually checked, are no longer sufficient to achieve comprehensive functional verification of complex systems respecting the time-to-market needs. A consistent engineering effort has therefore been put into the development of industry CAD

S. Marconi · P. Placidi · A. Scorzoni
INFN and University of Perugia (DI), Via G. Duranti, 06125 Perugia, Italy

S. Marconi (✉) · E. Conti · J. Christiansen
CERN, 1211 Geneva, Switzerland
e-mail: sara.marconi@cern.ch

T. Hemperek
Physikalisches Institut, Universität Bonn, Bonn, Germany

A. De Gloria (ed.), *Applications in Electronics Pervading Industry, Environment and Society*, Lecture Notes in Electrical Engineering 409,
DOI 10.1007/978-3-319-47913-2_5

tools and methodologies to meet the demanding requirements of the SoC industry. System-level design and verification are currently performed through complex environments based on standard verification methodologies such as Open Verification Methodology (OVM) and Universal Verification Methodology (UVM) [1, 2], built on top of the hardware description and verification language SystemVerilog (SV) which has been itself defined as a Verilog extension [3]. With respect to its predecessor, it offers both enhancements for the description of the Design Under Test (DUT) at different levels of abstraction and advanced verification features, based on a documented set of standard classes for the building blocks of the environment [4]. High level design and simulation have also become attractive to the High Energy Physics (HEP) community: description language such as Simulink (more suited for algorithmic design), SystemC and SystemVerilog are being used for different applications. As regards SystemC, a simulation environment has been for example defined in [5] to guide the evaluation of the performance of a new protocol at Transaction Level (TL) with clock-cycle accuracy. With respect to [5], where a separate VHDL testbench was needed to verify the synthesizable RTL description of the design, SV and verification methodologies allow the designer to re-use the same environment as the design progresses from TL to detailed gate level description. The design of integrated circuits for the readout of hybrid pixel detectors such as Velopix, Timepix3 [6] and FE-I4 [7], can be mentioned as examples of the use of SV documented in literature. In comparison to [6, 7] a higher level of flexibility and generality of the environment is required to perform extensive architecture evaluation and simulation for the presented application.

The international RD53 collaboration [8] and the INFN project Chipix65 have also been adopting such versatile methodologies in order to properly address the significant challenges of producing the complex integrated circuits required for the so-called phase 2 pixel detector upgrades of the ATLAS and CMS HEP experiments for the planned run of the High Luminosity-Large Hadron Collider (HL-LHC) at CERN.

In this work a flexible and re-usable simulation and verification framework developed in this context and based on SV and on the UVM class library will be presented.

2 Global Optimization and Simulation Framework

Large complex integrated circuits will be required for the readout of hybrid pixel sensors in HEP experiments, in order to handle very high particle hit rates which are expected to be up to 3 GHz/cm^2. Each cell of the pixel Read Out Chips (ROCs) will also have to include complex digital logic and buffering to support the selection of events of interest, which is normally performed using a dedicated trigger signal that is prospected to feature an increased latency time and rate (from 6 to 20 μs and 1 MHz, respectively). At the same time the chips will need to operate in an extremely hostile environment with radiation levels up to 1 Grad (10.000 times higher than in space applications) with low power consumption.

Whereas complex optimizations will need to be performed to meet such demanding specifications, the development of a flexible pixel simulation and verification platform is considered an indispensable tool and its main requirements have been identified by the community in [8]. With regard to the pixel chip architectures, the capability of simulating these architectures at multiple levels (Transaction, Behavioural, Register Transfer Level, etc.…) is required to this framework, not only to support comprehensive architecture optimization but also all incremental extensions and refinements of a final design. Large sets of automated stimuli need to be provided both in terms of triggers and pixel hits with the aim of properly covering the stimuli space.

VEPIX53 is the first release of the target platform and it is currently available for the RD53 community. In Fig. 1 a global view of the environment is shown. The testbench represents the core of the framework, both since it contains the UVM Verification Components (UVCs) together with the virtual sequencer (in charge of global stimuli control) and because it constitutes the reusable and configurable part of the platform. The user can identify a specific test scenario by using or writing a dedicated test in the library where a particular configuration of the testbench UVCs can be defined. This level of re-usability and flexibility, which is possible thanks to the use of UVM standard classes, makes the chosen methodology highly valuable for the purpose. The connection to the DUT, wrapped by the top module, is achieved through SV interfaces. A set of interfaces has been defined to meet the environment requirements as presented with more detail in [9].

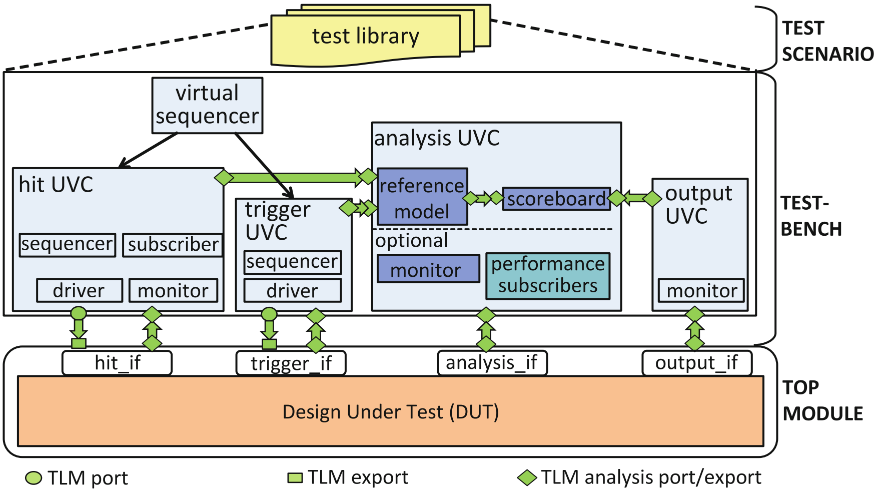

Fig. 1 Block diagram of the VEPIX53 simulation and verification framework

3 Applications of the Framework

3.1 Simulation of a Test Case

The framework could also represent a useful tool for designers willing to simulate finalized chips and verify them under a wide and highly configurable stimuli space. The integration of already existing and complete designs provides at the same time a useful feedback on the overall structure, on the functionality and scalability of the platform itself and represents a good reference test case for any future user. The ATLAS chip FE-I4 [7] has been chosen as a proof of concept for such an application since it represents a reference chip and it could constitute the starting point for more scaled, new generation chips.

The basic version of the reference model (i.e. the ideal model of the DUT part of the environment and responsible for predicting expected output data), has been kept very generic, therefore it has been possible to use it without any modification. Simulations of different submatrices have been run to prove the scalability of the implemented platform and a summary of the results is reported in Table 1. The software tool adopted has been Cadence Incisive Enterprise Simulator 13.2 and the hardware platform used has been a Intel Xeon E312xx 2.6 GHz single-core processor.

3.2 Architectural Study on Buffering Resources

Complex design optimization at all levels of the architecture is the baseline application of the developed framework. An example of the adopted design approach is described with reference to the combined increase in trigger latency and hit rate, which is a critical specification for the pixel ROC as it brings to an order of ~100 times higher buffering requirements, together with a strong impact on area and power consumption. A study has been conducted comparing the performance of two different architectures, whose block diagrams are displayed in Fig. 2. Both versions store information from multiple pixels in a shared pixel region (PR), in order to save storage resources. PR logic is fully shared in architecture A, while in

Table 1 Framework scalability in terms of simulation time (the time required by the different steps of the simulation flow is shown as a function of the size of the submatrix being simulated)

Submatrix size	Compilation time (s)	Elaboration time (s)	Simulation time (15,000 clock cycles) [s]
10 × 336	2.04	40.77	35.83
20 × 336	2.64	1 m 18	1 m 9
40 × 336	2.84	2 m 16	2 m 56
80 × 336 (full chip)	7.3	6 m 59	7 m 13

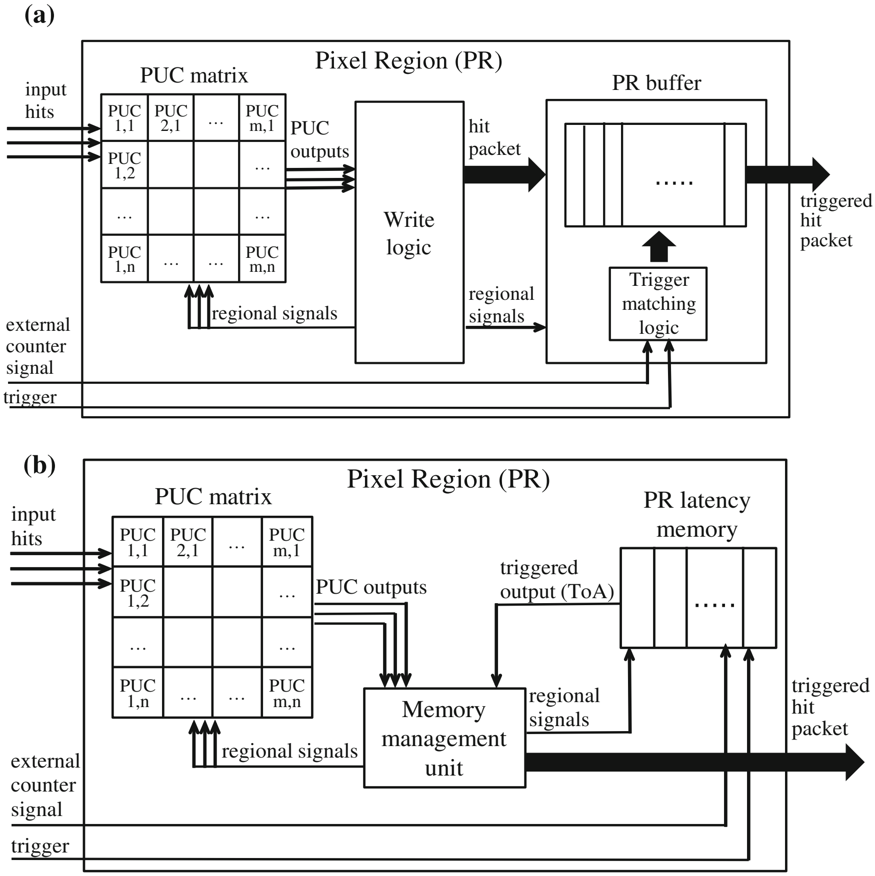

Fig. 2 Block diagram of the buffering architectures (**a**) A and (**b**) B, respectively

architecture B a distributed approach is used with local pixel memories for storing hit amplitude and a shared memory for storing hit time of arrival. The latter is based on FE-I4 design. Long simulations (500,000 clock cycles) have been run to collect sufficient statistics. Thanks to the hit UVC of VEPIX53, the worst-case expected hit rate of 3 GHz/cm^2 has been set and correctly monitored. Single charged particles crossing the detector perpendicularly have been modeled thanks to the hit UVC features and clusters with a typical distribution of the number of hit pixels (i.e. with an average of 4.215 hit pixels) have been generated [10]. Buffering performance have been investigated through the analysis UVC of VEPIX53, which collects statistical information on memory occupancy by monitoring dedicated internal signals as part of the *analysis_if*. From the obtained histogram of the PR buffer occupancy, comparative plots on the buffer overflow probability as a function of the buffer depth have been produced. An example is shown in Fig. 3 for a 4 × 4 square pixel region. It can be noted how architecture A achieves same overflow probability

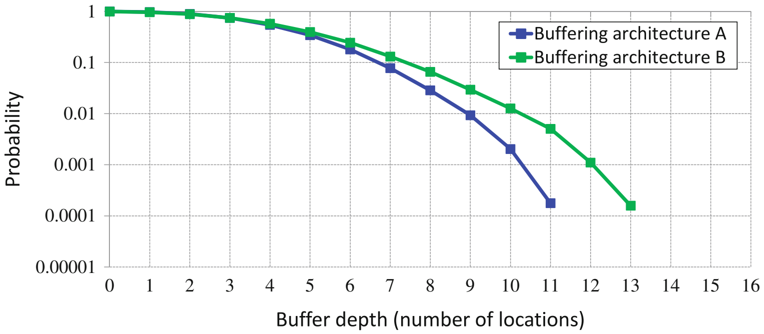

Fig. 3 Comparative plot of buffer overflow probability of two alternative architectures

with a lower number of buffer locations and it should therefore be preferred with respect to B in terms of buffering requirements. More detailed results, with comparison of multiple pixel region sizes, can be found in [9]. Using the described methodology and design approach, further studies can be conducted as far as other factors are concerned (e.g. number of lost hits) and at different levels (e.g. area, power) to achieve the best trade-off among the multiple specifications.

4 Conclusions

The VEPIX53 versatile simulation and verification environment has been developed as a design tool for the phase 2 pixel chips of the ATLAS and CMS experiments at the HL-LHC. The high level testbench structure consists of generic building blocks and interfaces to the DUT and, thanks to the chosen SV-UVM methodology, it provides high re-usability and configurability of the test scenario. The platform has been tested for two different applications: on the one hand, a final chip test case has been integrated and simulated proving good functionality and scalability of the framework; on the other hand a study of buffering architectures has been conducted comparing collected statistics on performance.

References

1. Hung-Yi, Y.: Highly automated and efficient simulation environment with UVM. In: 2014 International Symposium VLSI Design, Automation and Test (VLSI-DAT) (2013)
2. Zhong G., Zhou J., Xia B.: Parameter and UVM, making a layered testbench powerful. In: 2013 IEEE International Conference ASIC (ASICON) (2013)
3. IEEE Standard for SystemVerilog–Unified hardware design, specification, and verification language. http://dx.doi.org/10.1109/IEEESTD.2013.6469140 (2012)

4. OVM/UVM user's guide. https://verificationacademy.com/topics/verification-methodology (2014)
5. Magazzu G. et al.: Design exploration and verification platform, based on high-level modeling and FPGA prototyping, for fast and flexible digital communication in physics experiments. J. Instrum. **8**(2) (2013)
6. Poikela T. et al.: VeloPix: the pixel ASIC for the LHCb upgrade. J. Instrum. **10**(1) (2015)
7. Zivkovic V. et al.: The FE-I4 pixel readout system-on-chip resubmission for the insertable B-Layer project. J. Instrum. **7**(2) (2012)
8. Chistiansen, J., Garcia-Sciveres, M.: RD Collaboration proposal: Development of pixel readout integrated circuits for extreme rate and radiation. http://cds.cern.ch/record/1553467?ln=en (2013)
9. Marconi, S., Conti, E., Placidi, P., Christiansen, J., Hemperek, T.: The RD53 collaboration's SystemVerilog-UVM simulation framework and its general applicability to design of advanced pixel readout chips. J. Instrum. **9**(10) (2014)
10. Conti E., Christiansen J., Placidi P., Marconi S.: Pixel chip architecture optimization based on a simplified statistical and analytical model. J. Instrum. **9**(3) (2014)

Embedded System for In-Line Characterization of Industrial Fluids

Stefano Ricci, Valentino Meacci, Beat Birkhofer and Johan Wiklund

Abstract The in-line assessment of the rheological properties of fluids in chemical, cosmetic, pharmaceutical, and food industries is fundamental for process optimization and product quality. The rheology of a fluid in a process pipe can be investigated by combining the measured pressure difference over a fixed distance of pipe, and the velocity distribution of the fluid along the diameter. The latter data can be measured by Pulsed Ultrasound Velocimetry (PUV), which is a non-invasive Doppler technique. Till now, the few systems available need cumbersome electronics or computer for data post-processing and are not suitable for industrial applications. In this work we present a compact (10 × 12 cm), fully programmable and low cost system that embeds the ultrasound front-end and all of the digital electronics necessary for the signal processing. The board produces, in real time, 512-point velocity profiles at 45 Hz rate and is integrated in the Flow-Viz$^{\text{TM}}$ platform (SP Technical Research Institute of Sweden).

1 Introduction

A wide range of industries need to process fluids to get the final product. These fluids have very different compositions and chemical features, and their processing is carried out at in a wide temperature and pressure range. The monitoring of the fluid condition during the production process is of paramount importance for the quality of the final product. While the pressure or temperature can be acquired in-line by relatively simple sensors and electronics, rheological parameters like,

---

S. Ricci (✉) · V. Meacci
Information Engineering Dept, University of Florence, Florence, Italy
e-mail: stefano.ricci@unifi.it

B. Birkhofer
Sika Services AG, Tüffenwies 16, 8048 Zurich, Switzerland

J. Wiklund
SP Technical Research Institute of Sweden, Gothenburg, Sweden

A. De Gloria (ed.), *Applications in Electronics Pervading Industry, Environment and Society*, Lecture Notes in Electrical Engineering 409,
DOI 10.1007/978-3-319-47913-2_6

e.g., the viscosity are much harder to get. Currently, fluid specimens are collected, moved to laboratory, and checked with rheometers. The process is time consuming, only part of the fluid is monitored and the result of the analysis is not available in real-time. A system working in-line, like for temperature and pressure, is highly desirable. This lack is partially mended by laser velocimetry. A laser apparatus measures the radial velocity distribution of the fluid that runs in a production pipe. Its rheology can be recovered by combining the measured velocity profile with the pressure drop along a known tract of the pipe. Unfortunately, this method does not work in opaque fluids, where the laser does not penetrate.

The Multigate Doppler Ultrasound Velocimetry (MDUV) is an alternative method. A moving particle of the fluid, impinged by an ultrasound burst with known frequency, produces an echo. The frequency of the echo is affected by a shift that correlates to the particle velocity according to the Doppler Effect. A receiver, by measuring the frequency shifts acquired in a temporal range (corresponding, through the sound velocity, to a range of distances from the transducer) can recover the velocity of the fluid along the path of the ultrasound burst. Although MDUV is known since the 1980s [1], few systems are suitable for industrial applications, and they often need cumbersome electronics or computer for data post-processing.

In this work we present a compact (10 × 12 cm), fully programmable and low cost MDUV system that embeds all the electronics for generating/receiving the ultrasound bursts as well as for processing the data in real-time to generate the final velocity profile. The system represents the latest generation of a sequence of boards that starts with a multigate board dedicated to biomedical applications [2], followed by an electronics adapted to industrial use [3, 4]. The new system is currently integrated in the Flow-Viz$^{\mathrm{TM}}$ platform (SP, Sweden) [5, 6], where it is connected to a sbRIO 9606 board (National Instruments) that manages the communication to a host through an Ethernet network interface.

2 The System

2.1 Overview

The MDUV system is constituted by 2 boards, the first is the analog front-end board (AFEB) that performs the analog signal conditioning, the second is the Digital Signal Processing Board (DSPB) that includes the digital devices for the signal processing and the power suppliers. The AFEB is housed over the DSPB, so that the overall system dimensions are limited to 10 × 12 cm. Two transmit (TX) and two receive (RX) channels are available on the system, which can thus be connected to two separate ultrasound transducers. Although only a single TX and RX channel can be active simultaneously, this configuration allows the dynamic switching between pitch-catch and single transducer operations. The main features of the system are listed in Table 1.

Table 1 MDUV system main features

Feature	Value	Feature	Value
TX channels	2, multiplexed	Internal buffer	64 MB
RX channels	2, multiplexed	Sampling Freq.	100 Msps
Dimensions	10 × 12 cm	Processing time	42 μs/depth
Power	5 W	Input noise on 50 Ω	1.5 nV√Hz
Analog gain in RX	7–55 dB	On board Processing	Raw data
TX voltage	10–80 Vpp		Spectral profile
TX/RX freq.	0.8–7 MHz		Frequency profile

2.2 *The AFEB*

The main blocks included in the AFEB are reported in Fig. 1. The differential TX signal, synthetized in the DSPB, is forwarded to the active TX channel through an analog multiplexer, and processed by a power amplifiers realized with 2 linear differential amplifiers with current feedback. Their low impedance output, that can reach 30 Vpp, is applied to a transformer that rises the voltage up to 80 Vpp and adjust the impedance to fit the input of the ultrasonic transducer. Under the control of the DSPB, the power amplifiers are enabled only when the short excitation bursts should be transmitted. This allows a power reduction and a lower noise injection towards the sensitive input channels.

Each of the 2 inputs is connected to a transformer that adjusts the impedance between the transducer and the low noise amplifier (LNA). The LNA is followed by the programmable gain amplifier (PGA). This stage features a programmable gain between 7 and 55 dB and a bandwidth between 0.8 and 7 MHz. A multiplexer selects the signals from the active input channel, which is moved to the DSPB for digital conversion.

Since the echoes gathered from the transducer are quite weak (in the order of μV), the input noise is a major concern. A strong effort was paid to its reduction: the LNA section of the board is completely shielded, an 8-layer PCB is used to better

Fig. 1 The AFEB includes the analog electronics for the ultrasound front-end

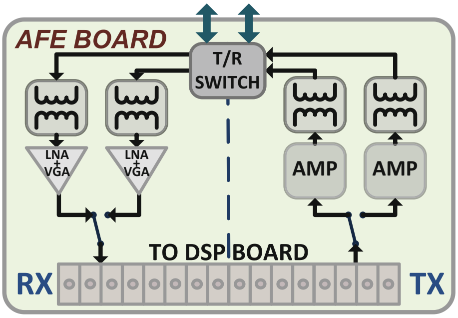

isolate the potential sources of noise, the power is locally re-generated through low-dropout regulators and filters, and every non-necessary device is switched down during the RX phase. These features allowed limiting the equivalent input noise to 1.5 nV/√Hz.

2.3 *The DSPB*

The heart of the DSPB is the low-cost Field Programmable Gate Array (FPGA) EP3C25F256, from the Cyclone family of Altera. It includes the communication module towards the host, the sequencer for the synchronization of the internal operations, the Arbitrary Waveform Generator (AWG) for the synthesis of the TX pulse, the processing modules, the interface to a 64 MB SDRAM (see Fig. 2).

When the host commands the start of operations, the sequencer, every Pulse Repetition Interval (PRI), triggers the AWG to generate a pulse and, simultaneously, switch on the power amplifiers on the AFEB. The AWG produces sinusoidal bursts of arbitrary frequency, amplitude and length at 100 Msps. A programmable Tukey window is applied before they are analog converted and sent to the AFEB. After the TX, the amplifiers are disabled and the received echo, conditioned in the AFEB, is digital converted by a AD9265 (Analog Devices, Norwood, MA) at 100 Msps, 16 bit resolution. The raw samples, moved in the FPGA, are coherent demodulated and stored to the 64 MB SDRAM buffer. Optionally, raw data can be directly stored in memory without applying the demodulation. When enough data are present in SDRAM (at least 128 PRIs), the sequencer triggers the multi-gate

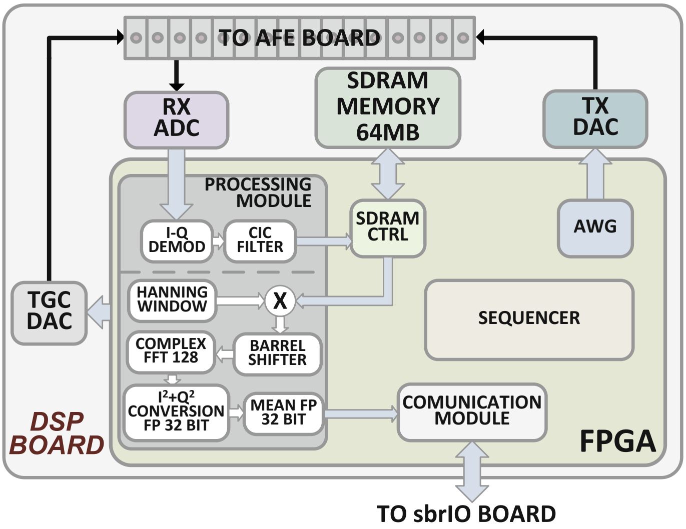

Fig. 2 The DSPB includes the digital devices for data processing and resource management

spectral analysis and the mean frequency detection. The main processing modules present in the FPGA are described below:

Demodulator. The acquired 16-bit samples are coherent-demodulated. They are multiplied with two 16 bit sin/cos signals synthetized by a DDS in the FPGA with the same frequency as the TX pulse. The resulting two data streams are processed by two 4-stage Cascated Integrator Combo (CIC) filters working at 48-bit. The resulting In-phase and Quadrature (IQ) data are down-sampled according to a programmable decimation factor and stored in the 64 MB SDRAM buffer at 32 + 32 bit per complex sample.

Multi-gate spectral estimator. The data are transferred from the SDRAM to the FPGA by reading blocks of 128 complex samples acquired from the same depth. The blocks, that can be partially overlapped, are Hanning-windowed and processed through a block-floating point FFT. The power spectrum is obtained by calculating the sums of the squares of the FFT output, then converted to 32-bit floating-point format. This calculation is repeated for all of the available depths (multi-gate processing) and the resulting power spectrum is stored in a row of a matrix, which represents the Doppler spectral profile (see, for example Fig. 3, left).

Mean frequency estimator. All of the following operations are performed in 32-bit floating point precision. A programmable number of Doppler spectral profiles are averaged to improve the signal-to-noise ratio (SNR). The noise below a programmable threshold is cut to zero. From each row of the denoised Doppler spectral profile matrix, the mean frequency f_d is calculated as:

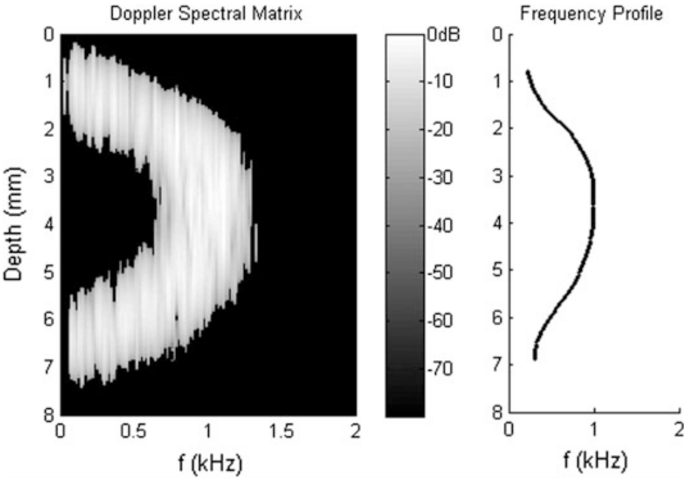

Fig. 3 Doppler Spectral Matrix (*left*) and corresponding frequency profile (*right*) calculated by the MDUV system when a 6 mm diameter pipe is investigated. A Newtonian fluid run at 10 cm/s insonified with 5 MHz bursts at PRI = 0.5 ms

$$f_d = \frac{1}{PRI} \cdot n_d \text{ where } n_d = \frac{1}{N} \sum_{i=0}^{N-1} i \cdot \left|C_{d,i}\right|^2 / \sum_{i=0}^{N-1} \left|C_{d,i}\right|^2 \quad (1)$$

$C_{d,i}$ is the matrix element corresponding to depth d and FFT bin i, N is the FFT size. A multiplier and an accumulator calculate the numerator of (1), while another accumulator calculates the denominator, and a final divisor concludes the calculation.

The data, processed as described above, are downloaded to the host through a 10 MB/s channel. The host can download, in real-time, the unprocessed raw data from the 64 MB SDRAM, the processed spectral profiles matrices, the mean frequencies vectors, or both.

3 Results and Conclusion

The MDUV system calculates a frequency profile (SDRAM reading, FFT, power spectrum, profile calculation) in 42 μs per depth (e.g. a 512-depth spectral profile matrix plus the corresponding frequency profile are generated at 45 Hz rate). The FPGA, clocked at 100 MHz, has still enough resources available for possible future improvements (65 % of the logics, 15 % of internal RAM, 33 % of multipliers are currently used).

Figure 3, left, shows, for example, the Doppler spectral profile matrix obtained by investigating a 10 cm/s flow in a 6 mm pipe with 5 MHz bursts fired at PRI = 0.5 ms. The fluid was constituted by degassed water with dissolved 15 μm plastic particles. The spectral power is reported in gray scale over a 80 dB range. The 8 mm depth range reported corresponds to 256 depths. The frequency profile extracted by the Doppler spectral matrix is displayed on the right of Fig. 3. As expected, the profile is roughly parabolic and the maximum flow velocity is around the middle of the vessel. The error with respect to the same processing carried out in Matlab® is −100 dB.

The MDUV board achieves high spatial and temporal resolution thanks to the possibility of rapidly processing a large number of pulses in the FPGA. This feature, jointly to the full programmability of acquisition and processing parameters, makes the system ideal for industrial application, like viscosity detection or volume flow measurement [7], in fluids where the attenuation of ultrasound is a major limitation. The board has been successfully installed, as an integral part of the Flow-Viz system, in pilot plants of international companies, and has been successfully verified for several industrial applications.

References

1. Kowalewski, T.A.: Velocity profiles of suspension flowing through a tube. Archiv. Mech. **32** (6), 857–865 (1980)
2. Ricci, S., Boni, E., Guidi, F., Morganti, T., Tortoli, P.: A programmable real-time system for development and test of new ultrasound investigation methods. IEEE Trans. Ultrason. Ferroelectr. Freq. Control **53**(10), 1813–1819 (2006)
3. Ricci, S., Liard, M., Birkhofer, B., Lootens, D., Brühwiler, A., Tortoli, P.: Embedded Doppler system for industrial in-line rheometry. IEEE Trans. Ultrason. Ferroelectr. Freq. Control **59**(7), 1395–1401 (2012)
4. Birkhofer, B., Debacker, A., Russo, S., Ricci, S., Lootens, D.: In-line rheometry based on ultrasonic velocity profiles: comparison of data processing methods. Appl. Rheol. **22**(4), 44701 (2012)
5. www.flow-viz.com
6. Wiklund, J., Kotzé, R., Birkhofer, B., Ricci, S., Meacci, V., Haldenwang, R., Stading, M.: Flow-Viz^{TM}—A fully integrated and commercial in-line fluid characterization system for industrial applications. In: Proceedings of 9th Ultrasonic Doppler Methods for Fluid Mechanics and Fluid Engineering (ISUD9), pp. 165–168, Strasbourg, France (2014)
7. Ricci, S., Cinthio, M., Ahlgren, Å.R., Tortoli, P.: Accuracy and reproducibility of a novel dynamic volume flow measurement method. Ultras. Med. Biol **39**(10), 1903–1914 (2013)

A Low Cost, Portable Device for Breath Analysis and Self-monitoring, the Wize Sniffer

Danila Germanese, Marco Righi, Antonio Benassi, Mario D'Acunto, Riccardo Leone, Massimo Magrini, Paolo Paradisi, Dario Puppi and Ovidio Salvetti

Abstract Here we describe the implementation of the first prototype of the *Wize Sniffer 1.x* (WS 1.x), a low cost, portable electronic device for breath analysis. The device is being developed in the framework of the Collaborative European Project SEMEOTICONS (SEMEiotic Oriented Technology for Individuals CardiOmetabolic risk self-assessmeNt and Self-monitoring). In the frame of SEMEOTICONS project, the Wize Sniffer will help the user monitor his/her state of health, in particular giving feedbacks about those noxious habits for cardio-metabolic risk, such as alcohol intake and smoking. The low cost and compactness

---

http://www.semeoticons.eu, grant N. 611516.

D. Germanese (✉) · M. Righi · A. Benassi · M. D'Acunto · R. Leone · M. Magrini · P. Paradisi · D. Puppi · O. Salvetti
Institute of the National Research Council, Institute of Information Science
and Technologies, via G. Moruzzi 1, 56124 Pisa, Italy
e-mail: danila.germanese@isti.cnr.it
URL: http://www.isti.cnr.it

M. Righi
e-mail: marco.righi@isti.cnr.it

A. Benassi
e-mail: antonio.benassi@isti.cnr.it

M. D'Acunto
e-mail: mario.dacunto@isti.cnr.it

R. Leone
e-mail: giuseppe.leone@isti.cnr.it

M. Magrini
e-mail: massimo.magrini@isti.cnr.it

P. Paradisi
e-mail: paolo.paradisi@isti.cnr.it

O. Salvetti
e-mail: ovidio.salvetti@isti.cnr.it

A. De Gloria (ed.), *Applications in Electronics Pervading Industry, Environment and Society*, Lecture Notes in Electrical Engineering 409,
DOI 10.1007/978-3-319-47913-2_7

of the device allows for a daily screening that, even if without a real diagnostic meaning, could represent a pre-monitoring, useful for an optimal selection of more sophisticated and standard medical analysis.

1 Introduction

Human breath is composed of nitric oxide, oxygen, water vapor, carbon dioxide, and numerous Volatile Organic Compounds (VOCs) [1–6]. These VOCs may have *exogenous origin* i.e., from inhaled air, from dermal absorption, from foods and beverages, or *endogenous origin* i.e., products of anabolic or catabolic reactions that occur in tissues or cells throughout the body. About 35 of the identified compounds in the exhaled breath have been established as biomarkers for particular diseases and metabolic disorders [1]. It means that any variation (with respect to baseline—BL-values) in VOCs' concentration levels may be an index of some diseases, or, at least, of metabolic disorders.

Breath gases have been identified as biomarkers using gas chromatography (GC) especially [6]. GC, the gold standard for gas analysis, is very accurate but expensive, time consuming and non portable. Another approach for gas analysis exploits Electronic Noses (E-noses) [6]. They are low-cost, and easier to use, but they are designed for broader applications (environmental, industrial ones), rather than for medical field. Recently, Toshiba (http://www.toshiba.com/tai/) has developed a Breathalyzer for exhaled acetone, as well as Bedfont's Smokerlyzer and NOBreath (http://www.bedfont.com) which detect, respectively, exhaled Carbon Monoxide and exhaled Nitric Monoxide. Nevertheless, all these devices exploit expensive approach for gas detection (i.e., quantum cascade laser, infrared laser, optical sensors, etc.).

Consequently, the need for a low cost, portable device for breath analysis has emerged. This device should be also easy to use, also in household environment, and sufficiently accurate for the typical gas concentrations of human breath. In this work, we introduce the design and functionality of a prototype of a portable device for the analysis of a limited number of breath molecules, the so-called Wize Sniffer (WS) 1.x. In particular, (i) the design of the hardware platform, (ii) the implementation of the communication protocol between the device and a laptop, (iii) the functionality of the WS 1.x are described.

2 Analyzed Gases

Our attention, in the frame of the SEMEOTICONS project, has been focused on the prevention of Atherosclerotic Cardiovascular Diseases (ACDs). Then, the WS1.x has been developed to detect the breath compounds associated to the noxious habits for cardio-metabolic risk (alcohol intake, smoking) [4]:

- ***Carbon monoxide*** (CO): abnormalities in endogenous CO have been linked to hypertension or inflammation. It is also the major component of tobacco fumes (75, 95 %). Its BL in a healthy subject is about 0.6–4.9 ppm.
- ***Hydrogen*** (H_2): it results from carbohydrate fermentation by anaerobic bacteria into caecum and/or into oropharingeal tract. Increased values may be due to lactose intolerances, or intestinal disorders. Its BL in a healthy subject is about 0.3–34 ppm.
- ***Ethanol*** (C_2H_6O): it derives from alcoholic drink, causing accumulation of free radicals and oxidative stress. Its BL in a healthy subject is about 0–3.9 ppm.
- ***Ammonia*** (NH_3): it is a component of tobacco fumes (about 22 %); its BL in a healthy subject is about 0–1.3 ppm.
- ***Carbon dioxide*** (CO_2) and ***Oxygen*** (O_2): Their quantities show how much O_2 is retained, and how much CO_2 is produced as a by-product of cellular metabolism. Higher/lower values may be due to respiration disorders. CO_2 and O_2 BL in a healthy subject are respectively about 4 % and 13 %.

3 Wize Sniffer 1.X's Hardware and Software Architecture

A general scheme of the WS 1.x's architecture is shown in Fig. 1. The core is an Acquiring Device (AD), a dedicated embedded hardware, including a corrugated tube through which the gases flow, a gas sampling box where six gas sensors are placed, and a micro-controller board. Since the sensors' output is affected by the water vapor present in exhaled gases, a Heat and Exchange Moisturizers (HME) filter is placed at the beginning of the corrugated tube. In addition, the humidity percentage is monitored within the sampling box, as well as the temperature. Other two gas sensors having shorter response time work in *flowing-regime* by means of a sampling pump. The sensors' output signals are read by a

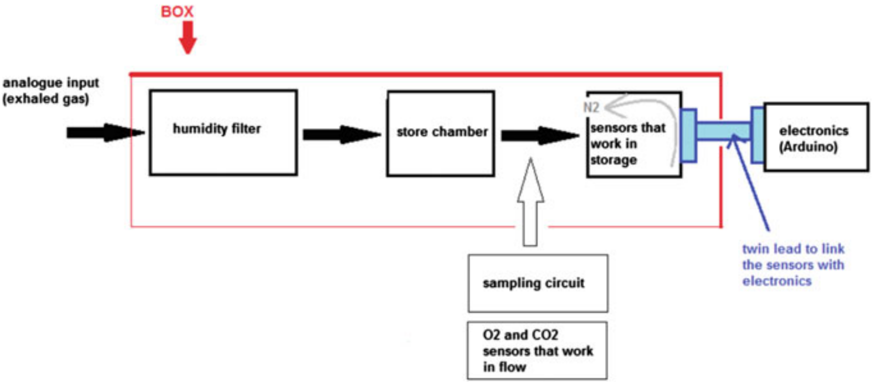

Fig. 1 Schematic sketch of the WS 1.x's architecture

Table 1 Gas sensors and Temperature-Humidity sensor used in WS 1.x

Sensor	Detected compounds
Figaro TGS2602	Hydrogen, ammonia, ethanol, hydrogen sulfide, toluene
Figaro TGS2620	Hydrogen, carbon monoxide, ethanol, methane, isobutane
Figaro TGS821	Hydrogen
Figaro TGS4161	Carbon dioxide
Figaro TGS2442	Carbon monoxide
Figaro TGS2444	Ammonia
City Technologies MOX20	Oxygen
Servomex IR1507	Carbon Dioxide
Sensirion SHt11	Temperature and humidity

micro controller board. Table 1 lists the commercial sensors used in the WS 1.x's architecture. As micro-controller board, an Arduino Mega2560 has been chosen, taking into account (i) its Analogue-to-Digital converter resolution for each input pins; (ii) the number of analogue input pins; (iii) availability of ethernet connection; (iv) SRAM capacity.

The WS system operates in three phases: gas collection, gas sampling, and data analysis. Once the gases are collected, the sampling process begins: the analytes are injected into the store chamber, where the gas sensors are placed, and changes in sensors' internal resistances are read and recorded by the Arduino micro-controller board. Then, a purge cycle allows to supply background air to the gas sensors to refresh the baseline measurement.

What makes the WS a portable device is, above all, the communication protocol between the Personal Computer and the device itself. Indeed, in order to receive the data from the AD even on a remote Personal Computer (PC), we use a client-server architecture. In particular, the AD executes a daemon on port 23, waits a command line from the PC and provides the data, that means the outputs from the several

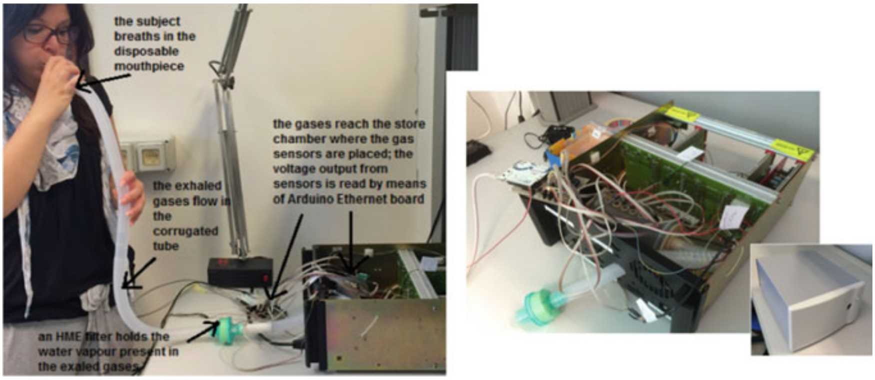

Fig. 2 WS 1.x final set-up

sensors. This approach allows us to use a dedicated unit for each task. Indeed, the AD works as dedicated hardware which collects and records the data; the computational capacity of a PC is used to analyze the data and calculate the gas concentrations. The final set-up of WS 1.x is shown in Fig. 2.

4 Preliminary Tests: Evaluation of the WS 1.X's Performances

A measuring protocol was draft in order to test the Wize Sniffer 1.x on a population of healthy subjects containing individuals of different age, habits, lifestyles, body type. Note that SEMEOTICONS project is focused on the prevention of cardio-metabolic diseases. Consequently, it pays attention not to make a diagnosis, rather than to the monitoring of healthy subjects' well-being, in order to make them avoid the dangerous habits for this type of disease. For our test (conducted following the individuals' habits and lifestyle), 11 non smokers-teetotal/occasionally drinkers ($\leq 2\,\text{times/week}$), 10 non smokers-moderate drinkers (3–5 times/week), 7 non smokers-heavy drinkers ($\geq 6\,\text{times/wee}k$), 9 light smokers (2–5 cig./day)-teetotal, 5 heavy smokers ($\geq 10\,\text{cig/day}$)-teetotal, 12 smokers-and-drinkers were chosen. The measuring protocol was draft taking into account also the methodological issues about sampling procedure. In practice are used three methods of sampling: "alveolar (end-tidal) sampling", if only systemic volatile biomarkers are to be assessed, "mixed expiratory air sampling" (which corresponds to a whole breath sample), "time-controlled sampling" (which corresponds to a part of exhaled air sampled after the start of expiration; this method shows large variations of samples compositions because of wide variations of individual breathing manoeuvers). For our purposes, mixed expiratory air sampling method was chosen, since our interest was focused on endogenous biomarkers, but also to the compounds of exogenous origin. In addition, since the composition of single breaths may vary considerably from each other, because of different modes and depth of breathing, in order to have samples that were as reproducible as possible, we preferred a sampling of multiple (three) breaths.

5 Results and Discussion

An example of an outcome of a test is shown in Fig. 3. The typical trends of "exhaled breath curves" can be seen: a few seconds after the sensors sense exhaled gas particles, the sensors' internal resistance varies, resulting in a voltage output rise, until the plateau curve. Further tests demonstrated that, from a qualitative standpoint, the WS1.x can discriminate the different alcoholic grades, and it is able to follow the trend in time of the alcohol intake/disposal. In addition, WS1.x is able to discriminate also between moderate/heavy smokers and non-smokers.

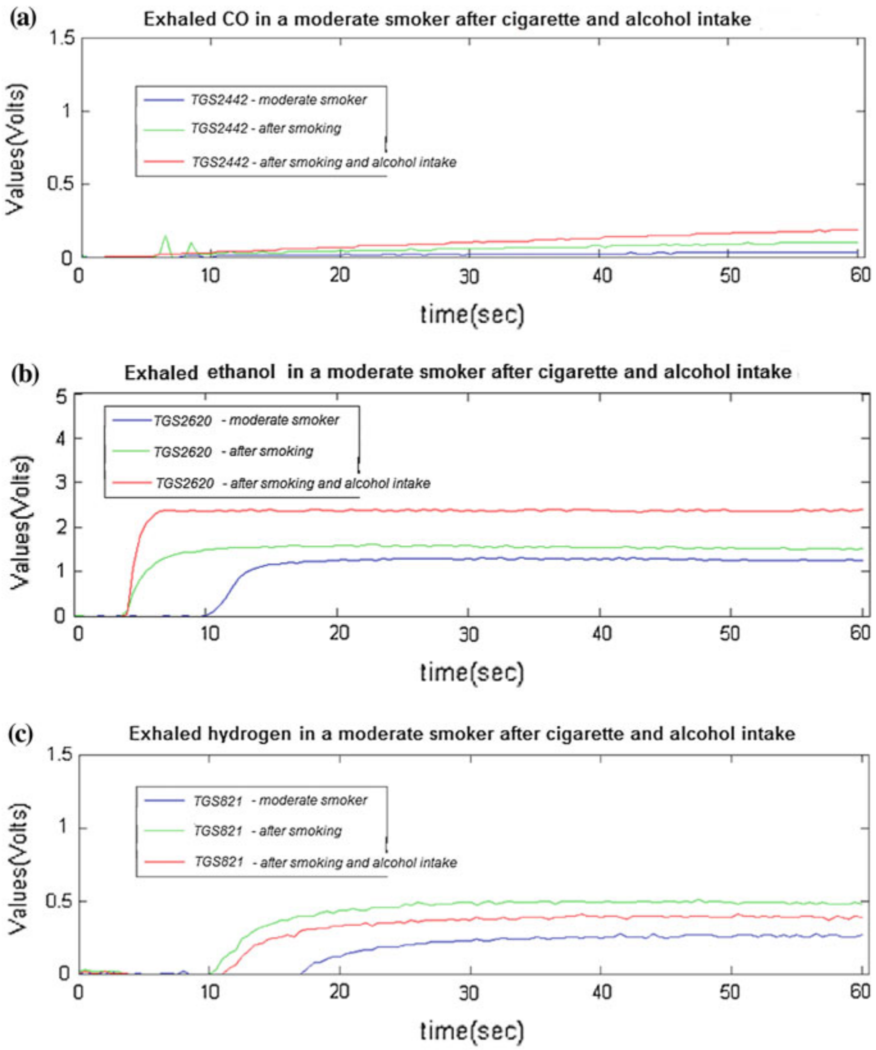

Fig. 3 An outcome of a test. It was carried out on a moderate-smoker, social drinker, healthy subj., female, in the age range (20–29), having normal body type, practicing sport 2 times a week. The subj. breathed before and after smoking, and before and after smoking and drinking alcohol. WS 1.x was able to follow the trend in time of smoking (see exhaled CO detected by TGS2442) and alcohol intake (see exhaled Ethanol detected by TGS2620). Exhaled H_2 (detected by TGS821) showed an increase after smoking and a decrease after drinking alcohol, in agreement with the literature [5]

Further studies and investigations are being carried on in order to develop a non-linear equation model able to calculate breath molecules concentration accurately, also overcoming the weakness of the semiconductor-based gas sensor, that is the cross-sensitivity. In addition, in order to improve the gas sensors' sensitivity, the development of a new version of the WS based on electrospun nanofibers [7] will be our great future challenge.

Acknowledgments This work was funded in the framework of the Collaborative European Project SEMEOTICONS (SEMEiotic Oriented Technology for Individuals CardiOmetabolic risk self-assessmeNt and Self-monitoring), grant N. 611516.

References

1. Di Francesco, F., et al.: Breath analysis: trends in techniques and clinical applications. Micromech. J. **79**, 405–410 (2005)
2. Miekisch, W., et al.: Breath analysis in critically ill patients: potential and limitations. Expert Rev. Mol. Diagn. **4**, 619–629 (2004)
3. Lison, M.W., et al.: What are the basic self-monitoring components for cardiovascular risk management? MC Med. Res. Meth. **10**, 105 (2010)
4. DAcunto, M. et al.: Wize Sniffer—A new portable device designed for selective olfaction. In: Proceedings of HEALTHINF 2014, pp. 577–582 (2014). ISBN: 978-989758010-9, doi:10.5220/0004938605770582
5. Thompson, D.G., et al.: Extra intestinal influences on exhaled breath hydrogen measurements during the investigation of gastrointestinal disease. Gut **26**(12), 1349–1352 (1985)
6. Guo G. et al.: A novel breath analysis system based on electronic olfaction. IEEE Trans. Biomed. Eng. **57**(11) (2010). doi:10.1109/TBME.2010.2055864
7. Puppi, D., et al.: Poly (vinyl alcohol)-based electrospun meshes as potential candidate scaffolds in regenerative medicine. J. Bioact. Compat. Polym. **26**, 20–34 (2011)

A Short Term Simulator for Vessel Manoeuvres Prediction

Paolo Neri and Bruno Neri

Abstract This paper presents a methodology for vessels manoeuvring prediction during navigation. The proposed algorithm allows to estimate future position and heading of the vessel on the basis of present position, velocity, propeller speed and rudder angle. The prediction algorithm, which can be very useful in emergency manoeuvres, uses a short term simulator which has been tuned up and validated in the framework of the Costa Concordia cruise ship trial. However, the methodology could be applied to any kind of ship, since it just requires a set of data recorded during a set of mandatory sea trials performed before the delivery of the ship. The prediction algorithm shows, on the electronic navigation chart, the foreseen position of the ship in the next 30–40 s, provided that helm and power settings remain unchanged, allowing the helmsman to check in advance the effect of the commands and to eventually modify the trajectory.

1 Introduction

The models for the simulation of ship manoeuvres can be grouped in two categories: models for prediction of the ship manoeuvrability at design level (predictive models) and models for ship simulators (time domain simulator), realized after ship construction. Unlike for predictive models, in the case of simulator models no structural and mechanical data are necessary, but a sort of "black box" approach can be used. In fact the data contained in the Manoeuvring Booklet (MB) of the ship and/or those recorded in the Voyage Data Recorder (VDR) can be used to tune the

---

P. Neri (✉)
Department of Civil and Industrial Engineering, University of Pisa,
Largo L. Lazzarino 1, 56122 Pisa, Italy
e-mail: paolo.neri@dici.unipi.it

B. Neri
Dipartimento di Ingegneria dell'Informazione, University of Pisa,
Via Caruso 16, 56122 Pisa, Italy
e-mail: b.neri@iet.unipi.it

A. De Gloria (ed.), *Applications in Electronics Pervading Industry, Environment and Society*, Lecture Notes in Electrical Engineering 409,
DOI 10.1007/978-3-319-47913-2_8

parameters controlling the equation of motion of the ship under the effects of internal (engines and rudder) and external (water and wind) forces. To build the simulator, the general equations of motion of the ship are written. Then the free parameters of the model, suited to describe the motion of a specific ship, are extrapolated from known data. Finally, the simulator is validated by comparing real trajectories recorded in the VDR system and simulated ones.

Whereas there are a lot of paper in literature facing with the problem of predictive simulators [1, 2], there are just a few papers in which a time domain simulator is presented. In all of the cases (see for instance [3]) the model validation and the error estimation is not really accurate. For this reason, a new time domain simulator [4] was developed for forensic scope: the target was to estimate the effects of the error of Costa Concordia helmsman, who misunderstood some orders of Commander Schettino just before the impact with Giglio Island rocks. The methodology adopted in [4] can be applied to any ship provided that some navigation data are available. More details are presented in Sect. 2, along with some already presented results.

Section 3 shows how the simulator has been customized to predict the position and heading of a ship subjected to given commands, 30–40 s in advance in a real time fashion; some preliminary results are also shown. Finally in Sect. 4 some conclusion are drawn.

2 Simulation Methodology and Experimental Data

This section firstly gives a brief description of the experimental data to be used to tune up the model and to validate the simulator, then ship modeling and the procedure for parameters extraction will be summarized.

2.1 Experimental Data

Two main sources of information and data were available: those recorded in the VDR and those contained in the MB of the ship. VDR systems consist of a computer, named concentrator, connected with a distributed sensor network which measure the main navigation parameters: position, speed and heading of the ship, round per minute (rpm) of the propellers, position of the rudder(s) and so on. The data collected by the concentrator are recorded in a local hard disk and a copy is sent to the Final Recording Medium, the so called “Black Box”. In this way the last hours or days of navigation data are available and they can be used a posteriori for several scopes as, for instance, accident reconstruction. The MB of a ship contains the results of some mandatory manoeuvres performed during sea trials, before its delivery. A Differential GPS is used in order to keep the position error below a maximum of 2 m. During sea trials the main navigation parameters are recorded at a sampling rate of 1 Hz and stored in the VDR hard disk for further elaboration.

2.2 Ship Modeling

A simplified three Degrees of Freedom (DOF) model has been adopted for ship modeling, neglecting roll and pitch angles and z position; the effect of wind and current were also considered not relevant: this approximation has been demonstrated to be valid for short term simulation [4]. In Fig. 1a heading ϑ and x, y coordinates are represented, along with the more relevant model quantities. The mathematical model and the equation describing the ship movements under the effect of propellers and rudders are described in [4]. The dynamic parameters, such as the torque made by rudder, water viscosity and propellers can be calculated considering known navigation and/or MB data. To this end an interpolation algorithm can be used to estimate all the unknown parameters of the equations, by means of a least square fit of the model with the recorded data. In a few words, the so called “black box” approach allows the model to “learn” from measured data how the ship answers to certain inputs (i.e. rudder angle and propellers rpm). Another important point for a reliable simulation is the correct estimation of the initial conditions, i.e. position, heading and velocity (linear and rotational) at the starting instant t_0. This step requires a special care because the data recorded in the VDR are affected by noise and fluctuations due also to the limited accuracy of the GPS. For this reason a pre-filtering step is needed [4] using a polynomial interpolation of trajectory and heading, which could filter out spurious effect.

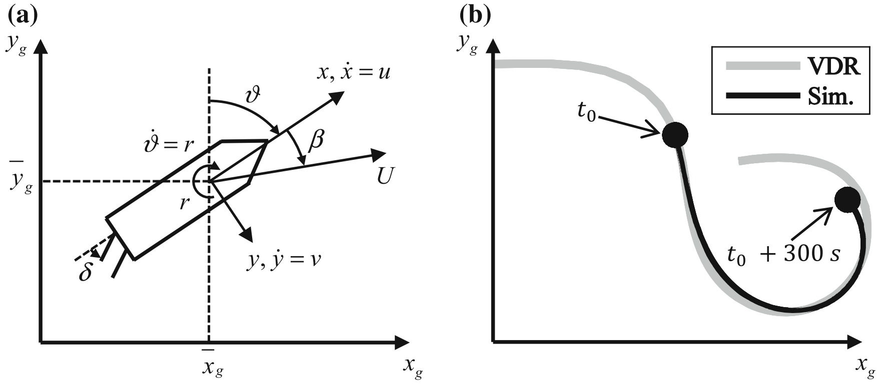

Fig. 1 Model reference frame (a) and Williamson turn simulation (b)

Table 1 Final error for different simulation time during two different manoeuvres

Palamos Turn				
Sim. time (s)	x_g error (m)	y_g error (m)	ϑ error (°)	Displ. err. (%)
30	−2.1	−3.2	−0.61	1.44
60	1.8	−6.6	−2.83	1.26
120	29.1	−74.9	−13.3	7.5
Palma Zig-Zag				
Sim. time (s)	x_g error (m)	y_g error (m)	ϑ error (°)	Displ. err. (%)
30	−0.6	−1.8	−0.01	1.28
60	−2.6	−6.5	−0.17	2.42
120	−11.0	−4.4	−0.48	4.83

2.3 Simulator Validation

The validation of the aforementioned short term simulator has been performed by comparing the simulated trajectory of the ship with previously recorded real data. To this end, starting from initial conditions (position and velocity) of the ship at t_0, instantaneous rudder position and propeller rpm recorded in the VDR were used as an input for the simulator. A variable simulation time Δt was used to evaluate its effect on final error (Δt = 30–120 s) and the simulated trajectory and heading of the ship were calculated. Finally the position and heading obtained by the simulator at $t_0 + \Delta t$ were compared with the actual data recorded in the VDR, so that the final error could be evaluated. This was done by using data contained in MB, as well as navigation data recorded by VDR during a cruise. The final errors (both position and heading) calculated in some time intervals for two independent manoeuvres are reported in Table 1. Moreover, Fig. 1b shows real and simulated trajectory corresponding to a mandatory manoeuvre (the so called Williamson Turn) performed during sea trials before ship delivering.

3 Manoeuvre Predictor

The described simulator proved its effectiveness in estimating ship's position under known commands. This section describes how this simulator is implemented in an algorithm to foresee vessel's trajectory during navigation, displaying predicted positions on electronic charts on the bridge. The algorithm is implemented in a real time fashion, so that it can run cyclically with the desired frequency (in the presented examples it runs once per second). The algorithm is intended to run in the same Personal Computer dedicated to the Integrated Navigation System and it can be considered as a part of this system itself.

3.1 Algorithm

The algorithm firstly computes the initial conditions. To do so, the procedure described in [4] is used. More precisely, the time interval needed to compute the polynomial interpolation is chosen to be 20 s long, from $t_0 - 20$ s to t_0 (being t_0 the time at which the simulation is launched). The polynomial interpolation proven to be more effective in velocity estimation for the points in the middle of the considered time interval, so that the better estimation of initial conditions is obtained at $t_0 - 10$ s. The actual simulation time interval will then start from $t_0 - 10$ s and it will end at $t_0 + 30$ s, so that 40 s of simulation time (Δt) are needed to estimate 30 s of ship's future behavior. The second step is rudder angle estimation. Rudder positions during the first 10 s of simulation time (i.e. from $t_0 - 10$ s to t_0) are known from VDR data. Anyway, it is not possible to know the exact rudder position from t_0 to $t_0 + 30$ s, since the rudder takes several seconds to go from the starting position to the ordered one. One solution could be to consider rudder angle at t_0 as a constant for the last 30 s of simulation: this is a good approximation if the rudder has already reached its final position at t_0. The alternative was to consider the angle set by the helmsman and to compare it with actual rudder position. A ramp could then be generated starting from the actual position (at t_0) to the final ordered position (the slope of the ramp is a constant for a given ship and can be calculated from recorded navigation data). When the ramp reaches the set angle position (at t_1), rudder angle are considered constant for the remaining portion of simulation time (i.e. from t_1 to $t_0 + 30$ s), since no other information are available. Figure 2 shows the comparison between the actual rudder angle recorded in the VDR file and the estimated angle: the two plots are perfectly overlapped in the time interval from $t_0 - 10$ s to t_0, the estimation is still good between t_0 and t_1, while a considerable difference is present for times greater than t_1 since there is no way to predict future orders given by the helmsman. Once the rudder angle vector is estimated, the algorithm can start the simulator to foresee ship's trajectory.

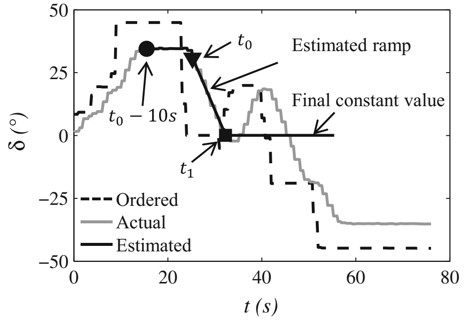

Fig. 2 Rudder angle estimation for the whole simulation time

3.2 Preliminary Results

The algorithm has been applied to several recorded manoeuvres to evaluate its performances. In this way, the actual ship's position at the end of the simulation time is present in the recorded data, and it can be compared to the simulated one. Results cannot be as good as the ones presented in the previous sections, since the rudder angles are not exactly known for the last part of the simulation time, and just the aforementioned estimation is available. Figure 3 shows the results obtained in two different situations during Costa Concordia navigation near Giglio island before the shipwreck. In Fig. 3a estimation errors are really low (in the same order of magnitude of GPS error), proving the reliability of the proposed methodology. Figure 3b shows the results obtained in the proximity of Giglio rocks. The greater error is due to the difference between actual rudder angle and estimated ones (Fig. 2). It is worth noting that the proposed algorithm would have helped the commander to foresee the impact with at least 30 s of advance, allowing to plan correction manoeuvres. Further development could implement the possibility to give a series of rudder positions as an input to the algorithm, so that more complicated manoeuvres can be foreseen. Anyway, this would not be a real time application anymore, since the time needed to set more complicated command sequences could be not neglectable during emergency operations.

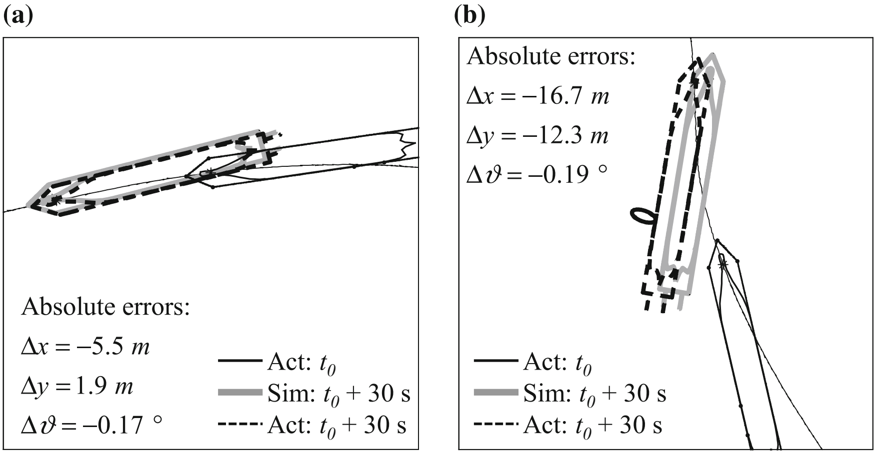

Fig. 3 Performances in final position estimation: left turn (**a**) and Giglio rocks impact (**b**)

4 Conclusion

This paper presents an algorithm capable to predict the effect of ordered manoeuvres in real time during navigation of any type of ship (provided that some mandatory data, recorded during sea trials before ship delivering, are known). The proposed procedure allows to foresee ships trajectory at least 30 s ahead in time, giving a precious help to commanders in shallow water or emergency conditions. The proposed algorithm implements a short time simulator tuned up for Costa Concordia manoeuvres evaluation. It has been shown that its utilization would have made possible to foresee the ship trajectory just on time to avoid the impact with Giglio Island rocks.

References

1. ITTC: Recommended Procedures-Testing and Extrapolation Methods-Manoeuvrability Validation of Manoeuvring Simulation Models, (1999)
2. ITTC: Manoeuvring Committee—Final Report and Recommendations to the 21st ITTC. Proceedings of 21st ITTC, Bergen-Trondheim, Norway, pp. 347–398 (1996)
3. Sandaruwan, D., Kodikara, N., Keppitiyagama, C., Rosa, R.: A six degrees of freedom ship simulation system for maritime education. Int. J. Adv. ICT Emerg. Reg 34–47 (2010)
4. Neri, P., Piccinelli, M., Gubian, P., Neri, B.: A ahip motion short term time domain simulator and its application to Costa Concordia emergency manoeuvres just before the January 2012 accident. Proceedings of 28th ECMS, Brescia (2014)

A Portable System for the Monitoring of Dissolved Oxygen in Aquatic Environment

**Luca Lombardo, Jiaran Zhang, Salvatore Gianluca Leonardi,
Davide Aloisio, Giovanni Neri, Daoliang Li and Nicola Donato**

Abstract Here is reported about the development of a sensing apparatus for dissolved oxygen (DO) in water. The purpose is achieved by means of a home-made electrochemical sensor, with working probe functionalized with Ag-iron oxide nanoparticles, and a readout system based on custom electronics for sensor interfacing and ATMEL microcontroller. Oxygen concentration was varied by bubbling an argon and oxygen mixture at different partial pressure (P_{O2}/P_0) into a 1 M phosphate buffer solution (pH = 7.4). A graphical user interface (GUI), developed in Python environment, allows the real-time visualization and recording of data coming from the sensor. The system is biased by USB connection and, employed with a notebook, it can be considered as a portable stand-alone one for outdoor applications.

1 Introduction

Dissolved oxygen (DO) is an essential indicator in chemical, biological and biochemical processes and needs to be rapidly measured in many cases. For example, the dissolved oxygen concentration in water is one of the main parameters to assess the quality of water for life of humans and animals in aquatic environment. Then, monitor DO in an aquarium water and wastewater is of outmost importance for water quality control and environmental monitoring containing different combinations of plant and animal species. Oxygen is indeed necessary to nearly all forms of

---

L. Lombardo · S.G. Leonardi · D. Aloisio · G. Neri · N. Donato (✉)
Department of Electronic Engineering, Chemistry and Industrial Engineering,
University of Messina, 98166 Messina, Italy
e-mail: ndonato@unime.it

J. Zhang · D. Li
China Agricultural University, Beijing, People's Republic of China

D. Aloisio
CNR, ITAE, Messina, Italy

A. De Gloria (ed.), *Applications in Electronics Pervading Industry, Environment and Society*, Lecture Notes in Electrical Engineering 409,
DOI 10.1007/978-3-319-47913-2_9

life and water systems require an adequate oxygen level in order to allow aerobic life forms to develop [1].

In such a context, the employment of low cost portable measurement systems can be important to spread the number of applications. In this work, we present a study devoted to the development of a home-made electrochemical sensor, with working electrode (WE) functionalized with Ag-iron oxide nanoparticles, and a readout system based on custom electronics for sensor interfacing and ATMEL microcontroller, for monitoring of dissolved oxygen in water. Cyclic voltammetry and chronoamperometric measurements, two electrochemical techniques widely employed in the characterization of electrochemical sensors [2], were carried out in order to evaluate the sensor performance.

2 Experiments

2.1 Electronic Redout System

The developed measurement system, the block diagram is reported in Fig. 1a, can be employed with a notebook, the on board microcontroller and the Python based interface allow to employ several operating systems.

The USB port is used to supply the power for instrument and communication with PC, since the Main Board is biased with a supply voltage of 3.3 V. The linear regulator SiP21106 is used: it supplies the voltage of 3.3 V (accuracy: 1 %) with a current capacity of 150 mA. The microcontroller ATMEGA16L ATMEL controls all functions of the instrument and carry out the operations required in the different measurement modes. It works with a 4 MHz clock provided by using a precise crystal resonator. An hardware reset can be achieved by an external system, but also a software reset is possible. A green LED is used as an indicator for working status of the measuring system (standby, working, ON/OFF). For communication with the PC, FTDI FT232 converter is used to convert bidirectionally the signal of the USART and the USB port. The converter works with 6 MHz clock by using an other resonator. An additional EEPROM can store PID, VID, and Serial Number when it is connected with PC by USB. A red LED is used to indicate the exchange of data by the USB port.

The microcontroller communicates with the Probe Board by using the interface TWI (Two Wire Interface)/I2C BUS protocol. The Probe board is equipped with its own voltage regulator, the power supply is also at 3.3 V, to decouple and avoid the effect of high frequency noise in the amplification and conversion stages. The controller also has an enable input that can enable/disable the Probe Board by the request of the microcontroller to reduce power consumption.

An integrated voltage reference at 1.25 V provides a stable and accurate voltage as the reference voltage value for the amperometric sensor. It is used to shift the reference potential in a system designed with a single positive supply, so giving the possibility to provide negative bias voltages and to measure negative currents.

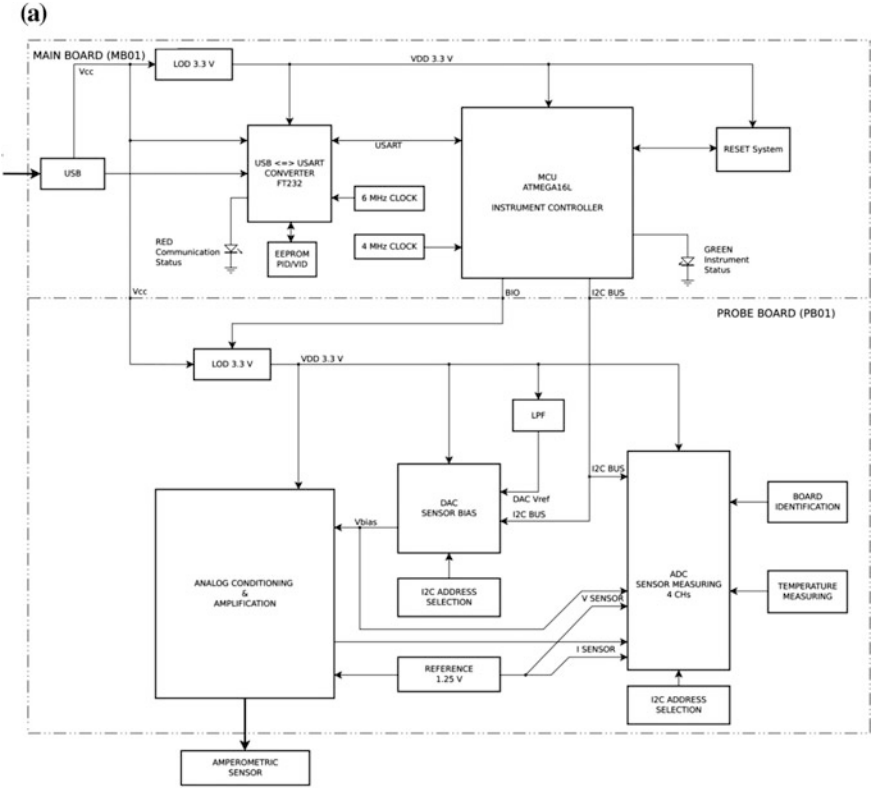

Fig. 1 **a** *Block* diagram of the measurement system. **b** Sensor analog conditioning circuit

The DAC converter is employed to generate the bias voltage: the adopted device is a DAC121C085, a 12 bits digital to analog converter based on I2C interface. The analog conditioning block polarize the sensor setting the potential: the output voltage from the DAC and the reference voltage are used. In Fig. 1b is shown how the output current from the sensor is amplified and converted into a voltage by a transimpedance amplifier, the MCP606. The output voltage from the amplifier is set in one of channels of the AD converter, it is converted into a digital value and then sent to the microcontroller by the I2C bus. The other three channels of the ADC are used to measure the bias voltage of the sensor, for the Probe Board identification and for the temperature measurement (by a thermistor). MCP3424 is a low noise and high accuracy 18-Bit delta-sigma analog-to-digital converter that has 4 channels with differential input. During each conversion, the device calibrates offset and gain errors automatically. This provides accurate results from conversion to conversion over temperature variations and power supply fluctuation. Finally, the sensor is connected to the instrument using a probe equipped.

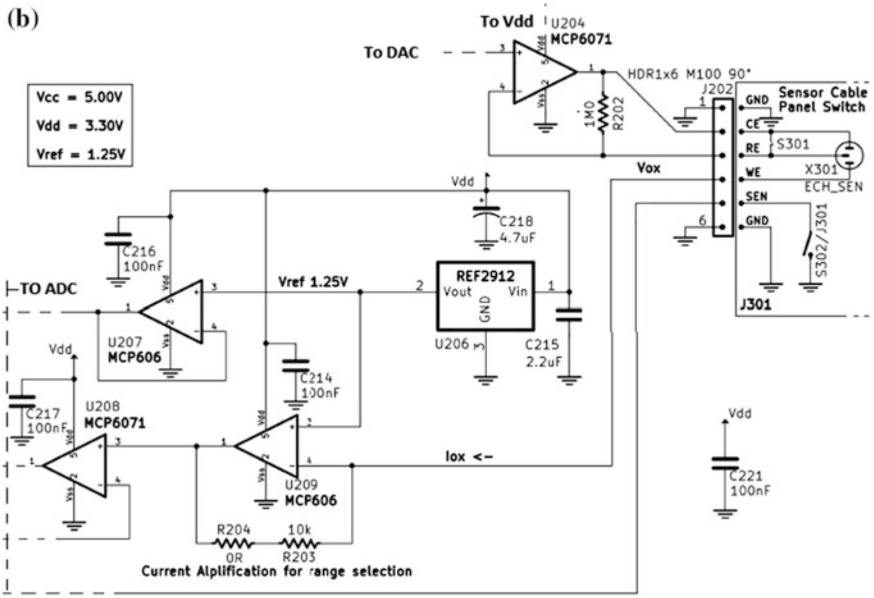

Fig. 1 (continued)

2.2 Material Synthesis

Ag-iron oxide sensing material was prepared in according to a procedure reported in a previous paper [3]. First, Ag nanoparticles were synthetized starting from a PVP (20 wt%) and $AgNO_3$ solution in deionized water and in presence of sodium borohydride ($NaBH_4$). Metallic silver nanoparticles were separated from the solution by centrifugation and then washed three times with distilled water and acetone to remove organic species. In the second step iron oxide covered Ag nanoparticles were obtained by a sol-gel method starting from a solution of iron sulphate in which were dispersed Ag nanoparticles. The mixture was refluxed for 2 h under moderate stirring at 70 °C. The Ag-iron oxide composite so formed was separated by centrifugation.

2.3 Sensor Preparation and Electrochemical Test

Sensor has been prepared employing a commercial screen printed carbon electrode (Dropsens C110) equipped with a 4 mm in diameter WE. The sensor was fabricated as follows: first a dispersion of the Ag-iron oxide in ethanol and Nafion (10 wt%) was prepared. Then, the suspensions were sonicated for 15 min in order to obtain a homogeneous dispersion of powder. Carbon working electrode was modified by dropping 5 μl of above suspensions and finally allowed to dry at room temperature.

All electrochemical tests were carried out by means of the above potentiostat. To keep the pH value constant during tests, dissolved oxygen measurements were performed in a phosphate buffer solution (PBS, pH 7.4) at room temperature (T_{sol} = 20.5 °C) and atmospheric pressure. Different oxygen concentrations were obtained by bubbling inside the above solution a mixture of argon/oxygen at different partial pressure (P_{O2}/P_0). Cyclic voltammetry and chronoamperometric measurements were carried out in order to evaluate the sensor performance.

3 Results

Figure 2 shows the cyclic voltammograms recorded at a scan rate of 100 mV/s in the potential range between 0 and −1.25 V with different oxygen concentrations. The cyclic voltammetry conducted in the absence of dissolved oxygen, after having purged the solution by means of pure argon bubbling, shows no significant electrochemical process but only an almost rectangular cycle due to phenomena of charge of the electric double layer. When the solution was saturated with oxygen, a significant reduction peak, with onset potential at about −0.25 V and maximum at −0.6 V, was clearly visible in the voltammogram.

Furthermore, the reduction peak current increased appreciably by increasing the oxygen partial pressure from 0 to 0.75 which indicates that the electrode is sensitive to oxygen (Fig. 3). However, for oxygen partial pressures higher than 0.75 was not possible to appreciate a useful signal. It was due to the limitation of measurement current range of the prototype potentiostat (~250 μA), and a new improved version of the measurement system is planned to be developed.

However, during the practical use, it is more convenient to work in amperometric mode. In this way the faradic current is the only variable, directly related to the concentration of the species of interest that will discharge at WE. To evaluate the sensor performance in according to this operation method, a fixed potential of −0.5 V was fixed to the working electrode and the current was recorded over time.

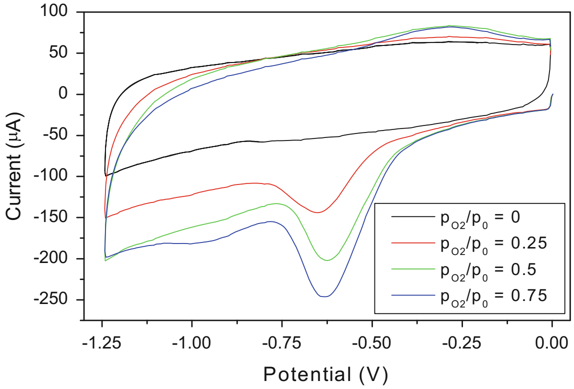

Fig. 2 **a** Cyclic voltammetry recorded for different oxygen saturation partial pressures in phosphate buffer solution, scan rate: 100 mV/s

Fig. 3 Calibration curve

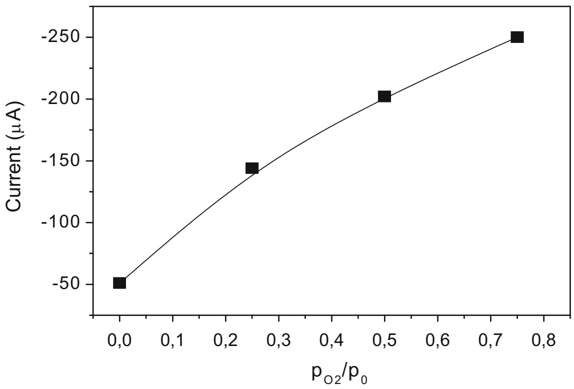

Fig. 4 Chronoamperometric test at potential of −0.5 V with O_2 partial pressure ranging from 0 to 1

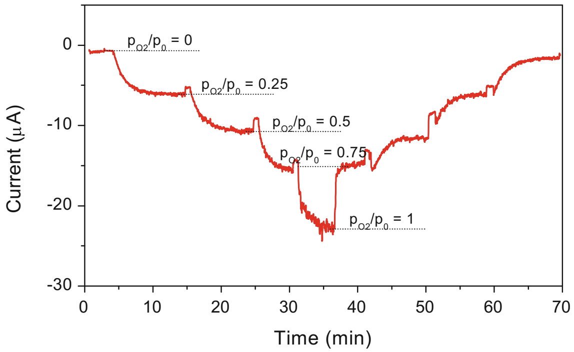

Figure 4 shows the current versus time plot recorded in real time meanwhile different oxygen partial pressures have been bubbled inside PBS solution under stirring. The sensor shows an increase of the reduction current with increasing of oxygen partial pressure inside the solution, and a good response reproducibility. Figure 5 shows the calibration plots of current values extracted from the above

Fig. 5 Calibration plots of current values

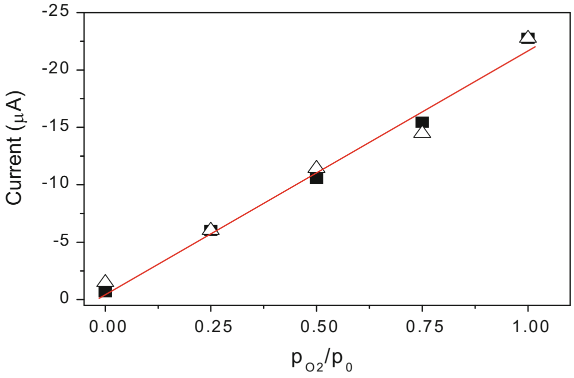

chronoamperometric test as a function of oxygen concentration in the range of partial pressure 0–1. The plots of current values as a function of oxygen concentration in the range yielded straight line: $y = -0.223 \times -0.594$, $R^2 = 0.946$.

4 Conclusions

Here we reported about the development of a portable monitoring system for dissolved oxygen in water. The system is based on custom electronics and electrochemical sensors with a working electrode provided with an Ag-iron oxide composite.

The proposed sensor presented a good response for dissolved oxygen at applied potential of −0.5 V. This sensor showed a simple and easy preparation along a good repeatability for the DO measurement with small hysteresis. Further activities are in progress in order to extend the measurement range of the readout electronic system.

References

1. Ansa-Asare, O.D., Marr, I.L., Cresser, M.S.: Evaluation of modelled and measured patterns of dissolved oxygen in a freshwater lake as an indicator of the presence of biodegradable organic pollution. Water Res. **34**, 1079 (2000). http://dx.doi.org/10.1016/S0043-1354(99)00239-0
2. Privett, B.J., Shin, J.H., Schoenfisch, M.H.: Electrochemical sensors. Anal. Chem. **80**(12), 4499–4517 (2008). doi:10.1021/ac8007219
3. Bonyani, M., Mirzaei, A., Leonardi, S.G., Bonavita, A., Neri, G.: Electrochemical properties of Ag@iron oxide nanocomposite for application as nitrate sensor. Electroanalysis. doi:10.1002/elan.201500240

Sensormind: Virtual Sensing and Complex Event Detection for Internet of Things

Davide Brunelli, Gianluca Gallo and Luca Benini

Abstract With the pervasive diffusion of smartphones and ultra low-power wireless devices, the capability of implementing new objects with smart sensors which can directly share data on the internet is exponentially growing. This extraordinary data deluge poses new challenges to the research community such as storing/retrieving in a fast and reliable way the information. In this paper we present *Sensormind*, a virtual sensor environment for Internet of Things providing scalable and flexible solutions to manage hundreds of smart objects and which can be easily customized by end-users.

1 Introduction

Internet of Things (IoT) enables the gathering of information coming from physical objects of everyday usage, by means of pervasive and non-intrusive sensors connected to the Internet. Today, there are already more "things" posting information to the Internet, than personal communication devices such as mobile phones or PCs [1–3]; and in the next years every object is expected to generate huge amounts of data during its lifetime.

Sensormind is an open source project. It is available for trials and professional uses. http://www.sensormind.net/.

D. Brunelli (✉)
Department of Industrial Engineering, University of Trento,
via Sommarive 9, 38123 Trento, Italy
e-mail: davide.brunelli@unitn.it

G. Gallo
University of Bologna, via Risorgimento 2, 40136 Bologna, Italy
e-mail: gianluca.gallo@unibo.it

L. Benini
ETH Zurich, Gloriastrasse 35, Zurich, Switzerland
e-mail: luca.benini@iis.ethz.ch

A. De Gloria (ed.), *Applications in Electronics Pervading Industry, Environment and Society*, Lecture Notes in Electrical Engineering 409,
DOI 10.1007/978-3-319-47913-2_10

Unfortunately, available tools for IoT, wireless sensors and Cyber-Physical Systems (CPS) appear inadequate to satisfy user's expectation. They lack an intuitive and interoperable way to create both simple and complex interactions between several source of information (sensors or objects) and target of specific actions (actuators) or recipients of particular results. The use of scalable service architectures that can accept and store data coming from multiple and heterogeneous sources (i.e. periodic scalar values, vectors, streams, files, images or video) is an important first step in this direction [4, 5].

In addition to this, additional services are fundamental to generate real-time feedback from the IoT live data to the real world. In particular, two important services are essential:

- A method to filter, to correlate and to process the real-time events remotely generated by the *smart things*. This method must be able to detect particular combinations of events. This capability is fundamental to predict events or to trigger actions using real-time intelligence. The rapidity of catching, analyzing and evaluating trends or predicting risks combined with the capability to provide feedback is fundamental because *things in the world* have to be in a cyber-physical feedback loop and not just logged at world scale;
- A service to facilitate also non-technical users to perform analysis and processing data coming from the things.

The possibility to *add-&-run* processing plug-ins to generate and extract new information from raw data is crucial. Since results are periodically updated, we can consider them generated by *virtual sensors VSs* which produces new information, that is not directly sensed, from raw data and can manage these streams as if they were coming from physical sensors. To handle in real-time these requirements, the usage of a Complex Event Processing (CEP) engine system is essential [6], since (i) it permits users to set triggers for VS execution and update, and (ii) it performs on the fly the production and computation of new values for each VS.

Current technologies and frameworks available for CPS do not fulfill all the requirements and needs of this vision of Internet of Things. IoT is intended to be used by millions of people which are totally unaware about the technology issues, but should be able to setup and connect intelligent objects to suit their needs. For this reason, low-complexity mechanisms and user interfaces must be designed.

The *Sensormind* framework consists in a combination of services, and permits to connect custom algorithms and data analysis blocks in a dynamic way. This framework also provides features to allow data from a sensor component to be streamed to a filter component for signal processing operations. The output from the filter component can be connected to other components, or can be stored as a data from a virtual sensor. The aim of the work is to provide a holistic approach for IoT moving towards new dimensions by integrating our daily lives through the objects and appliances we use.

2 Architecture

The architecture of *Sensormind* is shown in Fig. 1 and consists of two different logic blocks, which can be deployed separately or into the same host:

- The *ActiveStorage* is the core of the platform. It receives data from the IoT through the *System Input Interface* (SII). It manages the storage of the information into the internal database, and it executes the algorithms defined by the user. Finally, it checks the alarms and notifies when the user-defined events are detected;
- The *Dashboard* is designed to manage the interaction with users, to visualize the IoT data, and to communicate with external devices that can request elaborated data through a configurable *System Output Interface* (SOI).

The different sensor sources (e.g. WSNs and smartphones) can use several protocols for connecting to the SII, such as MQTT. After the authentication, the input data flow is replicated in two branches. The former stores the information into the database, and concurrently the latter is processed on the flight to check if particular patterns or events, defined by the users, have occurred by using an engine for Complex Event Processing (CEP). For each input the CEP compares the registered event with a desired activation list. In case of matching, notifications and dedicated instances of processing algorithms are activated in an engine called *Virtual Sensor Environment* (VSEnv), as described in Fig. 2.

In this way it is possible to execute user-defined runtime analysis and algorithms on the raw data in-flight, reducing the overhead of extracting the data from the DB. The results and the new data generated by VSEnv are considered as the output of "*virtual sensors*" and thus they are stored in the database using the same SII interface. Thanks to this configuration, the services can exploit few and optimized interfaces, making *Sensormind* highly reactive to specific triggering conditions, as discussed and characterized in the following sections.

Each algorithm instantiated on VSEnv can access also other data stored in the database using an optimized set of APIs, and in addition, they can publish alerts,

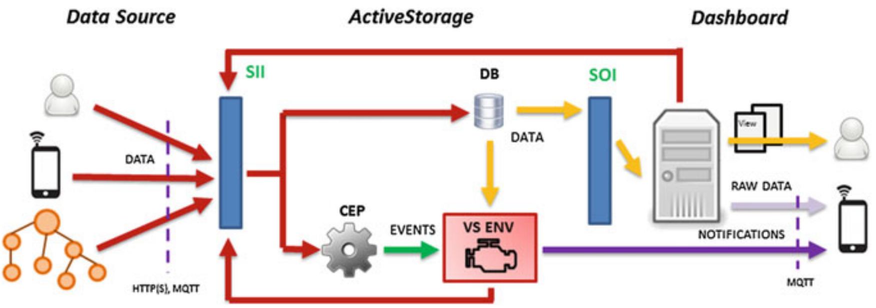

Fig. 1 Framework main architecture

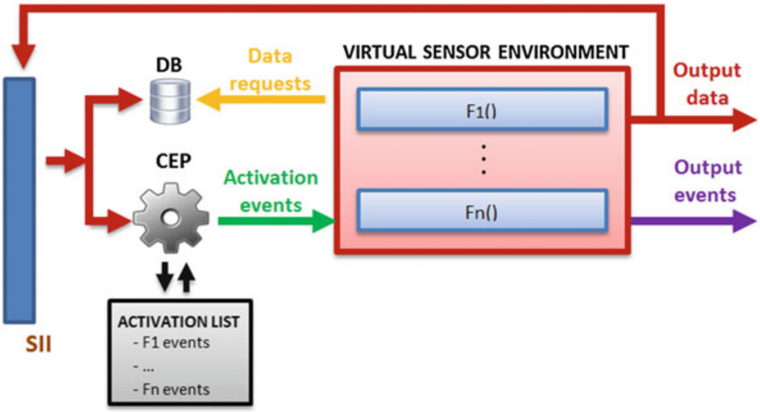

Fig. 2 Virtual sensor engine

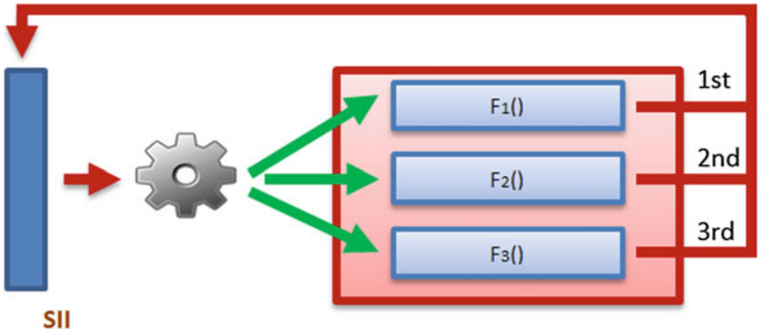

Fig. 3 Feedback loop for complex event detection

alarms and data through the *System Output Interface* (SOI). In this way, it is easy to create multiple custom chains of virtual sensing functional blocks triggered by the CEP as depicted in Fig. 3, or to design custom feedback control loops using external actuators through the SOI. *Sensormind* permits to configure the CEP engine with multiple alerts/notifications and support a number of data publication methods using different protocols (i.e. HTTP POST, MQTT PUBLISH or email).

The VSEnv can contain and execute thousands of instances of different *virtual sensors*. For example a thermal comfort algorithm is a *virtual sensor* (described later in Sect. 3.2) that determines the perceived ambient comfort by people in a room.

To define the aforementioned virtual sensor in the *Sensormind* framework, a five-step configuration is needed:

1. *Activation events*: it is a list of events and conditions that defines when a virtual sensor instance must be triggered and executed;

2. *Data request*: a list of data source and objects required for the data processing and the algorithm execution. Only the sources configured in this list can be accessed at runtime by the virtual sensor;
3. *Virtual Sensor Output*: it is the definition of the expected output, which can be both notifications or alerts (using the available protocols) and new data values of the virtual sensor which can be stored in the database;
4. *Algorithm*: it is the core of the virtual sensor which exploits the defined source of data to generate new information;
5. *Static parameters*: a set of predefined parameters which can be used as configuration setup or to adapt a general purpose algorithm to a specific set of things.

This model permits users to implement and to instantiate a *virtual sensor* from scratch or to adapt a generic available predefined algorithm. Implementing a new virtual sensor from scratch requires the setting of these 5-steps and the uploading of the algorithm. Next, the virtual sensor will be executed after the activation of an instance and at the first trigger event from the CEP. *Sensormind* allows generating an arbitrary number of different instances. In detail, the *virtual sensor* capability is provided by *Sensormind* framework through 3 main objects:

2.1 Virtual Sensor Environment

The *Virtual Sensor Environment* VSEnv is the algorithms container. It permits the creation of new algorithms and the configuration of new instances running on a sandbox infrastructure.

The framework drives an embedded CEP engine with the activation events from the configured algorithms (from its *Activation Events List*) with the desired actual sensor. The CEP engine receives data from the SII and compares continuously the incoming data with the activation pattern. For each matching, the CEP uses a callback to VSEnv to schedule and launch the registered *virtual sensor*.

Once a virtual sensor is activated, it may require other data from the database (e.g. a specific series of old values) or may need data from another sensor (either *real* or *virtual thing*). The VSEnv engine checks if the request is allowed (e.g. security and ownership of the requested information) and retrieves the data needed by the user-defined algorithm.

3 Performance Assessment

To evaluate framework performances we executed several tests focused on the *virtual sensors* functionality. In particular we measured the performance of the CEP engine and we discussed two real case studies to determine the computation time and the delay of the *Virtual Sensor Environment*. Tests are performed on a single host (even though any component can be deployed on multiple hosts), using the following configuration: Windows 7 Ultimate 64 bit SP1, CPU Intel i7-2600 @ 3.40 GHz, RAM 8 GB Java 1.7.0_51, using default 2 GB MaxHeapSize on the JVM.

3.1 Complex Event Processing and Detection

In this test we have measured the number of packets that the CEP subsystem can process and the number of concurrent events it can detect to trigger actions from the controller side. Moreover the system allows users to execute dynamically customized algorithms (processing blocks) on the real-time streams, and this test aims to assess also the number of processing blocks which can be served concurrently.

The execution time of the processing blocks is also another important feature which has been measured. Tests are performed varying the number of queries in the range (0–100). The number of events which can be managed and eventually detected decreases with the number of different matching we are seeking (queries). In Fig. 4 we show the number of events that *Sensormind* can check and serve in a second. The logarithmic scale points that if only one query is configured, the system can concurrently check and detect up to 3M events. While if there are 100 different patterns to check, the system can serve about 7000 event/s that is remarkably a good performance on a single machine. The detection delay is still quite low. As depicted in Fig. 5, in the previously worst case condition discussed the CEP subsystem is able to generate a trigger only 1.5 ms after the data has been received.

We have implemented several *case studies* that test the capability of the framework to interact with different sensor networks and sources. In particular, in this paper, we discuss an index for evaluating the environmental indoor comfort.

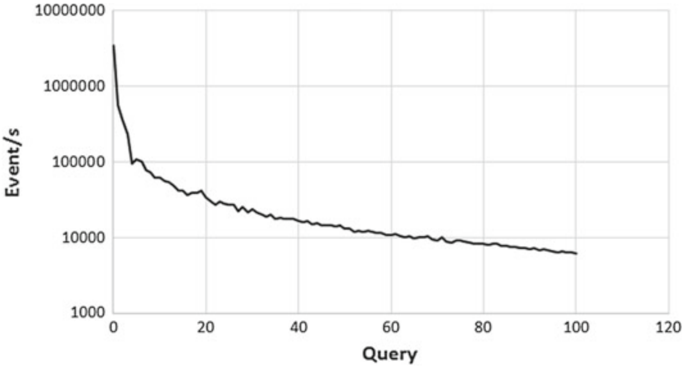

Fig. 4 Event processing throughput

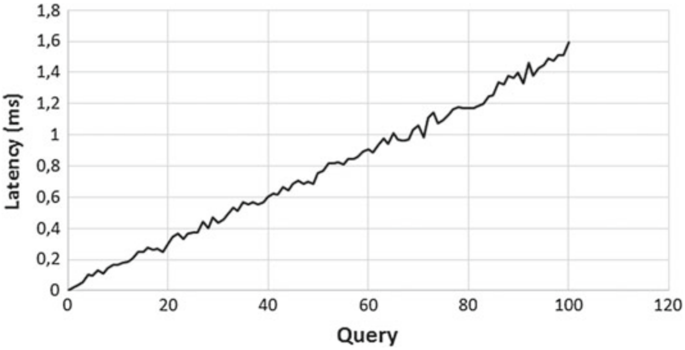

Fig. 5 Event processing latency

3.2 *Thermal Comfort Virtual Sensor*

The thermal comfort is mainly a condition of the human mind that expresses satisfaction with the thermal environment. Nevertheless, it has been characterized and an objective metric has been defined together with models [7]. The subjective thermal feeling is generally expressed using the Predicted Mean Value (PMV) index. PMV is defined as the mean of the votes of a large group of people on a 7-point integer thermal sensation scale ranging from −3 (cold) to +3 (hot), based n the heat balance of the human body in a given environment [8].

Although a physical transducer of thermal comfort does not exists, *Sensormind* permits to create a *virtual sensor* of Indoor Thermal Comfort, by simply combining in real-time data collected by the sensors in a room. Indeed, the PMV index can be calculated for different combinations of metabolic rate, clothing insulation, air temperature, mean radiant temperature, air velocity and air humidity [9].

The implementation of this *virtual sensor* in the *Sensormind* platform uses real sensors [10–12] to obtain the (i) room air temperature, (ii) room wall temperature and the (iii) relative humidity and request to static configure the other parameters, approximating the full PMV formula for indoor.

A new evaluation of the thermal comfort *virtual sensor* is triggered every time each of the three connected real sensors post a new value and the output of this data processing is a new integer value of “ThermalComfortValue” in rage [−3; +3]. We tested and verified how many processing blocks can be activated concurrently. A network of 480 smart sensors has been connected to the *Sensormind* platform and we configured each room to determine the Thermal Comfort Index.

We configured up to 120,000 different instances of the processing blocks and the execution time has been assessed. As expected the response time of the virtual sensor increases with the number of instances. In particular when the system experiences the maximum load, the time needed to complete an execution step is up to 1 min.

In a real world deployment to maintain the framework reactivity and avoid the explosion of algorithm execution time the VSEnv execution core can be parallelized on many nodes.

4 Conclusion

A web-based framework for Internet of Things has been presented in this paper. The main and innovative features are the capability to define *Virtual Sensors*, which are custom processing chains designed by users on aggregated multiple input streams, and to provide a sandbox execution environment for the algorithms (e.g. people counting [13], compressive sensing [14],…).

This framework simplifies development of IoT, speeds up the visualization of the heterogeneous information and allows the end-user to adapt the analysis of the data with fast and easy-to-define algorithm and processing method on the live data source. Typical application scenarios include home automation, heating and ventilation control, industrial monitoring and control. Moreover, the framework is open to data coming from smartphone and any kind of smart object.

The aim of the proposed framework is to provide a holistic approach for IoT-based monitoring and control applications, by combining the performance of the CEP system in detecting occurrences, with realtime processing chains on live data. Experimental results on our servers provide useful information about the flexibility of this system and the scalability of the *virtual sensors* execution time.

Acknowledgment The research contribution presented in this paper has been supported by the FP7 project GreenDataNet (grant no.609000).

References

1. Zorzi, M., Gluhak, A., Lange, S., Bassi, A.: From today's intranet of things to a future internet of things: a wireless- and mobility-related view. IEEE Wireless Commun **17**(6), 44–51 (2010)
2. Atzori, L., Iera, A., Morabito, G.: The internet of things: a survey. Comput. Netw. **54**(15), 2787–2805 (2010)
3. Miorandi, D., Sicari, S., De Pellegrini, F., Chlamtac, I.: Internet of things: vision, applications and research challenges. Ad Hoc Netw. **10**(7), 1497–1516 (2012)
4. Hadim, S., Mohamed, N.: Middleware: Middleware challenges and approaches for wireless sensor networks. IEEE Distrib. Syst. Online **7**(3), 1 (2006)
5. Yu, Y., Krishnamachari, B., Prasanna, V.K.: Issues in designing middleware for wireless sensor networks. IEEE Netw **18**(1), 15–21 (2004)
6. Luckham, D.: The Power of Events: an Introduction to Complex Event Processing in Distributed Enterprise Systems. Springer (2008)
7. UNI: ANSI/ASHRAE Standard 55-2013 thermal environmental conditions for human occupancy

8. UNI: EN ISO 7730 ergonomics of the thermal environment—analytical determination and interpretation of thermal comfort using calculation of the pmv and ppd indices and local thermal comfort criteria (2005)
9. UNI: EN ISO 7726 ergonomics of the thermal environment—instruments for measuring physical quantities (2001)
10. Brunelli, D., Minakov, I., Passerone, R., Rossi, M.: Smart monitoring for sustainable and energy-efficient buildings: a case study. In: IEEE Workshop on Environmental, Energy and Structural Monitoring Systems (EESMS) (2015)
11. Jelicic, V., Magno, M., Paci, G., Brunelli, D., Benini, L.: Design, characterization and management of a wireless sensor network for smart gas monitoring. In: 4th IEEE International Workshop on Advances in Sensors and Interfaces (IWASI), 2011, pp. 115–120 (2011)
12. Aderohunmu, F.A., Brunelli, D., Deng, J.D., Purvis, M.K.: A data acquisition protocol for a reactive wireless sensor network monitoring application. Sensors **15**(5), 10221 (2015)
13. Paci, F., Brunelli, D., Benini, L.: 0, 1, 2, many—a classroom occupancy monitoring system for smart public buildings. In: Conference on Design and Architectures for Signal and Image Processing (DASIP), 2014, pp. 1–6 (2014)
14. Milosevic, B., Caione, C., Farella, E., Brunelli, D., Benini, L.: Sub-sampling framework comparison for low-power data gathering: a comparative analysis. Sensors **15**(3), 5058 (2015)

RF-Powered HF-RFID Analog Sensors Platform

Demetrio Iero, Corrado Felini, Massimo Merenda and Francesco Giuseppe Della Corte

Abstract An RF powered HF-RFID passive sensors platform has been realized using discrete components and printed antennas designed to resonate at 13.56 MHz, used both for energy harvesting and data transmission. The tests demonstrate the possibility of the system to operate autonomously within the reading range of a standard RFID reader, that acts both as RF power source and receiver of the data stored in the tag user memory. The microcontroller on the platform can be interfaced with an analogic sensor made with polymeric material sensible to physical parameters or chemical agents.

1 Introduction

The new technologies allows to make RFID (Radio Frequency IDentification) tags with embedded sensors that can be remotely activated and powered by RF fields. These tags integrate a sensing stage, an antenna, a transceiver and a data memory.

RFID tags have a wide range of sensing and monitoring applications, allowing to know the state of a product at any time. The platform allows to acquire sensors data, sending and storing into the memory measurements and events [1, 2].

D. Iero (✉) · C. Felini · M. Merenda · F.G. Della Corte
DIIES, University Mediterranea of Reggio Calabria, 89122 Reggio Calabria, Italy
e-mail: demetrio.iero@unirc.it; info@senseame.com

C. Felini
e-mail: corrado.felini@unirc.it

M. Merenda
e-mail: massimo.merenda@unirc.it

F.G. Della Corte
e-mail: francesco.dellacorte@unirc.it

D. Iero · M. Merenda · F.G. Della Corte
HWA srl—Spin off UNIRC, Via F. Zeni 8, 38068 Rovereto, Italy

A. De Gloria (ed.), *Applications in Electronics Pervading Industry, Environment and Society*, Lecture Notes in Electrical Engineering 409,
DOI 10.1007/978-3-319-47913-2_11

The system includes a microcontroller for the acquisition of data and a 13.56 MHz tag chip for the RFID communication and data storage. The microcontroller ensures a low-cost alternative for achieving high-end features such as bi-directional communication, anti-collision and on-board computational power especially for acquisition systems. The presence of these devices in a small space allows the designer to exploit the benefits of using a microprocessor system, while reducing the use of external components. Circuits that until recently were made with conventional circuitry, can be easily made low cost using a microcontroller.

There are several approaches for incorporating sensing capabilities into RFID. Active tags use batteries to power their communication circuitry, sensors, and microcontroller, whereas passive tags are supplied though different forms of energy harvesting methods (RF fields, sunlight, thermal gradients, mechanical) that eliminate the need of battery replacement or maintenance. Active tags benefit from relatively long wireless range and can achieve high data and sensor activity rates. However, the batteries are disadvantageous for device cost, lifetime, weight, and volume.

In this paper an RF powered HF-RFID low-power passive sensors platform is presented. It is realized using discrete components and printed antennas used for energy harvesting and data transmission. The microcontroller on the platform governs temperature acquisitions, either from a sensor integrated in the tag, or from analog sensors fabricated onto the PCB, e.g. based on organic materials, and eventually stores data inside the tag memory.

2 System Description

The system has been realized on a flexible 0.4 mm tick FR4 substrate. The 13.56 MHz platform has ISO/IEC 7810 ID-1 card size (85.60 × 53.98 mm) and is shown in Fig. 1.

It includes two antennas. The biggest antenna is used for energy harvesting and is connected to the rectifier circuit. A single stage Dickson rectifier is implemented to power the platform from the RF field. The smallest antenna is used for RF data transmission and it is connected to the RF chip tag. The RFID tag IC is the M24LR64-R [3], a 13.56 MHz NFC/RFID tag with a dual-interface EEPROM.

Figure 2 shows a block diagram of the platform. As soon as the circuit gets into the RF field of a reader, the platform is activated, it harvests the RF energy and activates the rectifier circuit that provides a regulated DC supply voltage (1.8 Vdc) to the microcontroller (MCU) and to the tag IC.

The tag chip is connected to a second dedicated antenna used for data transmission. When the microcontroller is active, it provides the energy to the tag chip from the main supply through the energy harvested from the RFID reader. The supply system powers up the microcontroller and the tag chip when data are transferred from the microcontroller to the tag through the I^2C bus. Otherwise, the tag chip is passively powered by the RFID reader and its own antenna to ensure remote data acquisition.

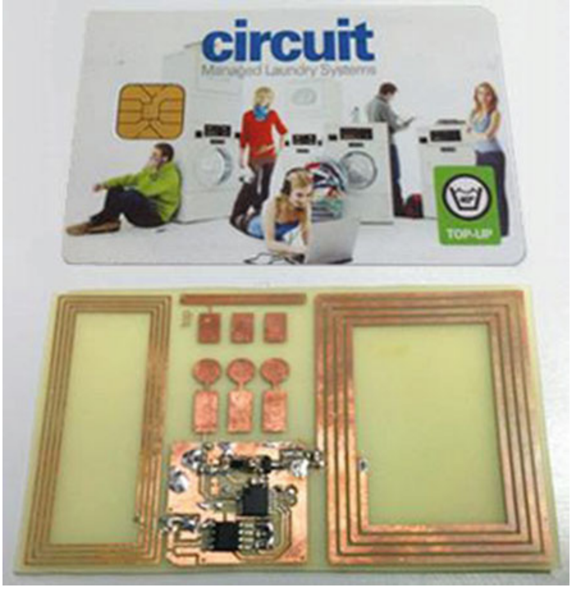

Fig. 1 Picture of the 13.56 MHz platform prototype compared with an ISO size card

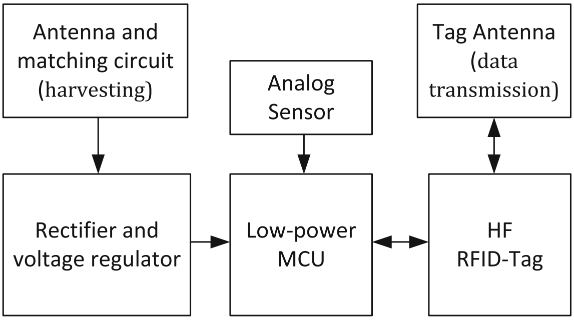

Fig. 2 Block scheme of the sensor platform

The microcontroller acquires data from an analog sensor, and stores it on the user memory of an RFID tag at a user selectable rate. The tag transmits the stored data according to the ISO 15693 standard.

3 Platform Components

The microcontroller is an 8-bit XLP (eXtreme Low Power) MCU from Microchip Technology (PIC16LF1503) that supervises the whole operations of the circuit. It integrates a 10 bit ADC that allows to acquire the measurements from an analog sensor. It uses the I^2C interface to communicate with the tag chip and store the measurements into the tag EEPROM memory.

The M24LR64-R tag has 8192 bytes of user programmable memory that can be accessed both from a reader and the microcontroller to read/write measured data and to read/write configuration parameters. The updated parameters can be read by the microcontroller to dynamically adjust the time intervals between sensor readings in order to modify the system power budget according to new application conditions.

The rectifier is made with HSMS2852 Schottky diodes (Avago) that implement a Voltage Doubler rectifier, whereas a linear voltage regulator (ON Semiconductor NCP583) is used to regulate and stabilize the voltage at 1.8 V.

The PCB includes some pads, connected to the ADC port of the microcontroller. These pads can be used e.g. to deposit a polymeric material sensible to physical parameters (e.g. temperature) or chemical agents. These pads are connected through a voltage divider to a pin of the microcontroller; the voltage is acquired and converted by the integrated Analog to Digital converter of the MCU and the value can then be converted to a resistance measurement proportional to the physical monitored parameter.

4 Antenna Design

A 13.56 MHz antenna can be designed with different shapes. A square antenna was chosen for this platform. It should be considered, however, that a resonating antenna at this frequency would be too big to fit in an ISO card size. Therefore resonance at 13.56 MHz is typically obtained by coupling an inductor (spiral square loop in our case) to a capacitor. The spiral loop inductance can be calculated with the following equation [4]:

$$L_{antenna} = K1 \cdot \mu_0 \cdot N^2 \cdot \frac{d}{1 + K2 \cdot p}. \tag{1}$$

The impedance of the realized inductors was calculated thought a simplified software tool provided by ST Microelectronics [4]. The small spiral loop (tag antenna), and the big one (harvesting antenna) were designed with a target inductance arbitrarily set to 1.1 μH. The two loops were characterized using an impedance analyzer Agilent 4395; the actual measured impedance values, shown in Table 1, are very close to the target.

Afterwards, in order to tune the receiving circuit at the resonance frequency of 13.56 MHz, a matching capacitor is applied at the inductor terminals, calculated according to the formula:

Table 1 Impedances of the realized loops measured with an impedance analyzer

	Main antenna	Tag antenna
Inductance ($L_{antenna}$)	1.09 μH	1.11 μH
Capacitance	2.40 pF	2.13 pF

$$f_{resonance} = \frac{1}{2\pi\sqrt{L_{antenna} \cdot C_{tuning}}}. \tag{2}$$

which provides a C_{tuning} of 100 pF. The effects are shown in Figs. 3 and 4. Figure 3 shows the impedance of the biggest spiral loop (harvesting antenna) as a function of the frequency. It is possible to observe that the inductance matches the design specifications and the resonance frequency is about 100 MHz. It is necessary to use an equivalent capacitance of about 100 pF in order to create a circuit resonating at about 13.56 MHz.

Figure 4 shows the impedance of the smallest loop (tag antenna); also in this case it is necessary to use an equivalent total capacitance of about 100 pF in order to

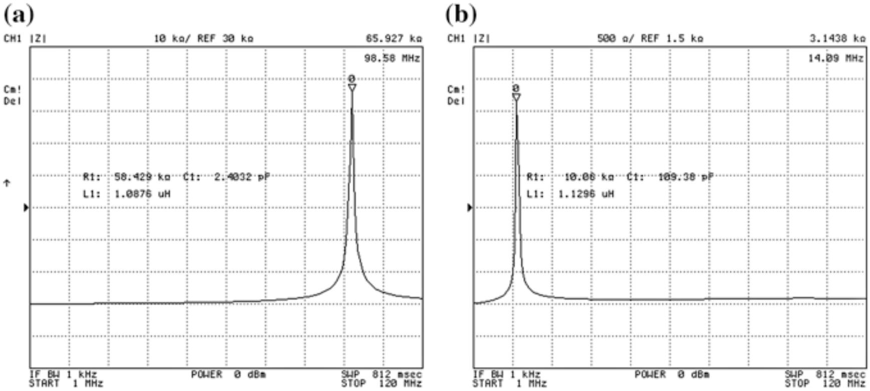

Fig. 3 Impedance of the biggest antenna on the PCB (harvesting antenna) without (**a**) and with the matching capacitor (**b**)

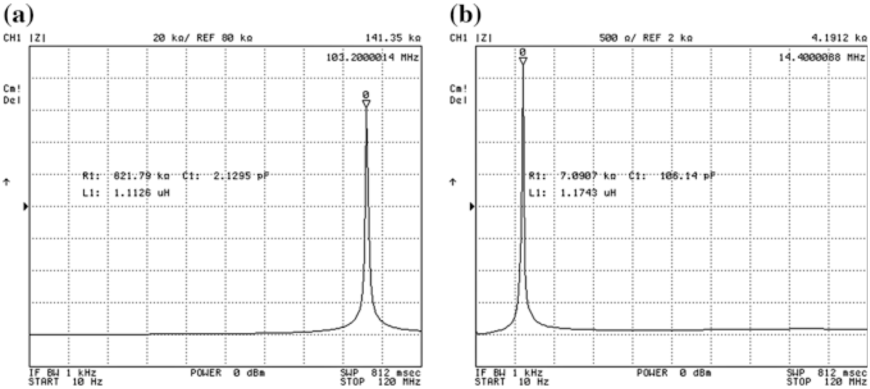

Fig. 4 Impedance of the smallest antenna on the PCB (tag antenna) without (**a**) and with the matching capacitor (**b**)

create a circuit resonating at 13.56 MHz. As the M24LR64-R has an internal tuning capacitance $C_{tuning} = 27.5$ pF, in order to create a circuit resonating at 13.56 MHz it is necessary to use a capacitance of about 72 pF.

5 Experimental Results

Figure 5 shows the measured output voltage of the rectifier as function of the distance between the reader antenna and the tag. The maximum working distance of the platform is about 0.9 m when a reader with 31 dBm of transmitting power is used. Moreover, the data transmission through the small tag antenna has been successful tested with commercial NFC enabled smart-phones.

Fig. 5 Rectifier output voltage as function of the distance of the tag from the reader

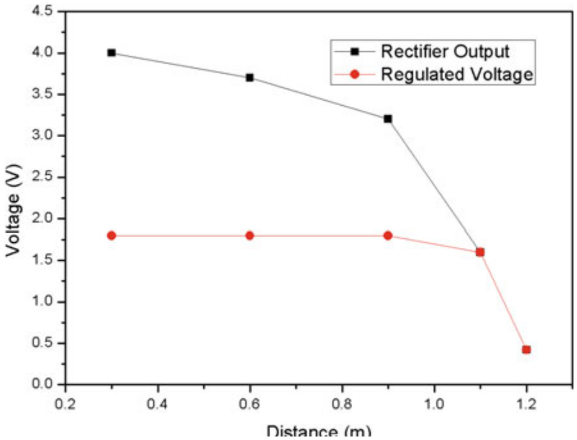

Fig. 6 Rectifier output voltage as function of the distance of the tag from the reader

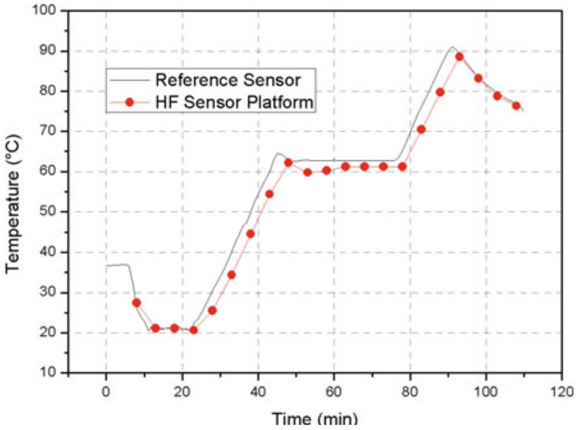

The platform has been tested by reading and logging temperature measurements of the analog sensor TMP20 in a climatic chamber; the results have been compared with the measurement of a commercial sensor (Magiant Serverflu). The system was powered from the energy harvested by a commercial HF reader (ID ISC MR100 RFID) and the results are shown in Fig. 6.

6 Conclusion

A Wireless Sensor Platform operating at 13.56 MHz was designed and realized to perform analog measurements from a sensor made with e.g. a polymeric material sensible to physical parameters (e.g. temperature) or chemical agents.

The low power microcontroller ensures very low power consumption in sleep mode, allowing an optimal energy harvesting and storage from the RF source, and to achieve a working distance near to 1 m.

Hardware improvements have been investigated for future enhancement of the energy transfer efficiency and the power consumption during the sensing activities.

References

1. Merenda, M., Della Corte, F.G., Lolli, M.: Remotely powered smart RFID tag for food chain monitoring. In: Lecture Notes in Electrical Engineering. pp. 421–424 (2011)
2. Merenda, M., Felini, C., Della Corte, F.G.: Battery-less smart RFID tag with sensor capabilities. 2012 IEEE International Conference on RFID-Technologies and Applications (RFID-TA), pp. 160–164 (2012)
3. ST Microelectronics: M24LR64-R NFC/RFID tag Datasheet. http://www.st.com/web/en/resource/technical/document/datasheet/CD00217247.pdf (2013)
4. ST Microelectronics: Application Note AN2972—Designing an antenna for the M24LRxx-R and M24LRxxE-R. http://www.st.com/web/en/resource/technical/document/application_note/CD00232630.pdf (2012)

Enabling Technologies for the In-house Monitoring of Vital Signs in Chronic Patients

Massimiliano Donati, Alessio Celli, Alessandro Benini, Luca Fanucci and Sergio Saponara

Abstract The in-house monitoring of vital signs represents a real opportunity to improve the effectiveness of the healthcare of chronic patients, integrating the traditional in-hospital healthcare model with a new out-of-hospital follow-up based on frequent monitoring of the clinical status. It allows clinicians and practitioners to realize and act promptly suspect aggravations, before they become irreversible and lead to hospitalization. This model relies on ICT, in particular biomedical sensors and concentrator devices (i.e. gateway) that enable to acquire vital signs at patient's home and to transmit collected data in secure way, making them remotely available for medical personnel. This paper presents two gateway devices enabling the in-house monitoring of vital signs according to the kind and severity of the diseases, being the first conceived to be used by the patient while the second studied for professional caregivers. Moreover, it presents a novel sensor for the self-acquisition of the ECG signal.

1 Introduction

The management of chronic diseases represents an important challenge for the National Health System (NHS) in any developed countries, especially due to the large amount of resources required for the healthcare of the patients. Chronic Heart Failure (CHF) and Chronic Obstructive Pulmonary Disease (COPD) are today the main causes of hospitalization in the older adult segment. Additionally, they show a very high re-hospitalization rate (i.e. subsequent hospitalizations after the first acute episode) that affects considerably the healthcare costs sustained by the NHS, the congestion of the specialized resource and the patient's quality of life.

M. Donati · A. Celli · A. Benini · L. Fanucci · S. Saponara
Department of Information Engineering, University of Pisa, via G. Caruso 16,
56122 Pisa, Italy

M. Donati (✉) · L. Fanucci · S. Saponara
IngeniArs srl, via Ponte a Piglieri 8, 56122 Pisa, Italy
e-mail: massimiliano.donati@for.unipi.it

A. De Gloria (ed.), *Applications in Electronics Pervading Industry, Environment and Society*, Lecture Notes in Electrical Engineering 409,
DOI 10.1007/978-3-319-47913-2_12

CHF affects approximately 15 million European citizens [1] and more than 5 million Americans [2], with a prevalence of 2 % and an incidence of 3.6 million and 550,000 of respectively in Europe and in U.S. [3]. It represents the 5 % of all hospitalizations [1] and it is the main reason of admission in people aged 65 years or older, accounting for the 2 % of the total healthcare expenditure [3]. Instead, more than 15 million Americans and approximately 210 million worldwide suffer from some forms of COPD [4], corresponding to a prevalence close to 8 % [5].

The traditional model of care, based on periodic visits provided by specialized centers or practitioners, does not allow an early detection and reaction to the signs of decompensation, and often they become irreversible. This dramatically causes a high hospitalization rate, posing an important societal and economical problem to the NHS. Moreover, considering that according to the World Health Organization (WHO) the number of people affected by chronic diseases is expected to double before 2030, new cost-effective models of treatment are required.

The ICT technologies have a key role in the implementation of new multi-disciplinary and integrated management models, in which the in-house monitoring of vital signs (i.e. ECG, blood pressure, oxygen saturation, pulmonary capacity, weight, etc.) and lifestyle information are the central points. The in-house monitoring of patients with telemedicine systems integrating all actors involved in the healthcare of chronic patients results in a reduction of the mortality, hospitalizations, length of hospital stay [6–8] and consequently benefits both the patients and the NHS.

This paper presents two gateway devices that allow the in-house acquisition of vital signs from Bluetooth sensors and the transmission of data towards remote platforms by which medical personnel can monitor the patients at distance. Moreover, it presents a novel sensor aiming at the self-acquisition of the ECG signal for telemedicine purposes. Hereafter, Sect. 2 gives an overview of the in-house monitoring model. Sections 3 and 4 present the gateway and ECG devices respectively. Finally, conclusions are drawn in Sect. 5.

2 The In-house Monitoring

The general architecture for the provisioning of in-house monitoring of vital signs during the out-of-hospital follow-up is shown in Fig. 1. The platform relies on the modern ICT that allows the acquisition, the storage and the secure circulation of the clinical information among all caregivers involved in the healthcare of chronic patients [9]. In this way, the medical personnel can monitor at distance the status of many patients though dedicated repository or the direct integration with the Hospital Information Systems, and they can take timely actions in case of aggravation.

Two kinds of in-house monitoring exist, depending on the disease and the severity of the clinical condition. The first is performed directly by the patient while the second envisages the involvement of professional caregivers during the

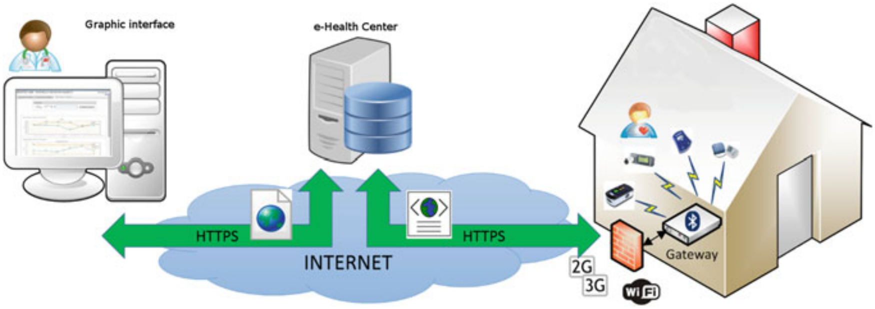

Fig. 1 In-house monitoring infrastructure

domiciliary visits. In both cases, the main enabling element to implement the in-house monitoring is a wireless sensor network (e.g. Bluetooth). It is composed of biomedical sensors for non-invasive measurement of the main vital signs under the coordination of a gateway device that contains all the computation and communication resources. The role of this part of the monitoring chain is to provide the rest of the platform with frequent (i.e. daily) and updated high-quality vital signs information collected at home.

3 The Gateway System

The gateway is the central node of the wireless sensor network, being in charge of collecting, storing and transmitting in secure way the data coming from the biomedical sensors. Depending on the target user, patient or caregiver, it has different features and user interfaces that allow to maximize its effectiveness. The following sections describe in details two kinds of gateway specialized for their applications. They are implemented for Android ≥4.3 devices (i.e. tablet, smartphone, set-top-box) equipped with Bluetooth and at least an Internet connection (e.g. WiFi, 3G, etc.).

3.1 Gateway for Patients

This model of gateway is usually delivered directly to the patient when enrolled in the telemedicine service, along with the set of sensors selected by the clinician. The gateway is conceived to minimize the impact on the patient and to maximize the usability. It enables the patient to follow autonomously the personalized treatment agenda (defined on the E-Health Center) exploiting reminder messages and audio-visual helps, while data acquisition and transmission are completely transparent.

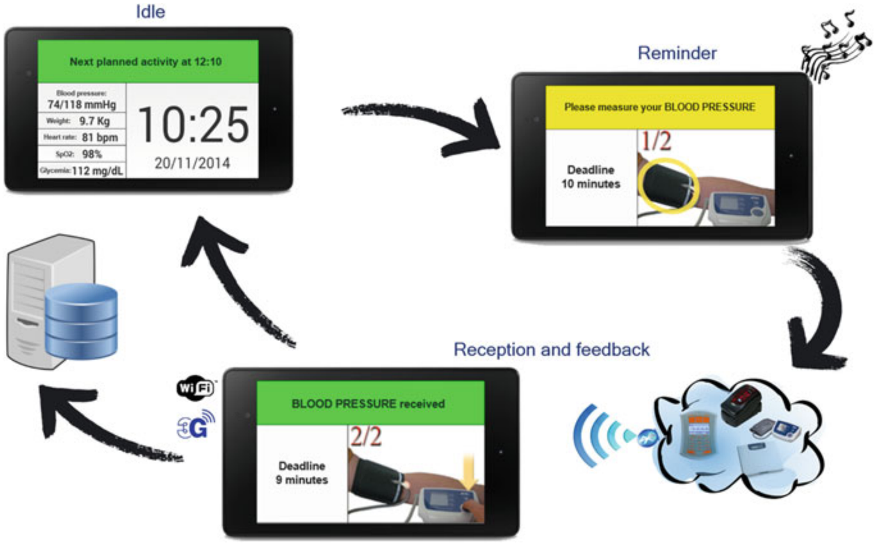

Fig. 2 Example of lifecycle in case of a blood pressure measure

Figure 2 shows the typical lifecycle of the gateway permanently assigned to a chronic patient. During the idle phase the device shows, on the left, the last value of each collected parameter (e.g. hearth-rate, systolic and diastolic pressure, etc.) while, on the right, the current time is shown. The upper green bar reminds the time of the next activity, if exist, or shows that no more interactions are requested for the current day. When the time of an activity is reached, the gateway switches to reminder phase. The upper bar changes to yellow (user interaction request) and indicates the scheduled activity, the right part of the screen displays the graphical helper that explains how to use the sensor and, on the left, the deadline is shown. Now the patient has the time to complete the activity before the deadline. Once executed successfully the activity, the gateway provides an immediate audio-visual feedback, then it returns in idle phase. Meanwhile, it tries to transmit the collected data to the E-Health Center. In case of failure during the acquisition, the gateway requests again the same activity while if transmission fails, it store temporarily the data that will be added in future transmission retries. Additionally, the gateway is also able to receive out-of-agenda activities: once received, the only additional interaction required to the patient is to confirm the acquisition through an acknowledgment dialog.

3.2 Gateway for Caregivers

This model of gateway is part of a specialized kit provided to professional caregiver to support their routinely domiciliary visits of chronic patients. It allows the

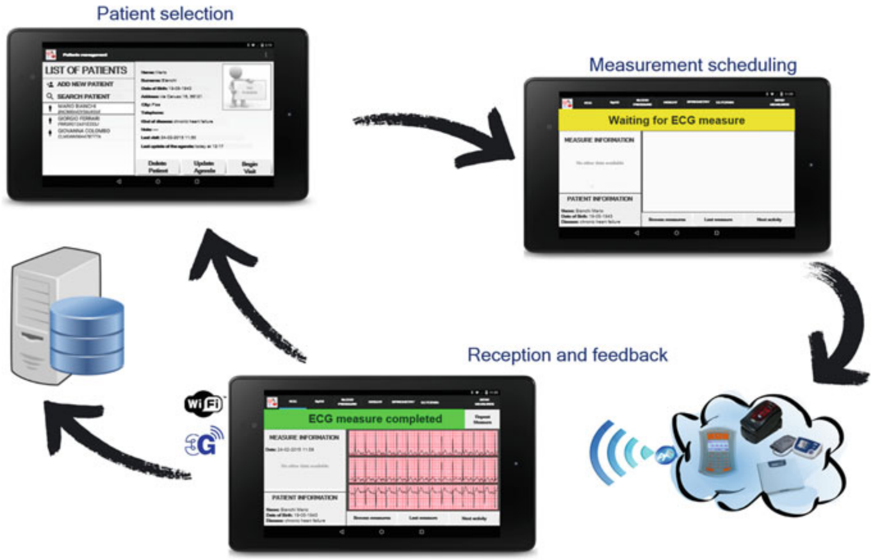

Fig. 3 Example of lifecycle in case of domiciliary visit including the ECG

management of the large list of assisted patients, specifying for each of them the personalized agenda of activities defined by the clinicians. The gateway derives from the previous version and maintains its basic functionality, but it includes more sophisticated data visualizations and interaction modes suitable for professional users.

Figure 3 shows the typical use case of the gateway during a domiciliary visit. The first step consists of the selection of the patient from the list, previously downloaded from the e-Health center, by textual search or by scanning the sanitary ID card. For each patient, personal data, information about the chronic diseases he/she is affected and expected activities are provided. Once selected the patient, the gateway switches to a specific screen with a series of in horizontal tabs that support the caregiver to perform all the requested activities. Each tab is related to a vital sign and indicates in the upper bar if the activity is requested or not through a message with yellow or gray background respectively. Moreover, it shows on the left the information about the last collected measure, if exists, while the area on the right it provides a graphical representation of the vital sign and the possibility to browse stored data. In particular, if the tab concerns scalar physiological measures (e.g. blood pressure, glycaemia, etc.), the graph represents the historical trend, otherwise for complex physiological measures (e.g. ECG, spirometry, etc.) the graph is related to the last wave collected. Now the caregiver can use the sensor to measure the requested vital signs, receiving immediately at the end of each activity an audio-visual feedback. Additionally, out-of-agenda activities can be always performed, activating manually the specific tab. At the end of the visit, the gateway sends all data to the E-Health center confirming the successful transmission.

A failure in data acquisition results in a request to repeat the activity while a temporary storage of the data ensures to avoid loss in case of failure in transmission, allowing for deferred attempts.

4 The ECG Sensor

Among all the vital signs, the heart activity is one of the most important in chronic patients management. Heart activity can be monitored via electrocardiographic devices. Many devices exist on the market able to forward the recorded ECG to a telemedicine gateway. Unfortunately, they are often hard to be set and operated autonomously by the patient (e.g. complex interfaces, adhesive electrodes to be placed, etc.). Instead, these devices are mostly conceived for professional users.

In order to allow patients that suffers of chronic diseases to record their own ECG signal autonomously, a new user-friendly and ergonomic ECG sensor is proposed. The device consists of two pairs of dry metal electrodes placed on a plastic body having approximated dimensions of 30 × 5 × 3 cm. It works by placing each hand in contact with a pair of electrodes, measuring for 30 s the first lead of the ECG signal with a sampling rate of 500 S/sec (band 0.05–37 Hz). The sensor provides real-time forwarding of the recorded data to a gateway exploiting a SPP Bluetooth connection. Moreover, it presents a minimal user interface consisting of a power button, a LCD display and a couple of LEDs. Once powered, the device displays a message inviting the patient to put the hands in contact with the electrodes. When contact is detected, the calculated HR is shown, a bar indicates the progress of the acquisition and a red LED blinks in correspondence of the R peaks (see Fig. 4).

The results of the testing phase, using Matlab to receive data and plot the signal, demonstrate the quality and the usability of the device. All the testers are able to use the device without any help and the position of the hands is comfortable and easy to

Fig. 4 User interface of the device while recording an ECG

Fig. 5 Comparison of the ECG acquired using Lifepak and the prototype

keep. The signals are clean and free of artifact due to muscular activity. Furthermore, a comparison of the first lead of the ECG signal recorded using simultaneously the prototype (i.e. by placing the hands on its electrodes) and a professional ECG monitor (i.e. by attaching wet electrodes on the chest) confirms that the signals are very similar and can be overlapped almost perfectly, as shown in Fig. 5.

5 Conclusions

The presented devices enable the implementation of the in-house monitoring of chronic patients integrated with the traditional in-hospital care. The gateway ensures data collection and transmission from a wide range of sensors adapting to the target user, while the ECG device enables high-quality self-acquisition of the ECG. All devices have been successfully tested in validation pilots with real patients and have been recently transferred to the spin-off IngeniArs that will take care of the CE certification and the commercialization of the final products.

References

1. Dickstein, K., Cohen-Solal, A., et al.: ESC guidelines for the diagnosis and treatment of acute and chronic heart failure 2008. Eur. Heart J. **29**, 2388–2442 (2008)
2. Go, A.S., Mozaffarian, D., et al.: Heart disease and stroke statistics-2014 update: a report from the American Heart Association. Circulation **128**, 18–209 (2014)
3. Zannad, F., Agrinier, N., et al.: Heart failure burden and therapy. Europace J. **1**, 1–9 (2009)
4. Diaz-Guzman, E., Mannino, D.: Epidemiology and prevalence of chronic obstructive pulmonary disease. Clin. Chest Med. **35**, 7–16 (2014)
5. Raherison, C., Girodet, P.O.: Epidemiology of COPD. Eur. Respir. Rev. **18**(114), 213–221 (2009)
6. Fergenbaum, J., et al.: Care in the home for the management of chronic heart failure. Cardiovasc Nurs J. (2015)
7. Ekeland, A.G., et al.: Effectiveness of telemedicine: a systematic review of reviews. Int. J. Med. Inform. (2010)
8. Finet, P., et al.: Review of current telemedicine applications for chronic diseases. IRBM (2015)
9. Fanucci, L., Donati, M., Celli, A., et al.: Advanced multi-sensor platform for chronic disease home monitoring. IEEE I2MTC (2015)

Measuring Tissue Compression: A Circuit for Sensing and Signal Conditioning

Sonja Hermann, Patrick Thomas, Richard B. Reilly and Martin J. Burke

Abstract Addressing the lack of available systems for pressure ulcer prevention and treatment, the development of a monitoring and prevention system for deep seated pressure ulcers (DSPU) is described here. The measurement system comprising of a charge-based front-end amplifier, which feeds subsequent stages for adjusting gain, offset voltage and filtering, uses a unique mechanical impulse wave as input signal. This signal is passed through an analogue-to-digital converter for digitisation before being transferred to a computer via a USB port using a microcontroller for signal processing. The system response, tested with a Bose Electroforce and a laser vibrometer, showed a linear response over the measurement range necessary for DSPU prevention and detection and thus it was confirmed that the described development can provide an accurate measurement system for DSPU.

1 Introduction

Pressure ulcers (PU) are of high prevalence amongst the critically ill, patients with chronic conditions, of compromised health and in the elderly, they are painful and debilitating. Affecting one million people annually in the US alone, the associated treatment costs are $1.6 billion [1]. PU's develop when tissues experience high stresses, in weight bearing tasks of sitting or lying supine, in which deeper tissues (e.g. muscle) experience up to 276 greater compressive stresses than skin [2–4]. Without adequate pressure relief deeper tissues will damage with resulting development of DSPU's. They are the most difficult PU's to treat as they only become visible days or weeks after substantial irreversible internal tissue damage has

---

S. Hermann (✉) · R.B. Reilly · M.J. Burke
School of Engineering, Trinity College, Dublin 2, Ireland
e-mail: hermanns@tcd.ie

P. Thomas
Electrical Engineer, Gehestrasse 33, 01127 Dresden, Germany

R.B. Reilly
School of Medicine, Trinity College, Dublin 2, Ireland

A. De Gloria (ed.), *Applications in Electronics Pervading Industry, Environment and Society*, Lecture Notes in Electrical Engineering 409,
DOI 10.1007/978-3-319-47913-2_13

already occurred. Best practise in PU prevention and treatment remains visual assessment of skin integrity and frequent load redistribution [1], however these methods for aforementioned reasons fail in prevention of DSPU's.

1.1 Development of a Tissue Health and Pressure Ulcer Prediction System

The SanaSense method [5] and system has been developed by the authors over several years to address the lack in available DSPU prevention and prediction systems [6–9]. The SanaSense system uses a thin film sensor (EMFIT), which, placed under a mattress or seat cushion (non-contact measurement) acquires an impulse signal from which pertinent information on muscle tension and viscoelastic tissue properties is extracted using the SanaSense method (patent pending). This mechanical impulse wave, has previously been described in relation to the ballistocardiogram (BCG) method [10, 11]. The body's viscoelastic tissue structures react to the mechanical impulse with a damped natural oscillation, which subsequently is being picked up by the SanaSense sensor. The reminder of the article describes the development and testing of the necessary circuitry to allow the acquisition of the above described damped tissue oscillations, which are of very small nature. Thus due to the very small input signal challenges in signal amplification and noise reduction are encountered, how these were addressed by circuit and system design is detailed in the following.

2 Signal Acquisition and Conditioning

The tissue compression signal is acquired using a low cost impact sensor, a cellular charged polymer sensor film EMFIT®Ferro-Electret Film (EMFIT Ltd., Finland). In order to meet the challenging interfacing requirements of this type of piezoelectric sensor material, a special-purpose amplification system had to be developed. This involved the design of a charge-based front-end amplifier as opposed to a standard voltage amplifier. The charge amplifier then feeds subsequent stages for adjusting gain, offset voltage and filtering. The damped tissue oscillation signal is then passed through an analogue-to-digital converter for digitisation before being transferred to a computer via a USB port using a microcontroller for signal processing (Fig. 1).

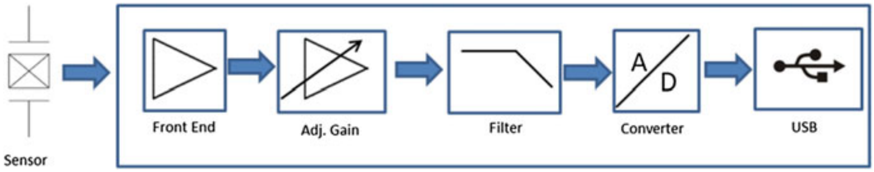

Fig. 1 Block diagram of the special-purpose amplification system

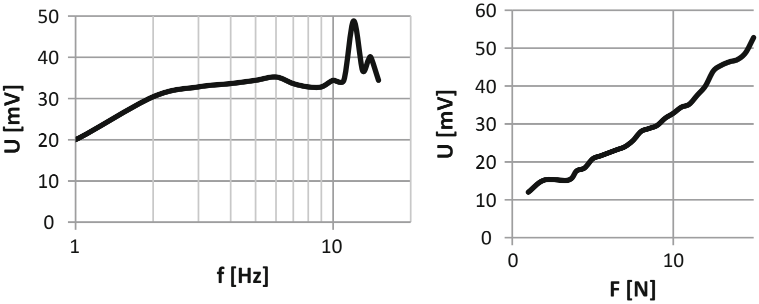

Fig. 2 Sensor frequency response *left* and calibration curve of sensor output *right*

2.1 The Tissue Compression Sensor

The EMFIT sensor behaves as an active capacitor with a force range of up to 100 N/cm^2. Force applied leads to a change in the internal charge which in turn leads to a minute output current that is proportional to the derivative of the applied force. To develop an adequate signal acquisition for damped tissue oscillations the linearity and frequency response of the sensor material was characterised. A Bose Electro-Force 3100 material testing machine was used to apply a mechanical sinewave of 5 N peak-to-peak to the sensor at a frequency range from 1 to 15 Hz, to simulate real life damped tissue vibrations ranges. The output was observed via a 1 MΩ oscilloscope probe. Results are shown in Fig. 2 on the left. The same test setup was used, this time with a constant 1 Hz sinewave input while the amplitude was varied between 1 and 14 N in order to derive a calibration curve for the sensor, depicted in Fig. 2 on the right.

Results confirm that the sensor material is suitable for the envisioned purpose. However as leakage currents between the sensors layers prevent the measurement of static forces it was decided to use a charge amplifier to act as a charge to voltage converter. This will allow quasi-static measurement with low cut-off frequencies as low as mHz and leads to improved overall system performance compared to a simple amplification of voltage output, how this was achieved will be explained in the next section.

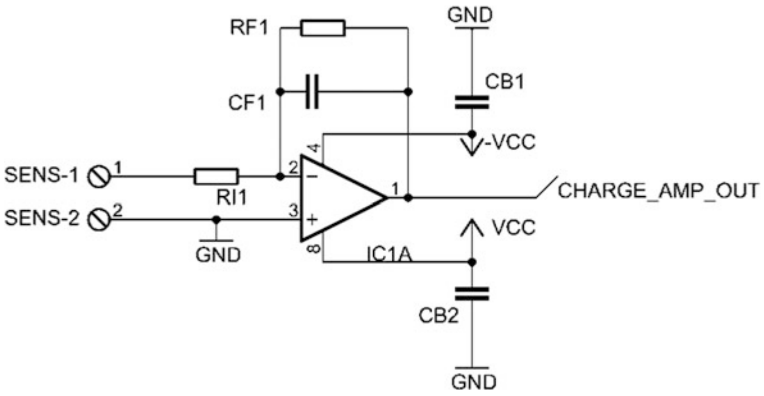

Fig. 3 The front end as used in the amplification unit

2.2 "Charge Amplifier"—Front End

The charge to voltage converter circuit uses the virtual ground potential existing at the inverting input of an op-amp (Fig. 3). Parasitic capacitances of connectors and sensor's cable must be considered in addition to the sensor's capacitance.

The charge from the sensor and the charge from the feedback capacitor compensate each other at the inverting input node. This gives:

$$q_{sens} = -q_f \tag{1}$$

Assuming that

$$C = \frac{Q}{V} \tag{2}$$

The output voltage is given as:

$$V_{out} = \frac{q_f}{C_f} = -\frac{q_{sens}}{C_f} \tag{3}$$

The gain of the charge amplifier is only determined by the feedback capacitor C_f. Resistor RF1 limits the lower cut-off frequency which is given as:

$$f_{cutoff\_low} = \frac{1}{2\pi R_{F1} C_f} \tag{4}$$

To control the bandwidth of the system an additional resistor RI1 is placed in the signal path to limit the upper cut-off frequency which is given as:

$$f_{cutoff\_high} = \frac{1}{2\pi R_{I1}(C_{Sensor} + C_{Cable})} \tag{5}$$

2.3 Signal Processing Stages and A/D Converter

The EMFIT sensor material is able to withstand the high stresses, tissue experiences under compression, while maintaining high sensitivity. The signal amplifier thus must cover this entire signal range. Linear amplifier operation is limited to approximately three decades of dynamic range while logarithmic amplifiers are able to handle up to 8 decades but requires special care in circuit design and temperature compensation. The proposed solution compromises between maximum range and circuit complexity, using a conventional amplifier with a rotary switch to select appropriate feedback resistors to alter the gain during operation. Amplification factors cover force ranges from <0.1 to 1000 N with 9 selectable gain factors. The resulting signal is passed to an anti-aliasing filter and digitalised by a 12-Bit SPI-interfaced ADC. The performance of the whole system was tested using the same test routine as described in Sect. 2.1. To test for the upper cut-off frequency a laser vibrometer was used. Results of the overall system performance (sensor, charge amplifier, gain stage, filters and A/D converter) are shown in Fig. 4. The upper cut-off frequency was verified to be above 300 Hz.

2.4 USB Transmission and Supply

The signal conditioning unit holds a Microchip-PIC microcontroller capable of receiving multiple ADC channel data via an SPI interface at rates of 1.5 kSample/s each. The 12-Bit variables are buffered and transmitted via a USB cable forming a virtual COM-Port at the host computer. Signal analysis, data logging and real-time

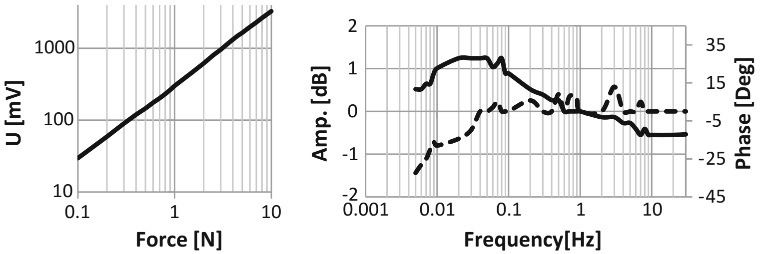

Fig. 4 Calibration curve, *left chart* and bode plot, *right chart* of the signal conditioning unit. Irregularities in the latter are caused by the non-ideal mechanical coupling between the material and the mechanical Bose testing system used

display takes place on the host computer within a customised LabView application. The use of USB for data transmission simplifies the signal conditioning unit's power supply. The voltage of 5 V provided by the USB host is inverted by a step-down charge-pump converter operating at 1 MHz switching frequency to provide the negative supply rail for the operational amplifiers. Any parasitic coupling of the 1 MHz switching frequency to the signal lines is filtered by the anti-aliasing filter.

3 Discussion

This article describes the development of the acquisition system for a novel tissue health and pressure ulcer prediction system "SanaSense" using a Ferro-Electret Film sensor (EMFIT Ltd., Finland), which, behaving as an active capacitor, captures a very small damped oscillation input signal. Using a Bose Electroforce and a laser vibrometer the overall systems response was tested; results confirmed a linear response over a range of 15 N. The here described circuit design thus enables measurement over the large force range <0.1–1000 N, this range is necessary as large forces may be experienced at the interface in load bearing tasks of sitting or lying supine (3–12 N/cm^2). At the same time the system allows for adequate resolution of the small force fluctuations of the damped oscillation signal input, which is central to enable for the first time a novel system for real time monitoring of DSPU risk and prevention.

4 Conclusion

SanaSense is addressing the gap in available systems for pressure ulcer prediction and prevention. The described circuitry and system development combined with the novel use of the impulse wave signal to detect changes in tissue/muscle viscoelasticity using a flexible thin film EMFIT sensor provided the building blocks for a prototype real time monitoring system for tissue viscoelasticity and pressure ulcer risk assessment. SanaSense may also find some use in sport applications where real time knowledge on muscle damage prediction is of great use in particular monitoring the development and training effects of professional athletes for rehabilitation purposes. As a next step it is planned to test the SanaSense system and method in a clinical environment with patients who are at risk of pressure ulcers to establish system reliability and robustness for a clinical usage case. The use of USB for data transmission only requires a 5 V power supply and can be transmitted and visualised with any PC or laptop. Thus the here described prototype measurement system provides a small form factor (5 × 8.5 × 2.2 cm), is easy to use and of low cost and may also be used for mobile and/or e-health application.

Acknowledgments This work has been funded by Enterprise Ireland EI-CF.2012.2312.

References

1. Haesler, E. (ed.): National Pressure Ulcer Advisory Panel, European Pressure Ulcer Advisory Panel and Pan Pacific Pressure Injury Alliance. Prevention and Treatment of Pressure Ulcers: Quick Reference Guide. Cambridge Media, Perth, Australia (2014)
2. Gefen, A., Gefen, N., Linder-Ganz, E., et al.: In vivo muscle stiffening under bone compression promotes deep pressure sores. ASME J Biomech Eng **127**, 512–524 (2005)
3. Gefen, A.: Pressure-sensing devices for assessment of soft tissue loading under bony prominences: technological concepts and clinical utilization. Wounds **19**(12), 350–362 (2007)
4. Linder-Ganz, E., Shabshinb, N., Itzchakb, J., Gefen, A.: Assessment of mechanical conditions in sub-dermal tissues during sitting: a combined experimental-MRI and finite element approach. J Biomech **40**, 1443–1454 (2007)
5. Method and system to measure tissue compression. EU 12778629, US 14/343953 filings
6. Hermann, S., Kashefi, A., Reilly, R.B, Motthagi, K.: The ballistocardiogram as a contactless registration method for cardiovascular parameters. XXXX. ESAO-Congresses (2013)
7. Hermann, S., Kashefi, A., Reilly, R.B, Motthagi, K.: A new method to evaluate the high variability in ballistocardiographic (BCG) records. XXXIX. ESAO-Congresses (2012)
8. Hermann, S., Power, D., Reilly, R.: Novel method for detection of blood flow in both young and older subjects at rest, as a model for identifying risk of pressure ulcers in vulnerable movement-restricted elderly subjects. Proceedings of the 7th Congress of the European Union Geriatric Medicine Society (2011)
9. Hermann, S., Vredewald, E., Power, D., Reilly, R.B.: The effects of body position on the IJK complex of the ballistocardiogram. Proceedings of the Annual Bioengineering in Ireland Conference (2010)
10. Starr, I., Rawson, A.J., Schroeder, H.A., Joseph, N.R.: Studies on the estimation of cardiac output in man, and of abnormalities in cardiac function, from the heart's recoil and the blood's impact; the ballistocardiogram. Am. J. Physiol. **127**, 1 (1939)
11. Starr, I.: On the later development of heart disease in apparently healthy persons with abnormal ballistocardiograms. Eight to ten years after-histories of 90 persons over 40 years of age. Am. J. Med. Sci. **214**, 23 (1947)

Narrowband Delay Tolerant Protocols for WSN Applications: Characterization and Selection Guide

Claudio S. Malavenda, Francesco Menichelli and Mauro Olivieri

Abstract This article focuses on delay tolerant protocols for Wireless Sensor Network (WSN) applications, considering both established and new protocols. We obtained a comparison of their characteristics by implementing all of them on an original platform for network simulation, and by testing their behavior on a common test-bench. Thereafter, matching the requirements linked to each application with the performances achieved in the test-bench, allowed us to define an application oriented protocol selection guide.

1 Introduction

The subject of this work is the presentation of a comparative analysis between communication protocols for Wireless Sensor Networks (WSNs), allowed by the development of an original simulation framework, and its link with the requirements of typical WSN applications in order to produce a comparative application-oriented selection guide for WSN protocols.

The focus of our work is on delay tolerant network (DTN) protocols. This category of protocols is particularly suited for mobile WSNs where the topology is dynamically constructed and there is the possibility to momentarily lose the connection between nodes.

The paper is organized as follows: Sect. 2 selects a set of protocols that will be the subject of our investigation and introduces the metrics that will be considered for the evaluation of the protocols. Section 3 analyzes and compares the protocols

---

C.S. Malavenda
Selex ES, Rome, Italy
e-mail: csmsan@gmail.com

F. Menichelli (✉) · M. Olivieri
Sapienza University of Rome, Rome, Italy
e-mail: menichelli@diet.uniroma1.it

M. Olivieri
e-mail: olivieri@diet.uniroma1.it

A. De Gloria (ed.), *Applications in Electronics Pervading Industry, Environment and Society*, Lecture Notes in Electrical Engineering 409,
DOI 10.1007/978-3-319-47913-2_14

behavior when the number of nodes is increased and a new evaluation metric is introduced to measure the power consumption of the protocol. Section 4 matches the results with the requirements of the considered applications, offering a new application-oriented selection guide for delay tolerant protocols that suit WSN communications.

2 DTN Protocols Set

In this section we describe a comprehensive set of protocols relevant in DTN applications [2]. We consider both established protocols and novel ones, the latter designed as variations of existing ones [3–6].

The protocols are the following:

- Controlled Flooding (C.F.) [10]: a custom version of the controlled flooding protocol. The message is logically forwarded just once from each relay node. The relay node assumes that the packet is relayed when a maximum number of retransmission is reached or when an ack packet is received before the maximum number of retries is reached.
- Epidemic [11]: a variation of the conventional controlled flooding protocol. When a node is in contact with a new one it starts a "anti-entropy" phase where two nodes exchange a message vector containing information about messages that each node stores. This phase is followed by the message exchange. Each node implements heuristics to determine if it wants to receive an unseen message from its neighbor. This protocol is particularly resource-hungry.
- Spray and Wait [12] (SnW): a node generating a new message has to deliver it to certain number ('*L*') of different neighbors. This is called "Spray Phase". When a relaying node receives the message, it starts the "Wait phase", where each relay node will transmit the packet only if the destination node is found (direct delivery).
- Prophet [13]: this algorithm associates a delivery probability to every node. When a node meets another, their stored "encountering" probabilities are updated and merged with each other data. Packet transmission occurs only if the encountered node has a better probability to meet the destination node than the source one.
- Controlled Flooding with Hop Limitations (Lim.): an improved version of the above-mentioned "Controlled Flooding" algorithm. In addition to its base version, this protocol limits the number of packet copies to fixed number of replies. This protocol uses a sort of Time to Live parameter embedded into each packet, each hop decreases that parameter, when it reaches zero, no receiver node can reply to the packet.
- Controlled Flooding SnW: a custom version of controlled flooding protocol where copies are limited on the network with a SnW-like strategy. (Referred below as C.F. SnW or C.F. Lim. SnW).

All protocols have been tested in the simulator "ONE" [7, 8], a protocol level simulator chosen for the speedup it offers over architectural level simulators [9].

Established protocols, such as “Epidemic”, “SnW” and “Prophet” have been simulated using a set of optimized parameters embedded in the simulator itself. The new protocols introduced in this paper have been optimized with an exploration of their parameters that is presented in the following.

Results are presented using a set of metrics suitable for both the asynchronous “Medium Access Control” (MAC) layer [1] and the delay tolerant “Logical Link Control” (LLC) level.

The adopted evaluation metrics are the following:

- *Delivery Probability*: the ratio between the number of successfully delivered data packets and the number of packets generated by source nodes.
- *Latency*: time delay of the message transmission from the source node to its arrival to the destination node. The *average* measurement is the arithmetic mean value of measured latencies. The *mean* measurement is the value positioned in middle of all ordered vectors of measured latencies.
- *Average Hop Count*: The average number of nodes that a packet need to traverse in order to be delivered.
- *Overhead*: number of redundant packet copies that are disseminated in the network and extra control-packets exchanged for protocol specific purposes calculated as

$$\frac{(msgR - msgD)}{msgD}. \tag{1}$$

Where $msgR$ is the number of messages relayed by the node and $msgD$ is the number of messages delivered.

In Sect. 3 we introduce an additional indirect measurement of protocol complexity, linked to simulation time.

The simulation scenario assumes that a random sender node generates a packet addressed to a random destination-node. All nodes that sniff such packet can act as relay nodes, i.e. capture the packet and retransmit it or just drop it. The strategies that lead to such choice define the Delay Tolerant (DT) protocol itself.

In the simulation scenario, mobile nodes interact with each other with variable length messages composed by few bytes. The simulation field and node dynamicity involve fast topology changes. Table 1 shows the parameters adopted in the simulations.

Table 1 Scenario common parameters

Scenario parameter	Value
Simulation period	6 h
Payload	30–60 Bytes
Transmission velocity	100 kbps
Transmission range	300 m
Mobility model	Random waypoint
Mobility pause	From 0 to 120 s
Mobility velocity	From 0 to 2 m/s
Message buffer dimension	2 MB

2.1 Controlled Flooding—Protocol Calibration

For calibration of Controlled Flooding protocol, we used a scenario with 1 km × 500 m size, populated with four mobile nodes. Two protocol parameters are explored:

- the maximum number of transmission retries before declaring a transmission failed (*Tnum*)
- the minimum wait time for™ packet re-transmission (*Trep*).

Protocol performances are analyzed for two different cases, flat traffic (nodes are characterized by small data size periodic transmission) and burst traffic (nodes are characterized by a burst of high data rate transmission).

(1) *Flat Traffic Test*

In this scenario each node randomly generates a message every 300–330 s. The source and destination of each message are chosen with a pseudo-random scheme. With an exploration analysis of the main protocol parameters, performed running one simulation for each parameters pair, we achieves the results in Figs. 1 and 2. Latency values presented in Fig. 1 seem to be not affected by *Tnum*, but only by *Trep*. We see that we achieved latency values below 1 s for *Trep* in the [0.1; 1] discrete interval. Figure 2 shows the dependency of delivery ratio to *Tnum* and *Trep*. We see that for the [0.1; 1] range of *Trep* values, delivery probability has a quite flat response for *Tnum* values greater than 3.

This test evaluates protocol metrics when a burst of transmissions is initiated during the first minute of simulation, with a new message every second (the minimum

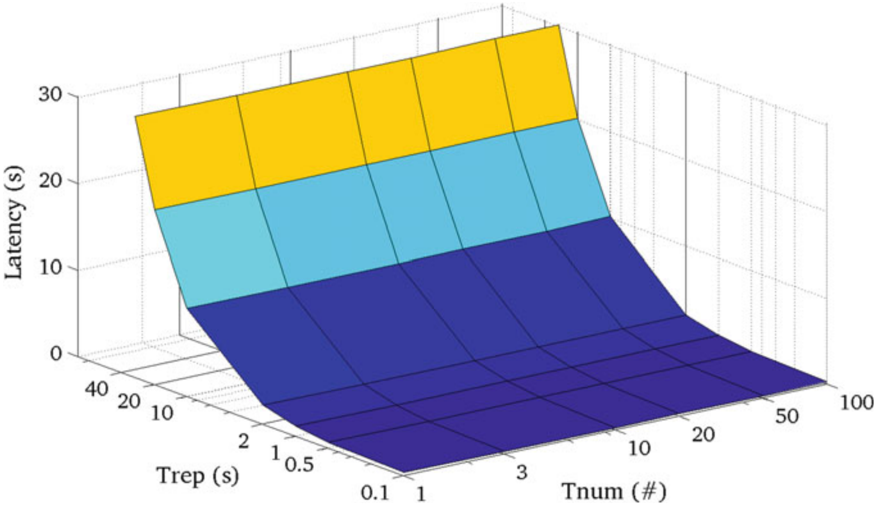

Fig. 1 Pre-operational test—latency

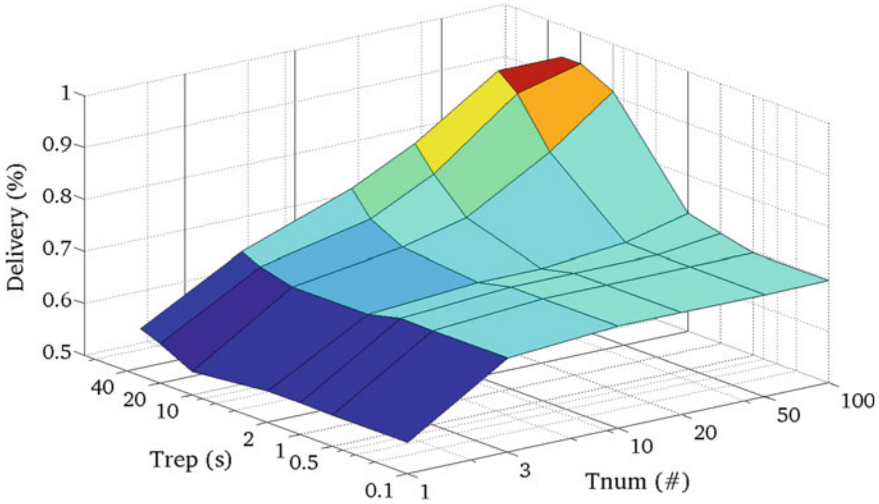

Fig. 2 Pre-operational test—delivery probability transmission peak test

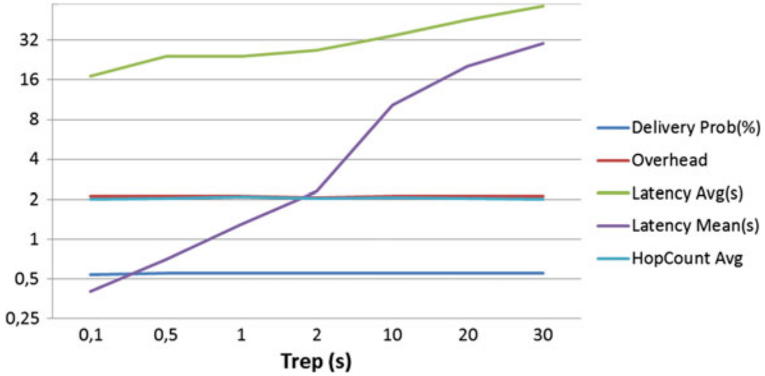

Fig. 3 Evaluation metrics versus Trep

value allowed by the simulator). Figure 3 traces metrics evolution with *Trep*, considering a *Tnum* value of 3.

We see that all metrics report performance degradation for increasing *Trep* values, so we selected *Trep* = 0.1 s for this protocol.

In order to set the value of *Tnum* for the two scenarios considered, we report the simulation results in Fig. 4, obtained for increasing *Tnum* values. Considering the huge increase of the latency and also the increase of energy needed for re-transmissions, we decide to set *Tnum* to 3, even if it is characterized by lower delivery probability.

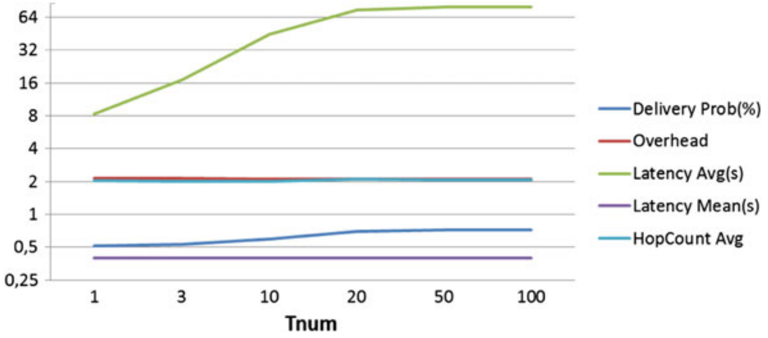

Fig. 4 Evaluation metrics versus Tnum

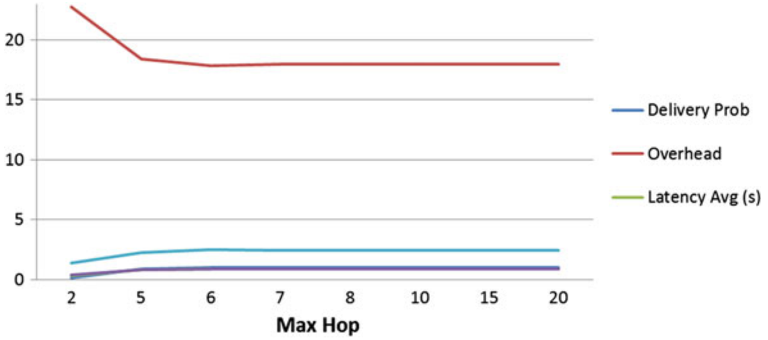

Fig. 5 Evaluation metrics versus Max Hop

2.2 *C.F. With Hop Limitation—Protocol Calibration*

The scenario parameters are presented in Table 1. The traffic simulated is the same as in Sect. 2.1.

This protocol also introduces a new parameter, referenced as *Max Hop* number. It is the maximum number of Hops that a packet can perform before being discarded. In Fig. 5 it is possible to see how our metrics are dependent to this parameter, while *Tnum* and *Trep* have been assigned the values *Tnum* = 3 and *Trep* = 0.1.

We can see that, starting from *Max Hop* = 5, all metrics have stable values. In order to verify that the protocol have the same behavior regarding the variation of *Trep* and *Tnum* parameters, we report the metric measurement obtained varying them while keeping *Max Hop* = 5. In Fig. 6 we report *Trep* dependency considering *Tnum* = 3. It is possible to see that all metrics, except Latency, have constant values starting from Trep = 0.1 s.

Figure 7 reports simulation results setting *Tnum* = 0.1 and *Max Hop* = 5. Metrics are all stable from *Tnum* = 3.

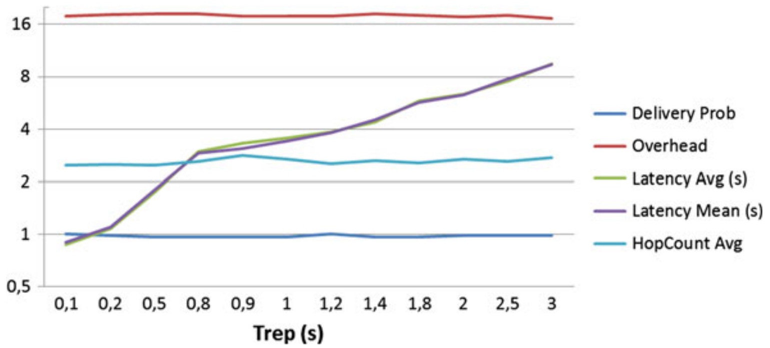

Fig. 6 Evaluation metrics versus Trep

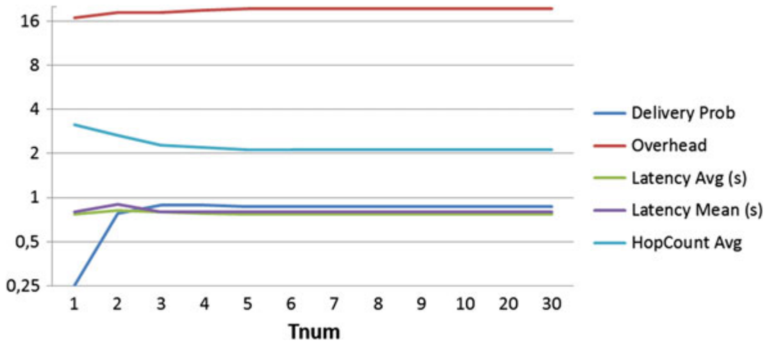

Fig. 7 Evaluation metrics versus Tnum

2.3 C.F. SnW—Protocol Calibration

Here we present the results of the optimization process applied to the controlled flooding protocol with copy limiting algorithm imported by the spray-and-wait algorithm. The objective is to quantify the benefits of the SnW protocol in terms of delivery rate and low overhead [14].

The scenario parameters are summarized in Table 1 and the traffic is the same of the test described in Sect. 2.1.

The first set of simulations aim at calibrating protocol parameters *Trep* and *Tnum* and are presented in Fig. 8. Latency has a quite stable value between 300 and 400 ms. The Hop count is stable around 1.7. Delivery probability and Overhead assume constant values of 1 (i.e. 100 % delivery probability rate) and 18, respectively.

Since varying *Tnum* did not affect any of metrics, we do not show the corresponding results.

According to the above results, we chose *Tnum* = 1 (as low as possible to minimize transmissions [15]) and *Trep* = 0.2. These values have been used in the

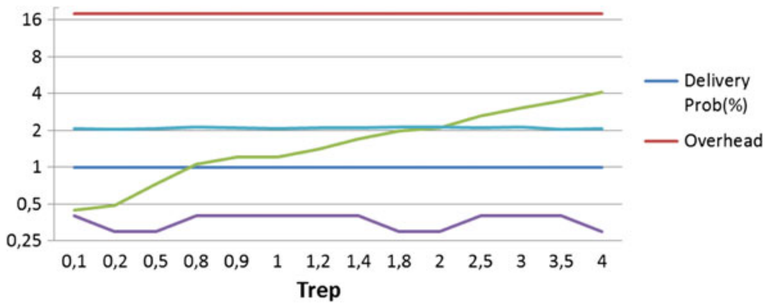

Fig. 8 Evaluation metrics versus Trep

simulations to explore the behavior of the "number of copies" parameter (*CPY*), that introduces a limitation of the copies in the network. Increasing *CPY*, we see that the average latency and other metrics have no significant improvements, so we set this value to 3.

3 Protocol Performance Comparison Versus Number of Nodes

In this section, we explore protocols performances considering growing nodes number (selected among 4, 10, 20, 50, 100, 200) inside the scenario described in Table 1. In particular, for our protocols we use the optimal values found in the previous section. The results are summarized in the following.

Figure 9 shows the delivery probability results. All protocols follow the same behavior of the "C.F. SnW" protocol, except for the two controlled flooding versions that have lower delivery probability for scenarios with lower number of nodes (4–20). The tendency of the "C.F. Limited" is peculiar, as when the number of nodes increases its delivery probability decreases. This can be explained since the protocol allows a limited number of repliers, then when the number of node

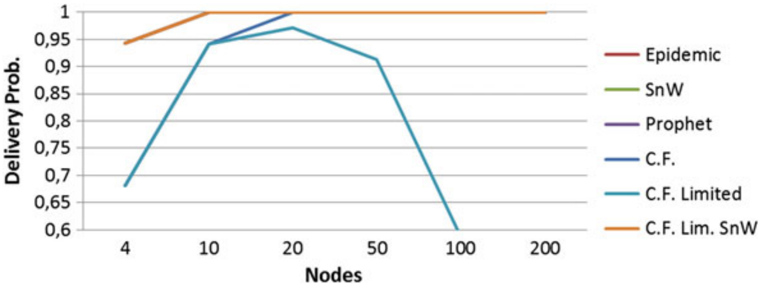

Fig. 9 Delivery Probability versus number of nodes

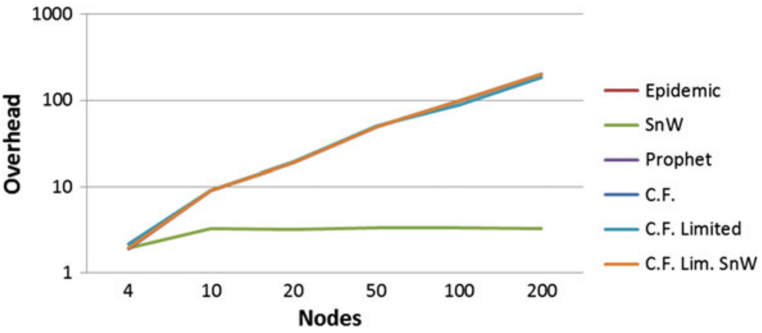

Fig. 10 Overhead versus number of nodes

increases the probability to find the destination node inside a maximum "hopping-range" decreases.

Figure 10 shows the overhead metric. We can see that all protocols follow the same tendency while increasing the number of nodes, except for the SnW, that limits its overhead to an upper bound. In the following, we see that this behavior is accompanied by higher latency values.

Figure 11 shows average Latency. The SnW protocol obtains the highest values among all. All "C.F." protocols and "Epidemic" have an upper bound when the number of nodes increases. Regarding the average latency, for scenarios with more than 50 nodes, a remarkable performance is achieved by Prophet, with same latency value achieved by "C.F. SnW".

Figure 12 shows the Hop Count metric. All protocols stay in a range from 1, 5 to 2 except for "C.F" that has a linear growing tendency with the number of nodes. The "C.F." with limited number of copies seems to grow linearly up to a certain value, the hop count metric is saturated by the protocol behavior that limits the number of replies.

Finally, we tried to measure the relative protocol complexity by using the simulation time as an indirect index. In fact, in the same scenario, the simulation time of one protocol can be attributed directly to the number of operations that each

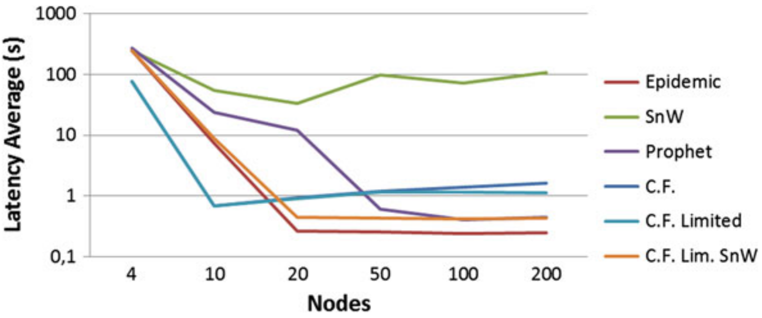

Fig. 11 Latency versus number of nodes

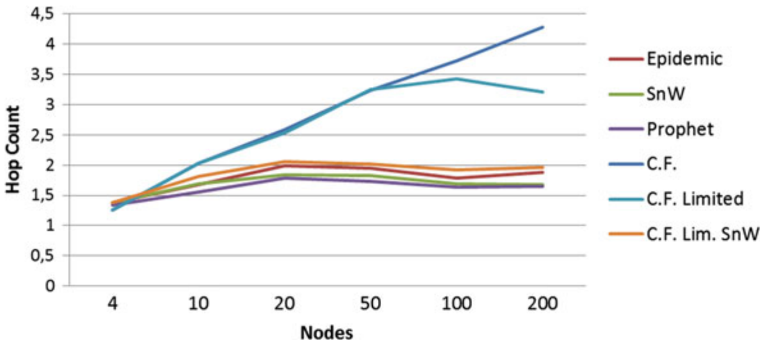

Fig. 12 Hop Count versus number of nodes

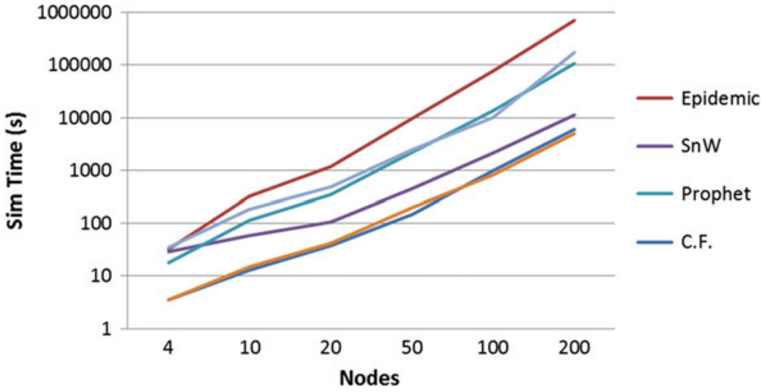

Fig. 13 Simulation Time versus number of nodes

node performs. Figure 13 shows the simulation time for each protocol for increasing number of nodes. We can see that all protocols have a linear dependency with the number of nodes. As it is possible to see, the worst performance is achieved by Epidemic. The smartest ones are the “C.F.” and “C.F. Lim.” that achieve lowest simulation time. “SnW” achieves simulation time about twice greater than these ones.

4 Matching Applications with Protocols

After having characterized the protocols in Sect. 3, we finally propose a selection criteria for applications considered in Sect. 2. We note that applications have specific constraints that lead to particular requirements, but here we take into account common driver factors for each application domain, regarding coverage area, number of nodes and maximum latency. These drivers will be given a qualitative index (Low, Medium, High) and linked to one of the metrics for DTN protocol exposed in Sect. 2. Such index is listed in Table 2.

Table 2 Recommended protocol for each application cluster

	Driver	Metric constraints	Protocol
Smart cities	• Large area coverage • Large number of nodes • Medium/high response time • Medium node computational power • Medium mobility	A. Medium/high delivery probability B. Medium/low latency C. Low average hop count D. Medium protocol complexity	Prophet
Smart building	• Small/medium area • Medium Number of nodes • Low response time • Medium battery life • Low node computational power • Low node mobility	A. High delivery probability B. Low average hop C. Low overhead D. Low protocol complexity	Spray and Wait
Tele medicine	• Small area • Small of nodes • High response time • Low/high battery life • Medium computational power • Low node mobility	A. High delivery probability B. Low average hop C. Low latency	C.F. SnW
Smart vehicle	• Small/medium area • Small/medium Number of nodes • High response time • Low battery life (rechargeable) • Medium/high node computational power • High node mobility	A. High delivery probability B. Low average hop C. Low/medium latency D. Low/medium protocol complexity	C.F. SnW
Intrusion detection/reconnaissance	• Medium/large area • Large number of nodes • Low/medium response time • Large battery life • Low/medium node computational • Low node mobility	A. High delivery probability B. Medium latency C. Low protocol complexity	C.F.
Industrial/commercial	• Medium/large area • Medium/large number of nodes • High response time • High battery life • Low node computational power • Low/high node mobility	A. High delivery probability B. Low average hop C. Low latency	Epidemic

5 Conclusions

In this article we have classified WSN applications according to their scope and their application domain. A set of DTN protocols, some from literature, some proposed by authors, have been analyzed and compared. Focusing on the drivers that lead a particular application domain, we have given an example of how to use simulation results in order to select a protocol, given the application domain. The proposed method have been practically used for a defense WSN called Masterzone [16].

Acknowledgments The authors are grateful to Dr. Alfonso Farina from Selex E.S. for his valuable directions.

References

1. Kim, J. et al.: Performance evaluation of synchronous and asynchronous MAC protocols for wireless sensor networks. In: Proceedings of the 2008 Second International Conference on Sensor Technologies and Applications. IEEE Computer Society, 2008, pp. 500–506. 23 August 2008
2. Delay tolerant networking research group. http://www.dtnrg.org. Last access 22 July 2014
3. Miller, F.P., Vandome, A.F., McBrewster, J.: Delay-tolerant Networking. Alpha Press (2010)
4. Malavenda, C.S., Menichelli, F., Olivieri, M.: Delay tolerant, low power protocols for large security-critical wireless sensor networks. J. Comput. Netw. Commun. (2012)
5. Malavenda, C.S., Menichelli, F., Olivieri, M.: A regulation-based security evaluation method for data link in wireless sensor network. J. Comput. Netw. Commun. (2014)
6. Malavenda, C.S., Menichelli, F., Olivieri, M.: Wireless and Ad Hoc sensor networks: an industrial example using delay tolerant, low power protocols for security-critical applications. In: Lecture Notes in Electrical Engineering, vol. 289, pp. 153–162 (2014)
7. “ONE” simulator web page http://www.netlab.tkk.fi/tutkimus/dtn/theone/. Last access 22 July 2014
8. Keränen, A., Ott, J., Kärkkäinen, T.: The ONE simulator for DTN protocol evaluation. In: Proceedings of the 2nd International Conference on Simulation Tools and Techniques. ICST (Institute for Computer Sciences, Social-Informatics and Telecommunications Engineering), p. 55 (2009)
9. Menichelli, F., Olivieri, M.: TikTak: a scalable simulator of wireless sensor networks including hardware/software interaction. Wirel. Sens. Netw. J. **2**(111), 815–822 (2010)
10. Harras, K.A., Almeroth, K.C., Belding-Royer, E.M.: Delay tolerant mobile networks (dtmns): Controlled flooding in sparse mobile networks. In: Networking 2005. Networking Technologies, Services, and Protocols; Performance of Computer and Communication Networks; Mobile and Wireless Communications Systems, pp. 1180–1192. Springer, Berlin Heidelberg (2005)
11. Vahdat, A., Becker, D.: Epidemic routing for partially connected ad hoc networks. Technical Report CS-200006, Duke University (2000)
12. Spyropoulos, T., Psounis, K., Raghavendra, C.S.: Spray and wait: an efficient routing scheme for intermittently connected mobile networks. In: Proceedings of ACM SIGCOMM Workshop on Delay Tolerant Networking, WDTN ‘05 (2005)
13. Lindgren, A., Doria, A., Davies, E., Grasic, S.: Probabilistic routing protocol for intermittently connected networks. ISSN: 2070-1721 (2012)

14. Bijal, P., Krupa, D., Vyomal, P.: Spray and wait routing protocol in delay tolerant networks. Int. J. Emerg. Technol. Adv. Eng. **4**(5). ISSN 2250-2459 (2014)
15. Yun, Y., Xia, Y.: Maximizing the lifetimeof wireless sensor networks with mobile sink in delaytolerantapplications, Mobile Computing, IEEE Transactions, **9**(9), p. 1308–1318, 19 July 2010.
16. www.selex-si-uk.com/pdf/Masterzone.pdf. Last access 3 Jan 2014

New X-Ray Radiation Sensor for Dosimetry Imaging

Calogero Pace, Evgeny Pikhay, Anna Santaniello, Yael Nemirovsky and Yakov Roizin

Abstract In this work we study the response of floating gate (FG) ionizing radiation sensors to X-ray radiation with different quanta energies and different doses. Single cell sensors and array-type sensors were irradiated with X-rays of different wavelength. The calibration of the absorbed by the FG sensors dose was performed using LiFo electron paramagnetic resonance dosimeters.

1 Introduction

Sensing of ionizing radiation is required in medical, military, space/avionic and nuclear safety applications, the latter attracting increased attention following recent nuclear power station incidents. FG sensors based on the discharge of the MOS structure allow building compact and low-cost dosimeters, implemented in CMOS VLSI technology, for the use in various applications. In this work we study the response of TowerJazz C-Flash based FG sensor [1, 2] to X-ray radiation of different energy, in the range from 40 to 130 kVp, typical for medical imaging applications. The distinguishing feature of FG dosimeters is their small size and operation in the integration mode. This suggests specific demands to the precise dosimeters of other types that are used for their calibration. In particular, such dosimeters must be also small in size (to allow placing them in close proximity to the FG sensors) and operate in integration mode being not subject to noises, typical

---

C. Pace
DIMES, University of Calabria, Rende (CS), Italy

E. Pikhay · Y. Nemirovsky
Technion, Israel Institute of Technology, Haifa, Israel

A. Santaniello
Department of Physics, University of Calabria, Rende (CS), Italy

E. Pikhay (✉) · Y. Roizin
TowerJazz, Migdal Haemek, Israel
e-mail: evgenypi@towersemi.com

A. De Gloria (ed.), *Applications in Electronics Pervading Industry, Environment and Society*, Lecture Notes in Electrical Engineering 409,
DOI 10.1007/978-3-319-47913-2_15

in systems where the signal from the radiation sensor is integrated by electronic means. This was the reason why in this work LiFo electron paramagnetic resonance (EPR) dosimeters were used to calibrate the absorbed dose of FG sensors.

2 Method and Experiment Description

2.1 LiFo Electron Paramagnetic Resonance Dosimeters

Electron paramagnetic resonance (EPR) Dosimetry is based on the quantitative detection of the stable radicals induced in sensitive materials by a radiation beam. This is performed by measuring the intensity of the spectral lines associated with these radicals. The free-radical spectral intensity is proportional to the dose absorbed by the radiation sensitive material.

Dose values as low as a fraction of a Gy can be detected by using dosimetric materials like formates (methanoates) [3]. As compared to conventional alanine dosimetry, these salts of the formic acid offer a lower detection limit owing to the absence of native radicals, and a higher sensitivity since the spectral intensity is mostly originated from one prevalent radical ($CO_2{}^{*-}$). In particular, Li formate (LiFo) dosimetry has to do with a single symmetric line (unresolved g-tensor anisotropy). The radical line (halfwidth 15 G) is widened by the magnetic coupling to the nuclear spin of the neighboring atoms (unresolved hyperfine splitting). The LiFo lineshape is ideally suited for the accurate determination of the dose of radiation, provided the signal is stable.

The uncertainty of the dose determination with LiFo EPR dosimetry is of the order of 2.5 % for doses of the order of a few Gy [4]. The ambient conditions before and after the irradiation, namely, humidity and temperature fluctuations during storage of the dosimetric material, are known to reduce the EPR signal (fading), which might affect, in turn, the accuracy of the dose determination [5, 6]. Repeated readings performed over one month from irradiation of LiFo monohydrate pellets kept under controlled conditions ($T < 40$ °C and relative humidity $Hr = 33$ %) demonstrated that the signal is stable within a few % [7, 8]. On the other hand, high values of the ambient relative humidity (above 70 %) were reported to induce an important fading in LiFo powders [9]. A certain variability of the EPR reading also has an instrumental origin (because of circuit instabilities and thermal drifts of the EPR spectrometer). The scattering of the dose readings with our apparatus is presently within 7 % [10], for pellets obtained from the same batch of LiFo, kept in the dark at the ambient conditions of the EPR laboratory, and measured in the same session within one month from the irradiation with megavoltage X-rays from a medical accelerator (Elekta Sli-Plus), in reference conditions in a geometrical water equivalent slab phantom (IAEA TRS 398 protocol), dose interval 0.5–10 Gy as measured by ionimetry (Farmer-type ionization chamber Scdx-Wellhöfer FC65-P). Two groups of ten pellets each, irradiated with an identical dose (10 Gy) and kept for one year in the laboratory showed a similar scattering (within 10 %).

Li-formate monohydrate pellets were obtained by pressing the commercial powder (Sigma-Aldrich) without addition of binding material. The typical pellet dimensions were of the order of 1 cm (diameter) by 2 mm (thickness), though smaller pellets (linear dimensions of the order of a few mm) guarantee masses adequate to the EPR measurement. The reduced size of the dosimeters and the ease of handling (absence of cables and housings) make pellet EPR dosimetry well-suited to the determination of the dose as obtained from orthovoltage beams of X-ray irradiators. During irradiation, the specimen is locked in the exposure chamber of the irradiator, which is fully screened for radioprotection purposes. Pellets can easily be located side by side to the specimen (see Fig. 1) in order to monitor the dose absorbed during the exposure.

The Faxitron RX-650 irradiator unit used in the present study provides photon beams with a peak energy in the interval 10–130 keV. The beam is characterized by a wide angular aperture (divergence 40°), a rather flat radial profile near the beam axis, and an azimuthal angle dependence (heel effect) which is averaged by rotation of the sample holder (rotation speed 1.7 rpm). No additional filters besides inherent filtration (1.6 mm Be) are present. The specimens can be located at source-sample distances approximately ranging from 30 to 60 cm (beam diameter accordingly varying from 22 to 44 cm), which correspond to dose rates between 8 and 1.5 Gy/min in the axial position at 100 keV peak energy. The distance can be further increased to 70 cm (floor position, no sample rotation). At a given source-sample distance, the dose rate increases by a factor of ~4 with a beam peak energy increasing from 40 to 130 keV.

Dose calibration of the RX-650 irradiator by EPR dosimetry indicated a dose rate of 2.20 Gy/min at the intermediate distance of 50 cm, axial position, 100 keV. The dose calibration was performed by comparing the EPR signal of LiFo pellets irradiated during chosen time intervals to the signal obtained from a set of pellets irradiated at known doses with megavoltage beams in reference conditions, as determined by ionimetry (dose interval 1–32 Gy). We chose a source-sample

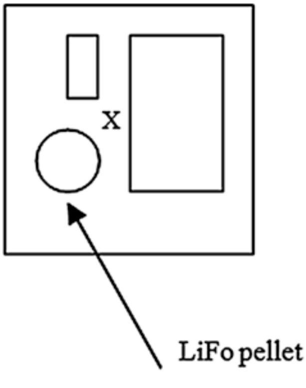

Fig. 1 LiFo pellets located side by side to the electronic devices in order to measure by EPR the dose absorbed during the exposure to orthovoltage beams

Table 1 Irradiation energies (tube voltage), exposure times and the corresponding absorbed doses as measured by EPR dosimetry

Device number	Tube voltage (kV)	Exposure time (sec)	Calibrated dose (Gy)
1	100	63	1.9
2	100	126	2.5
7	100	189	2.8
3	100	316	4.5
4	100	632	11
5	100	1264	24
6	100	3158	60
8	40	2118	12
9	70	878	10
10	130	537	11

distance of 60 cm in the present study. This allows the most uniform irradiation of the electronic device and the nearby LiFo pellet, with an estimated dose rate of about 1 Gy/min in the peak energy interval of the beam. The value was derived from comparison of our dose calibration at 50 cm with the exposure rate datasheets of the irradiator. The chosen dose rate is convenient for absorbed dose values above 1 Gy at a peak energy of 100 or 130 keV, and of the order of 1 Gy at the lower peak energies (40 and 70 keV), where it corresponds to exposure times above a hundred of seconds (see Table 1). We exposed seven samples at 100 keV peak energy for time intervals which gave estimated dose values ranging from 1 to 50 Gy. Besides this, three further samples were exposed at 40, 70 and 130 keV peak energy, for time intervals corresponding to comparable, estimated doses of the order of 10 Gy.

2.2 *Floating Gate Semiconductor Radiation Sensors*

The sensor of ionizing radiation, developed in TowerJazz, is based on the discharge of a single-poly non-volatile memory cell (C-Flash [11]), modified to enhance its sensitivity to the radiation. The single cell sensors can be arranged in arrays allowing X-ray imaging.

Single cell consists of Polysilicon floating gate, which is capacitively coupled to a CMOS inverter for readout, tunneling capacitor for charge injection and control capacitor to facilitate the control over the floating gate potential, as schematically shown in Fig. 2. The capacitance of control gate to the floating gate is significantly higher (about 20 times) than the sum of the tunneling and inverter capacitances to the floating gate. The inverter and tunneling capacitor employ 110 Å Gate Oxide (in this experiment), and control capacitance is implemented on Shallow Trench Isolation (STI, 3500 Å). Sensors with different periphery length of the control capacitor (Fig. 3) were studied in this work.

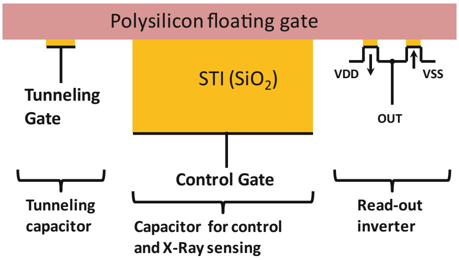

Fig. 2 Schematic diagram of C-sensor

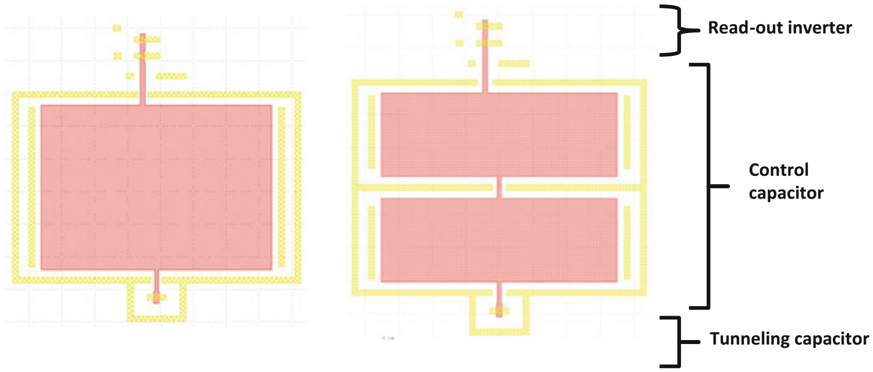

Fig. 3 Layout of different C-sensor flavors (poly and active regions shown): small periphery (*left* embodiment); large periphery (*right* embodiment)

The sensor read-out is performed by measuring Vin-Vout curve of the CMOS inverter (Fig. 4). The control gate is the input terminal of the inverter, while the tunneling gate is grounded.

Fowler-Nordheim tunneling mechanism is utilized for pre-charging of the sensor: high positive voltage is applied to the control capacitor, while the negative voltage is applied to the tunneling capacitor, and the inverter terminals are

Fig. 4 Read-out curves of C-sensor

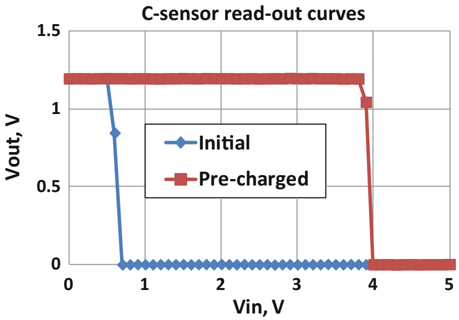

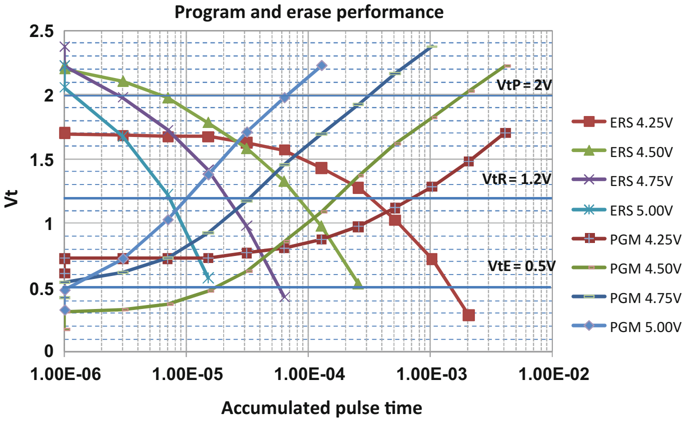

Fig. 5 Typical pre-charge curves of C-sensor; *PRG* corresponds to electron injection into floating gate, *ERS*—to holes injection

grounded. Due to the much higher value of the control gate capacitance compared with the rest of the sensor components, the main part of the applied voltage drops across the gate oxide of the tunneling capacitor. This results in F-N injection of electrons into the floating gate. The injection of electrons into the floating gate leads to the shift of the inverter midpoint voltage (defined as the cell Vt) towards higher values (Fig. 5).

When the sensor is exposed to the ionizing radiation, the high energy electrons are produced in the sensor volume. These electrons can transfer energy to the electrons stored in the floating gate, allowing them to overcome the potential barrier of the silicon oxide surrounding the floating gate. When the electrons leave the floating gate, the Vt of sensor decreases. The absorbed dose can be calculated from the Vt change and calibrated using an external dosimeter.

3 Experimental Data

3.1 LiFo Dosimeters Exposure

Figure 6 shows the EPR intensity of the LiFo pellets, placed next to the FG sensors during irradiation, as a function of the irradiation time. The corresponding absorbed dose values are listed in Table 1. We notice the scattering of the dose at the different beam energies (12, 10, 11 and 11 Gy, at a tube voltage of 40, 70, 100 and 130 kVp, respectively), as expected, because the chosen exposure times derive from dose estimations. Besides this, the measured intensities/dose values do not depend linearly on time for low irradiation times. Systematic and random uncertainties, resulting from the manual setting of the operating voltage, affect the dose delivery

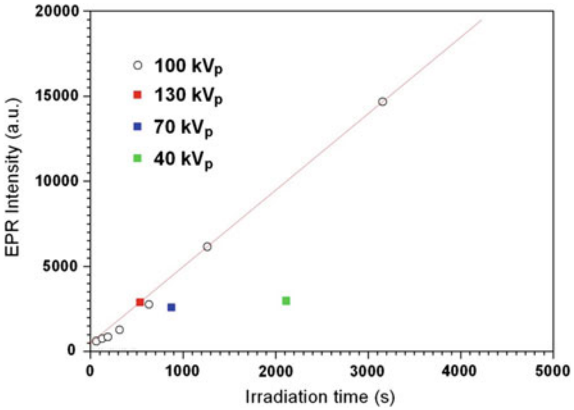

Fig. 6 EPR intensity as a function of the irradiation time (see calibrated dose values in Table 1). The line visually represents a constant slope of approximately 1.14 Gy/min

by the irradiator. The variations are not negligible for the shortest exposures, when the time needed to manually achieve the operating voltage (ranging from a few seconds to a few tens of seconds, depending on the voltage) becomes a significant fraction of the irradiation time. Besides this, residual azimuthal angle dependence may show up, especially at the lowest doses, where the sample holder rotational period (about 30 s) is comparable to the exposure time. These operational and instrumental features explain the apparent deviation from linearity versus time at the low dose values of Fig. 6. They put forward the need of additional filters for future studies at lower doses. The filters will allow longer exposure times by reducing the beam intensity, thus decreasing the relative importance of the fluctuations induced by manual start-up and shut-down operations.

3.2 *Semiconductor Sensor Exposure—Single Cells and Matrices*

The described above FG sensors were exposed to X-Rays of different energies and doses.

The sensor shows linear response to the dose at the beginning of the discharge. Vt stabilizes at the level close to the initial Vt when the charge flows from and to the FG become equal (Fig. 7). The precise level of Vt stabilization depends on the floating gate 3D surface area—for higher area (top and bottom Poly surfaces and its periphery—right embodiment of Fig. 3), Vt drops to a lower level. No significant influence of the discharge on X-ray photon energy was observed in the range of 40–130 kVp for the same doses (Fig. 8). Comparing the response of EPR dosimeters to

Fig. 7 Response of C-sensor to X-rays of different dose

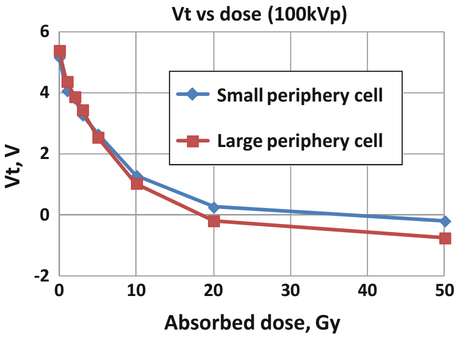

Fig. 8 Response of C-sensor to X-rays of different energy

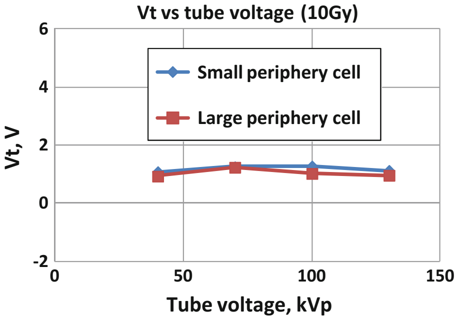

C-sensor, we observe similar response trend w.r.t. to dose (in linear region of C-sensor) and energy.

The matrices of 64 by 64 sensors were exposed to the X-rays with the doses and energies mentioned above. All the sensors in the matrix are pre-charged to the same level. Measuring Vt distribution after exposure allows to estimate the mean absorbed dose and uniformity of the discharge effect. The distributions remain very tight at different stages of the irradiation, indicating excellent cell-to-cell repeatability (Fig. 9). Highly reproducible results allow to perform X-ray imaging with high spatial resolution at the micro-scale. An example of X-ray imaging is shown in Fig. 10, where a fiber over the sensor matrix lead to a reduced absorbed dose in the array cells.

Compared with other low dose radiation measurement techniques employing semiconductor sensing elements [12], the developed device does not require supply voltage in the detection mode and is much less sensitive to dielectric degradation (in contrast to [12] where degradation of the drain current in a transistor with thick gate oxide is used as a radiation monitor). Due to low degradation, the suggested device allows repeated use and thus much large range of the measured doses, while the achieved sensitivity of 0.5 V/Grey is at the level of the state of the art values [12].

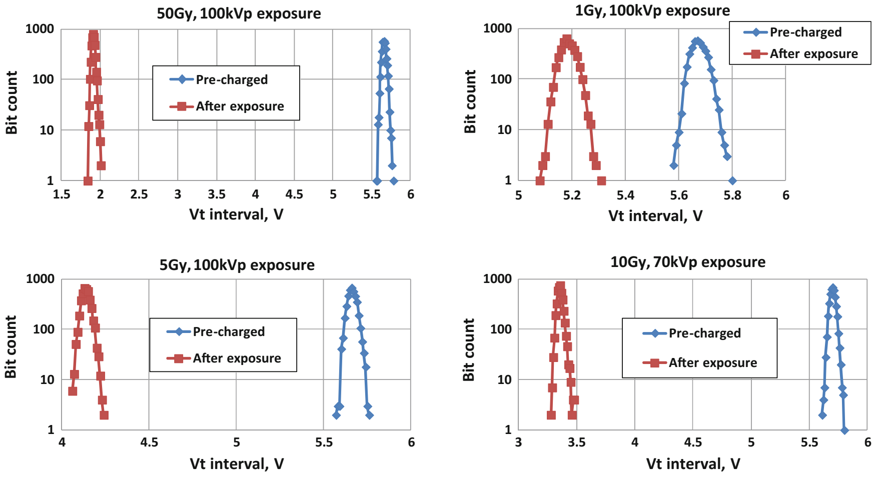

Fig. 9 C-sensor matrices response to X-ray

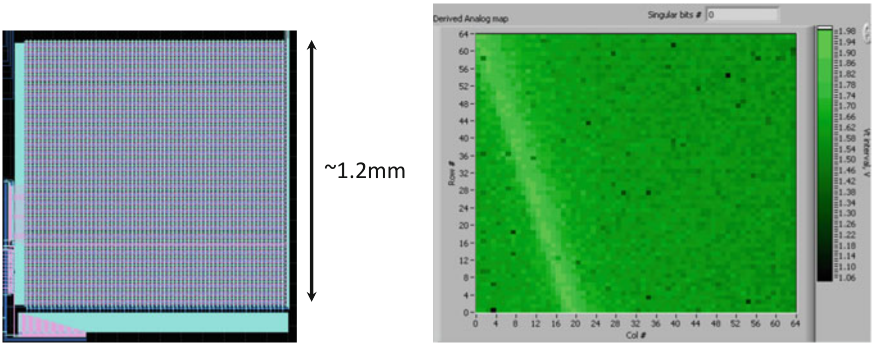

Fig. 10 C-demonstrating direct X-ray imaging: matrix L/O (*left*); Vt map sensor matrices response to X-ray (*right*)

4 Summary

In this work we studied the response of direct semiconductor ionizing radiation sensor to X-ray irradiation in energy range of 40–130kVp and dose range 1–50 Gy. Linear dose response of about 0.5 V/Gy was observed (before the sensor discharge). No remarkable dependence of sensor response on dose was observed. The presented examples of sensors matrix exposure demonstrated high repeatability of C-sensor response and a possibility of X-ray imaging. The calibration of absorbed dose was performed using LiFo electron paramagnetic resonance dosimeters.

References

1. Villani, E.G., Gabrielli, A., Khan, A., Pikhay, E., Roizin, Y., Zhang, Z.: Monolithic 180 nm CMOS dosimeter for in vivo medical applications. IEEE Trans. Nucl. Sci. **60**(2), 843–849 (2013)
2. Pikhay E., Nemirovsky Y., Roizin Y, Villani E.G.: Radiation array sensor based on C-flash floating gate device. SENSO-2014, Gardanne, Aix-En-Provence, France (2014)
3. Vestad, T.A., Malinen, E., Lund, A., Hole, E.O., Sagstuen, E.: EPR dosimetric properties of formates. Appl. Radiat. Isot. **59**, 181–188 (2003)
4. Gustafsson, H., Lund, E., Olsson, S.: Lithium Formate EPR dosimetry for verification of calculated dose distributions prior to intensity modulated radiation therapy. Phys. Med. Biol. **53**, 4667–4682 (2008)
5. Sleptchonok O.F., Nagy V., Desrosiers M.F.: Advancements in accuracy of the alanine dosimetry system. Part 1. The effects of environmental humidity, Rad. Phys. Chem. **57**, 115–133 (2000)
6. Garcia, R.M.D., Desrosiers, M.F., Attwood, J.G., Steklenski, D., Griggs, J., Ainsworth, A., Heiss, A., Mellor, P., Patil, D., Meiner, J.: Characterization of a new alanine film dosimeter: relative humidity and post-irradiation stability. Rad. Phys. Chem. **71**, 373–377 (2004)
7. Adolfsson, E., Karlsson, M., Carlsson, G.A., Tedgren, A.C., Lund, E., Olsson, S., Gustafsson, H.: Investigation of signal fading in lithium formate EPR dosimeters using a new sensitive method. Phys. Med. Biol. **57**, 2209–2217 (2012)
8. Lelie, S., Hole, E.O., Duchateau, M., Schroeyers, W., Schreurs, S., Verellen, D.: The investigation of lithium formate hydrate, sodium dithionate and N-methyl taurine as clinical EPR dosimeters. Radiat. Meas. **59**, 218–224 (2013)
9. Komaguchi, K., Matsubara, Y., Shiotani, M., Gustafsson, H., Lund, E., Lund, A.: An ESR and ENDOR study of irradiated 6 Li-formate. Spectrochim. Acta A **66**, 754–760 (2007)
10. Santaniello A., Løvik I., Sportelli L., Licandro M., Scalzo G., Scalzo C.: Medical EPR dosimetry at low doses. VIII national meeting of the Italian Association of Medical Physics (AIFM), Turin (Italy) (2013)
11. Roizin, Y. Aloni, E. Birman, A. Dayan, V. Fenigstein, A. Nahmad, D. Pikhay, E. Zfira, D.: C-flash: an ultra-low power single poly logic NVM. Proceedings of NVSMW/ICMTD, pp. 90–92 (2008)
12. Sarrabayrouse, G., Siskos, S.: Low dose measurement with thick gate oxide MOSFETs. Radiat. Phys. Chem. **81**, 339–344 (2012)

A Novel Instrumentation for an Advanced High Temperature Reverse Bias (HTRB) Testing on Power Transistors

Calogero Pace, Jorge Hernandez Ambato and Carlo Giordano

Abstract In this paper, a novel instrumentation for High Temperature Reverse Bias (HTRB) reliability test on power transistors is presented. The proposed equipment overcomes the drawbacks of the traditional instrumentation (large thermal capacitance, lack of individual thermal control for each sample, no thermal runaway detection), enabling a new methodological approach. Several electrical measurements during the test are allowed. Multiple benefits derive from this new approach: the identification of early warnings in accordance with configurable thresholds of degradation and thermal runaway quenching. Furthermore, the test can be stopped solely for the out-of-specification devices. The instrumentation design and advanced HTRB test method are presented as well as experimental results obtained on Power MOSFETs.

1 Introduction

Nowadays, discrete power transistors are still used in many every day's life consumer goods, such as laptop power supplies, washing machines, air conditioners, and so on. Before going on the market, power devices are qualified through accelerated reliability tests, in order to prevent their infant mortality [1, 2]. In fact, because of lack of control, contamination and random defects in the manufacturing

---

C. Pace (✉) · J.H. Ambato · C. Giordano
Department of Computer Science, Electronics, Modeling and Systems (DIMES),
University of Calabria (UNICAL), Via P. Bucci 42 C, 87036 Rende (CS), Italy
e-mail: cpace@unical.it

J.H. Ambato
Escuela Superior Politécnica de Chimborazo, Riobamba, Brasil
e-mail:jhernandez@dimes.unical.it; jorge.hernandez@espoch.edu.ec

C. Giordano
Advanced Research Center on Electronic Systems, University of Bologna,
Viale Risorgimento 1, Bologna, Italy
e-mail: cgiordano@dimes.unical.it; carlogiordano85@libero.it

A. De Gloria (ed.), *Applications in Electronics Pervading Industry, Environment and Society*, Lecture Notes in Electrical Engineering 409,
DOI 10.1007/978-3-319-47913-2_16

process, some devices may experience unexpected failures in the first years of their operating life [3, 4].

There are several reliability tests oriented to highlight potential failure mechanisms on Metal Oxide Semiconductor Field Effect Transistors (MOSFETs). Among them, the most widely used test on power MOSFETs is the High Temperature Reverse Bias (HTRB) [5, 6]. According to standard regulations [7–9], this test applies both electrical and thermal stress on Devices Under Test (DUTs). The ambient temperature is set into the range of 150–175 °C; the gate and source terminals are shorted, while the drain-source reverse bias is set nearby to the breakdown voltage (BV_{DSS}) (see Fig. 1). The HTRB test could last between 500 and 1000 h. Electrical parameters of DUTs are measured at room temperature, both before and after the test, in order to identify any parametric variation. Typically, the most susceptible parameter is the drain-source leakage current (I_{DSS}), which may increase even by 2 or 3 orders of magnitude. Sometimes, this degradation could be so severe to initiate a thermal runaway, leading to junction burnout and package explosion. Once a device is so catastrophically damaged, it cannot be easily inspected with a microscope or submitted to a post-failure analysis [10].

In order to clearly understand the degradation trend of the devices and to prevent their over-damaging, several intermediate measurements should be performed during the HTRB test. However, this approach cannot be actuated with the conventional HTRB equipment (basically a big oven), because of quite large thermal capacitances which lead to long-lasting cooling-down operation for the DUTs. Furthermore, only the temperature inside the chamber is controlled instead of the temperature of each sample: then, even if a device approaches thermal runaway, it cannot be cooled.

In this paper we present the prototype of a new instrumentation for the HTRB test. The case temperatures of each DUT are controlled with custom mini-heaters. Thermal runaway is avoided by the automatic regulation of the power heating. Failed devices are automatically detected and isolated from the power supply. Thanks to lower thermal capacitances, several electrical characterization measurements can be performed during the test, enabling a detailed reconstruction of the degradation history for the failed DUTs. Experimental results for 6 power MOSFETs are also reported.

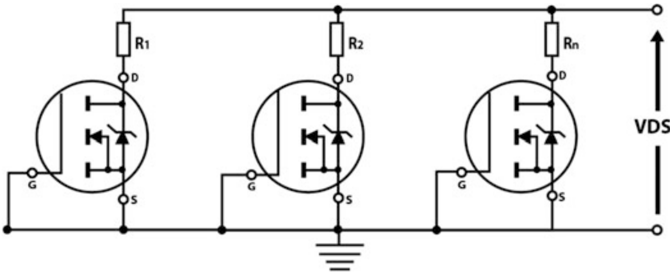

Fig. 1 Biasing condition for HTRB testing on power MOSFETs, as suggested by [8]

2 Innovative Instrumentation Description

The block diagram of the instrument is shown in Fig. 2. The overall system is controlled by a PC, through a Virtual Instrument (VI) developed with National Instrument LabWindows CVI. The electrical connections between the DUTs and the Source Measuring Unit (SMU) (Model 2410-C, Keithley) are realized by a switch matrix. The PC remotely controls the SMU with an IEEE 488 interface. For each DUT, we designed a dedicated Thermal Control Module (TCM). Each TCM communicates with a master module on an I^2C bus. Currently, we have developed a small prototype with 6 DUTs; however this modular architecture allows controlling up to 127 DUTs because of the 7-bits addressing implemented by the I^2C protocol. The master module is controlled by the PC with a RS232 interface.

The TCM is a complex sub-system which provides several functionalities. First of all, a Proportional Integrative Derivative (PID) controller, realized with an 8-bit microcontroller (Atmel AVR Atmega16). The PID controller acquires the case temperature of the DUT [with an integrated 10-bit Analog to Digital Converter (ADC)] and generates 2 Pulse Width Modulated (PWM) signals (respectively for the temperature sensor and the thermal actuator). As shown in Fig. 3, the sensing and the actuating parts of a TCM are embedded into a single device, the Simple Added Feature Field Effect Transistor (SAFeFET). In particular, we used the STZ150NF55T (available into a single P^2PAK package), produced by

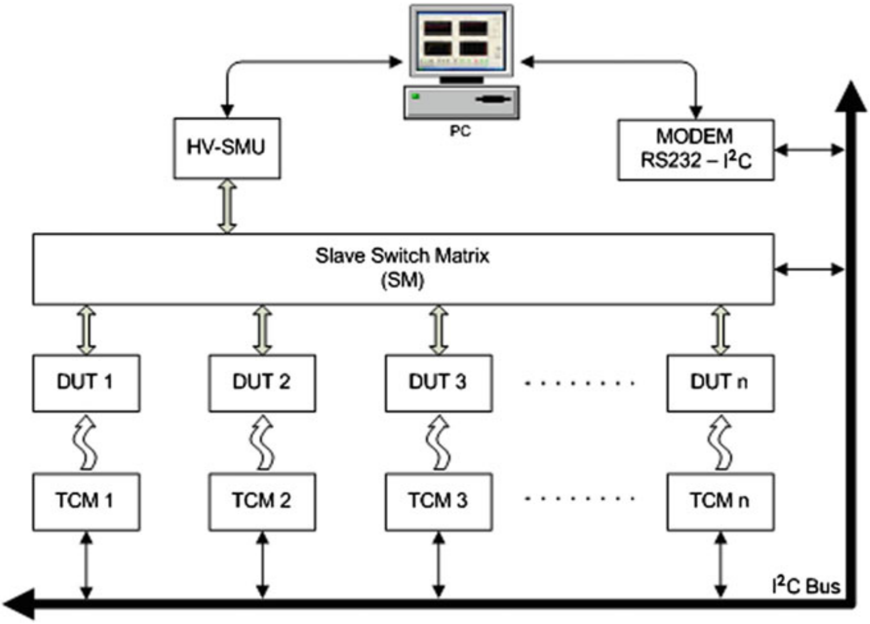

Fig. 2 Block diagram of the proposed system

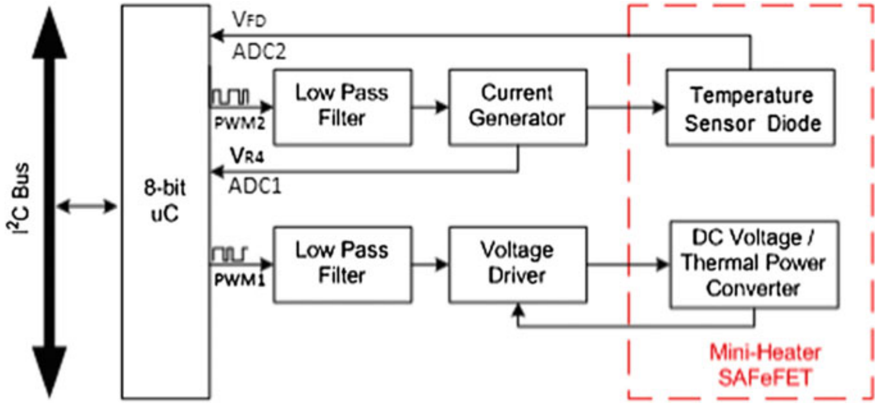

Fig. 3 Block diagram of a TCM

STMicroelectronics [11]. The SAFeFET and the DUT are placed respectively on the bottom and on the top of a metal holder (see Fig. 4).

The thermal resistance between the heater and the DUT case ($R_{thjH\text{-}cD}$) is estimated in ~1.2 °C/W. The DUT case temperature (T_{cD}) can be calculated as:

$$T_{cD} = T_{jH} - R_{thjH-cD} \cdot (P_H - P_{DUT}) \tag{1}$$

where T_{jH} and P_H are respectively the SAFeFET junction temperature and the generated thermal power; P_{DUT} represents the DUT power dissipation. This last term can be usually neglected. However, when the DUT undergoes thermal runaway, the P_{DUT} term is no longer negligible: therefore the TCM reduces the generated thermal power by the heater, in order to maintain the case temperature at the set point value.

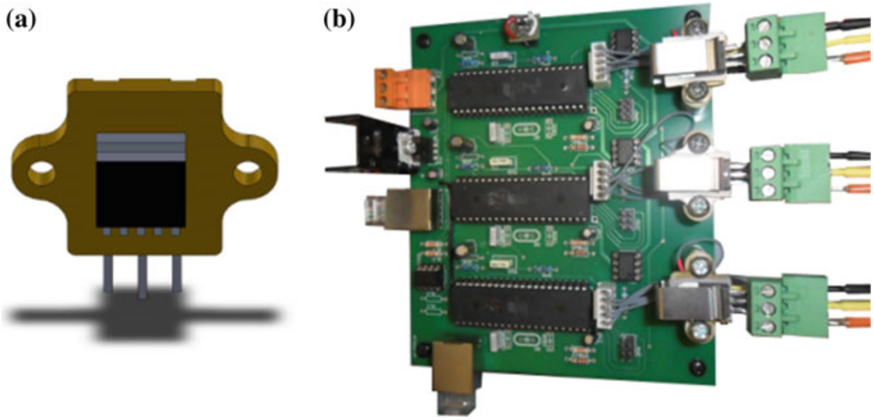

Fig. 4 **a** Detailed 3D view of the mini-heater; **b** A prototype board with 3 TCMs

The proposed equipment assures a maximum temperature error lower than 1 % at 175 °C; furthermore the case temperature of one DUT can be changed from 30 to 175 °C (and vice versa) in about 3 min. More details can also be found in [12, 13].

3 New Proposed Methodology

With the new equipment, an alternative HTRB procedure can be proposed. In particular, we suggest splitting the overall time length of a standard HTRB test into shorter sequences of stress and electrical verification steps. In the stress steps, the DUTs are maintained at high temperatures (e.g. 175 °C) and polarized with a high reverse drain-source voltage. In the electrical verification steps, the DUTs are cooled down and electrically characterized, measuring the following electrical parameters: I_{DSS}, BV_{DSS}, V_{TH}. The duration of this phase should be as short as possible, to minimize any recovery/annealing effect. The bottle-neck is represented by the time required for cooling down all the devices. For this reason we suggest performing the electrical characterization not at the room temperature, but at an intermediate value, in the range of 85–125 °C. Electrical parameters measured in this temperature range are more in agreed with work conditions of power applications.

Besides the scheduled electrical verification steps, some emergency measuring procedures could be performed when:

1. the heating power on a DUT is lower that a configurable threshold P_{Hth};
2. the total current measured by the SMU, i.e. the sum of all I_{DSS} currents, is higher than a configurable threshold $I_{\max}$.

In both cases, the system is able to identify the most degraded DUT and to stop its thermal and electrical stresses, ensuring the test prosecution for the remaining DUTs.

4 Experiment and Results

We characterized 20 Commercial On The Shelf (COTS) power MOSFETs (STMicroelectronics STP18N55M5) in terms of drain-source leakage current and breakdown voltage. Then we selected 6 samples in order to obtain a BV_{DSS} as uniform as possible. In fact, this electrical parameter can have a very large lot-to-lot variance. We measured a mean value of 637 V.

Using COTS transistors, we had to set a stress test voltage (671 V) slightly higher than the BV_{DSS}, in order to observe at least 1 failure. The test lasted 500 h, divided into 41 stress cycles of 12 h and 1 stress cycle of 8 h (see Fig. 5). At the end of each stress cycle, an Electrical Verification Test (EVT) at 125 °C was performed. Finally, a standard Electrical Characterization Test (ECT) at the 30 °C was performed both before and after the test.

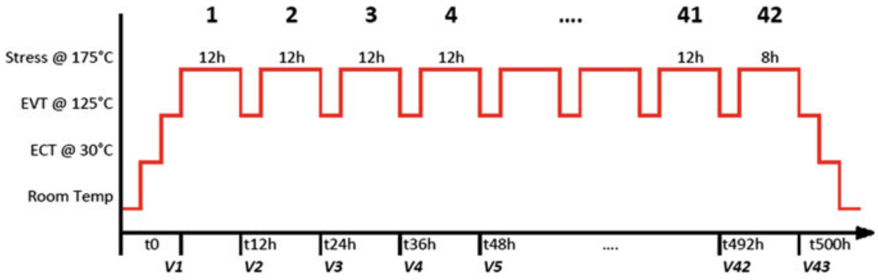

Fig. 5 Proposed time scheduling for a 500 h long HTRB test

Table 1 Stress parameters and failure criteria

Parameter	Value	Observations
Time duration stress	500 h	Time divided in 42 stress cycles
V_{DS} stress	671 V	122 % of nominal BV_{DSS}. (105 % of practical BV_{DSS} at 25 °C)
T for stress	175 °C	Tj max of DUTs is 150 °C
T for ECT	30 °C	ECT performed at t = 0 h and t = 500 h
T for EVT	125 °C	EVT performed at the end of every stress cycle
Min. P_{Hth}	1.5 W	Minimum heater power: failure criterion during stress to detect thermal runaway
Max I_{DSS} @ V_{DS} = 550 V, T = 125 °C	100 µA	I_{DSS} failure criterion during EVT
Min V_{th} @ $V_{DS} = V_{GS}$, I_D = 250 uA, T = 125 °C	1 V	V_{th} failure criterion during EVT

Stress parameters and failure criteria set for the experiment are summarized in Table 1. We observed 2 failures during the test. In particular, both DUT2 and DUT6 failed in accordance with the V_{TH} failure criterion, as in [14]. Anyway, the equipment prevented the DUTs over-damaging, shutting down both the electrical and the thermal stress.

Furthermore, the proposed methodology allowed us to trace the whole temporal evolution of the electrical parameters of interest, i.e. I_{DSS}, BV_{DSS} *and* V_{TH} (see Figs. 6, 7 and 8). In particular, the failed DUTs have a quite different degradation trend, which our equipment allowed us to catch. During the first 12 h, DUT6 leakage current rose suddenly from 1.72 mA until 2.8 mA, but then recovery seemed to start and finally the device failed. On the other hand, DUT2 degradation began to rise slowly until 2.6 mA and, after that, failure also occurred. Furthermore, it is worth noting how the recurrent EVT cycles, preceded by a partial cooling of the DUTs, did not affect neither the degradation trend nor the electrical properties of devices. This aspect can be appreciated, observing the total leakage current trend in a linear plot (see Fig. 9), where the effects of the DUTs cooling down for each EVT is clearly visible (several and limited I_{DSS} drops) as well as the general trend.

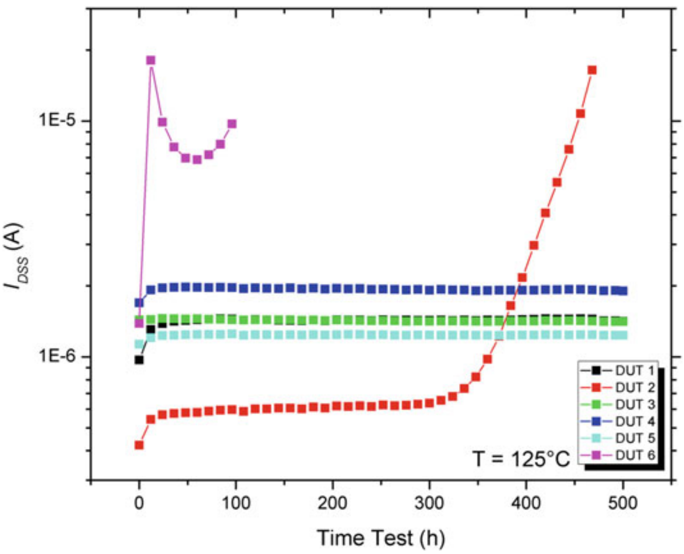

Fig. 6 Drain-source leakage currents at V_{DS} = 500 V, during EVTs (T = 125 °C)

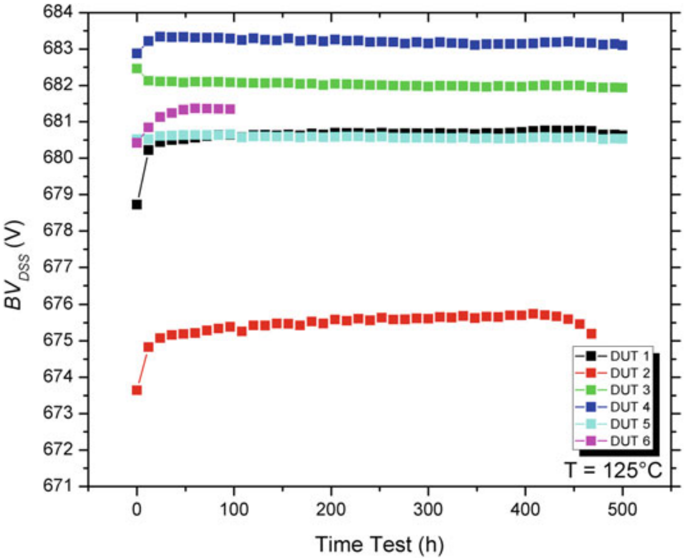

Fig. 7 Breakdown voltages at I_{DS} = 1 mA, during EVTs (T = 125 °C)

Finally two thermal processes were performed on the failed DUTs, in order to verify whether their degradations were irreversible or not. We also took a not failed device during the HTRB test (DUT3), as reference. In the first process, the DUTs

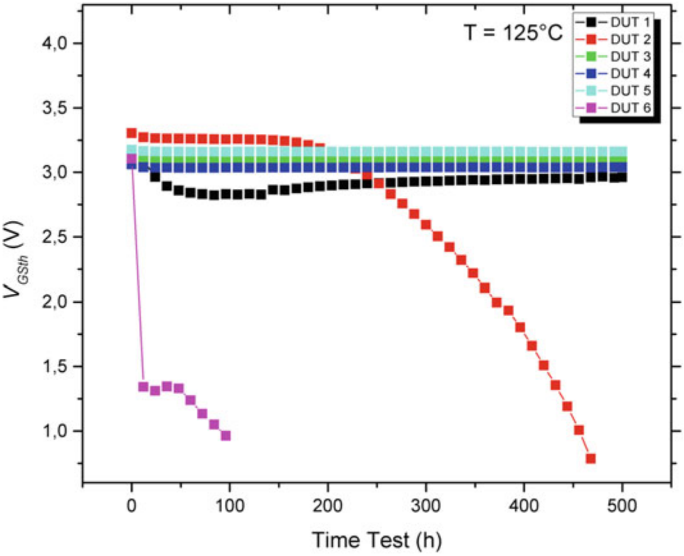

Fig. 8 Gate-source threshold voltages at I_{DS} = 250 uA and $V_{GS} = V_{DS}$, during EVTs (T = 125 °C)

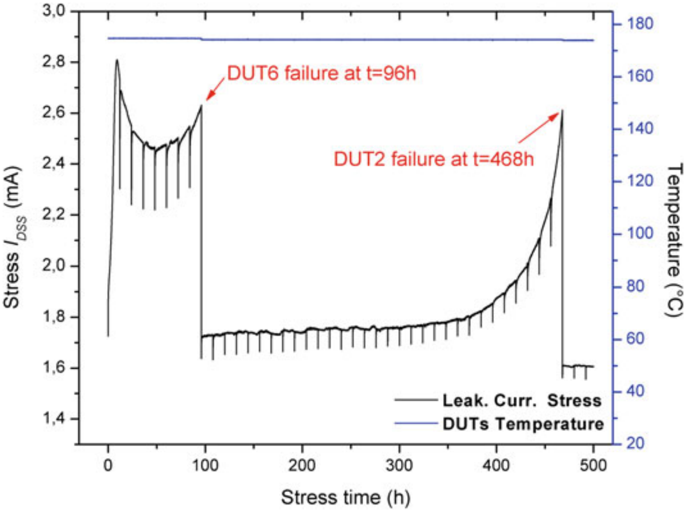

Fig. 9 Total leakage current degradation during HTRB stress test (T = 175 °C)

were maintained at the room temperature for 100 h, without bias. Subsequently, the devices were short-circuited to ground and heated at 175 °C for 24 h. As in the HTRB test, we performed several EVTs over the time. In contrast to the other devices, DUT2 continued its degradation trend, as if it were not fully damaged during the HTRB test (see Fig. 10).

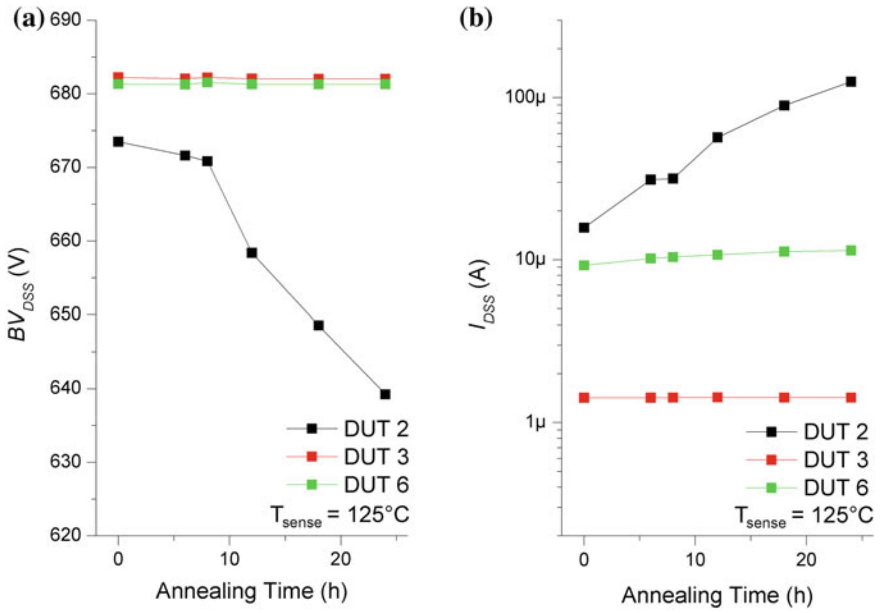

Fig. 10 Electrical characterization performed during the annealing phase (T = 175 °C). **a** Breakdown voltages at I_{DS} = 1 mA. **b** Drain-source leakage currents at V_{DS} = 550 V

5 Conclusions

An innovative and automatic instrumentation for the High Temperature Reverse Bias (HTRB) testing on power transistors was reported in this paper. The individual Device Under Test (DUT) case temperature was controlled by a dedicated Thermal Module Control (TCM). Thermal runaway (and then, catastrophic failures or package explosions) was prevented due the individual regulation of the heating power for each DUT. Furthermore, obtaining lower thermal capacitances with respect to the traditional equipment, we could change the DUT temperatures from 30 to 175 °C (and vice versa) in few minutes. All these features allowed us to propose a new methodology for the HTRB testing, based on the cyclic iteration of a stress and an electrical characterization phase. As a result, we could reconstruct the progressive deterioration of the DUTs over the time.

Currently, our prototype is able to test 6 samples per run: however, the modular architecture of the system allows us to easily expand the sample size, with a little effort. In fact, all DUTs are heated simultaneously (i.e. the heating and cooling phases have the same duration for 6 or more samples) and the characterization throughput can be augmented using 2 or more SMUs.

We also reported the experimental results of an HTRB test on 6 Commercial On The Shelf (COTS) power Metal Oxide Semiconductor Field Effect Transistors

(MOSFETs). In particular we observed 2 failures with different trends: DUT6 had a monotonic degradation, whereas DUT2 failed after a partial recovery. A subsequent thermal annealing process (100 h at room temperature and then 24 h at 175 °C) revealed a permanent damage in the first case and a further degradation trend for DUT2. These different behaviors could represent two different signatures of failure. Consequently, the proposed equipment could be used not only for reliability testing, but also for diagnostic and investigation purposes.

References

1. Lutz, J., Schlangelotto, H., Scheuermann, U., De Doncker, R.: Semiconductor power devices: physics, characteristics, reliability. pp. 380–385. Springer, Heidelberg (2011). doi:10.1007/978-3-642-11125-9
2. Elsayed, E.A.: Overview of reliability testing. IEEE Trans. Reliab. **61**(2), 282–291 (2012). doi:10.1109/TR.2012.2194190
3. Testa, A., De Caro, S., Panarello, S., et al.: Stress analysis and lifetime estimation on power MOSFETs for automotive ABS systems. IEEE Power Electronics Specialists Conference, pp. 1169–1175. (2008). doi:10.1109/PESC.2008.4592088
4. Alpha and Omega Semiconductor (2010) Power semiconductor reliability handbook
5. Choi, S., Lee, K.L.: Failure analysis of P-N junction degradation by high temperature reverse bias operating condition. Physical and failure analysis of integrated circuits, pp. 587–590 (2013). doi:10.1109/IPFA.2013.6599229
6. Tosic, N., Pesic, B., Stojadinović, N.: High temperature storage life (HTSL) and high temperature reverse bias (HTRB) reliability testing of power VDMOSFETs. Microelectronics Proceedings, vol. 1, pp. 285–288 (1995). doi:10.1109/ICMEL.1995.500882
7. JEDEC Standard: Temperature, Bias, and Operating Life. JESD22-A108D (2010)
8. DoD Military Standard: Test methods for semiconductor devices, test methods standard. MIL-STD-750F (2012)
9. Automotive Electronic Council: Stress test qualification for automotive grade discrete semiconductors. AEC-Q101-Rev-D1 (2013)
10. Green, R., Lelism A., Habersat, D.: Application of reliability test standards to SiC power MOSFETs. Reliability Physics Symposium (IRPS), pp. EX.2.1–EX.2.9 (2011). doi:10.1109/IRPS.2011.5784573
11. Consentino, G., Scandale, T.: Power MOSFET with integrated poly-silicon diode to monitor junction temperature, with simplified external electrical shutdown circuit to prevent thermal runaway. PCIM Europe Conference (2009). ISBN: 978-3-8007-3158-9
12. Consentino, G., De Pasquale, D., Galiano, S., et al.: Innovative instrumentation for HTRB tests on semiconductor power devices. AEIT Annual Conference, pp. 1–5 (2013). doi:10.1109/AEIT.2013.6666814
13. Pace, C., Hernandez Ambato, J.L., De Pasquale, D., et al.: Instrumentation for innovative semiconductor power devices reliability tests. Int. J. Eng. Ind. (IJEI) **4**, 119–127 (2013). doi:10.4156/ijei.vol4.issue2.14
14. Hao, J., Rioux, M., Suliman, S.A., et al.: High temperature bias-stress-induced instability in power trench-gated MOSFETs. Microelectron. Reliab. **54**, 374–380 (2014). doi:10.1016/j.microrel.2013.10.004

A Wireless Sensor Node Based on Microbial Fuel Cell

**Simone Acciarito, Gian Carlo Cardarilli, Luca Di Nunzio,
Rocco Fazzolari and Marco Re**

Abstract In recent years there has been a widespread use of wireless sensor networks that found their application in complex systems where a lot of physical quantities have to be monitored. This nodes must deal with different physical quantities and must operate in different environments. In many applications the most critical aspect is the power supply, because frequently is possible to provide power supply by wires and sometimes the use of batteries is not an acceptable solution. This latter limitation occurs when the number of nodes is very high and/or the operation of battery substitution is very complex. Moreover, environmental requests for pollutant reduction and for renewable materials represents another limitation for the use power supply generation based on battery. For these reasons it can be useful to develop power sensor nodes which use energy harvested directly on the operation site, making the sensors energetically autonomous. In this paper we present an innovative sensor node based on Microbial Fuel Cells (MFCs). The implemented node proves the viability of MFC for the energy harvesting in sensor networks. This system uses the electric energy provided by the bacteria present in the soil as power supply for an ultra low power electronic system, based on a micro-controller equipped with a digital transceiver. The designed system is able to acquire data from a sensor and transmit them wirelessly. The scarcity of available energy and the limited voltages of the MFC require to design new schemes for the

---

S. Acciarito · G.C. Cardarilli (✉) · L. Di Nunzio · R. Fazzolari · M. Re
Department of Electronic Engineering, University of Rome Tor Vergata,
Via Del Politecnico 1, 00133 Rome, Italy
e-mail: g.cardarilli@uniroma2.it

S. Acciarito
e-mail: acciarito@ing.uniroma2.it

L. Di Nunzio
e-mail: di.nunzio@ing.uniroma2.it

R. Fazzolari
e-mail: fazzolari@ing.uniroma2.it

M. Re
e-mail: re@ieee.org

A. De Gloria (ed.), *Applications in Electronics Pervading Industry, Environment and Society*, Lecture Notes in Electrical Engineering 409,
DOI 10.1007/978-3-319-47913-2_17

energy harvesting and the power supply, as well as new working modes which must satisfy the strong energy constraints.

1 Introduction

The spread of wireless sensor networks to which we're assisting in recent years, is sometimes hampered by problems of energetic nature. It is not always possible to distribute the power among the various nodes of the network using a wired approach and frequently the solution based on the use of batteries appears not completely suitable. In facts the batteries need to be replaced periodically and various factors, as an elevated number of nodes and/or particular locations of deployment, can make it difficult their substitution. In some cases a solution for these problems is given by the photovoltaic. But, in many applications this solution is not very efficient for the presence of dust and other substances which reduce the panel efficiency. Another important aspect is the protection of the environment. Photovoltaic panels and batteries have a negative impact on the environment, due to the difficulty of their disposal. For all these reasons it is very useful to identify new methods of energy harvesting that can be used to make the sensors as much as possible energy independent.

In this work we present a wireless sensor node powered by the energy supplied by some species of bacteria present in the ground. The power comes from the ability of these bacteria to release charges to an electrode electrochemically affine, creating a flow of electrons when there is a cathode on which convey these charges. The charges are generated by bacteria anaerobic digestion. Bacteria having this characteristic are Shewanella and Geobacter. The opportunity to obtain energy using this approach, is supported by the particular conformation of the harvester, which makes this transducer immune to the variation of the external elements that, instead, penalizes other techniques. The only constraint is the presence of nutrients, such as the acetic acid, for the sustenance of the biofilm on the anode [1]. This condition is implicitly satisfied in a cultivation environment where the organic substances are always abundant. The proposed sensor node can be used in many applications. One of the most interesting is the precision agriculture.

The precision agriculture is an innovative technology. Its purpose is to improve the agronomic management (optimize the tillage in terms of, for example, irrigation and fertilization) through the application of different techniques of production on the cultivated fields. The premise on which this set of techniques are based is spatial variability: in most of the plots the physical, chemical and biological properties may be different from one point to another, often within a few meters. This implies a uncontrolled development of the plants, both from the point of view of quantity and quality. So a punctual knowledge of the soil properties is needed. For obtaining this knowledge, sensor networks based on MFC appear a promising solution.

This work is organized as follow, in Sect. 2 the Microbial fuel cells are introduced, in Sect. 3 is shown the description of the proposed system, in Sect. 4 the experimental results are illustrated and finally in Sect. 5 conclusions will be drawn.

2 Microbial Fuel Cells

Microbial Fuel Cells operation, but more generally of Bioelectrochemical Systems, exploit electrochemically active bacteria metabolisms to produce electrical power. Microbes inside MFC feed nutrients in their surrounding environment and release a portion of the energy contained within these substances in the form of electric power. Some particular species of microbes called Electrogenic microbes have the feature to release electrons onto metal compounds. Many studies [2] have shown that some species are able to perform this operations for example Geobacter can release electrons to Iron (III) and the Shewanella bacteria manage to reduce the manganese (IV).

A Microbial Fuel Cell is characterized by two carbon electrodes, a cathode and an anode (Fig. 1) [3].

The anode is buried in the the soil, while the cathode remains on top in contact with the air. In this way a biofilm will spontaneously develop on the anode surface with consequently generation of electric power [4, 5]. This is possible because soil is full of complex sugars and other nutrients that have accumulated over millions of years as consequence of plant and animal material decay.

Power generated by an MFC is continuous so long as there are nutrients readily available. The MFC works in the following way, when a microbial community is formed on the anode, it will start to exploit the nutrients in the soil to generate biomolecules with extra electrons attached to them. These biomolecules can give spare electrons to the anode in one of these way:

- Direct transfer from the microbe cell wall to the anode surface;
- Employing a secondary biomolecule to bring the electron to the anode,
- Transferring the electron through conductive appendages, termed “nanowires”, grown by the microbe.

An electron in the anode can travel to the cathode, where it reacts with an oxygen molecule and a proton, a byproduct of electrogenic metabolism, to form water. As result a Electromotive force is provided between the cathode and the anode. This force can be used to power electric and electronics devices. In this work we use this Electromotive force to power a wireless sensor node.

Fig. 1 Conceptual diagram of a microbial fuel cell (after [3])

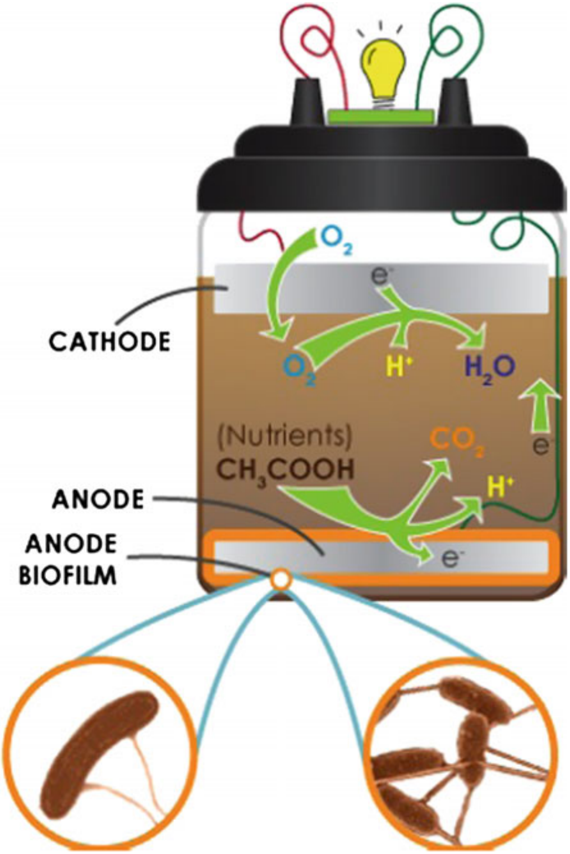

3 Sensor Node Realization

Wireless sensor networks (WSN) are composed by a number of wireless sensor nodes that communicate each other and with a local router able to send and receive data from the LAN and the web. The purpose of this work is the realization of a low-power sensor node able to use the energy provided by a MSC for the powering of the node sensors, the processing and controlling elements and the transmitter/receiver RF circuits. The proposed node is composed by the following main components:

- A resistance temperature sensor.
- A Microbial Fuel Cell.
- A Charge Pump.
- A digital converter/transmitter.

The MFC is used to harvesting the energy from bacteria and to power the whole sensor node. Since the voltage supplied is very low and unsuitable for conventional ICs, a charge pump and a capacitor for energy storing are required. The subsystem composed by the analog to digital converter and the transmitter has two main objectives, the data acquisition from the sensor and the wireless data transmission.

3.1 Choice of the Microbial Fuel Cell

The Microbial Fuel Cell that has been chosen for the development of the wireless sensor network is produced by Keego Technologies, LLC [3]. The system is composed by a 1 L PET container, in which we inserted the terrain, two graphite electrodes and a titanium wire. Since the voltage directly obtained from the MFC is very low (about 0.3 V), MFC system is also furnished of an electronic board with a charge pump capable of translate the voltage to 2.4 V. The system operations are organized according to the following procedure. MFC accumulates the charge (i.e., energy) on the storing capacitor until it reaches the energy required for activating the node. At this point the sensors and the conditioning circuitry is switched on along with the acquisition and transmission subsystems. The used MFC is shown in Fig. 2.

Fig. 2 Keego technologies microbial fuel cell

3.2 Digital Converter/Transmitter

The wireless digital transmitter is composed by two blocks, a low power micro-controller and a digital RF transceiver. The control of the data acquisition and the transceiver is performed by the micro-controller MSP430F2274. The firmware was developed in C language using the Code Composer Studio (CCS) Integrated Development Environment.

We have chosen the MSP430F2274 for its ultra low-power features. The device can be powered with a supply voltage in the range 1.8–3.6 V and can work in different low-power modes. The consumptions for the different modes are summarized in the following table.

- Active Mode: 270 μA at 1 MHz, 2.2 V;
- Standby Mode: 0.7 μA;
- Off Mode (RAM Retention): 0.1 μA.

The block diagram of the MSP430F2274 is provided in Fig. 3.

The transceiver used for the wireless communication is the Texas Instrument CC2500, the main features of this devices are:

- 2400–2483.5 MHz Wireless band;
- OOK, 2-FSK, GFSK, or MSKe configurable digital modulation;
- 1.2–500 kBaud programmable data rate.

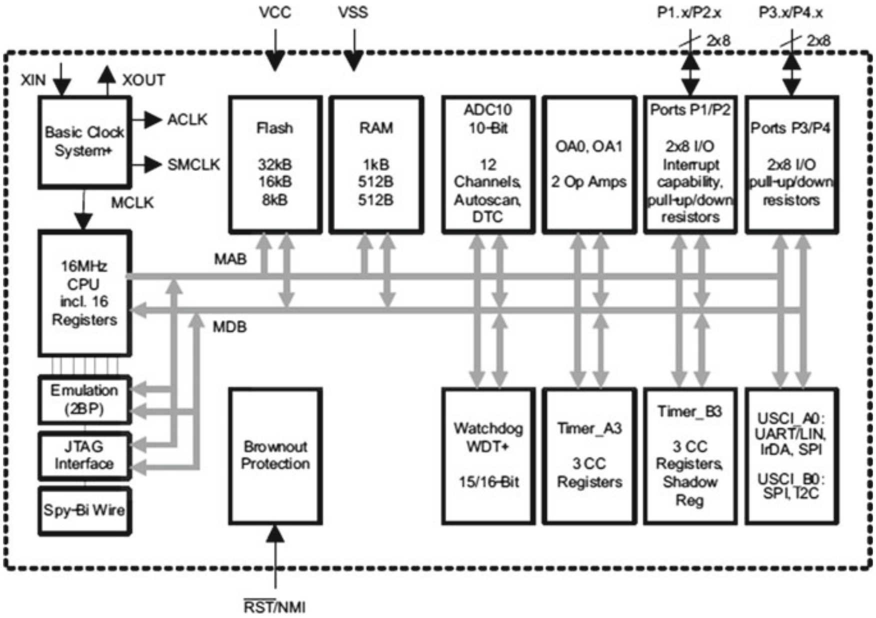

Fig. 3 MSP430F2274 block diagram

4 Experimental Results

In order to evaluate the performance of the wireless sensor node, several experiments were performed. The experimental setup was composed by the following elements:

- The proposed wireless sensor node composed by a temperature sensor, a MSC and the Texas instrument eZ430-RF2500 starter kit, containing the above cited microcontroller and wireless transceiver;
- A receiver composed by a general purpose Personal Computer and a Texas instrument eZ430-RF2500 starter kit.

The system is shown in Fig. 4, the material used to fill the MFC is the normal Potting Soil (humidity 50 %, pH 7.5). We filled the container with a first soil layer 1 cm height. On this layer we positioned the anode electrode which was covered with further another soil layer until to reach a distance of 4 cm from the bottom. The soil was enriched with sodium acetate in aqueous solution (pH = 7), that has been spilled into the ground gradually over a period of 7 days. The solution of sodium acetate was supplied to the soil by watering the surface, avoiding wetting of the upper electrode.

After seven days the Microbial full cell presented a voltage of 0.8 V and a power of 90 µW, for a load resistance of 1 KΩ. The node works in the following way: the MFC charges the capacitor using the charge pump, when the voltage on the capacitor reaches a certain value (corresponding to an energy value) sufficient to power the MSP430, the system performs the following operations:

- The MSP430 turns on.
- The ADC, integrated in the microprocessor, acquires data from the temperature sensor.
- Data are sent to the transceiver using the SPI interface.
- The transceiver sends the data and the system turn off.

In order to estimate the performance of the entire system we perform several experiments:

The first experiments were carried out with the following conditions:

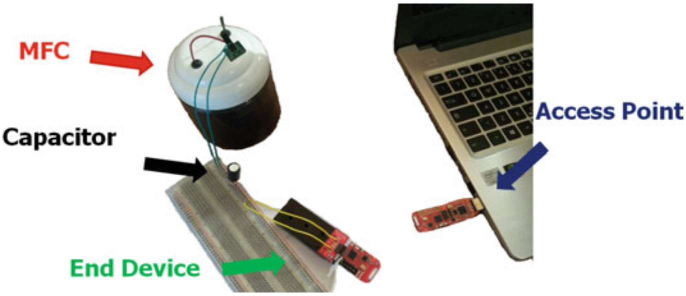

Fig. 4 The proposed system

- A 100 μF capacitor.
- A transmission power of 0 dBm.
- A FSK Digital modulation.
- A transmission data-rate of 2.4 KBaud.
- A distance between the node and the receiver of 20 m.

Under these conditions the systems did not work because the energy stored in the capacitor was not sufficient to complete all the operations performed by the node. On the other hand, using a 470 μF capacitor a complete transmission with period 58 s was obtained. Increasing the capacitor up to 1000μF a transmission period of 4 s was obtained.

5 Conclusion and Future Works

In this work a sensor node for ultra-low power applications is proposed. The node is powered by a Microbial Fuel Cell using a normal potting soil. Depending on the capacitance used for energy storing, MFC allows a data transmission rate up to one transmission each 4 s. The measurement results show that the use of suitable architectures for the power supply and data processing, together with a adapt operation strategy, makes possible the realization of a sensor network with low environmental impact, with energy harvester based on MFC. These results open the possibility to use MFC for powering sensor nodes in sensor networks to employ in very innovative applications as the precision agriculture and farming.

Acknowledgments The authors would like to acknowledge Agrivol s.r.l., and in particular Dr. Claudia Fagiolini, for their support to the experiments.

References

1. Dunaj, S.J., Vallino, J.J., Hines, M.E., Gay, M., Kobyljanec, C., Rooney-Varga, J.N.: Relationships between soil organic matter, nutrients, bacterial community structure, and the performance of microbial fuel cells. Environ. Sci. Technol. **46**(3), 1914–1922 (2012)
2. Rabaey, K., Rodriguez, J., Blackall, L.L., Keller, J., Gross, P., Batstone, D., Verstraete, W., Nealson, K.H.: Microbial ecology meets electrochemistry: electricity driven and driven communities. ISME J. (2007)
3. http://www.keegotech.com
4. Schroder, U.: Anodic electron transfer mechanism in microbial fuel cell and their energy efficiency. Phys. Chem. Chem. Phys. **9**(21), 2619–2629 (2007). Epub 2007 May 9
5. Reguera, G., McCarthy, K.D.: Extracellular electron transfer via microbial nanowires. Nature (2005)

Autonomous Wireless Sensor Network for Structural Health Monitoring of Aerostructures

Andrea Corniani, Simone Faccini, Enrico Turri, Nicola Testoni and Luca De Marchi

Abstract In this work we demonstrate the feasibility of an embedded, cheap, miniaturized active sensor node for detection of damages on laminate composite or metallic structures by means of ultrasonic guided waves (GWs). The device is meant as the basic building block of an autonomous wireless sensor network (AWSN) able to monitor the integrity of the aerostructure and locate possible damages. Each node is permanently mounted on the surface and wirelessly powered by electromagnetic (EM) waves, which are also used for communication with the base station. The electronic circuit is interfaced with an innovative, patent-pending piezoelectric transducer (piezo) capable of generating and sensing directional ultrasonic GWs in the inspected structure. Elastic waves propagating through the structure and reflected back to the piezo are recorded and processed by each individual node thanks to embedded processing functionalities to detect and locate defects. The information is then sent back to the base station for further analysis and evaluation. The results highlight that a small, lightweight and low power system can be designed with off-the-shelf hardware. The proposed system provides good reliability and accuracy and brings many advantages over current systems.

1 Introduction

The monitoring and assessment of structural components integrity is of vital importance for aerospace vehicles and systems, land and marine transportation, civil infrastructures, oil and gas industry as well as other industrial and mechanical applications. In particular, the current design and maintenance procedure for

---

A. Corniani · S. Faccini · E. Turri · N. Testoni (✉) · L. De Marchi (✉)
Dipartimento Dell'Ingegneria Dell'Energia Elettrica E Dell'Informazione,
Alma Mater Studiorum—Università Di Bologna, Viale Risorgimento 2,
40136 Boogna, Italy
e-mail: nicola.testoni@unibo.it

L. De Marchi
e-mail: l.demarchi@unibo.it

A. De Gloria (ed.), *Applications in Electronics Pervading Industry, Environment and Society*, Lecture Notes in Electrical Engineering 409,
DOI 10.1007/978-3-319-47913-2_18

composite or metallic aerostructures must consider the several types of loads and environmental stresses these structures undergo, as well as the fatigue and damages, which could result from the aforementioned causes. As long as the presence of cracks can be monitored and the propagation of the damage controlled, lighter weight aircraft can be designed to reduce direct operating cost. At the same time more frequent and accurate inspection has to be done in order to avoid any safety or reliability issue. Particularly dangerous are damages invisible to the human eye such as hidden delaminations in composite materials.

Several non-destructive approaches have been developed to support visual inspection with techniques based on ultrasonics or eddy current [1, 2]. Also, exploiting concepts from the structural health monitoring (SHM) field, the integration of a sensor platform in structural components can be performed to allow for easier and effortless inspection procedures. In fact SHM allows for the early detection of damages and the monitoring of its progression, leading to improvements in safety, reliability, and in maintenance and operating costs reduction above all.

Nevertheless, State-of-the-Art SHM systems feature piezo transducer interface electronics either based on general-purpose lab equipment or voluminous PCB assemblies. As such, when systems move from the lab into the field, where sensor nodes are deployed in multitude, the size, power and reliability of the control circuitry quickly becomes a bottleneck. This said the main motivation behind this work is the development of SHM devices with both high accuracy in damage detection and localization, and low hardware complexity and low power consumption for autonomous, reliable, in situ, real time operation.

Within this framework, the current work demonstrates that building a lightweight, small footprint circuit board with minimal hardware and energy harvesting and wireless communication capabilities is feasible. The key driver for this platform is an innovative sensor technology developed in collaboration with the Georgia Institute of Technology, Atlanta, namely the wavenumber spiral frequency-steerable acoustic transducer (FSAT) as discussed in [3].

Also, an impedance measurement device to ensure the transducer is properly coupled with the surface has been included in the sensor node's design. To rid the system of wires, energy harvesting capabilities are provided to each sensor node by means of a circuit capable of harvesting electromagnetic energy supplied by an RF power supply unit. Wireless power solutions based on RF energy harvesting overcome the limitations of alternatives (such as vibration harvesters) being reliant on ambient sources, because power can be replenished when desired.

2 System Implementation

The system is composed of three main sections: energy harvesting, self-diagnosis and actuation/detection circuitry. To prove the validity of the whole concept, the system has been split in almost independent parts so that it would have been easier to go through the development process in parallel. Tests have been conducted with three prototype off-the-shelf electronic boards to verify:

(a) The RF power transmission. A one-to-many charging system was implemented, basing on the “Lifetime Power Energy Harvesting Development Kit for Wireless Sensor” by Powercast as prototype circuit board. Each sensor board houses a microcontroller, which reads data from three different sensors and sends them to a remote PC via a 2.4 GHz radio module. The energy cost of wireless communication is in the range of J/bit. To perform these operations the sensor board drains 15 mA of average current at 3.3 V for 10 ms.
(b) The electro-magnetic impedance measuring circuit. An evaluation board AD5933 designed by Analog Devices was used to measure the impedance value of the piezo with a frequency sweep analysis. Graphical user interface software was provided to control the board and to download the impedance data.
(c) The sensing device. In order to test the damage detection capability and accuracy of the system we assembled the circuit responsible for the actuation of the piezo and tested it in different operation conditions. Both actuation and sensing has been addressed to ensure proper behavior for different modes of operation: active or passive, pulse-echo or pitch-catch.

3 Experimental Tests

3.1 Energy Harvesting

Multiple tests were performed to quantify the transmitted power versus distance. It is worth noting that, in many aerostructures made of composite materials, there are hollow stiffeners, which could be used to accommodate waveguides, as described in [4]. An obvious advantage of using guided over free space propagation for RF energy is that the first exhibits with much lower loss than the latter. For this reason, some tests were performed introducing the transmitter and the power receiver in a waveguide mockup: although not designed for this scenario, the hardware able to continuously collect up to 60 mW at a distance of 75 cm. The passive sensor node reported in [5] operates with a power consumption of 40 mW. As such, the implemented power transfer system allows for continuous monitoring of acoustic events while accumulating energy for the active inspections.

3.2 Electro-mechanical Impedance

The impedance value of different specimens of piezo transducers bonded to composite and aluminum plates was measured in the frequency range between 20 and 200 kHz. In this range the piezoelectric transducer can be modeled as a capacitance

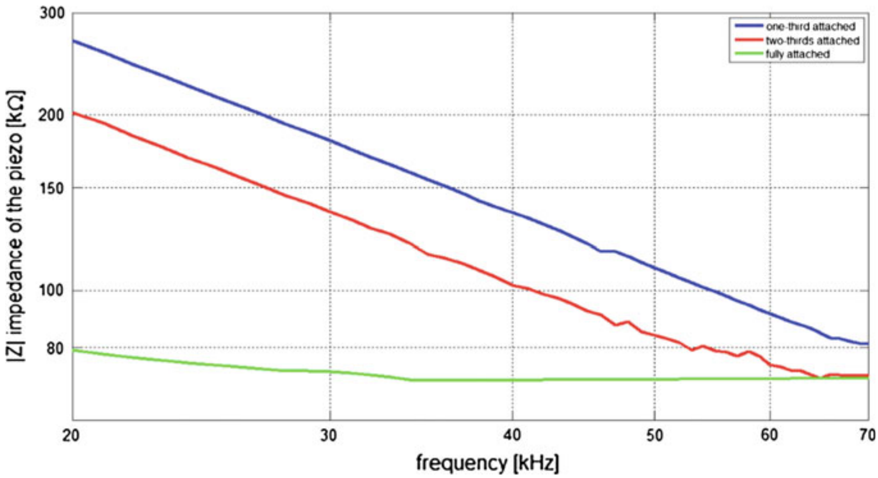

Fig. 1 Electro-mechanical impedance measurements: the different behavior between fully bonded (*bottom*) and partially disbanded sensors (*top*) allows for simple detection procedures

whose value can be easily extracted from measurements. Such a value changes when the acoustic coupling between the transducer and the surface becomes compromised due to disbonding. Multiple measurements were performed to assess this statement by varying the fraction of piezo surface attached to the composite plate.

The graph in Fig. 1 depicts the measured impedance for three of the aforementioned cases. Since the difference between the measurements for the detached piezos and that for the correctly bonded one are tens of kΩ, it is easy for the impedance measuring system to reveal an incorrect acoustic coupling.

3.3 Frequency Steerable Sensor

To test the performance of the FSAT the transducer was bonded at the center of an aluminum plate. Four other identical, omnidirectional piezos were glued at a radial distance of 25 cm and spaced 30° one from the other. The FSAT was used as the active element of the setup and it was connected to a waveform generator through a RF power amplifier. The four other transducers were used as sensors and connected to the oscilloscope. This setup is depicted in Fig. 2.

The FSAT was excited with a 10 cycle sinusoidal burst to achieve a sufficiently narrow frequency spectrum. Results show that the FSAT is capable to steer the ultrasonic wave according to the frequency of the sinusoidal burst.

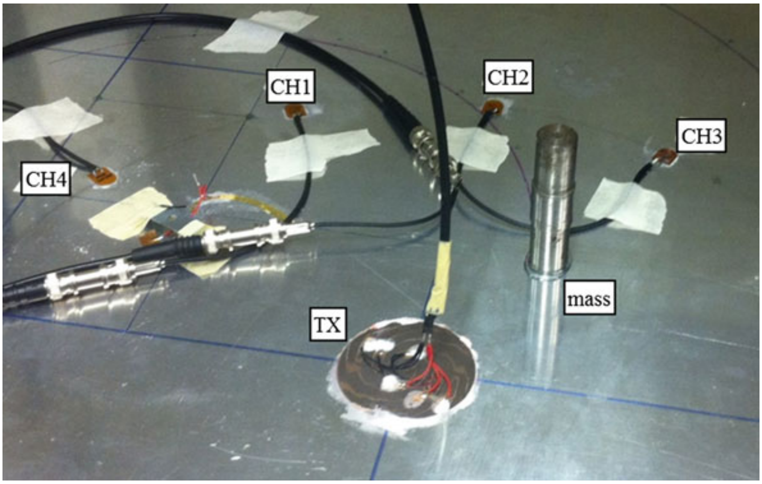

Fig. 2 Experimental setup for the assessment of the FSAT directionality and sensitivity to defects; the latter is simulated by means of a test mass stitched to the plate using ultrasound coupling gel

Finally, to simulate the presence of a damage, a cylindrical mass with a diameter of about 2.5 cm was placed between the FSAT and one piezo. The acoustic coupling between the mass and the aluminum structure was realized through an ultrasound transmission gel. When the mass was added to the setup, its presence produced the scattering of the ultrasonic waves and an attenuation of the intensity of the sensed signal. The presence of the simulated damage could be seen through the attenuation in the output signal of the first piezo sensor as depicted by the highlighted trace in Fig. 3.

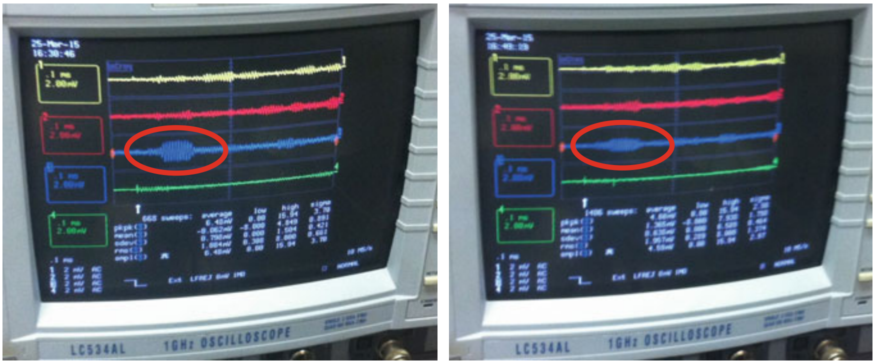

Fig. 3 Results of the signal acquisition phase: the FSAT was excited with a 10 cycles sinusoidal burst around 78 kHz. The presence of the mass is evident on the right hand side image where a noticeable decrease in signal amplitude is present

4 Conclusions

In this work, the feasibility of an embedded, cheap, miniaturized active sensor node for detection of damages on laminate composite or metallic structures by means of ultrasonic guided waves was demonstrated. Sensors could be made to be inherently dormant, requiring zero stand-by power. When a reading is desired, power can be transmitted until all of the stages of the inspection process are completed, namely the sensor's activation, the inspection and the sending back of the results. The continuous power transfer achieved in the waveguide case allows the sensor node to work in passive mode, i.e. sensing the ultrasonic waves already present in the surface and generated by impacts. When active mode operation is required for deep and extensive inspection, energy has to be stored in a super-capacitor like device so that it can reach the amount required for the actuation of the ultrasonic wave to take place. It is worth noticing that designing specifically dedicated directional antennas can further optimize the transmission efficiency and the overall results concerning energy harvesting. The results of the tests made highlight the concrete possibility of detecting the detachment of the piezo element from the surface by means of an impedance measuring system, which can be easily integrated on the node's circuit board. Such auto-diagnostic feature allows the sensor node to reveal a change with respect to the nominal operating conditions and ensures that the system can always offer high safety and reliability standards. The spatial filtering characteristics of the FSAT have been experimentally demonstrated and validated. This kind of sensor is perfectly suitable for actuating the ultrasonic waves, for arbitrarily steering them by changing the frequency of the actuating signal and for providing the information about the angular position of the reflected wave in the frequency content of the sensed signal. When compared with state-of-the-art guided waves inspections system based on phased arrays, the proposed solution features lower hardware complexity and lower power consumption by eliminating the digital beamforming delays, multiplexing, switching and spatial combination of multiple channels for image generation thanks to the exploitation of frequency-based steerability.

Acknowledgments This work describes a research activity performed in response to the Airbus "Fly Your Ideas" 2015 Challenge. The authors gratefully acknowledge Stuart King from Airbus for the constant support and his useful comments.

References

1. Pisupati, P., Dewangan, S.K., Kumar, R.: Structural health monitoring (SHM): enabling technology for paradigm shift in next generation aircraft design and maintenance. Infosys white paper
2. Boller, C., Buderath, M.: Fatigue in aerostructure. Philos. Trans. R. Soc. A Math. Phys. Eng. Sci. **365**, 2007 (1851)

3. Baravelli, E., Senesi, M., Ruzzene, M., De Marchi, L.: Fabrication and characterization of a wavenumber-spiral frequency-steerable acoustic transducer for source localization in plate structures. IEEE Trans. Instrum. Meas. **62**(8), 2197–2204 (2013)
4. Bommer, J.P., Green, W.P., Lewis, D.M.: Method and apparatus for wireless aircraft communications using fuselage stringers. AU2010259160 (2011)
5. Testoni, N., De Marchi, L., Marzani, A.: A coin size, 40 mW, 20 grams sensor node for guided waves detection. Proceedings of SPIE NDE-Smart Structures (2015)

Wearable Speech Enhancement System for Motor Impaired People

Alessandro Palla, Luca Fanucci, Roberto Sannino and Mattia Settin

Abstract Automatic Speech Recognition (ASR) is a valid solution for smartphone and PC interaction from people with motor skill impairments. However recognition performances are reduced in scenarios affected by environmental noise. We propose a speech enhancement system based on MEMS microphone array and a digital signal processor capable to increase signal-to-noise ratio (SNR) of the user's voice. The difference in Time of Arrivals (TOA) audio samples between microphones is exploited by the array to separate speech and environmental noise. In such way the system can obtain an increment in SNR about 16.5 dB using an Adaptive Noise Reduction filter. Due to the small array size, the proposed system has been integrated in a wearable device. Theoretical analysis and in-system measurements prove the effectiveness of the proposed solution.

1 Introduction

Automatic speech recognition (ASR) software can be a valid alternative for disabled people, especially those with motor skill impairments, to interact with personal computers and smartphones. Furthermore many devices also include a built-in ASR software, like Siri for Apple or S-Voice for Samsung smartphones, and many efforts have been made in recent years to improve quality of those softwares.

Anyway, voice recognition should be usable in different environments in order to be a valid alternative to common input interfaces. In particular ASR service reduces its recognition performance in scenarios with low signal to noise ratio (SNR), because the speech recognition reliability strongly depends on quality of recorded audio. If samples are greatly corrupted by noise, ASR software may loses or misunderstands one or more words.

A. Palla (✉) · L. Fanucci
University of Pisa, Pisa, Italy
e-mail: alessandro.palla@for.unipi.it

R. Sannino · M. Settin
STMicroelectronics, Agrate Brianza, Italy

A. De Gloria (ed.), *Applications in Electronics Pervading Industry, Environment and Society*, Lecture Notes in Electrical Engineering 409,
DOI 10.1007/978-3-319-47913-2_19

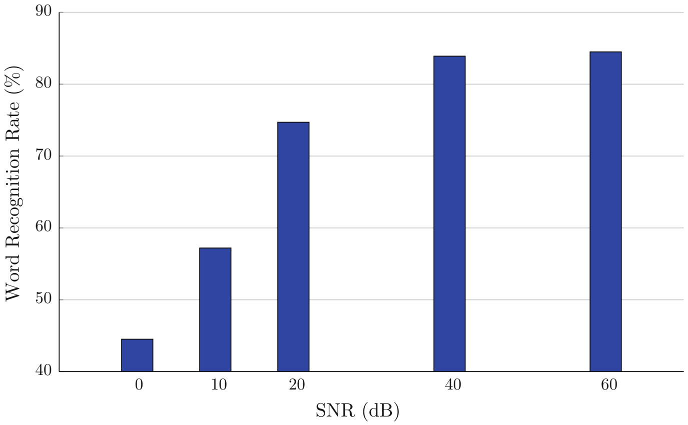

Fig. 1 Word recognition rate of ASR engine versus SNR

Word Recognition Rate (WRR), a common metric for evaluation of speech recognition systems [1], is defined as:

$$WRR = \frac{H - I}{N} \tag{1}$$

where

- N is the total words in the sentence
- H is the number of correctly recognized words
- I is the number of insertions words, not pronounced by the user.

The ASR performance degradation has been evaluated, see Fig. 1, using a set of more than one thousand common sentences in human-machine interaction,[1] acquired using a single microphone with white background noise. When SNR is lower than 10 the WRR of the recognition is lower than 50. For such noise levels the ASR software used for that tests, Google Speech API, is not reliable and the disabled person isn't able to interact with the device using speech recognition.

2 System Architecture

The solution proposed, as shown in Fig. 2, is a wearable speech enhancing system based on a MEMS microphones array, an embedded CPU for Digital Signal Processing and a computing platform (PC or smartphone) for Speech Recognition purpose. The system is composed of two parts:

---

[1] like dial, call, send etc.

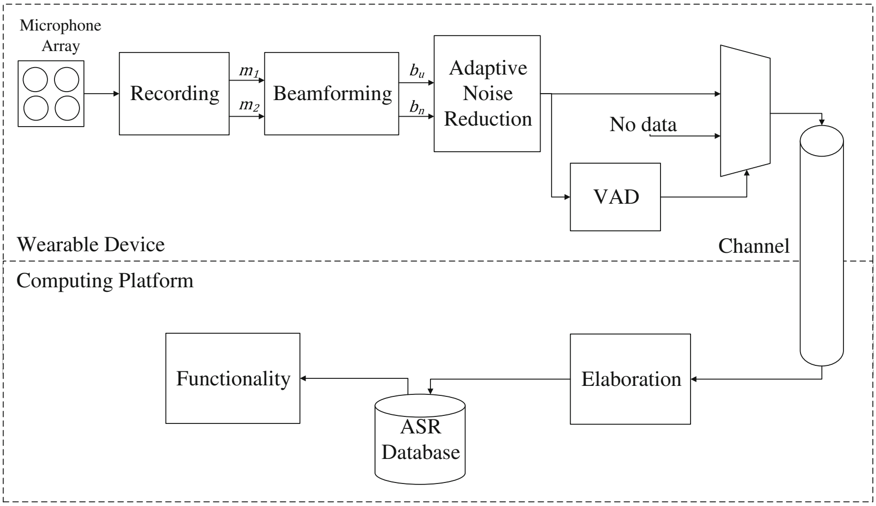

Fig. 2 Architecture of the speech enhancement system

- Wearable device: an embedded electronic system based on a Cortex-M4 microcontroller, devoted to microphones data samples acquisition and processing.
- Computing platform: a software running on the device (PC or smartphone) for speech recognition service and user interaction.

The key point of our work is the integration and the implementation of all the processing blocks into an embedded system, which leads many application advantages like small size, reduced power consumption and low cost.

2.1 Wearable Device

The beamforming block implements a delay and subtract algorithm as explained in [2–4]. The output beam $b(t)$ is calculated as shown in Eq. (2)

$$b(t) = m_1(t) - m_2(t - \tau) \tag{2}$$

while the difference in Time of Arrivals (TOA) between the two microphone is.

$$\tau_0 = \frac{d}{c}\cos(\theta) \tag{3}$$

where d is the distance between m_1 and m_2, c is the sound speed (334 ms^{-1} in dry air, 20 °C) and θ is the input angle (see Fig. 3).

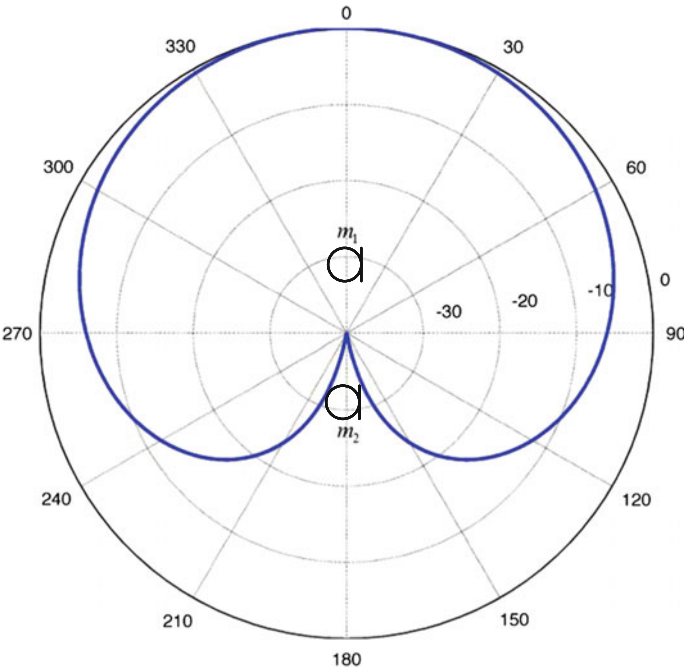

Fig. 3 Directivity pattern of delay and subtract beamforming for $f = 1$ kHz

The algorithm explained in Eq. (2), applied twice, can be used to separate audio input in two different audio streams:

- User beam b_u, focused in the maximum SNR direction.
- Reference noise r_n, focused in the minimum SNR direction.

The Adaptive Noise Reduction (ANR) block is an adaptive filter aimed to delete environmental noise using an adaptive LMS filter [5, 6, 7]. It deletes noise in the user beam that is correlated with reference noise, while keeps unaltered speech signal that is present only in the user beam because of the beamforming [5].

Anyway reflections of speech in walls and physical objects create voice path for different angles, so voice cannot be completely deleted in reference beam. In that case ANR filter partially suppresses and distorts useful signal, depending on attenuation of voice in user and reference beams. In particular if we define SNR_{r_n} as signal-to-noise ratio in reference beam, output SNR is [5]

$$SNR_{out} = \frac{1}{SNR_{r_n}} \tag{4}$$

According to Eq. (4), to increase SNR of output signal is extremely important to have a great attenuation of user's voice in reference beam.

The purpose of the Voice Activity Detection (VAD) routine [8] is to discriminate the presence of speech in audio stream for data compression.

2.2 Computing Platform

Data coming from wearable device need to be processed before speech recognition. Because ASR service is cloud-based, to decrease latency of transmission, the samples are encoded using speex codec. The trade-off between bit-rate and speech quality was evaluated in function of the recognition results, in order keep unchanged the mean WRR of the recognition.

Compressed data are sent to the ASR service via HTTP POST protocol using Dragon Naturally Speaking web API, which returns to the software the utterance of the recognition. The result of the recognition is used by the device to execute commands to perform user's requests.

3 Evaluation

Figure 4 shows a picture of the developed prototyped based on a wearable device (glass embedding a MEMS microphone array) and an embedded CPU (STM32F439 ARM microprocessor) that performs audio algorithms. Figure 5 shows the evaluation results of the system in real life scenario with user speech in front of the system and omnidirectional white noise. The improvement of SNR is on average 16.4 dB using the same sentences of Fig. 1. The voice level was attenuated about 6 dB due to the non-perfect cancellation of user's voice for $\theta = 180°$. The attenuation of omnidirectional white noise is about 22.5 dB, which means that the power of the disturbances is reduced ≈180 times.

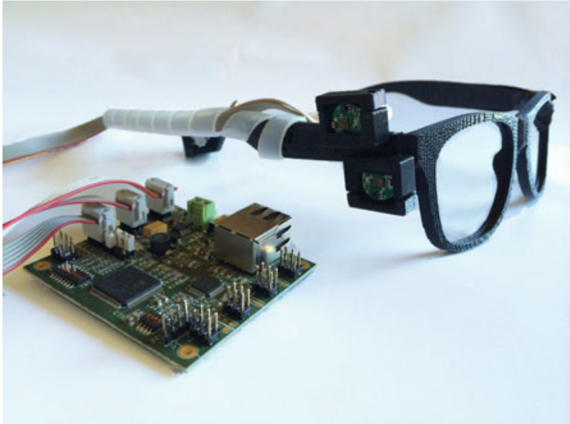

Fig. 4 Wearable device prototype

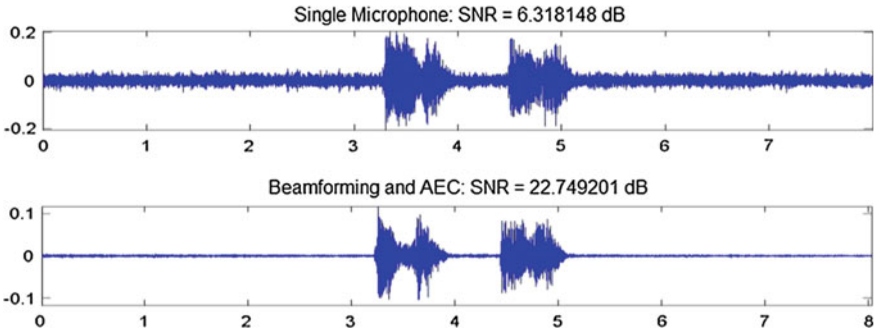

Fig. 5 SNR enhancement with beamforming and ANR

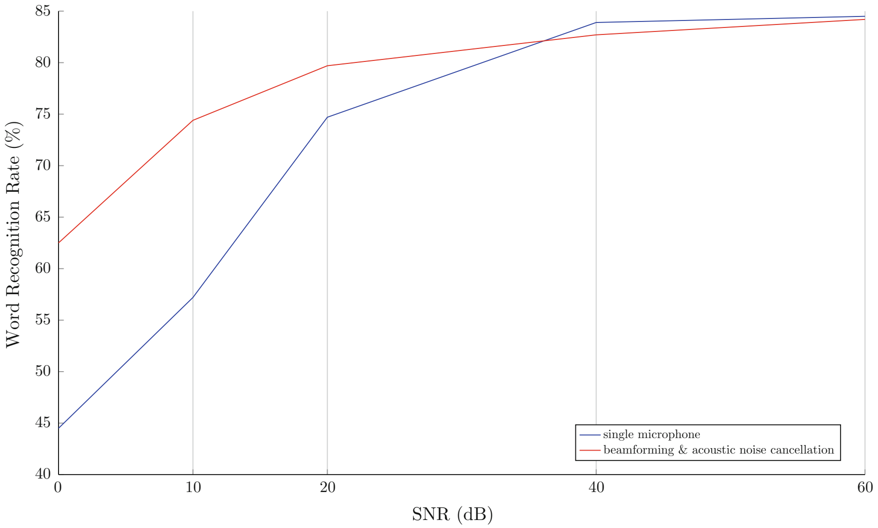

Fig. 6 Word recognition rate of ASR with speech enhancement system

For SNR greater than 40 dB, the difference in WRR between speech enhancement and single microphone is less than 1 %, as shown in Fig. 6. The increment of WRR becomes more effective when the SNR of input audio decreases less than 20 dB, when the system improves it about 16.5 %.

4 Conclusion

In this paper we proposed a wearable system based on microphone array to improve speech recognition in noisy environments. In scenarios when user's voice and environmental noise come from different directions, the system is able to reduce noise of recorded audio exploiting the different time of arrival of input sound for each microphone, using beamforming and adaptive noise reduction techniques. This device can be efficiently used by people with disability as a replacement for standard PC and smartphone inputs.

References

1. McCowan, I., Moore, D., Dines, J., Gatica-Perez, D., Flynn, M., Wellner, P., Bourlard, H.: On the use of information retrieval measures for speech recognition evaluation (2005)
2. Benesty, J., Chen, J., Huang, Y.: Microphone array signal processing, vol. 1. Springer (2008)
3. Luo, F.-L., Yang, J., Pavlovic, C., Nehorai, A.: Adaptive null-forming scheme in digital hearing aids. IEEE Trans. Signal Process. **50**(7), 1583–1590 (2002)
4. McCowan, I.: Microphone arrays: a tutorial, pp. 1–38. Queensland University, Australia (2001)
5. Widrow, B., Glover Jr., J.R., McCool, J.M., Kaunitz, J., Williams, C.S., Hearn, R.H., Zeidler, J.R., Dong Jr., E., Goodlin, R.C.: Adaptive noise cancelling: principles and applications. Proc. IEEE **63**(12), 1692–1716 (1975)
6. Widrow, B., Stearns, S.D.: Adaptive signal processing, vol. 1, 491 pp. Prentice-Hall, Inc., Englewood Cliffs (1985)
7. Valin, J.-M.: On adjusting the learning rate in frequency domain echo cancellation with double-talk. IEEE Trans. Audio Speech Lang. Process. **15**(3), 1030–1034 (2007)
8. Bachu, R., Kopparthi, S., Adapa, B., Barkana, B.: Separation of voiced and unvoiced using zero crossing rate and energy of the speech signal. American Society for Engineering Education (ASEE) Zone Conference Proceedings, pp. 1–7 (2008)

System-Level Analysis for Integrated Power Amplifier Design in mmWave Consumer Wireless Communications

Sergio Saponara and Bruno Neri

Abstract System-level specifications for the design of integrated power amplifiers in mmWave wireless communications are derived in the paper. To this aim emerging standards for consumer applications such as wireless ultra-high definition (UHD) multimedia streaming or Gbit wireless LAN are considered (WirelessHD, WiGig, ECMA387, IEEE.802.11.ad, IEEE802.15.3c and upcoming 5G). A power amplifier design in 65 nm CMOS Silicon on Insulator (SOI) technology, targeting a 9 GHz UWB window from 57 to 66 GHz, is also proposed. To increase the power delivered to the antenna up to 18 mW, being still in the limit of maximum 1 dB compression point, multiple PA cores have been combined through a Wilkinson power combiner, but other solutions can be also explored for a better power efficiency and linearity.

1 Introduction

Emerging consumer applications in the millimeter-wave (mmWave) wireless domain for short-range multi-Gbps links pose new challenges for the design of the key blocks of the transceivers, particularly the power amplifier (PA).

Traditionally consumer wireless applications have been developed in a spectrum from few hundreds of MHz to 5 GHz. This portion of spectrum includes Bluetooth and Wireless Local Area Networks (WLAN) at 2.4 or 5 GHz, domotic wireless applications or Radio Frequency Identification (RFID) for logistics in the ISM (Industrial Scientific Medical) unlicensed bands (typically sub-GHz bands are considered for this aim), radio and TV broadcasting in VHF/UHF bands, multi-band cellular communications from 800/900 MHz to 2 GHz. Being focused on large volume and low cost markets, these applications witnessed the development of the RF hardware equipment using low cost silicon technologies, BiCMOS and in the last years mainly CMOS. Most of the above systems are narrow band.

S. Saponara (✉) · B. Neri
Dip. Ingegneria della Informazione, Università di Pisa, via G. Caruso 16, 56122 Pisa, Italy
e-mail: sergio.saponara@unipi.it

A. De Gloria (ed.), *Applications in Electronics Pervading Industry, Environment and Society*, Lecture Notes in Electrical Engineering 409,
DOI 10.1007/978-3-319-47913-2_20

Therefore, system specifications require that the relevant hardware building blocks should sustain a given performance (e.g. gain, noise figure…) at high operating frequency, in the order of some GHz, but for a limited bandwidth. Efficiency problems at transmitter side are typically addressed using switching-mode amplifiers or class-C and class-E topologies.

On the other hand higher frequencies in mmWave spectrum (from 10 GHz to hundreds of GHz) have been addressed in the state of art though hetero-junction Bipolar transistors (HBT) and/or high electron mobility FET (HEMT) technologies such as SiGe HBT or GaAs, InP, GaN HEMT [1–3]. Main applications have been radar transceivers not only for defense but mainly for civil applications, e.g. automotive radar at 24 GHz (short-range) or 77 GHz (long-range), mmWave body scanners for security (e.g., in airports, banks,…), mmWave imaging for medical applications, satellite communications. Heterojunction technologies, being characterized by a niche market, entails high costs for the wireless transceivers that cannot be justified in emerging mmWave consumer applications.

By exploiting the large spectrum available at mmWave, multi-Gbps links can be obtained with conventional modulations schemes and this can enable a lot of new services for consumer users in short-range home or office scenarios such as:

- Wireless Gbps LAN, realizing a convergence with already existing Gbps cabled connections like Gbps Ethernet or 100 Mbps FTTC (Fiber To The Cabinet), or announced Gbps FTTH (Fiber To the Home); convergence of mmWave wireless service and free space optical (FSO) services for last mile connections are also envisaged at the state of art.
- Ultra high definition (UHD) video playing and uncompressed multimedia streaming creating a wireless high speed network among 4K UHD TVs, UHD blue-ray players/recorders, tablets/smart phones, internet access points.
- Multi-view (3D already available) video playing and teleconferencing and digital holography applications.

The development of such applications at mmWave poses new specifications on the wireless transceivers (in terms of cost of the technologies to be used, bandwidth, power, linearity, gain…) that cannot be addressed by traditional chipset. To this aim in Sect. 2 we derive from a system-level analysis the main specifications for PA in mmWave multi-Gbps consumer applications. An implementation in CMOS SOI technology is proposed in Sect. 3. Section 4 presents a comparison with recent state of art and draws some conclusions.

2 System-Level Specifications for mmWave PA Design

Several standards and industrial consortia have been already proposed for mmWave consumer wireless applications [4–7]. The WiGig industrial consortium is promoting the development of multi-Gbps wireless connections. Besides classical 2.4 and 5 GHz operating frequencies, also 60 GHz is considered in WiGig as a key operating band for the new generations of multi-band RF transceivers. The WirelessHD consortium is focusing more on UHD video and multimedia streaming, playing and recording and is envisaging the use of a 7 GHz spectrum around 60 GHz. With such a large channel even with simple modulations schemes with a few bits/Hz efficiency is easy to achieve up to 10 Gbps connections. From a standardization point of view these services are covered by standards such as the ECMA-387 or the IEEE 802.15.3c High Speed Interface PHY (HSI PHY) or the 802.11.ad [4–7]. As example, Fig. 1 shows the channelization and worldwide spectrum allocation in the ISM unlicensed band around 60 GHz highlighting multiple-channel bonding options foreseen in ECMA-387. The approach in Fig. 1 allows for scalable data traffic capacity since the wide spectrum from 57 to 66 GHz can be dynamically partitioned in multiple channels (hence allowing to multi services). The above considerations lead to a specification of a transceiver operating around 60 GHz, with a large bandwidth of 9 GHz, and realized in silicon technologies, CMOS bulk or SOI version, to keep low the cost of the devices in large volume consumer markets. Considering that for analog and RF applications is not required to adopt the last (and more expensive) technology nodes (14 nm/28 nm), target CMOS technologies between 90 and 45 nm can be addressed [8–10].

65 nm CMOS technologies are today mature. They allow for a good trade-off between performance and cost for all the different signal domains of a fully-integrated wireless terminal (analog baseband, digital, RF up to tens of GHz). The voltage supply considering battery duration should be at maximum 1.2 V, this influences at circuit level the design style limiting the number of transistors that can be stacked between supply and ground. On the contrary, ultra low-voltage designs (sub-thresholds circuits with few hundreds of mV supply have been proposed in literature) lead to more complicated circuit-level design limiting too much the

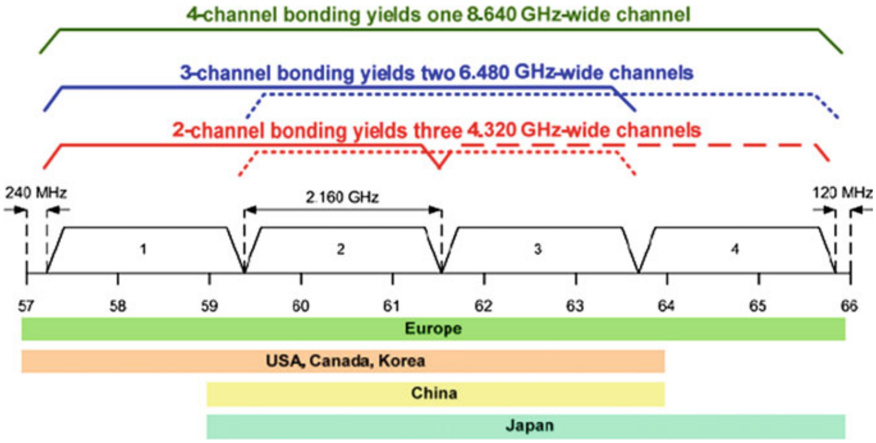

Fig. 1 Worldwide spectrum allocation for multi-Gbps mmWave communications in consumer applications and flexible channelization foreseen in ECMA-387

output dynamic range, the performance of the transistors, and the transceiver robustness vs. external interference or changing environmental conditions.

Communication services around 60 GHz are also candidate to represent the high-speed connection part of the upcoming 5G wireless networking standard. 5G communication systems, whose deployment and commercialization is expected in 2020, intend to create a synergy among a variety of cellular and wireless LAN systems through the use of the heterogeneous networking (het-net) paradigm. The aim is to maximize the use of RF bandwidth by switching between different systems, based on channel availability at the local level. Among the key technology challenges towards this goal, let recall here the support for high data rates and the need for increased capacity in dense urban environments, both outdoor and indoor. Due to air and water absorption, transmissions in the mmWave band have shorter range than in the "sub-3 GHz" bands used for current cellular systems. This reveals a key advantage in high-density environments, allowing base stations to be situated closer together. In particular, the portion of spectrum around 60 GHz (with wavelength of few mm) experiences a dramatic attenuation (about 15 dB/km) due to the presence of the absorption peak of molecular oxygen and as such it has been allocated worldwide for unlicensed services as reported in Fig. 1. The link distance to be covered is up to 10 meters in short-range home or office scenario. Considering also what is specified in the standards in terms of Bit Error Rate (BER), modulation and channel coding scheme and expected ratio between the average received energy per bit Eb and the one-sided overall receiver noise power spectral density N_0, denoted as Eb/N_0, the transmitted power for the transceiver should be about 10 dBm. As last consideration, we have to consider that standards building up the new 5 G generations massively relies on multi-carrier schemes. Due to large number of sub-channels, OFDM (Orthogonal Frequency Division Multiplexing), widely used for communication of multimedia data [11–13], is characterized by a high PAPR (Peak to Average Power Ratio) i.e. the signal has large envelope fluctuations.

As example in [1] a N-carrier OFDM signal with 4-DPSK modulation has a PAPR of about 10Log10 N, i.e. roughly 18 and 30 dB for a 64-carrier and 1024-carrier OFDM signals respectively. The system degradation due to PA non linearity are [1] the following: additional interference in the receiver, spectral spreading of the transmitted signal which can cause adjacent channel interference, intermodulation effects when several channels are amplified concurrently by the same PA, interference between in-phase and quadrature components of QAM modulated signals due to AM-PM conversion. To avoid distortions a linear PA is needed, thus limiting the use of switch-mode and class C RF PA topologies. Table 1 summarizes the main specifications derived for the mmWave PA for consumer applications.

Table 1 Specifications for PA design in mmWave consumer communications

Topology	Peak power (dBm)	Center freq. (GHz)	Band. (GHz)	Tech.	Max. supply (V)
Class-A	10	60	9	CMOS bulk/SOI 45–90 nm	1.2

3 mmWave PA in 65 Nm Silicon Technology

Giving the specifications derived in Sect. 2, see Table 1, a class-A amplifier with a 2-stage Common Source (CS) topology and inter-stage LC matching networks has been designed in 65 nm CMOS SOI. The circuit schematic is reported in Fig. 2. At technology level we considered both a 65 nm bulk CMOS technology and a 65 nm SOI one, but for the final PA design we selected the SOI version. The bulk CMOS version allows for minimal fabrication cost being that used for large volume digital and mixed-signal baseband designs. The SOI version, thanks to its high resistivity substrate (1 kΩcm instead of standard 20 Ωcm), has several advantages vs. bulk technology for 60 GHz design of active and passive devices while avoiding the high extra costs of hetero-junction technologies (SiGe HBT, GaAs or InP HEMT and so on). The CMOS SOI allows for:

- reduction of substrate interference cross-coupling between different circuits integrated in the same chip;
- significantly reduction of junction capacitances so circuits can operate at higher speed or with lower power at the same speed;
- elimination of latch-up and better immunity to short-channel effects;
- reduced amount of energy stored in the supporting substrate leading to higher gains in case of on-chip integrated antennas.

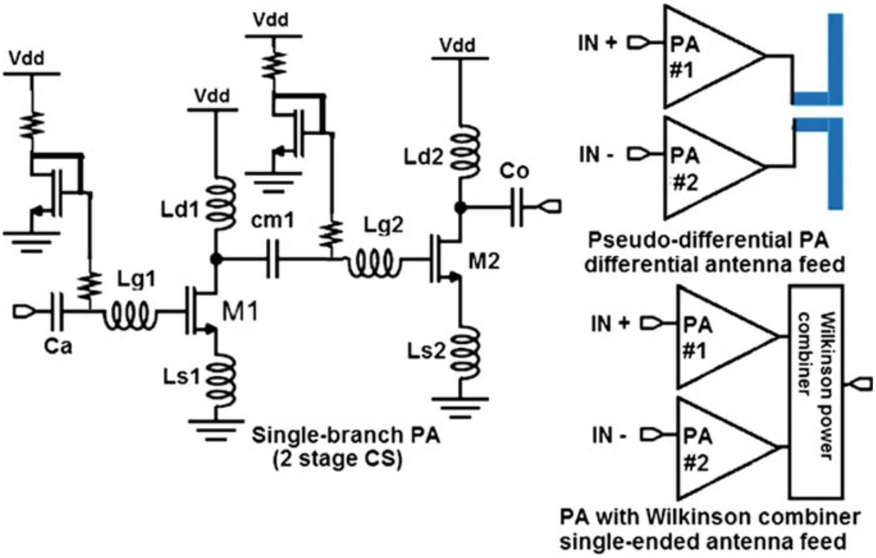

Fig. 2 2-stage CS PA with pseudo-differential or Wilkinson power combiner

From a circuit topology point of view a cascode topology is normally more efficient for achieving high gains, at low-voltage operation (1.2 V in our case), vs. the CS stage with a single transistor. However stacking the CS and the CG transistors in a cascode approach would determine a limited output voltage-swing that would compromise the output power 1 dB compression point (OP1 dB) performance of the amplifier. For multi-carrier OFDM systems with high PAPR the linearity and hence the 1 dB compression point performance is a key figure of merit. As alternative to CS or cascode stages a folded-cascode topology could be employed cascading several stages, but this way the power consumption is nearly doubled vs. a conventional cascode. This is why we preferred a multi-stage class-A CS topology. To properly size the width of the MOS devices in the proposed class-A PA circuit we exploited the benefit of the invariance of the maximum linearity (and also maximum Ft) bias current density across technology nodes, 0.3 mA/μm as demonstrated in several works at state of art.

With a 1.2 V power supply, in CMOS SOI technology, the PA circuit shows an insertion gain of 7 dB (the S21 parameter) at 60 GHz varying from roughly 8 dB at 57 GHz to 6 dB at 66 GHz. The 1-dB input compression point IP1 dB is 1.76 dBm while the OP1 dB is 8.2 dBm (6.6 mW). The DC power is 44 mW. The peak PAE (power-added-efficiency) is 11.5 %. The return loss (S11 parameter) is always below -10 dB, in the target 57-66 GHz spectrum. The stability factor is K > 4 for all the frequencies from 57 to 66 GHz, resulting in the unconditional stability of the two-ports active network. To meet the 10 dBm system-level specifications about the transmit power outlined in Sect. 2 (Table 1) the power of 2 PA blocks of Table 2 is combined in a pseudo-differential mode if the antenna has differential feed or in case of single-ended feed through Wilkinson Power combiner. The Wilkinson combiner is a 3-port circuit capable of simultaneously achieving port-to-port isolation, impedance matching and ideally not dissipating power in the resistance across ports 2 and 3 when the two ports are balanced. As a result, the OP1 dB of the whole amplifier in 65 nm CMOS SOI is 10.7 dBm with Wilkinson combiner (10 % loss vs. ideal case) and 11 dBm in the pseudo-differential case. The Wilkinson power combiner can be used also in a cascaded mode to combine the power of 4 PA blocks in a single PA feeding the transmitter antenna: the OP1 dB achievable power growths up to 12.51 dBm (roughly 18 mW) with about 25 % loss vs. the ideal case of the x4 power level increase. To be noted that maximum output power where the amplifier saturates (Psat) is more than 4 dB above the OP1 dB.

Obviously, by increasing by a factor K the number of PA blocks, taking into account also the extra circuit needed to combine their power towards the transmitter antenna, the total area and power consumption increases by a factor higher than K while the maximum transmitter power increases by a factor below K.

Table 2 Performance of single PA block in 65 nm CMOS SOI at 1.2 V

IP1 dB (dBm)	OP1 dB (dBm)	S11 in 57–66 GHz spectrum (dB)	S21 in 57–66 GHz spectrum (dB)	PAE (%)	DC power (mW)
1.76	8.2	<−10	6–8	11	44

4 Comparison to State of the Art and Conclusions

In our experiments, the power combination mechanism can be useful to meet transmitted power of 11.8 and 17.9 mW by combining 2 or 4 basic PA blocks respectively. Comparing these results vs. recent state of art [14, 15] it is worth noting that the above power levels refer to OP1 dB and hence are obtained with a very high linearity (less than 1 dB compression vs. the ideal amplifier response). In state of art of mmWave CMOS amplifier for 60 GHz consumer applications such high power levels are typically obtained as maximum saturated power with higher distortions.

An area estimate (excluding pads) of the core for the structure with 2 PAs and a Wilkinson power combiner is about 0.11 mm^2 for each PA plus 0.1 mm^2 for the 2-way Wilkinson combiner for a total area of 0.32 mm^2. The DC power consumption is roughly 90 mW. The single PA channel has an area of 0.11 mm^2 and a DC power of 44 mW.

As future work, we are planning to exploit the whole amplifier curve up to Psat, including also the non linear part above the 1 dB compression point, to increase amplifier efficiency by exploiting the low probability that in real OFDM transmissions certain power levels are reached. Also the utilization of an integrated Marchand Balun will be explored in the future to combine the output power of up to 8 transistors [16] so reducing the nonlinearities in the amplitude output characteristic.

References

1. Rapp, C.: Effects of HPA-nonlinearity on a 4-DPSK/OFDM-signal for a digital sound broadcasting system. In: Proceedings of second European Conference on Satellite Communications, ECSC-2, 1991
2. IEEE 802.11.09/1213r1, 60 GHz impairment models (2009)
3. High Rate 60 GHz PHY, MAC and PALs, Standard ECMA-387, 2nd edn (2010)
4. Yilmaz, T., et al.: Employing 60 GHz ISM Band for 5G Wireless Communications. IEEE BlackSeaCom14 (2014)
5. Krone, S., et al.: Physical layer design, link budget analysis, and digital baseband implementation for 60 GHz short-range applications. Int. J. Microwave Wirel. Technol. **3** (2), 189–200 (2011)
6. Seyedi, A.: On the Physical Layer Performance of ECMA-387: A standard for 60 GHz WPANs, IEEE ICUWB (2009)
7. Nicolàs, M., et al.: Physical layer simulation results for IEEE 802.15.3 c with different channel models, Advances in Radio Science, vol. 9 (2011)
8. Voinigescu, S., et al.: Algorithmic design of CMOS LNAs and PAs for 60 GHz radio. IEEE JSSC **42**(5), 1044–1057 (2007)
9. Yeh, J.-F., et al.: A 57–66 GHz power amplifier with a linearization technique in 65-nm CMOS Process, IEEE EUMIC, pp. 309–312 (2014)
10. Hamidian, A., et al..: 60 GHz power amplifier utilizing 90 nm CMOS technology. IEEE RFIT (2011)

11. Saponara, S., Martina, M., Casula, M., Fanucci, L., Masera, G.: Motion estimation and CABAC VLSI co-processors for real-time high-quality H.264/AVC video coding. Microprocess. Microsyst. **34**(7–8), 316–328 (2010)
12. Marsi, S., et al.: Integrated video motion estimator with Retinex-like pre-processing for robust motion analysis in automotive scenarios: algorithmic and real-time architecture design. J. Real-Time Image Proc. **5**(4), 275–289 (2010)
13. Fanucci, L., et al.: Parametrized and reusable VLSI macro cells for the low-power realization of 2-D discrete-cosine-transform. Microelectron. J. **32**(12), 1035–1045 (2001)
14. Abbasi, M., et al.: A broadband differential cascode power amplifier in 45 nm CMOS for high-speed 60 GHz system-on-chip. IEEE RFIC, pp. 533–536 (2010)
15. Wei, F., Hao, Y., Yang, S., Kiat, S.Y.: A 2-D distributed power-combining by metamaterial-based zero phase shifter for 60-GHz power amplifier in 65-nm CMOS. IEEE Trans. Microw. Theory Tech. **61**(1), 505–516 (2013)
16. Jia, H., Kuang, L., Wang, Z.: A W-Band power amplifier utilizing a miniaturized marchand Balun combiner. IEEE Trans Microwave Theory Tech. **63**(2), 719–725 (2015)

UDOO-Based Environmental Monitoring System

**Giulio Borrello, Erica Salvato, Giovanni Gugliandolo,
Zlatica Marinkovic and Nicola Donato**

Abstract In this paper we present the development of a compact and stand-alone system for environmental monitoring based on gas, humidity, temperature sensors and UDOO Quad board. The sensors are connected with the UDOO board by means of a very simple designed and home-made developed shield. Here, the system developed has been preliminary evaluated by detecting hydrogen, methane, oxygen and humidity, for air quality monitoring in industrial environments.

1 Introduction

The monitoring of air quality takes place in many applications, spanning from automotive to assisted living and home automation. For example, in the automotive field, the quality of air in the car cabin is monitored by means of sensors that monitor humidity, temperature and pollutants such as carbon monoxide (CO), nitrogen oxides (NOx) and carbon dioxide (CO_2) [1–4]. Many car models are already equipped with these systems and their employment is still increasing, considering the limitations for NOx emissions recently introduced by the Euro 6 legislation [5]. In home automation the employment of sensors able to monitor the presence of methane and CO can be the best solution to prevent intoxication accidents [6]. In such a context, the development of monitoring system with a high grade of configuration, small, powerful, can achieve the right consideration by many users. For this scope, we developed a compact and stand-alone system based on gas, humidity, temperature sensors and UDOO Quad board, designed for different applications in the field of environmental monitoring. Here, we evaluated the

---

G. Borrello · E. Salvato · G. Gugliandolo · N. Donato (✉)
Department of Electronic Engineering, Chemistry and Industrial Engineering,
University of Messina, Contrada di Dio, 98166 Sant'Agata di Militello, Italy
e-mail: ndonato@unime.it

Z. Marinkovic
Faculty of Electronic Engineering, University of Niš, Niš, Serbia

A. De Gloria (ed.), *Applications in Electronics Pervading Industry, Environment and Society*, Lecture Notes in Electrical Engineering 409,
DOI 10.1007/978-3-319-47913-2_21

performance of the system developed by monitoring combustible gases such as hydrogen and methane, along oxygen and humidity, for air quality monitoring in industrial environments (e.g. refinery).

2 Experiments

The design of the measurement chamber was performed with Sketchup software, then it was realized by means of a 3D printer (Sharebot PRO) in ABS polymer. The chamber is composed of two parts, where the sensors take place, and one part working as gas dispenser, when the chamber is connected to laboratory equipment for calibration procedures. The design of the chamber allows the exposition of the calibration gas for each mounted sensor and a complete reflow avoiding stagnant area. In Fig. 1a–c are reported the design of the chamber, the picture of the 3D printer and the printing of the gas dispenser, respectively.

In Fig. 2 it can be seen the measurement chamber with the gas sensors mounted in it. In the present configuration, the following commercial sensors: DHT22 (humidity and temperature sensor), MQ4 (methane), MQ8 (hydrogen) and ME2-O2 (oxygen), are interfaced by means of a shield able to be connected in the Arduino 2 socket already present in the UDOO board. The UDOO MiniPc board is the "quad" version, equipped with two processors, Freescale i.MX 6 ARM Cortex-A9 CPU Quad core 1 GHz and Atmel SAM3X8E ARM Cortex-M3 CPU (same as Arduino Due).

The measurement software is composed of two functional blocks: the Firmware written for Arduino to handle the sensor array, and the Java GUI for display and

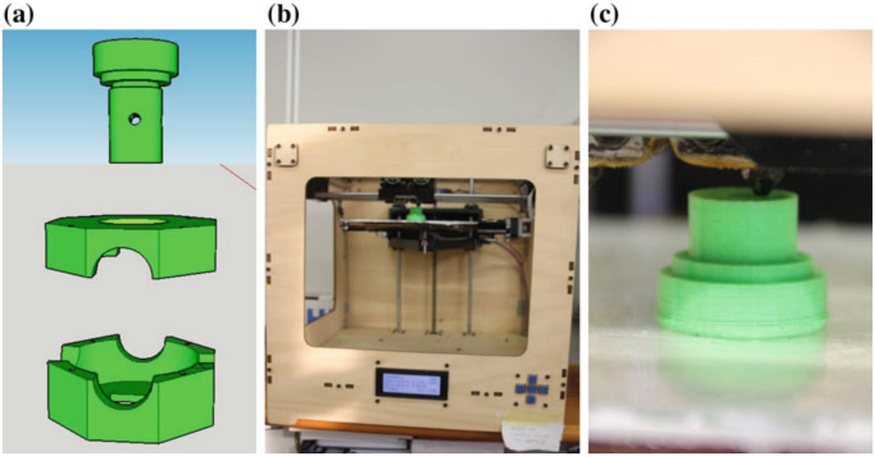

Fig. 1 **a** Design of the chamber. **b** Sharebot Pro printer. **c** Printing of the gas dispenser

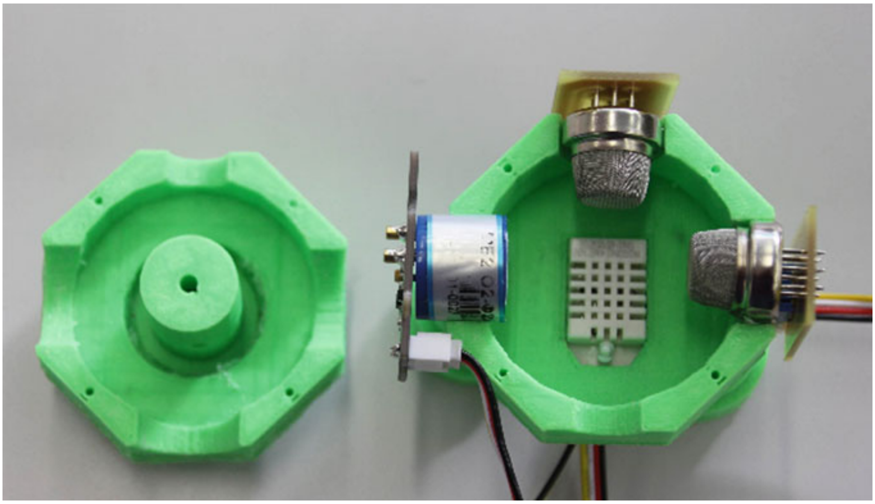

Fig. 2 The measurement chamber with the sensors mounted in it

record the data coming from the sensors. The software was realized by means of open source packages (NetBeans), and it can be employed not only with UDOO hardware, but also with a notebook connected with an Arduino2 board. In Fig. 3 it can be seen a screenshot of the developed software. In Fig. 4 is shown the automated gas control setup, equipped with a flowmeter array and certified concentration gas bottles. This system allows to expose the sensors to well defined gas concentration values to evaluate the response and the cross sensitivities of the sensors composing the array.

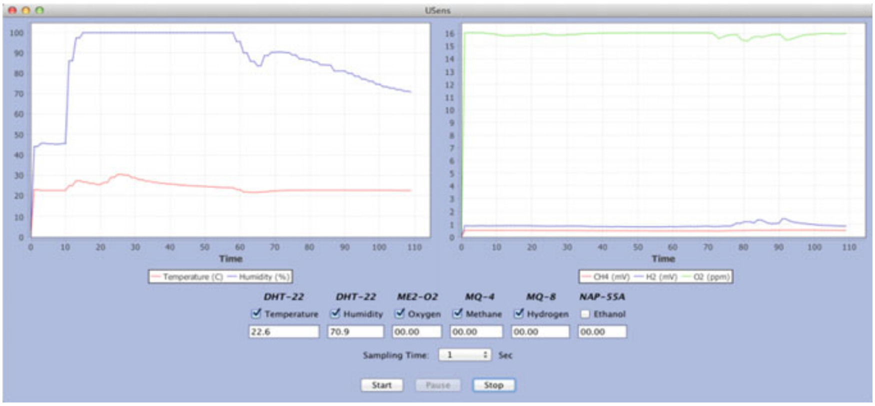

DHT-22	DHT-22	ME2-O2	MQ-4	MQ-8	NAP-55A
☑ Temperature	☑ Humidity	☑ Oxygen	☑ Methane	☑ Hydrogen	☐ Ethanol
22.6	70.9	00.00	00.00	00.00	00.00

Sampling Time: 1 Sec

Fig. 3 The GUI developed in Java environment

Fig. 4 The gas control setup

3 Results

Measurements were carried out exposing the sensor array to oxygen, methane and hydrogen pulses of different concentrations. Temperature and humidity sensors are also used to acquire information about the ambient conditions surrounding the sensor. In these preliminary experiment measurements were performed in a controlled environment at constant temperature (25 °C) and humidity level (10–15 %). In Fig. 5 is reported the output voltage of the sensor array towards oxygen in a concentration range spanning from 5 to 30 %. The output of oxygen sensor is very high, which make it able to detect the presence of this gas up to 25 % in nitrogen, being the output voltage at higher concentration in the overflow range, while the remaining sensors are little affected, presenting small cross-sensitivity.

In Fig. 6 is reported the output voltage of the sensor array towards methane, in a concentration range spanning from 200 to 2000 ppm. The output of the methane sensor is clearly visible. However, an appreciable output coming from hydrogen sensor has been also recorded.

In Fig. 7 is reported the output voltage of the sensor array towards hydrogen. Hydrogen sensor show good response in the whole concentration range (5–40 ppm). In the same conditions, the other sensors show no response.

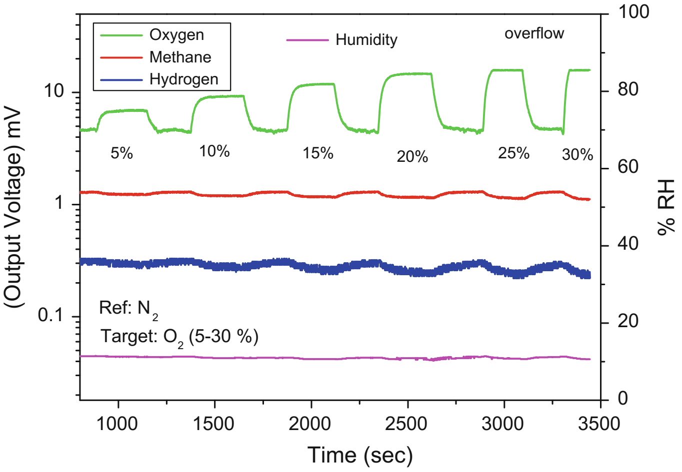

Fig. 5 Sensor array output voltage to oxygen (concentration range 5–30 %)

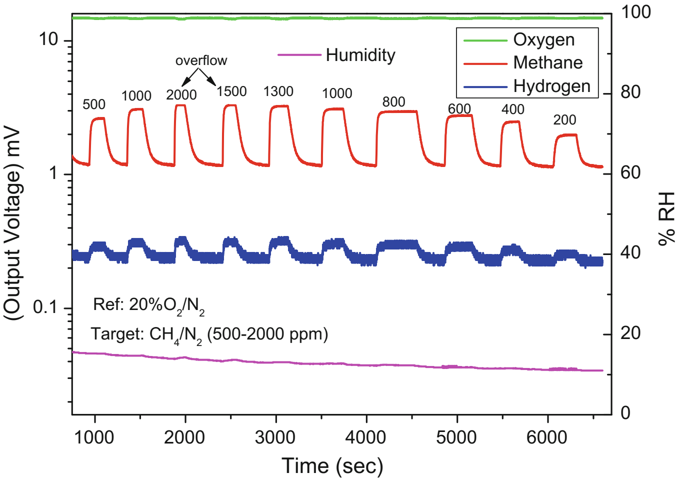

Fig. 6 Sensor array output voltage to CH_4 (concentration range 200–2000 ppm)

Preliminary data obtained demonstrated that the sensor system developed can be used to monitor simultaneously the combustible gases H_2 and CH_4, as representative of the refinery environments. Cross-sensitivity tests and measurement at higher humidity values are planned in order to evaluate the potential of this device under practical conditions of use.

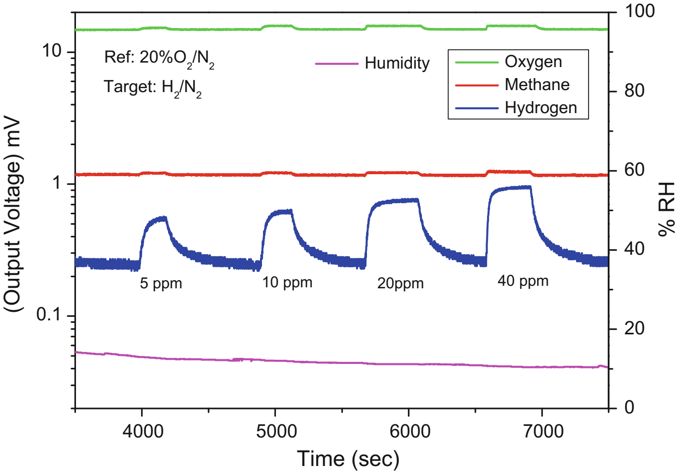

Fig. 7 Sensor array output voltage to hydrogen (concentration range 5–40 ppm)

4 Conclusions

Here it was reported about the development of a system for air quality monitoring in industrial environments. The system is portable and totally open source with an high level of configurability, allowing the possibility of its application in several operative fields. Further activities are in progress to include pattern recognition algorithms for electronic nose applications.

References

1. Abi-Esber, L., El-Fadel, M.: Indoor to outdoor air quality associations with self-pollution implications inside passenger car cabins. Atmos. Environ. **81**, 450–463 (2013)
2. Kim, Y.-S., Hwang, I.-S., Kim, S.-J., Lee, C.-Y., Lee, J.-H.: CuO nanowire gas sensors for air quality control in automotive cabin. Sens. Actuators B Chem. **135**(1), 298–303 (2008)
3. Fleming, W.J.: New automotive sensors—a review. IEEE Sens. J. **8**(11), 1900–1921 (2008)
4. Saponara, S., Petri, E., Fanucci, L., Terreni, P.: Sensor modeling, low-complexity fusion algorithms, and mixed-signal IC prototyping for gas measures in low-emission vehicles. IEEE Transactions on Instrumentation and Measurement, vol. 60, no. 2, February (2011)
5. Asselt, H., Biermann, F.: European emissions trading and the international competitiveness of energy-intensive industries: a legal and political evaluation of possible supporting measures. Energy Policy **35**, 497–506 (2007)
6. Preethichandra, D.M.G.: Design of a smart indoor air quality monitoring wireless sensor network for assisted living. 2013 IEEE International Instrumentation and Measurement Technology Conference: Instrumentation and Measurement for Life 6555624, 1306–1310

A Smart LED Light Control System for Environmentally Friendly Buildings

Michele Magno, Tommaso Polonelli and Luca Benini

Abstract This paper proposes a low cost, wireless, easy to install, adaptable smart LED lighting system to automatically adjust the light intensity of LED panels to save energy and to maintain user satisfaction. The wireless control system is based on ZigBee communication and combines a light sensor with a motion sensor to perform an energy saving algorithm. Measurements of total energy consumption over a continuous six-month period were acquired to verify the performance and evaluate the benefits in terms of power savings of the proposed solution. In the monitored application scenario, the total energy consumption has been reduced by over 60 % during a six-month period and up to 70 % in spring months.

1 Introduction

Current statistics show that even to this day, energy used for lighting continues to be a significant share of the entire energy consumption. For example, around 25 % of electricity in commercial buildings in the United States is used for lighting [1]. Although there has been a considerable research effort in recent years, there is still much that can be experimented to reduce energy waste. It is evident that artificial lighting uses a considerable amount of energy, and even a 1 % saving on that part alone will significantly increase the energy efficiency. For this reason, new intelligent lighting systems have been created in the past years and many continue to be developed. The goal has always been the pursuit of an optimized system from the energy efficiency point of view, paying less attention to the user's comfort. This can have an enormous effect on the productivity of employees, creating less than optimal working conditions, especially for focus intensive, problem-solving activities. Lighting does not just illuminate the office, it can affect the mood, energy and efficiency of workers and even increase their sense of comfort [1].

M. Magno (✉) · T. Polonelli · L. Benini
DEI, University of Bologna, Bologna, Italy
e-mail: michele.magno@unibo.it

A. De Gloria (ed.), *Applications in Electronics Pervading Industry, Environment and Society*, Lecture Notes in Electrical Engineering 409,
DOI 10.1007/978-3-319-47913-2_22

Wireless sensor networks are today a mature technology used in many applications for energy conservation applications such as light control [1–4] or other applications [4–10]. In [3], the authors present a light controlling system that achieves both energy saving and user's satisfaction. The proposed approach on the decision of the controlled light is based on the user's location and his luminosity preference. Due to the centralized algorithms controls the light dimming and minimizes the consumed power. In [11] light sensors are added to the control system to take into account the change of daylight during the day. Due to the light sensors, it is possible to achieve better performance in terms of power saving of the controlled LED panels, as the control system can evaluate the optimal dimming level. The work described in [12] targets to minimize the overall cost of the energy spent in media production system. To achieve this goal, their control algorithm uses both cost functions and user's preferences. The authors' approach is interesting and show the benefit to use controlling system also in different application scenarios. The authors in [13], present a similar approach deploying a sensors network with wireless communication to minimize the energy consumed by lights in buildings. Unfortunately, the paper does not give enough detail on the proposed approach, especially it is not clear if the proposed control algorithm is centralized or distributed. However, the authors show an interesting approach similar to our work, where both motion sensors and lights sensors are used to adjust the light intensity with the aim to minimize the energy consumption. In this work we present long-term (over several months) and evaluation in a real office of the energy saved during three different seasons and weather conditions.

The contribution of this work is the in-field evaluation of real-time monitoring and control lighting system designed to improve the energy efficiency of building, optimizing the dimming of the LED lights. A flexible wireless sensor network has been deployed in-field in a real office to evaluate the energy saving performance in a long period. The developed system has been designed and developed in a previous work [2] and reduces the installation cost and guarantees smart and energy efficient building and office with a high return on investment in terms of energy saved. The presented system is composed of a ZigBee wireless sensor network that controls the lights according of user preferences and light/occupation condition and a distributed control module on a base station that will be able to control the lights of that system. For this reason, this prototype will provide a graphical user interface to allow the user to work on it. This system has been developed and deployed in collaboration with a Verde LED, Ireland.

2 Smart Lighting System Architecture

Figure 1 shows the architecture of the developed control system, and more information can be found in [2]. There are several wireless nodes connected through ZigBee [14] radios in a mesh network. The whole system includes one coordinator, many routers and several End Devices (EDs). In the proposed network, each

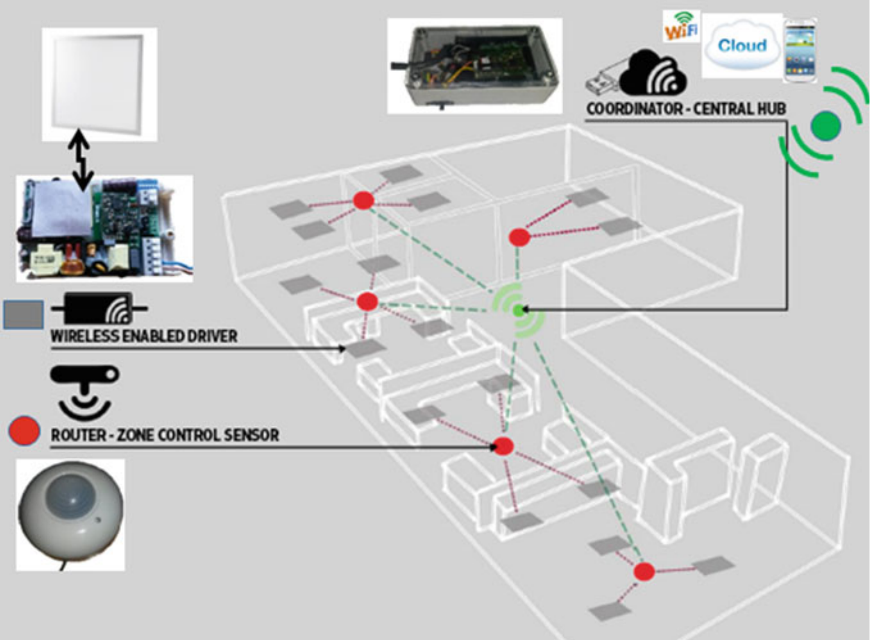

Fig. 1 Depolyment of the proposed wireless system with the types of nodes designed: (i) The network coordinator connected with a PC to the user interface and other wireless protocol (WiFi/Bluetooth); (ii) Sensor node programmed as a network router to monitor the controlled area with motion and light sensors, (iii) Wireless driver device inserted directly in the LED panel driver to dim the light intensity according with the user's preferences and the sensor data to minimize the energy consumption and reach the optima brightness in the rooms

ZigBee ED is directly connected to a LED panel driver that can directly set the dimming level of the panel through a pulse-width modulation (PWM) signal. The routers host one light sensor and one pyroelectric infrared (PIR) sensor to decide the optimal value of the brightness intensity of the associated LED panels according to sensors and users' preferences. The control algorithm evaluates the optimal value to minimize the energy used from the panels. The scalability of the network is permitted by the mesh configuration of the standard Zigbee allowing a modular system which is easily extendable. Moreover, each LED panel group is completely independent and comprises several units to monitor/control several different area sizes. In fact, the number of controllable associated LED panels and ED devices by every router/sensors device it is variable and can be dynamically adapted according to deployment requirements. Finally, the coordinator is responsible for the management of the whole wireless network ensuring that all the other devices are connecting in the proper way. The second important role of this device is to work as the main gateway with an ultra low power embedded device with Wireless Lan/Bluetooth interface to enable the simple user interface with phone or PC. Due to the user interface the manager of the network (or the user self) can set the light preferences allowing the control system to match them to adapt the dimming of the LED panels. The designed system includes also a graphical user interface on pc or phone to allow the user to monitor run-time the value of the energy saved during all the activity period. The user can also group the LED panels with a specific sensor node in order to optimize the control system. The graphic interface allows the user also to be aware of the energy saved according to the light preferences. In fact, the energy consumed depends on different variables but the dominant is the user's preference. Another crucial factor that affects the energy saving is the position of the controlled lights, for instance in a room with a huge window and in direction of the sun it is possible to save much more energy than in a room without windows. Other factors are of course the weather conditions, season, geographical location, etc.

The wireless devices of the network have been designed using the CC2530 system on chip (SoC) from Texas Instruments. The main reason of the choice is the low power consumption, the integration of the 802.15.4 radio with the ZigBee Pro stack and the possibility to have a cheap and fast deployment in the field. All the designed devices have a dual core architecture including two chips: the MSP430 microcontroller has been used to implement the control algorithm and the firmware developed, while the CC2530 is the responsible of the wireless communication trough ZigBee PRO stack. As we used the ZigBee Stack there are three possible types of devices: 1 Coordinator, Routers, and end devices. In our implementation the coordinator is connected via an USB port the PC where the user interface has been developed. On the other hand, the routers are equipped with the light and motion sensors to monitor the buildings, finally the end devices are connected inside the LED driver to control the dimming level with a standard PWM or 0–10 V control port.

2.1 Wireless Driver Device

As we mentioned before, the intelligence is provided by a MSP430 microcontroller that is embedded in all the devices. The MSP430 is also managing the CC2530 SoC to exploit the ZigBee stack implemented on it. The architecture of the wireless driver device is presented Fig. 2. The wireless device includes the electronic circuits to control the industrial driver and the dc-dc converter to be supplied with an external power supply with a voltage rage of 3–24 V. This range allows the wireless driver to be adaptable for several LED panels to increase the flexibility of the solution (Fig. 2). The most important subsystem of the wireless driver is the PWM-Driver block shown in Fig. 2. In fact, this block converts the 3.3 V PWM signal provided by from the MSP430 in a 0–10 V signal adopted by most of the commercial LED drivers to control the diming of the LED panels. This control interface makes the developed wireless driver adaptable to a wide range of drivers on the market. The only requirements for the driver is to provide a standard 0–10 V port. In this work we present a wireless driver that has been directly incorporated directly into a commercial driver by Meanwell as shown in figure.

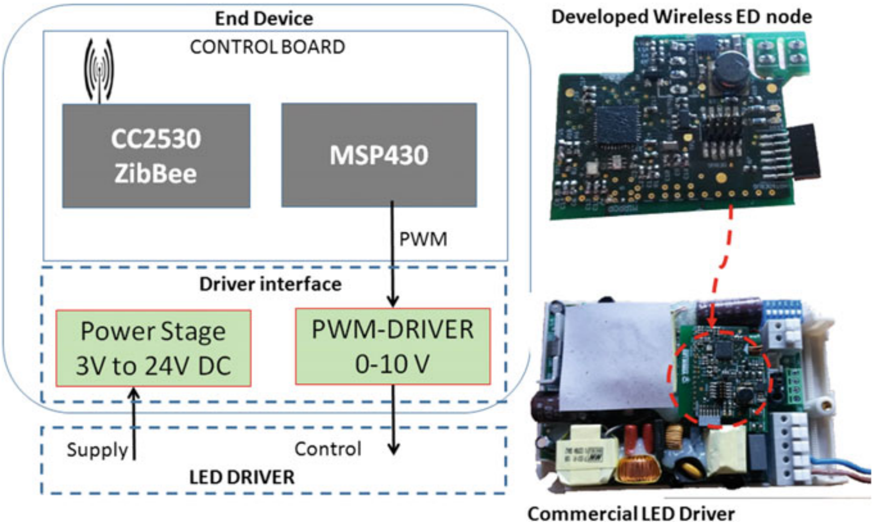

Fig. 2 Wireless driver device architecture designed to be inserted directly into commercial drivers. The wireless node can dim the panel trough the 0–10 V port and take supply voltage from it

2.2 *Router for Monitoring and Decision Making*

The router hardware architecture is presented in Fig. 3. The architecture is very similar to the wireless driver, with the only difference that the PWM driver block is replaced by the light and PIR sensors block. The PIR block includes also the coupling circuit that generates an interrupt when an everything is moving in its filed of view. The PIR selected is the Panasonic EW—AMN34111J due to its fast and accurate trigger in the range of 10 m of field of view. The PIR out trigger is directly connected to a General Purpose Input Output (GPIO) pin of the microcontroller that in this way is aware of every motion in the field of view. The designed sensor node includes also a low power light sensor to continuously monitor the intensity of light on the room or monitored area of interest. The light value is the most important information need by the controlling algorithm to decide the dimming level of the LED panels. The selected light sensor has been the Osram SFH 5711 that provides a analog output proportional to the light intensity. The analog output of the sensor is connected with th internal Analog digital converter of the microcontroller that can run the controlling algorithm to according with the user's preferences and the implemented power policy. As for the wireless driver, the wireless communication protocol is managed using the CC2530 that includes the ZigbeePRO stack. The routers are in charge of the most important duties for the wireless systems with the following main duties: (i) manage the routing protocol of the Zigbee stack, monitoring the environmental parameters throughout the sensors, (ii) take the decision

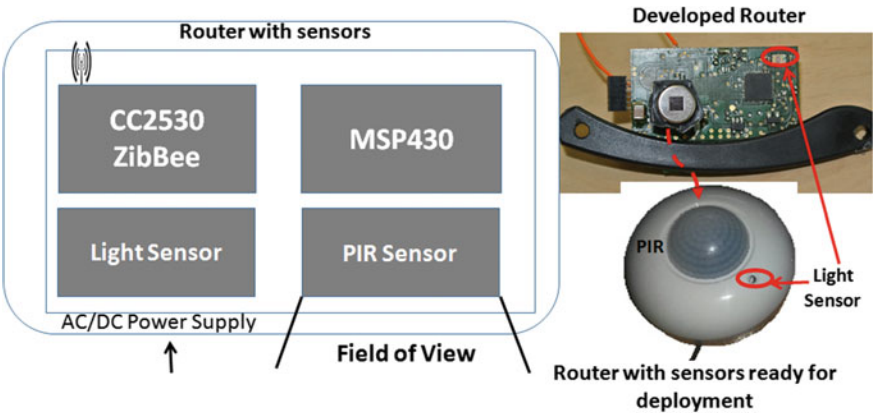

Fig. 3 Architecture of the sensor node designed. The node works also as a router of the Zigbee network [2]

on the light intensity, and (iii) send the control configuration to the panels that are assigned under its control during the network configuration.

2.3 *Base Control Station*

The base control station is the hub of the proposed system as it allows the visualization of the lighting system and the setting of important parameters such as the users' preferences. The role of the coordinator is only to manage the network and allow the user interface through a remote host (Fig. 4). Thanks to the interface and the remote host, it is possible to set the users' preferences, and monitor the whole network and store all the data to evaluate the power saving.

3 Experimental Results

The system was designed, implemented and deployed in a real office testbed to evaluate the benefits in terms of energy saving. Separate groups of LED panels were deployed in separated areas controlled by the sensors device. Although the entire area can be set with different users' preference, we set a default value to 600 lx, which is a standard value for office light. The wireless system has been run continuously for 12 months and the all the data of dimming value and power consumed by panel were stored in a database. Figure 5 shows the average power saving and consumption of 6 months for all the monitored LED panels in the office deployment. The data were compared with an office scenario without the smart control and the energy saving was from 60 % in October up to 70 % on May.

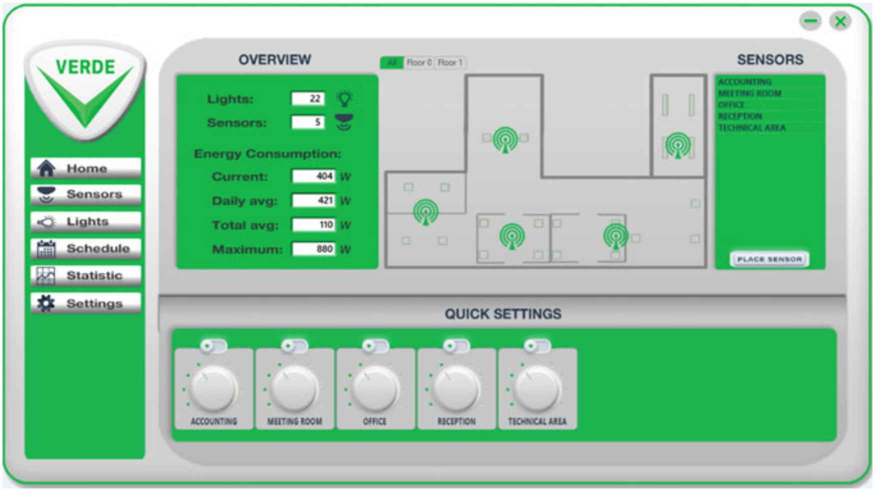

Lights: 22

Sensors: 5

Energy Consumption:

Current: 404 W

Daily avg: 421 W

Total avg: 110 W

Maximum: 880 W

Fig. 4 User interface to manage the whole system network and the preferences. The user interface has been developed in collaboration with Verde LED

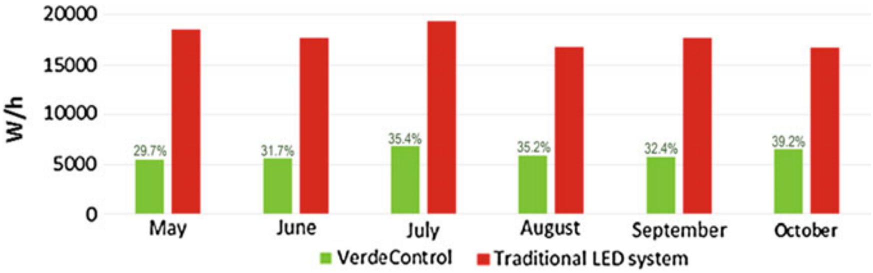

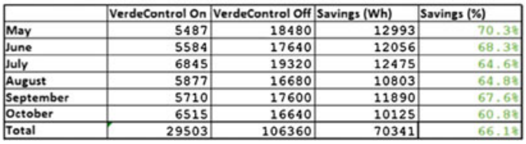

	VerdeControl On	VerdeControl Off	Savings (Wh)	Savings (%)
May	5487	18480	12993	70.3%
June	5584	17640	12056	68.3%
July	6845	19320	12475	64.6%
August	5877	16680	10803	64.8%
September	5710	17600	11890	67.6%
October	6515	16640	10125	60.8%
Total	29503	106360	70341	66.1%

Fig. 5 Energy saving and comparison with a system without smart control during 6 months

4 Conclusions

In this paper we presented the long term in-field evaluation of a novel smart lighting control system which has been designed and developed using a ZigBee network. The system has as main goal to be unobtrusive, low power, low cost, easy to be installed and scalable. Experimental results in a real office during several months show the developed systems is able to introduce up to 70 % power savings over the same system without control. Due to the ZigBee communication protocol would be possible to cover huge deployment and future work will be focus on the scalability of the system deploying it in bigger buildings with more than 1000 devices.

Acknowledgments This work was supported by "Transient Computing Systems", SNF project (200021_157048), by SCOPES SNF project (IZ74Z0_160481), and by ETHZ Grant funding.

References

1. Caicedo, D., Pandharipande, A.: Distributed illumination control with local sensing and actuation in networked lighting systems. IEEE Sens. J. **13**(3), 1092–1104 (2013)
2. Magno, M., Polonelli, T., Benini, L., Popovici, E.: A low cost, highly scalable wireless sensor network solution to achieve smart LED light control for green buildings. Sens. J. IEEE **15**(5), 2963–2973 (2015)
3. Singhvi, V., Krause, A., Guestrin, C., Garrett, J.H., Matthews, H.S.: Intelligent light control using sensor networks. In: Proceedings of ACM International Conference Embedded Networked Sensor Systems, SenSys'2005, San Diego, CA, USA, pp. 218–229. 2–4 November 2005
4. Kerhet, A., Leonardi, F., Boni, A., Lombardo, P., Magno, M., Benini, L.: Distributed video surveillance using hardware-friendly sparse large margin classifiers. In: Advanced Video and Signal Based Surveillance, 2007. AVSS 2007. IEEE Conference on, pp. 87–92. 5–7 Sept 2007
5. Magno, M., Tombari, F., Brunelli, D., Di Stefano, L., Benini, L.: Multi-modal video surveillance aided by pyroelectric infrared sensors. In: Workshop on Multi-camera and Multi-modal Sensor Fusion Algorithms and Applications-M2SFA2 2008 (2008)
6. Şuşu, A.E., Magno, M., Acquaviva, A., Atienza, D., De Micheli, G.: Reconfiguration strategies for environmentally powered devices: theoretical analysis and experimental validation. In: Transactions on High-Performance Embedded Architectures and Compilers I, pp. 341–360. Springer, Heidelberg (2007)
7. Magno, M., Spagnol, C., Benini, L., Popovici, E.: A low power wireless node for contact and contactless heart monitoring. Microelectron. J. **45**(12), 1656–1664 (2014)
8. Jeličić, V., Magno, M., Paci, G., Brunelli, D., Benini, L.: Design, characterization and management of a wireless sensor network for smart gas monitoring. In: Advances in Sensors and Interfaces (IWASI), 2011 4th IEEE International Workshop on, pp. 115–120. IEEE (2011)
9. Srbinovski, B., Magno, M., Edwards-Murphy, F., Pakrashi, V., Popovici, E.: An energy aware adaptive sampling algorithm for energy harvesting WSN with energy hungry sensors. Sensors **16**(4), 448 (2016)
10. Jeličić, V., Magno, M., Brunelli, D., Bilas, V., Benini, L.: An energy efficient multimodal wireless video sensor network with eZ430–RF2500 modules. In: Pervasive Computing and Applications (ICPCA), 2010 5th International Conference on, pp. 161–166. Maribor (2010)
11. Wen, Y.J., Granderson, J., Agogino, A.M.: Towards embedded wireless-networked intelligent daylighting systems for commercial buildings. In: Proceedings of the IEEE International Conference on Sensor Networks, Ubiquitous, and Trustworthy Computing, SUTC'2006, Taichung, Taiwan, 5–7 June 2006
12. Park, H., Srivastava, M.B., Burke, J.: Design and implementation of a wireless sensor network for intelligent light control. In: Proceedings of the 6th International Symposium on Information Processing in Sensor Networks, IPSN'2007, Cambridge, MA, USA, 25–27 April 2007

13. Hong, S.H., Kim, S.H., Kim, J.H., Kim, Y.G., Kim, G.M., Song, W.S.: Integrated BACnet-ZigBee communication for building energy management system. In: Industrial Electronics Society, IECON 2013—39th Annual Conference of the IEEE, pp. 5723–5728, 10–13 Nov 2013
14. Baronti, P., Pillai, P., Chook, V.W., Chessa, S., Gotta, A., Hu, Y.F.: Wireless sensor networks: a survey on the state of the art and the 802.15.4 and ZigBee standards. Comput. Commun. **30**(7), 1655–1695 (2007)

A Low-Cost, Open-Source Cyber Physical System for Automated, Remotely Controlled Precision Agriculture

**Davide Cimino, Alberto Ferrero, Leonardo Queirolo,
Francesco Bellotti, Riccardo Berta and Alessandro De Gloria**

Abstract The paper presents a low-cost solution to the problem of remote control in agricultural applications. This choice is due to the growing importance of agriculture in modern times and so to the need of subsidizing this field. Keeping in mind the constraint of low-cost, we propose the design of a flexible embedded system architecture, based on the Arduino and Raspberry platforms, able to support various kinds of remote control tasks in the agricultural field. The goal is to support management of remote cultivations (in greenhouses and/or open-air) by exploiting sensors (e.g., temperature, moisture, radiometers, cameras) and actuators (e.g., motorized windows, irrigators, tools to deploy chemical products) through a mobile app. This approach could improve fertilization and overall planning of the farming activity based on the actual weather and environment conditions. A simple prototype of the proposed system has been successfully tested and results confirm feasibility of the approach both in terms of performance and of costs.

1 Introduction

In the recent years, the agriculture sector has seen a considerable phase of technological development. Electronics technologies are now enabling automatic irrigation fields and greenhouses, where temperature is remotely controlled through motorized windows and convectors. We believe that a next significant step in these open and closed environments would be the implementation of situation recognition and event monitoring/detection, in order to allow a prompt response to events.

D. Cimino · A. Ferrero · L. Queirolo · F. Bellotti (✉) · R. Berta · A. De Gloria
DITEN Department, University of Genoa, Genoa, Italy
e-mail: franz@elios.unige.it

R. Berta
e-mail: berta@elios.unige.it

A. De Gloria
e-mail: alessandro.degloria@unige.it

A. De Gloria (ed.), *Applications in Electronics Pervading Industry, Environment and Society*, Lecture Notes in Electrical Engineering 409,
DOI 10.1007/978-3-319-47913-2_23

Significant examples in this direction could involve detection of cultivations devastated by the passage of animals, or identification of diseases in plants.

In such applications areas, we expect that employment of leading-edge electronic technologies could be particularly beneficial, especially for large territories with low population density, in extreme environmental conditions. Cyber physical systems—interconnected systems of physical and computational components able to interact with the physical environment through sensors and actuators—represent a possible conceptual and operative framework for tackling this issue.

The main aim of this project is to study a low-cost solution for remote control in agriculture. This choice is due to the growing importance of agriculture in modern times and so to the need of subsidizing this field. In this project, keeping in mind the constraint of low-cost, we propose the design of a flexible embedded system architecture able to support various kinds of remote control tasks in the agricultural field. The goal is to offer the possibility of managing remote cultivations (in greenhouses and/or open-air) by exploiting sensors (e.g., temperature, moisture, radiometers, cameras) and actuators (e.g., motorized windows, irrigators, tools to deploy chemical products) directly through a smartphone app. This approach could allow controlling irrigation at different times of the day, optimizing fertilization and overall planning of the activities based on actual weather and environment conditions.

The main innovation proposed by our work consists in the fact that the platform is entirely based on low-cost electronic components assembled on open system architectures. These architectures, typically based on Arduino and Raspberry, have become ever more popular and used by embedded systems in several application areas. Moreover, being based on low cost electronics, the system is easily usable by small-sized company, which couldn't afford high level technology systems.

2 Related Works

Several projects, mostly based on wireless sensor networks (WSN) have been recently developed in order to monitor a terrain's parameters and make them available on a platform accessible by several users. References [1–4], for instance, provide very efficient WSN able to monitor entire cultivated fields, thanks to cellular telephony gateways and to Information Monitoring Systems able to display data on a web application. Other solutions, like [5], apply and implement in the agriculture sector the innovative and useful concept of Wireless Underground Sensors Network (WUSNs) which consist of a Zigbee-based network which nodes operate below the ground surface. Finally, mobile devices are employed in some of the latest projects, like [6].

References [7, 8] are advanced, complete systems that do monitor environmental parameters and implement a closed-cycle control system in which the actuators are controlled on the basis of values read by sensors. However, [7] still misses a complete Human-Machine Interaction sub-system, while [8] is just a theoretical solution.

Several companies have recently developed drone-based systems aimed at capturing images at different wavelengths in order to provide a constant overview the physical and chemical conditions of the terrain. Different types of camera-equipped drones are already available on the market (e.g., from Precision Hawk, senseFly, Agribotix), that take medium-high resolution pictures (up to 20 MP) in various regions of the electromagnetic spectrum, mostly in the visible and Near Infrared (NIR) fields.

Generally speaking, all the existing solutions present some common features. Besides allowing programming the flight-plan through a graphical interface (at different levels of detail) and choosing the sensors to use, the cited drones are always supplied with a data analysis software that computes important figures, such as, for instance, the crop water stress index (CWSI) and the normalized difference vegetation index (NDVI). However these systems tend to be quite expensive, redundant and complex to use being priced around 5000–10,000 € and going into a too deep scientific detail.

Another interesting system is under development by the Spanish Agroptima start-up. This system does not involve hardware components such as sensors and actuators but provides an excellent graphic interface for field cataloguing and management and irrigation and fertilization planning. Finally, Agrodron has been designed in view of fighting parasites and is thus optimized for spraying activities over plantations.

3 System Architecture

The proposed system architecture consists of three main parts, as depicted in Fig. 1. The first one involves the devices that will be deployed in the field to monitor the parameters and make a first, minimal control of the actuators. These devices can be of different kind, e.g., dedicated to a greenhouse, to an open air field, or just consisting of a monitoring drone. The second component is a central device with a database, used to store information. The Central Unit (CU) manages the information traffic between all the sensors and the user devices and performs strategy-level decision. The third block is a mobile app, implemented on a smartphone, for remote control. The communication is performed at application level (HTTP protocol) on one side and at transport level (TCP protocol) on the other side. The infrastructure can been seen in Fig. 1.

The architecture is based on low-cost components, mostly based on the Arduino and Raspberry platforms. These platforms implement the concept of open-source embedded systems, that we consider highly important in order to give the proposed system an added-value based on the versatility and on the ease-of-use aspects of the system. Moreover, the mentioned platforms are now ever more widespread thanks to their versatility in terms of attachable sensors and actuators and supported by

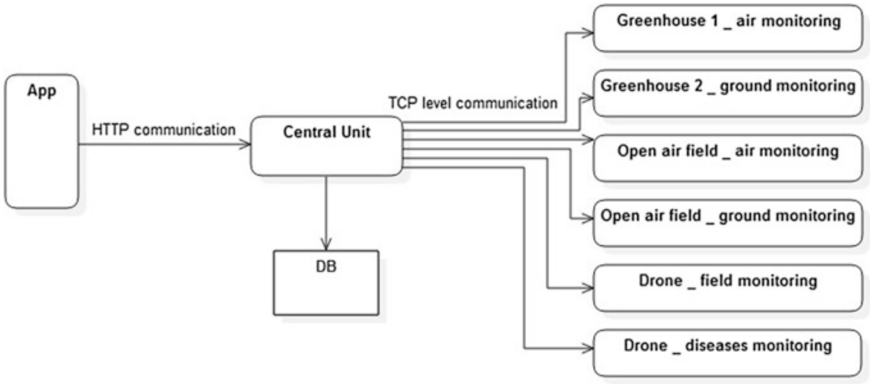

Fig. 1 System architecture. It's possible to notice the app (on the *left*), the CU (in the *center*) and the field devices (on the *right*)

quite an active community of developers. Available sensors span a wide variety of typologies (e.g., temperature, air and terrain moisture, photocells, anemometers, rain gauges and more complex devices such as RGB, infrared and thermal cameras) and of cost and precision ranges. Finally the main task of this paper is to underline the possibility to develop a high level automation system with costs, precision and number of applications however acceptable, even if not comparable to commercial systems' ones. We believe that this is a key factor to support continuous development and improvement.

3.1 Field Devices

Field devices have to be positioned in the cultivated field, with the goal of monitoring the environment. Here, the Arduino architecture, with a microcontroller equipped with easily pluggable sensors and actuators looks an effective and promising solution.

Information from the sensors is typically transmitted to a remote control station, for data integration and human control. However, every device is organized for a first degree of autonomy, being able—at a tactical level of decision making—to operate on actuators, heaters, windows, lighting, irrigation, fertilization, etc. This allows establishing a first closed-cycle system control, which is useful for simple tasks. Such basic first autonomy level could consist of a closed-loop control on temperature range (controlled with convectors and windows) or of the monitoring of activity time, in order to give advices to the user when a high cost is being reached. An example of a good monitored tactical autonomy level can be found in [9]. This autonomy, despite limited, allows decentralizing computation, reducing the computational load of the CU and increasing the overall system's robustness.

A minimal graphic user interface and pushbutton can be added on any device to allow management independent of the CU.

Every device communicates with the CU through a mesh network (which is the best network configuration for this kind of applications, as in [10]), and on the other side periodically asks about the status of the sensors, or updates internal parameters. The device also alerts the CU when sensed data are outside the typical ranges.

Field devices may be deployed also on drones, especially to supervise large fields and spray fertilizers. A drone would receive from the CU commands on the mission and provide back reports and measures (from cameras and other sensors).

A field device is typically implemented on an Arduino-based system. This choice has been made in order to propose an open-source system that is easily configurable. Particularly, after purchasing an Arduino board with relative shield and downloading the firmware the user already has a ready-to-use system that can be positioned in the greenhouse/open-air field and connected to the network. Moreover, the purchase of an Arduino system involves considerably low costs, which represent a crucial aspect to support continuous development and improvement of the system.

3.2 Central Unit

The CU is mainly responsible for the communication between the mobile app and the field devices. According to the Service Oriented Architecture (SOA) paradigm, the unit hosts a web-server that exposes a set of REST-web services easily accessible by any kind of clients. The client's HTTP request is then translated into a TCP/IP request, that is without any superior level, that allows the CU to communicate with the field devices, which will be provided with a TCP/IP interface (usually a special shield). Within this last communication the server-client roles are not fixed and depend on the application, although a bidirectional (not hierarchical) communication is often desirable.

The CU also will implement a database with the chronology of the measures, events and requests. This allows periodic back-ups, increasing robustness in case of faults, besides being an important data source for a statistic analysis.

The CU also is able to perform a second level control that could involve several field devices to perform a multivariable closed-loop control. Although the human represents the main decision maker, indeed, the CU also hosts a series of machine-learning based algorithms that are used to perform some kind of high level analysis. This kind of analysis will be better explained in the next chapter.

The CU is typically implemented on a Raspberry system. This choice is due, on one hand, to the necessity of a computer-based board with enough computational capabilities to host an http server (therefore running an OS), on the other hand, for achieving a small-sized embedded system that could be easily positioned and configured to operate as a gateway node. Moreover, the choice of an open-source easy-to-use computational unit allows the user to benefit from the web community in terms of new OS, more efficient machine-learning algorithms, innovative applications etc.

3.3 Mobile App

The mobile app is the graphical interface through which the user can observe the status of the system, input commands and receive feedback. The app is designed in order to optimize the user experience and allow an easy and detailed control on all the system.

4 Prototype Implementation

We are developing the system architecture in a prototype aimed at evaluating functionalities and performance. The current implementation involves four main modules: greenhouse control device, drone simulator, CU, mobile app.

The greenhouse control device is implemented on platform with an Arduino Uno board with an Ethernet shield. Connected to the microcontroller are internal and external temperatures sensors, a heating convector, an engine for opening/closing a window, an Lcd display to show values and push buttons for parameter setting. The program implements the communication protocol towards the CU, allowing the Arduino Uno shield to manage the TCP/IP requests from the CU. It also implements a closed-loop, that performs a first level control; the system keeps the internal temperature within the set range, turning on a convector if the temperature drops or opening a window through pulleys if the temperature rises too much. A simple hysteresis is implemented in order to avoid oscillations around the threshold values. The system tracks the min and max temperatures and the heating activity time, in order to allow checking the consumptions. Figure 2 shows an Activity Diagram that shows the field device's behavior.

The use of drones can be evaluated considering that recent technologies allowed drones to perform in-depth plantation health analysis and fertilizers spraying. These two applications have been simulated using an Arduino board, for prototyping requirements. The Arduino board simulates the reception of parameters (e.g., GPS coordinates, field's shape) and the information about the on-board instrumentation. In our prototype the drone is supposed to piggyback two cameras (one in infrared and one in visible), and a fertilizer spraying system. The drone is also supposed to perform a first basic-level analysis, calculating useful indexes (NDVI and CWSI). The simulation board monitors all the received instructions on an LCD screen.

The CU is implemented on Raspberry, hosting Tomcat, a Java open source application server managing servlet life-cycle. The server forwards HTTP requests from mobile clients to the field devices. In the present implementation, a basic machine learning algorithm provides the CU with some sort of intelligence.

In the present implementation, the CU acts like an intermediary between the mobile application and the field device, translating messages from the incoming protocol (HTTP) to the protocol used with the field devices (TCP). The translation is performed simply by coding the communication phases of the TCP protocol (opening connection, managing input and output streams, parsing messages) into

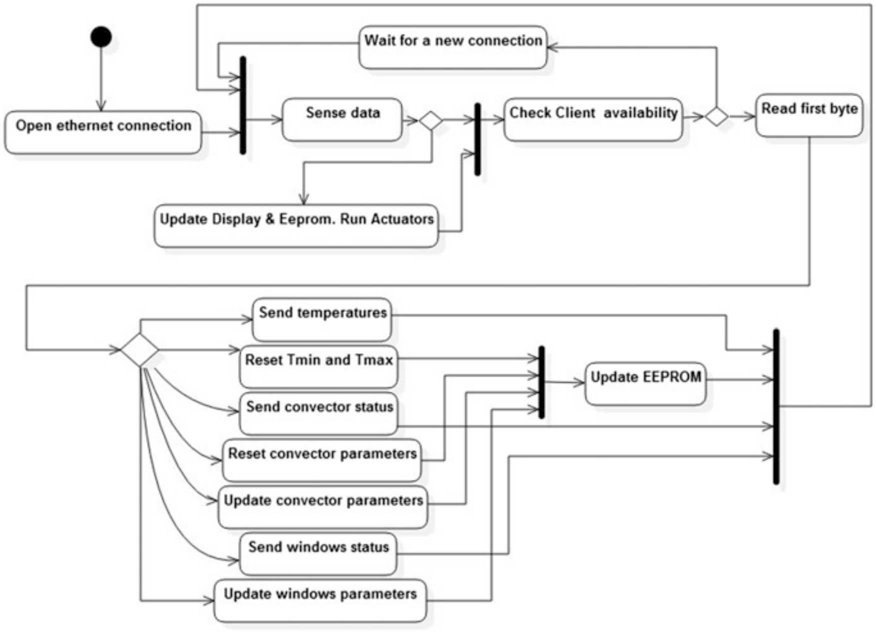

Fig. 2 Greenhouse device behaviour. The field device performs the loop, sensing data and answering client requests

the servlet exposed by Tomcat. The servlet receives the parameters via a GET or POST request, opens the TCP request to the field device, waits for the completion of the field devices task, receives a response and returns immediately, returning a response string to the mobile application. Figure 3 shows an Activity Diagram of Raspberry's behavior.

A more important role that is played by the CU is the second-level decision maker role. The CU implements a set of machine-learning based algorithms in order to be able to take second-level importance decision, where the first level of automation was implemented by the field devices. Particularly, the CU will be able to understand the hysteresis of soil temperature under different soil moisture and fertilizer in solar greenhouse conditions, as in [11].

The mobile app is implemented on Windows Phone. It features a simple graphical user interface, that allows setting the context and the preferences, checking the environment's status and inputting commands. Going slightly deeper into the mobile app operative phase we can identify the main user page, where a list of all the user's active cultivations is presented. This list has been thought to provide the user with a complete overview about all his work and a status flag that indicates the health conditions of the plantation. By selecting each cultivation, the user can see all the desired parameters, from greenhouse temperature to terrain moisture level, in order to thoroughly understand the physical conditions of his

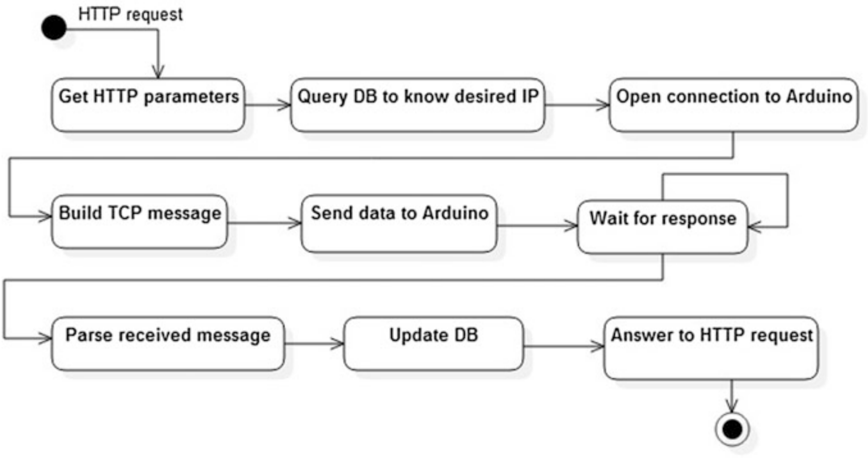

Fig. 3 CU behaviour. Following the http requests, the CU interacts with the DB, communicates with the field devices and finally answers to http requests

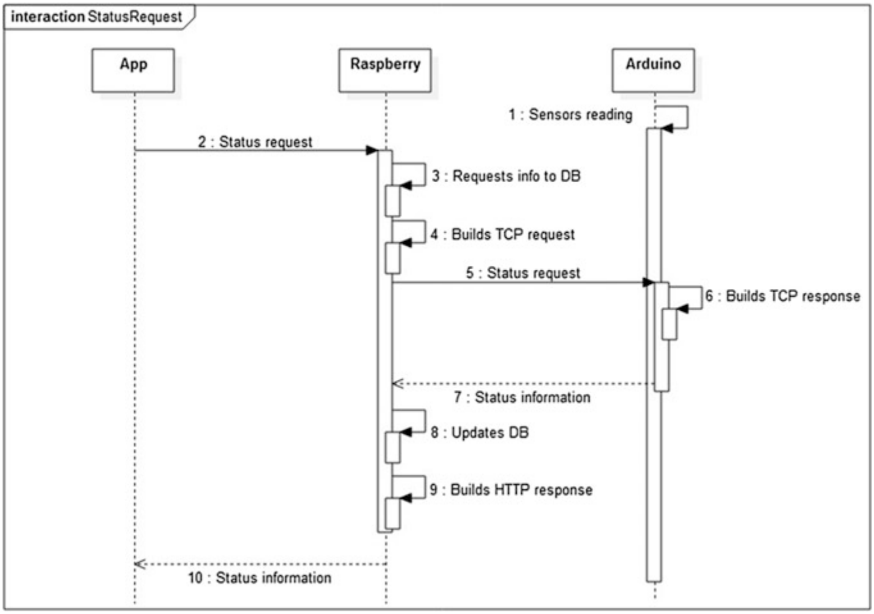

Fig. 4 Example of a status request. The app communicates with Arduino through Raspberry, in order to check the sensors status

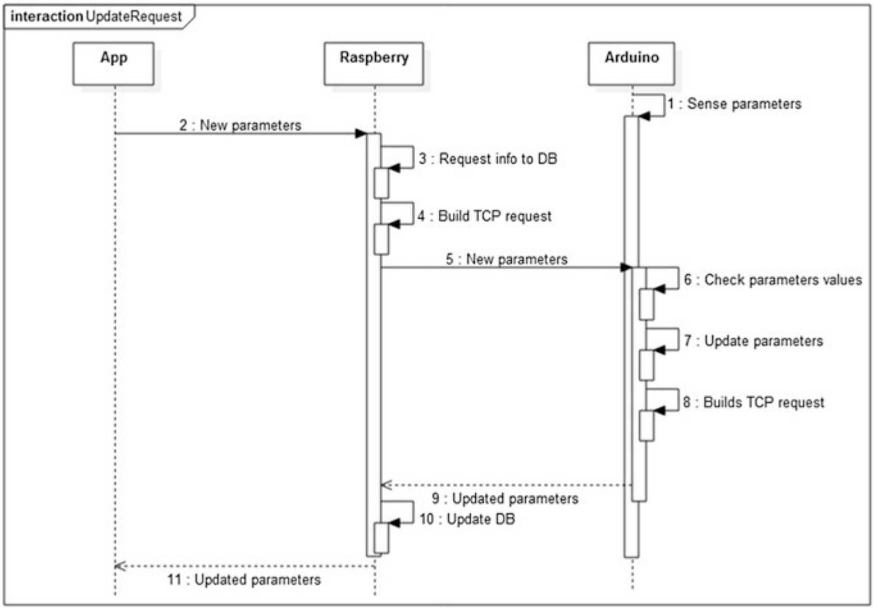

Fig. 5 Example of a update request. The app imposes new parameters to be set on the Arduino

cultivation. Moreover, the user is able to visualize statistics and graphs of the time trend of his plants' health conditions.

From this first list, through a button the user can add a new cultivation to his list. The app will then guide the user through the configuration of a new cultivation area, keeping saved all data relative to a certain cultivation: cultivated specie, quantity of cultivated plants, scheduled harvesting date, with the aim of helping the farmer to better organize his work. It will also monitor any kind of danger deriving from the CU information, such as not responding sensors, abnormal situations etc.

From a system point of view, we can consider two main and request flows in the system. The first one, showed in Fig. 4, shows the Status Request, which represents the messages exchanged in order to know the status of a particular Arduino board sensors. The second one, showed in Fig. 5, consists of an Update Request, which better explains the request flow when the user needs to update some parameters on the Arduino board.

5 Decision Levels

As the system's nature involves mixed nature variables, such as temperature, humidity, fertilizers, as well as actuator's data such as coordinates for drones or irrigation scheduled time, it has been necessary to study an autonomy structure on which the functioning of the system could have been based. The system has been studied to be structured on three decision levels. The first two of these levels are autonomy, that means that are supposed to be performed by the system itself, without human intervention.

Particularly, the first autonomy level is based on the single field device and implements the tactical level. A tactical level closed-loop control involves only the physical quantities coming from the environment that a field devices is in charge to monitor (i.e. greenhouse air, open air ground etc.). A good example of tactical level automation, based on a single environment can be found in [9]. In our case, the prototype includes the greenhouse air manager Arduino, which is in charge to conjugate user settings with rules that are defined on the device itself. The present prototype implements a closed-loop that performs a first level control; the system is programmed to manage temperature and humidity variations and to monitor consumption due to convector activity. This first control level is useful to decentralize the responsibility of the system towards the leaf nodes, in order to make the central system independent from the field events, letting it focus on higher degrees of autonomy (strategic level).

The second autonomy level is based on the CU and implements the strategic level. As such, it is concerned by the need to perform a multi-environment analysis, which takes into consideration temperature, humidity, fertilizers and some info given as input during the cultivation initialization phase, such as cultivation specie, scheduled harvesting period etc. This kind of decision can be taken only having a complete view on all the field subsystems and all the considered environments. For example, the CU could consider to combine data deriving from the greenhouse sensors (temperature, humidity) with the information already present on itself (cultivated specie) to tune the fertilizers application period, in order to optimize consumptions. In the same way it could detect the presence of plant diseases (evaluating humidity and photos), in order to treat them properly.

The third decision level is delegated to the user, who can turn on or off any actuator. The user is also provided with a complete information framework, which indicates all the preferable treatments for each product, in order to maximize production and quality.

6 Results

Results are still qualitative, and concern the validation of the functioning of the system, that is achieved through the testing of all the functions exposed by the system through the mobile app. For what concerns the greenhouse monitoring Arduino and the drone simulator, the list of the functionalities includes:

- Request of the status of the temperature sensors
- Update of the sensors' temperature thresholds
- Reading, recording and resetting the minimum and maximum temperature values
- Request of the status of the windows

- Request of the status of the heating system (also including activity length)
- Request of immediate take-off of the drones, with related flight-path instructions.

Verification also involved the communication infrastructure. The functioning of the closed-cycle control loop in the field devices has been tested as well.

Overall, the most interesting result of the proposed system consists in its versatility. In particular, the system is easily extensible by plugging different field sensors (open and closed environment, drones for monitoring and for spraying fertilizers, etc.), that can be seamlessly integrated. The user will only need to purchase a new device, equipped with its communication shield, and reconfigure the CU to manage requests from the new device, without intervening in the mobile app or the field device firmware. The mobile app will be consequently upgraded online.

7 Costs and Maintenance

The presented solution, as seen previously, has been conceived to consider all the user-friendly, open-source, low-cost solutions nowadays offered from the market. This choice has been done to maximize versatility, efficiency, ease-of-use, and so without pushing off the scientific state of the art. The main reason for this is to allow the user to move some of the functions that he would have been forced to do manually on the top of his hand, enabling him to perform tasks simply by pressing buttons.

If we consider that an Arduino board costs about 20 €, an Arduino Ethernet shield (used for prototyping) is about 20 €, an Arduino LCD shield costs 10 € and a Raspberry Pi costs about 40 €, we can clearly see that the expected costs are extremely low, especially if compared to commercial systems, which costs usually goes around 1000 € minimum. Obviously commercial systems are equipped to perform deeper analysis (such as to detect the presence of interesting elements in terrain's chemical composition), but we think this kind of technology could often enhance the amount of work a farmer would end up carrying out, as the systems often provides a complex interface, not easy to understand without a specialized course.

The system's maintenance is not expected to be unmanageable. Certainly, it depends on the field conditions and the sensors position within the field (if sensors are buried it will be necessary to design a special case for preventing the system's failure caused by an excessive moisture). In case of hardware/software system updates, the mobile app will be updated with an online update, which will be extremely simple for users. The field devices will be purchased as new, so the user is not involved in configuring the hardware, being this entirely configured from producers. The only system that will need an ad-hoc update will be the CU, which will need to account for the new network configuration, managing the new network nodes and implementing the new communication protocol.

8 Conclusions and Future Work

In this work we have presented a component-based cyber physical system for agriculture. A simple prototype of the proposed system has been successfully tested through the exchange of instruction between the various units. Results confirm feasibility of the approach both in terms of performance and of costs.

The system has been ad-hoc designed to be low cost, especially for small entrepreneurs. Obviously this low cost characteristic is coupled with the open source feature, which allows every farmer to become familiar with the system in a short time.

A major feature consists in the modularity and extensibility of the architecture. At present the system implements a simple algorithm for irrigation planning. We are now enhancing the system by adding capabilities to the CU. Future works, that could be done by us or other parties, include the following: sensor fusion for semantically interpreting the signals from drones and other sensors deployed in the field, drone flight path planning (for instance for monitoring the status of a plant's disease), classification and regression algorithms to support agricultural decision making. The drone's control board may also include processing capabilities for monitoring presence of chlorophyll and copper, air moisture level and presence of weed in the field. In this way, the CU would receive pre-processed data, thus focusing on sensor fusion and higher-level artificial intelligence. On the mobile app side, we plan to extend user interaction by supporting information cataloguing and intervention planning.

The main expected benefits concern the possibility of performing remote architecture operations with a low cost system implementation, reducing the need for human physical presence (while the system is always manageable by people through mobile apps) and enhancing timeliness of response to events.

References

1. Wang, Y., Wang, Y., Qi, X., Xu, L.: OPAIMS open architecture precision agriculture information monitoring system. In: Proceedings of ACM CASES (2009)
2. Pande, M., Choudhari, N.K., Pathak, S.: Energy efficient hybrid architecture and positioning of sensors in WSN for precision agriculture. In: Proceedings of the ACM CUBE International Information Technology Conference (2012)
3. Abu, M.A., Yacob, M.Y.: Development and simulation of an agriculture control system using fuzzy logic method and visual basic environment. In: Proceedings of IEEE ROBIONETICS (2013)

4. Lim, W., Torres, H.K., Oppus, C.M.: An agricultural telemetry system implemented using an Arduino-Android interface. In: Proceedings of HNICEM (2014)
5. Silva, A.R., VuranI, M.C.: $(CPS)^2$ Integration of center pivot systems with wireless underground sensor networks for autonomous precision agriculture. In: Proceedings 1st ACM/IEEE International Conference on Cyber-Physical Systems, CCPS ACM (2010)
6. Yoo, S.-E., Kim, J.-E., Kim, T., Ahn, S.: A^2S: automated agriculture system based on WSN. In: IEEE International Symposium on Cyber Physical Systems, ISCE (2007)
7. Nandurkar, S.R., Thool, V.R., Thool, R.C.: Design and development of precision agriculture system using wireless sensor networks. In: Automation, Control, Energy and Systems (ACES), 2014 First International Conference on Cyber Physical Systems (2014)
8. Bing, F.: Research on the agriculture intelligent system based on IoT. In: Image Analysis and Signal Processing (IASP), 2012 International Conference on Cyber Physical Systems (2012)
9. Rani, M.U., Kamalesh, S.: web based service to monitor automatic irrigation system for the agriculture field using sensors. In: ICAEE (2014)
10. Rani, M.U., Kamalesh, S.: energy efficient fault tolerant topology scheme for precision agriculture using wireless sensor network. In: Proceedings of ICACCCT (2014)
11. Lin, X.-J., Liang, Y.-L., Wei, Z.-X.: Hysteresis of soil temperature under different soil moisture and fertilizer in solar greenhouse conditions. Afr. J. Biotechnol. (2011) doi:10.5897/AJB10.2447

Assessment of Driver Behavior Based on Machine Learning Approaches in a Social Gaming Scenario

Gautam R. Dange, Pratheep K. Paranthaman, Francesco Bellotti, Marco Samaritani, Riccardo Berta and Alessandro De Gloria

Abstract The estimation of user performance analytics in the area of car driver performance was carried out in this paper. The main focus relies on the descriptive analysis with our approaches emphasizing on educational serious games, in order to improvise the driver's behavior (specifically green driving) in a pleasant and challenging way. We also propose a general Internet of the Things (IoT) social gaming platform (SGP) concept that could be adaptable and deployable to any kind of application domain. The social gaming scenario in this application enables the users to compete with peers based on their physical location. The efficient drivers will be awarded with virtual coins and gained virtual coins can be used in real world applications (such as purchasing travel tickets, reservation of parking lots, etc.). This research work is part of TEAM project co-funded within the EU FP7 ICT research program.

G.R. Dange (✉) · P.K. Paranthaman · F. Bellotti · M. Samaritani · R. Berta · A. De Gloria
DITEN, University of Genoa, Via Opera Pia 11A, 16145 Genoa, Italy
e-mail: gautam.dange@elios.unige.it

P.K. Paranthaman
e-mail: pratheep.paranthaman@elios.unige.it

F. Bellotti
e-mail: franz@elios.unige.it

M. Samaritani
e-mail: Marco.Samaritani@elios.unige.it

R. Berta
e-mail: riccardo.berta@elios.unige.it

A. De Gloria
e-mail: adg@elios.unige.it

A. De Gloria (ed.), *Applications in Electronics Pervading Industry, Environment and Society*, Lecture Notes in Electrical Engineering 409,
DOI 10.1007/978-3-319-47913-2_24

1 Introduction

The driver behavior has the direct impact on all the factors that are concerned to efficient driving characteristics such as the road safety, fuel efficacy or the reasonable driving patterns. Also let it be the fatalities or vehicle collisions, it is again a genesis from the behavior of the driver [1, 2]. As the driver behavior holds a significant role in modeling the safe and green driving patterns, there are many models that are emerging under this roof. Providing necessary coaching to drivers under simulated environments would act as a test bed to facilitate the process of designing various safe driving methodologies [3]. Other approaches would be the prior and post analysis of driver behavior with reference to the impact [4, 5], by predicting the outcomes and adjusting the current behavior. The experiment conducted by [6] comprised of 3D auditory display to reduce the eye-off-road time by using spatial localization and sound messages. However there is a mild patch between the simulation and real-world entity, most of the simulated results have to be adjusted to cope with the real-world situations. These safety and efficient driving measures must be approached from the perspective of system design [2], where the modeling must accommodate the dynamic environment.

The major aim of our project is to inculcate the better driving practices using driver behavior evaluation and social gaming scenario. This research activity was carried as a part of TEAM (Tomorrow's Elastic Adaptive Mobility) project [7]. For the real time evaluation, we have collected the vehicle signals from the test run conducted by Centro Ricerche Fiat (CRF) [8] and the test site was located around the CRF office in Trento, Italy. As a viewpoint of our approach, the competitive gaming scenario would induce a good conduct in driving pattern and the evaluators used would ensure that the proper driving behavior is exhibited. As the evaluators are comprised of four different approaches such as Linear Distances to categorize the harsh and smooth driving patterns, Kohonen Neural Networks to map the event-based behavior and K-Nearest Neighbor approach to plot the relativity between the vehicle signals and to penalize the harsh behaviors attempted by the drivers. The Dynamic Sliding Window captures the deviation from optimal level and tracks the harsh events. Therefore the evaluators are designed to analyze various driving styles and fit to the dynamic environment.

2 Related Work

When designing a driver behavior model there are many aspects that are taken into account such as data acquisition tools equipped with the system, extraction of vehicle signals based on the dynamics and most importantly the evaluation methods (algorithms) to process and analyze the vehicle signals to estimate the performance of the driver. Estimation of driver behavior is always a topic of interest in vehicle research sector, out of which we had handpicked certain approaches from state-of-art related to our work and they are as follows.

To estimate the performance of the driver, [9] conducted an experiment involving in acquiring the time-series steering angle data during the lane changes by the driver. The experimental setup was under a controlled simulated environment and driver behavior model was designed using conditional Gaussian model on Bayesian network and there was also a comparison along with traditional Hidden Markov Model. The final reports stated that, there were some minor problems in predicting the sudden changes in the environment, such as drastic change of steering wheel for dynamic happenings. Another comparison approach performed by [10] involved the estimation of driver behavior model by implementing Gaussian mixture model and piecewise auto regressive exogenous (PWARX). The major task was the car-following approach, where both of the probabilistic models outperformed each other on various occasions, for instance PWARX produced a good prediction in handling the Gas and brake pedal signals compared to Gaussian mixture model. However both of the algorithms performed well for the limited signals, as in the main focus was on gas and brake pedals only.

The different approach that was implemented in car following task using Dirichlet Process Mixture [11]. The outcome stressed on the fact that, the metrics observed from this experiment can be a good step for future analysis in developing context-adaptive system. These are some of the significant probabilistic models on current practice and let's flip the side of the approach and look out the implementation of driver behavior models using machine learning and adaptive algorithms. The ultimate challenge comes only when things are tested on the real-world applications in a rapidly changing environment, on such aspect the experiment [12] carried out by research team, comprised of "UYANIK", a passenger car equipped with multiple sensors and CAN architecture for data acquisition was put up on real–world testing in estimation of driver behavior. This was also a collaborative research conducted by NEDO (Japan), Drive-safe Consortium (Turkey) and the Trans-European Motorway (TEM), Istanbul. Almost the passenger car was equipped with all possible metrics to gather the signal, so as to make the prediction in an enhanced way. Post the data acquisition by CAN-bus, the signals were sent for processing to a SVM (Support vector machines) model, the labelled data were classified by SVM and the results of SVM were forwarded to a Hidden Markov Model (HMM), which performed the final prediction of driver behavior. As the processing involved ample number of input signals, the classification and prediction using the machine learning approach was feasible by the system and the outcomes were formulated in an efficient manner. ANN was used as a major tool to classify the driving styles in various roads in the work carried out by [13]. The analysis of traffic flow is also considered as vital aspect, where the research carried out by [14] provided a good insight in qualitative and performance aspects of Nearest Neighbors regression models. The vehicle signals such as speed, engine RPM and acceleration were extracted and sent to the remote data center, over there the analysis of data is performed by the neural networks. The ANN would categorize the types of roads (urban, suburban and highway) in which the vehicle was navigating and also the characteristics of the driver as well. However there exists various neural networks architectures, but only Multi-Layer Perceptron (MLP) is preferred predominantly [15]. Different architectures of neural networks must be experimented, so as to emerge out with better solutions for the problems in analysis tasks. On the basis of the state-of-art study on various driver behavior modelling algorithms, there are many evident facts in handling the approach, firstly the probabilistic and mathematical models were considerably well on simulated and controlled driving environments and they exhibited a certain amount of error ratios and uncertainty when it came to real-world applications [9], whereas on other side the Machine Learning algorithms had the tendency to adapt to sudden changes in the environment and performed well with viable accuracy on all aspects such as classification, estimation and importantly the prediction. Another significant issue that has to be noted with respect to adaptive algorithms is, the incoming data signals should be more in number, because that particular aspect makes the task of evaluation a better one. It is also necessary for the evaluation parameters to hold the ability to adapt to environments, as most of the implementation happens on real-world applications. So it's always necessary to design the system architecture with reliable model that would facilitate for the varying environments.

3 System Architecture

The major tasks of this approach involves the estimation of driver behavior and to establish a social gaming platform (SGP) to inculcate green driving patterns. The social gaming platform (SGP) comprises of a distributed platform which has three layers: the field devices, the cloud servers and the user personal devices, as displayed in Fig. 1.

Secondly, for evaluating the driver behavior, the vehicle comprises of an OSGi environment [16], where the evaluators and signal receivers are deployed in the OSGi environment as bundles. Vehicle Signals are transmitted over to VDP consumer bundle using VDP APIs in the OSGi framework and from which the signals are assessed by driver performance assessment module (comprises of the four

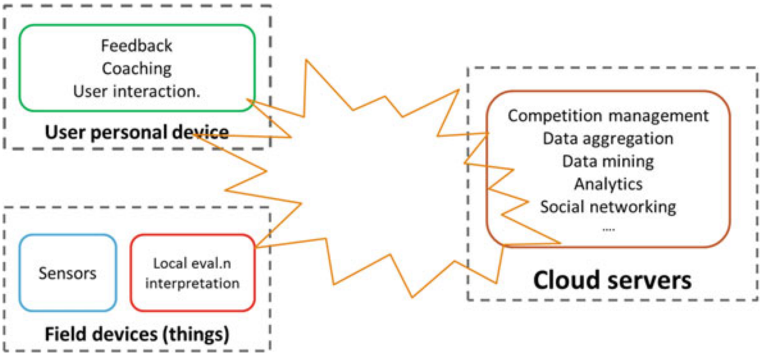

Fig. 1 The IoT social gaming platform concept

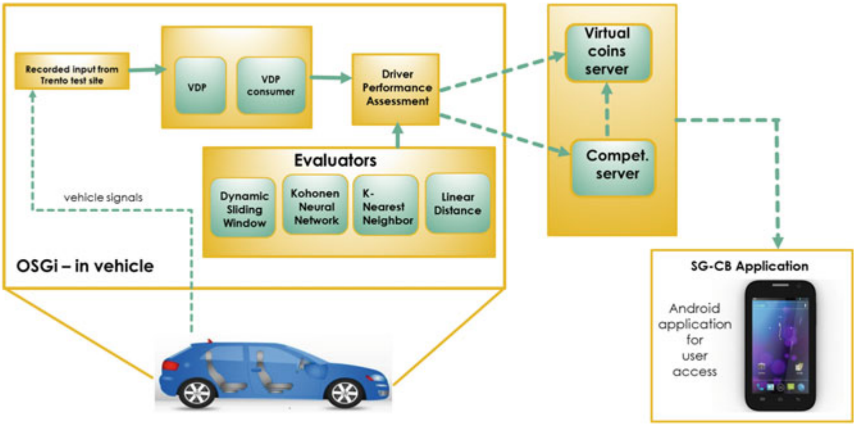

Fig. 2 System overview comprising the entire control flow with the recorded vehicle signals from the test run conducted at Trento, Italy

evaluators) and then the evaluation scores are sent to the cloud servers namely Virtual coins server and competition server and they are updated constantly. The data from the respective servers (virtual coins and competition server) can be accessed using a smartphone application called SG-CB (Serious games and community building) (Fig. 2).

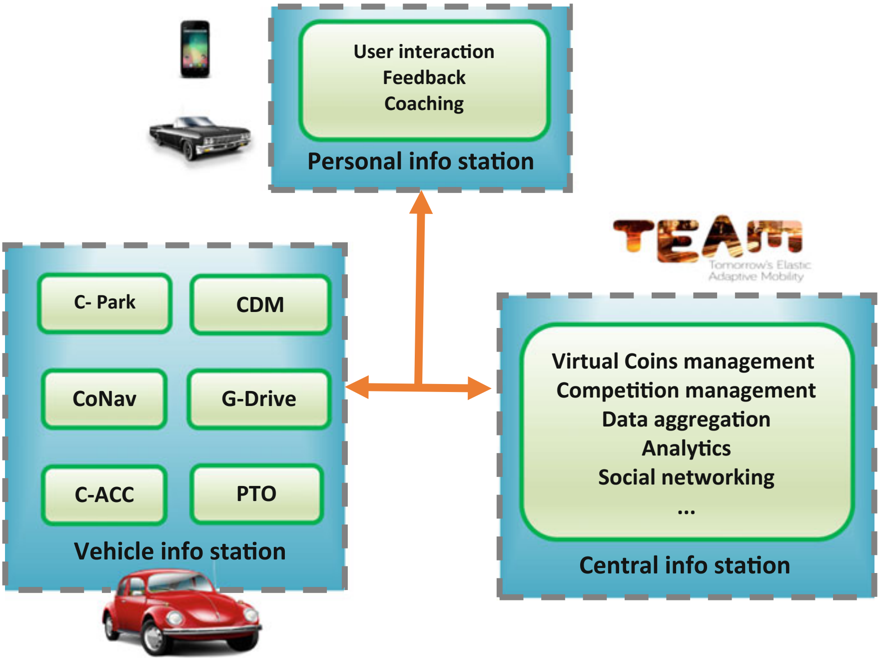

Fig. 3 Application in the automotive domain

In the OSGi environment, the signal values are interpreted from the recorded data and it is transferred to VDP Consumer using VDP APIs. VDP Consumer is another bundle running in OSGi environment, which receives data from Trento bundle and subsequently sends the signals to different evaluator applications, which are running in OSGi environment and have subscribed for signals. Due to this approach of pipelining, the addition of new evaluator would not require any code changes, and modification of the configuration file would do this job.

The internet of the things (IoT) social gaming platform (SGP) in TEAM implementation on automotive domain is illustrated in Fig. 3. Over here the different applications exploiting vehicular and other mobility information contributes to the player performance evaluation, thus enabling the game dynamics.

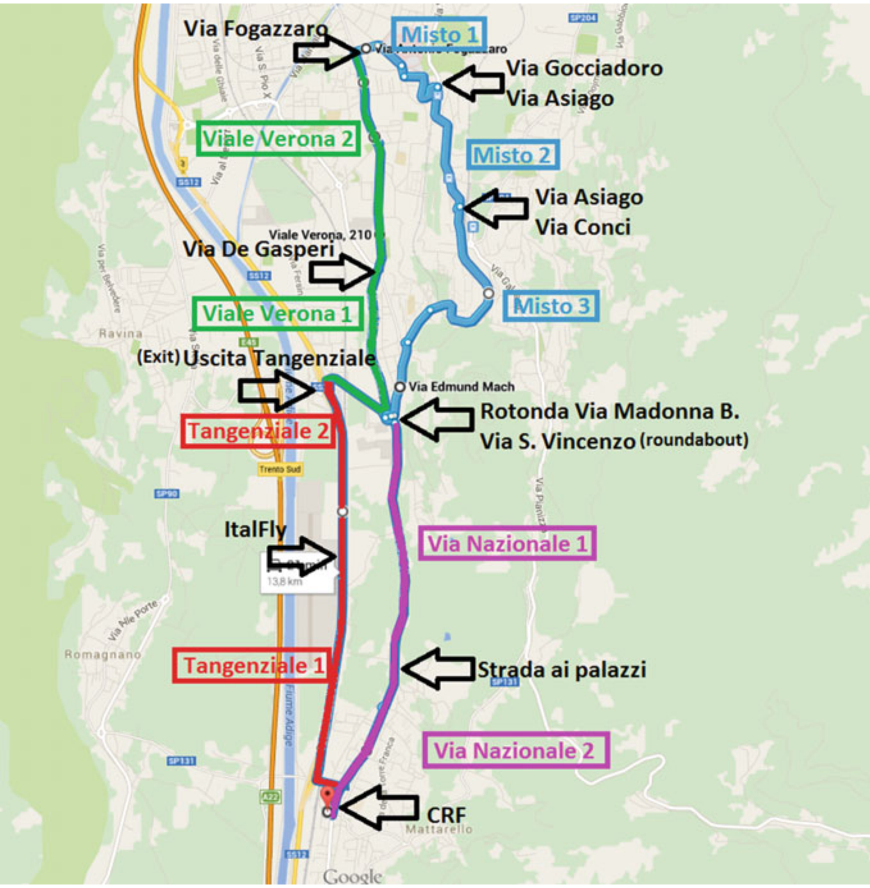

Fig. 4 Map of the test site in Trento, Italy with locations comprising of urban and sub urban zones. The *red* route highlighted on the map is the suburban zone (Tangenziale) and the *green* route is of urban zone (Viale Verona). The *blue* and *purple* routes are the mixture of urban and suburban zones

4 Test Site Description

The test run was conducted by Centro Ricerche Fiat (CRF) and the test site was located around the CRF office in Trento, Italy and the test site comprised of various road segments such as urban, suburban and the mixture of both. The test site was divided into four major zones such as Tangenziale, Viale Verona, Misto and Via Nationale and expands around 13 km, with approximate completion time of the entire run around 28–30 min (Fig. 4).

5 Driver Performance Assessment

The four evaluators used are:

- Kohonen Neural Networks
- K-Nearest Neighbors
- Linear Distances
- Dynamic Sliding Window.

While designing the evaluators for our process, we considered certain metrics to estimate the behavior of driver such as capturing harsh events, mapping the relativity of signals and segmenting the signal patterns to plot the coarse driving behavior. By having all these considerations on ground, we developed four evaluators to handle the metrics stated. When it comes to the issue of processing the large amount of data and capturing the patterns from the given data, the data mining algorithms will be the best tool to handle the circumstance with at most robustness. As our process involves the classification of the raw signals into harsh and smooth patterns based on events, we preferred Kohonen Neural Networks [17], which is a classifier based on unsupervised learning approach and it has the ability to classify the data into clusters without any reference samples. The dynamic sliding window was specifically used to track the harshness in the signal patterns that are ranging continuously without any expeditious changes (such as vehicle speed signal pattern, in which the rise and fall happens gradually). The Linear Distances approach was used to segment the signals based on a thresholding point. Another evaluation metric involves the mapping of relativity between signals and we used K-Nearest Neighbors algorithm to handle the task, here we plotted the harshness by analyzing the conflict between the related signals (Example: Speed vs. Brake).

5.1 Kohonen Neural Networks

The predominant architectures of Neural Networks work on supervised learning approach, but as our classification is not dependent on samples and also the pattern of input signals (Ex: acceleration, RPM and speed) is not constant and varies depending on the drivers, so we preferred an unsupervised learning architecture for neural networks (i.e.) Kohonen Neural Networks. The network architecture consists of two input neurons and two output neurons with the connection weights. The acceleration and brake signals are broken into two samples and sent to the neural networks. Based on the input patterns only one output neuron is fired and it is considered as the winning neuron, on subsequent iterations the network forms the clusters in the attained input patterns. As a consolidation the output clusters consists of harsh and smooth patterns and then the data is further processed and the harsh patterns based on the events are penalized (Fig. 5).

Once the harshness is calculated the virtual coins are awarded for the users on the overall performance and the updates of virtual coins are forwarded to the virtual coins server. In the time slots allotted for competitions, the scores for the performance of the user for respective competitions are forwarded to the competition server. The same architecture of neural networks was used for the evaluation of acceleration and brake signals separately in order to maintain the bifurcation of the clusters. The average score of the two independent evaluations are calculated and it is comprised under the application name of Green drive 2. Post the calculations, the scores are transmitted to the server.

5.2 K-NN (Nearest Neighbors)

The significant reason for using K-NN is to map the relativity between the speed and brake signals and to penalize when the conflict between them increases

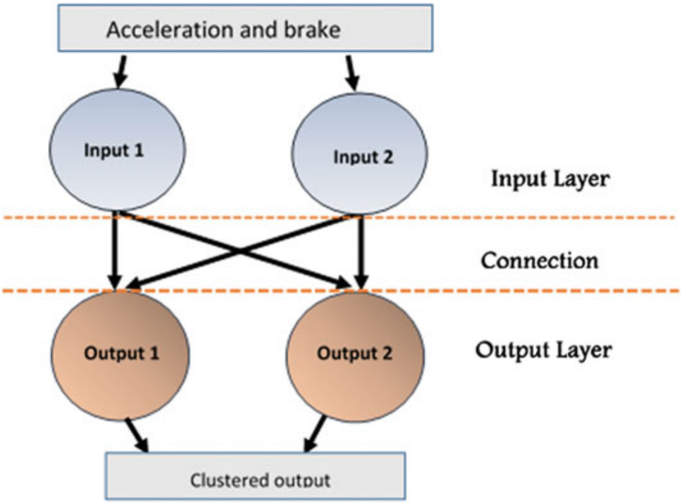

Fig. 5 Kohonen neural networks structure used for evaluation. The neural networks structure represents the parameters used such as the input and output neurons with the signals that were evaluated

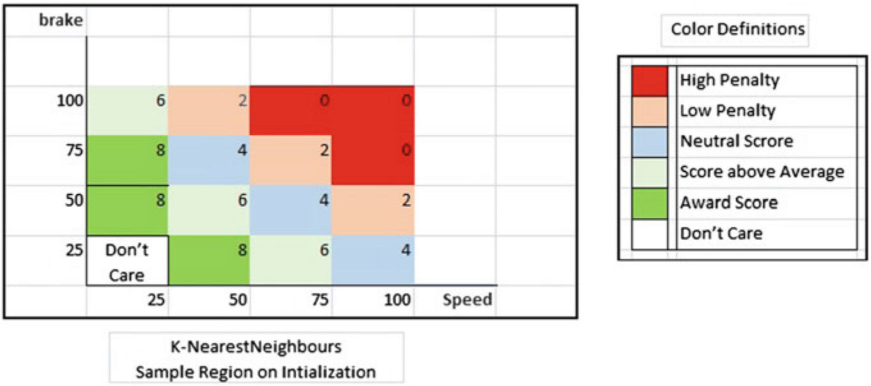

brake				
100	6	2	0	0
75	8	4	2	0
50	8	6	4	2
25	Don't Care	8	6	4
	25	50	75	100

Color Definitions

- 🟥 High Penalty
- 🟧 Low Penalty
- 🟦 Neutral Scrore
- 🟩 Score above Average
- 🟩 Award Score
- ⬜ Don't Care

K-NearestNeighbours
Sample Region on Intialization

Fig. 6 Representation of the evaluation pattern of K-NN algorithm having multiple regions with different colors. The algorithm evaluates and maps the relativity between speed and harsh brake pattern. In case of high speed, if user applies harsh break, it will result in high penalty, which in turn will reduce the score

(Example: when the vehicle is at high speed, the brake should be applied minimally, If the driver applies high pressure brake, then the action will be highly penalized). The samples of harsh patterns are supplied as a training set to the algorithm and from which the specific harsh values are picked up and penalized. The signals such as speed and brake values are supplied as inputs to the algorithm and the harsh patterns of these signals are provided as a training set to the algorithm. In the K-NN Implementation here, K = 1, that is nearest neighbors reference used to calculate the penalty for the single signal value. For each signal value, the algorithm refers to the sample set to calculate penalty value. We have control on penalty and award values, and they can be set as per the changes in the criteria. This gives the possibility of customization to change expected conditions and deviations. K-Nearest Neighbors approach can evaluate the relativity of more than one signal at the same time, such as Steering wheel versus Speed and Steering wheel versus brake (Fig. 6).

5.3 Linear Distances

Unlike Kohonen Neural Networks, where the batch processing is performed, the Linear Distances holds a thresholding based evaluation in which every single signal is processed and evaluated for harshness. The metrics for evaluating harshness is devised using the linear equation from which the certain criterion forming the boundaries for penalty and award regions are derived.

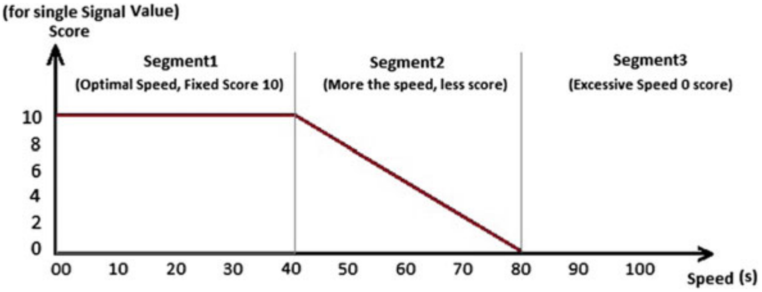

Fig. 7 Evaluation criterion for linear distances with representation of segments involving variation of speed signal values

$$y = mx + b. \tag{1}$$

The slope (m) and intercept (b) for the linear equation are supplied through the XML file and from which the penalty values are calculated (Fig. 7).

The above figure represents the processing of speed signal using Linear Distances approach, the entire space is divided into three segments (segment 1, segment 2 and segment 3). Each segment holds the set of limits such as segment 1 has the limit from 0 to 40 and segment 2 holds the limit from 41 to 80 and the values exceeding 80 will be gathered in segment 3. Let's assume that the vehicle speed is around 35 km/h, now this signal would fall in segment 1 where the limit ranges from 0 to 40 and it is considered to be optimal driving and the user would get the score of 10. In another case let the vehicle speed be 60 km/h, this signal would fall under segment 2, where the limit ranges from 41 to 80 and as the speed limit exceeds the optimal criteria the score would be 5. Thus, when the speed exceeds certain limits the scores would reduce considerably. The signals such as acceleration, RPM and speed are evaluated using Linear Distances in our approach, the results of the evaluation will be sent to the virtual coins and competition server.

5.4 Dynamic Sliding Window

Dynamic Sliding Window is an event-based signal evaluation. The algorithm comprises of two states (i.e.) standard window and penalty window. In this implementation, the Dynamic Sliding Window is evaluating every single Signal. When the signals are in optimal range, state is considered to be standard (normal region for signals) and when signal values deviate above from the optimal level, then the state is considered to enter the penalty window. Once the signal starts to deviate above the optimal level, the penalty window starts and remains till the point when it comes back to optimal level. The size of penalty window and the deviation amount in that period of time are the factors which are getting evaluated under this

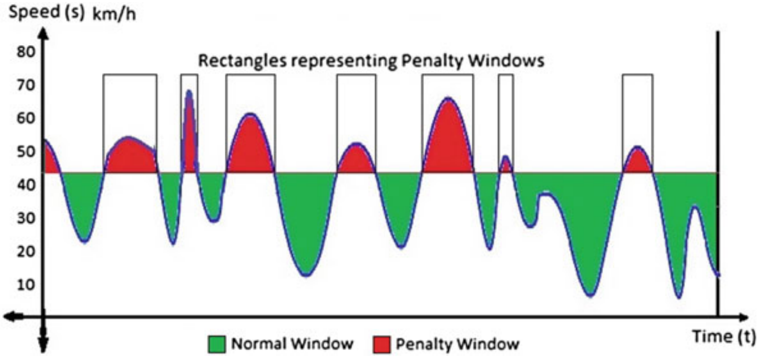

Fig. 8 Representation of dynamic sliding window with the evaluation of speed signal

algorithm. For example, if the user exceeds a particular speed limit, then the state changes from normal window to Penalty window. If speed limit is 60 km/h, then user who drivers at speed of 65 km/h for 1 min will deserve same penalty as of another user, who is driving at the speed of 90 km/h for 10 s (Fig. 8).

6 Social Gaming Prototype Scenario

The social gaming scenario consists of various competitions (drive around a location, for example: a city) comprising a self and social comparisons, where the competition involves the participation of multiple users and each user in the competition will be evaluated and granted a score out of 100 (scores will be calculated based on the results of the evaluators used). The competition user holding a highest score will be declared as the winner of competition and will be awarded with the virtual coins. The users can get virtual coins at any time by exhibiting safe and green driving behavior, as virtual coins are continuous

Table 1 The List of evaluators, signals evaluated, score contribution and the application names associated with the evaluators are displayed in the table

Application name	Evaluator	Signals evaluated	Score contribution (%)
Green drive 1	Linear distances	Acceleration and RPM	20
Fluid traffic	Linear distances	Speed and fuel consumption	20
Green drive 2	Kohonen neural networks	Acceleration and brake	20
Green drive 3	K-Nearest neighbors	Speed and brake	20
Green drive 4	Dynamic sliding window	Speed	20

evaluation of driver performance independent of peers, routes and competitions. In order to manage the signals evaluated by the evaluators and to make the scoring pattern tractable, we labelled each evaluator with an application name, where each application would constitute a set of signals for the evaluation and transmit the evaluation results under the roof of an application name (Table 1).

7 Results

In order to compare the efficacy of the four evaluators, we performed the test in evaluating the acceleration signal with all the four evaluators on the time interval of 2 min. The below figure represents the evaluators test results (four evaluators) of acceleration signal for 8 min (Fig. 9).

From the observations of the four evaluators, it can be noted that the evaluators have different grading patterns, where the Kohonen Neural Networks have a penalizing feature for minor harsh patterns as well and this approach can be used for correcting the mistakes in novice driving style. Whereas, the K-NN has a nominal penalizing criterion in which certain harsh patterns are provided as a sample set to the system and specific harsh patterns are captured and penalized. The Linear Distances has a penalizing scheme based on segments with standard flow of virtual coins and dynamic sliding window's evaluation has an event based penalizing criterion. These four evaluation approaches have been designed to provide a viable solution to the various needs of the user and most importantly for the betterment of the driver behavior. The dimensions involved in evaluation mechanisms can facilitate the process of model adaptation, because model adaptation is one common problem in evaluation methods used for tracking the driver behavior.

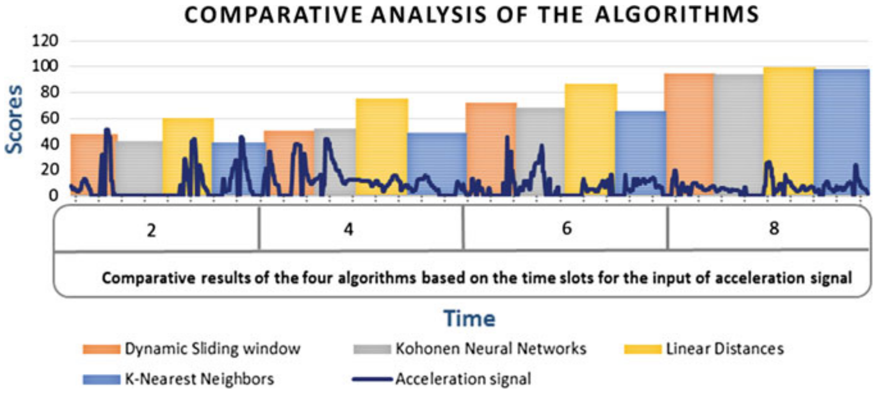

Fig. 9 Comparative analysis of the algorithms

8 Conclusion

As a consolidation, we have implemented set of algorithms including the significant Machine Learning approaches to evaluate the driver behavior based on various vehicle signals acquired from the test run conducted by Centro Ricerche Fiat (CRF) in Trento, Italy. By using certain strategies in designing the evaluation metrics such as event-based, relativity mapping of signals and segmenting, we have attained a viable solution to track the driver behavior on all occasions and driving standards. This methodology would be a stable approach as it is a collection of model adaptive tools and the tests involved were carried out on data acquired from real-world scenario. The model adaptive approach has the tendency to accommodate the needs of the user and also can be resilient for dynamic environments. The system can be further extended in future by integrating different applications (Public transport Optimization, Collaborative navigation, collaborative driving and maneuvering) and a comparison approach can be introduced, with which the users can gauge their performance and compare with their peers. Finally, the social gaming chain introduced in this approach would induce a competitive learning traits and enhances the efficiency of driving. Henceforth, this approach has coherent mechanism to inculcate safe and green driving patterns and caters the various types of drivers with the aid to improvise the driving proficiency.

References

1. McCall, J.C., Trivedi, M.M.: Driver behavior and situation aware brake assistance for intelligent vehicles. Proc. IEEE **95**(2), 374–387 (2007)
2. Sajan, S., Ray, G.G.: Human factors in safe driving—a review of literature on systems perspective, distractions and errors. In: Proceedings—2012 IEEE Global Humanitarian Technology Conference, GHTC 2012, pp. 83–88 (2012)
3. Punzo, V., Ciuffo, B.: Integration of driving and traffic simulation: Issues and first solutions. IEEE Trans. Intell. Transp. Syst. **12**(2), 354–363 (2011)
4. Nor, N.M., Wahab, A., Kamaruddin, N., Majid, H.: Post accident analysis of driver affection. In: Proceedings of International Symposium on Consumer Electronics ISCE, pp. 278–283 (2011)
5. Gong, J.: Driver pre-accident behavior pattern recognition based on dynamic radial basis function neural network. In: Proceedings 2011 International Conference on Transportation Mechanical and Electrical Engineering (TMEE), pp. 328–331 (2011)
6. Bellotti, F., Berta, R., De Gloria, A., Margarone, M.: Using 3D sound to improve the effectiveness of the advanced driver assistance systems. Pers. Ubiquit. Comput. **6**(3), 155–163 (2002)
7. TEAM, [Online]. Available: http://www.collaborative-team.eu/overview/. Accessed 13 April 2015
8. CRF, [Online]. Available: http://www.crf.it/en-US/Company/Pages/CompanyProfilo.aspx. Accessed 08 May 2015
9. Tezuka, S., Soma, H., Tanifuji, K.: A study of driver behavior inference model at time of lane change using bayesian networks. In: IEEE International Conference on Industrial Technology ICIT 2006, pp. 2308–2313 (2006)

10. Angkititrakul, P., Miyajima, C., Takeda, K.: Modeling and adaptation of stochastic driver-behavior model with application to car following. In: Intelligent Vehicles Symposium (IV), pp. 814–819 (2011)
11. Angkititrakul, P., Miyajima, C., Takeda, K.: Impact of driving context on stochastic driver-behavior model : quantitative analysis of car following task. In: Vehicular Electronics and Safety (ICVES) (2012)
12. Erdog, H., Ozgu, A., Akan, B., Karabalkan, H., Sezer, V., Karaca, M., Abbak, M., Eritmen, K.: In-Vehicle Corpus and Signal Processing for Driver Behavior. In: Springer Publishing Company, Incorporated (2008)
13. Meseguer, J.E., Calafate, C.T., Cano, J.C., Manzoni, P.: DrivingStyles: a smartphone application to assess driver behavior. In: Proceedings—International Symposium on Computers and Communications (2013)
14. Acqua, P.D., Bellotti, F., Berta, R., De Gloria, A.: Time-aware multivariate nearest neighbor regression methods for traffic flow prediction. In: IEEE Transactions on Intelligent Transportation Systems, pp. 1–10 (2015)
15. Dougherty, M.: A review of neural networks applied to transport. Transp. Res. C Emergerging Technol **3**(4), 247–260 (1995)
16. Lee, C., Nordstedt, D., Helal, S.: Standards, tools and best practices enabling smart spaces with OSGi. Pervasive Comput. IEEE **2**(3), 89–94 (2003)
17. Huang, S.-J., Hung, C.C.: Genetic algorithms enhanced Kohonen's neural networks. In: Proceedings of the ICNN'95—International Conference on Neural Networks, vol. 2, pp. 1–5 (1995)

A Novel Technique for the CMRR Improvement in a Portable ECG System

Pietro Di Buono, Leonardo Mistretta and G. Costantino Giaconia

Abstract This paper presents a new technique to improve the quality of the ECG signals, increasing the Common Mode Rejection Ratio (CMRR). We developed a portable wireless Bluetooth ECG system able to acquire 12 leads, communicating with Smartphones and PCs. Many experiments have been made for measuring CMRR decay due to the difference on skin-electrodes impedances, the asymmetries of the amplifiers input stages and external components. Using some digital potentiometers, the system is able to compensate for these, increasing the CMRR of about 18 dB.

1 Introduction

Electrocardiography is one of the most important diagnostic methods to heart monitoring. It is widely used in clinical environment but more and more it is applied in home healthcare scenarios. In the event of a cardiac arrest, early intervention (in the first 30 min) can drastically reduce heart damage, resulting on increased survival rate and reduced prognosis. Therefore, ECG monitoring is a key solution, particularly for already suffering patients.

In order to make feasible a monitoring system, much attention should be paid to the comfort of the patient. Ag/AgCl electrodes are widely used in clinical scenario, but in long terms, they present several drawbacks. These electrodes require an

---

P. Di Buono (✉) · L. Mistretta · G. Costantino Giaconia
Department of Energy, Information Engineering and Mathematical Models, DEIM,
University of Palermo, Viale delle Scienze (Bldg. 9), 90128 Palermo, Italy
e-mail: pietro.dibuono@unipa.it

L. Mistretta
e-mail: leonardo.mistretta@unipa.it

G. Costantino Giaconia
e-mail: costantino.giaconia@unipa.it

A. De Gloria (ed.), *Applications in Electronics Pervading Industry, Environment and Society*, Lecture Notes in Electrical Engineering 409,
DOI 10.1007/978-3-319-47913-2_25

electrolyte paste or a conductive adhesive whose drying action over time leads to a degradation of the signal to noise ratio (SNR). Furthermore, they may cause irritation and discomfort and are a potential cause of skin allergy and inflammation. Alternatively, several authors [1–4] have developed dry electrodes that are able to acquire an ECG signal but accepting a larger noise at the inputs.

Noise is mainly due to the Electromagnetic Interference (EMI) which are capacitively coupled to the measurement system. Since the noise is coupled to both branches of a differential acquisition channel, commonly, amplifiers with high CMRR are used, but, with time, the goodness of the electrode-skin contact degrades introducing an asymmetry in the system, deteriorating the CMRR and ultimately the SNR.

This paper presents a method that allows compensating for these asymmetries bringing the CMRR to acceptable values even in presence of a poor skin-electrode contact.

2 CMRR Decay and Known Techniques for Its Improvement

The goodness of a front-end for ECG signal strongly depends on the CMRR. ECG signal (with peaks of few millivolts) is affected by a common mode noise of few volts, typically at power line frequency. Assuming a wanted resolution of 5 V, the system must have at least a CMRR of 106 dB. The CMRR, because of external components and the differences between skin-electrodes contacts, can deteriorate down to 60 dB. Supposing that the impedances of the amplifier input branches were perfectly matched (although it isn't true), the insertion of a first order low-pass RC filter leads to a CMRR approximated by

$$CMRR = -20\log\left(\frac{\delta R}{R} + \frac{\delta C}{C}\right) - 20\log\frac{f}{f_c} \tag{1}$$

where R and C are the nominal resistance and capacity of the filter, δR and δC are the mismatch respectively in R and C, f is the frequency of the common mode signal and f_c is the -3 dB frequency of the filter.

Several techniques are known to improve CMRR [5], but all these are trying to solve the problem by attenuating the common mode signal without taking any steps to reduce the mismatch of the front-end branches. The simplest technique is to realize an isolated system, so it can follow the common mode potential [6]. Another technique, widely used, is to force the potential of the patient with a reference electrode that can be used for feeding back the inverted common mode signal, measured from the first stage of the amplification channel [7].

3 System Overview

In order to improve the native SNR an embedded system has been designed and implemented. It can be divided into the following parts (as shown in Fig. 1): an ADS1198 as analog front-end; a block containing second order filters to avoid aliasing; some digital potentiometers driven toward asymmetry compensation; a few pull-up resistors and a conditioning circuit to measure the contact resistances; a microcontroller and a Bluetooth wireless module. The system is powered by four 1.5 V (size AAA) batteries, that gives a low noisy power supply in combination with a linear regulator. To compensate asymmetries, eight potentiometers have been inserted within the four channels of interest (RA, LA, LL, V1). The AD5254 family [8], from Analog Devices, is a 256 taps, I^2C, non-volatile digital potentiometers suitable for our purposes. In each channels, a 10 kΩ potentiometer has been used to compensate the input stage asymmetries between channels, mainly due to the front-end filter, while another one of 100 kΩ has been used to compensate the skin-electrode differences.

The ADS1198 is an analog front-end (AFE) optimized for scalable medical instrumentation systems manufactured by Texas Instruments with a minimum declared CMRR of 100 dB [9].

It has eight channels, 24 bit delta-sigma ($\Delta\Sigma$) analog to digital converters (ADCs), with integrated differential programmable gain amplifiers and dedicated circuitry for the generation of the Wilson Central Terminal (WCT) and the Right Leg Drive (RLD) voltages. It also embeds an internal voltage reference and oscillator, hence by using a small amount of external components this chip is ready to develop a compact and simple ECG system [10].

To measure the contact resistance of electrodes, referred to the Right Leg (RL) electrode, a 10 MΩ pull-up resistor was added to the leads. This value was found as tradeoff between attenuation of the ECG signal, resolution of the

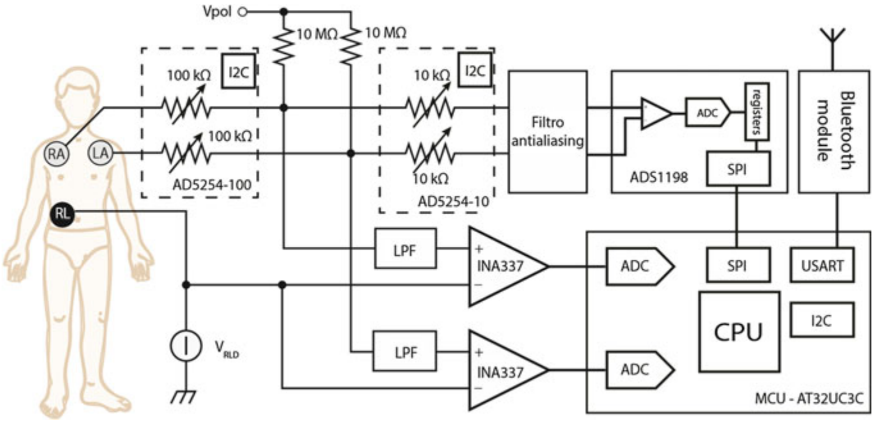

Fig. 1 Simplified scheme of the ECG system

impedance measurement and current injected into the patient. The signal is amplified with a INA337 [11] and then filtered with a fourth order Chebyshev low pass filter, implemented with three AD8694 [12], that attenuates the unwanted frequencies. The cutoff frequency has been chosen taking in account the system response speed.

The signal is processed by the AT32UC3C2256C, a 32-bit microcontroller made by Atmel [13]. This device features a floating point unit, a 12-bit ADC with a sampling frequency up to 1.5 Msps, and several serial interfaces (USB, I2C, SPI, USART). The microcontroller deals with data acquisition from ADS1298, Bluetooth communication, potentiometers managing and resistance measurement with its integrated ADC.

The Bluetooth module is connected to the microcontroller via USART, with the SPP protocol, and it allows communication with smartphones. A host PC can also be used for analyzing, saving and visualize the data, via USB communication.

4 Experimental Results

At first, the CMRR of a differential channel has been evaluated, applying the same signal to the leads, after removing pull-up resistors and impedance measuring circuit. The value of CMRR showed by the system, without compensation, is about 58 dB, much lower than the maximum value possible (Fig. 2).

Thus, to compensate the input stage, the system starts to vary the value of the 10 kΩ potentiometers by doing a full span of possible values. The resulting values of CMRR shows that, using an impedance of 5.7 kΩ in the RA lead, the CMRR

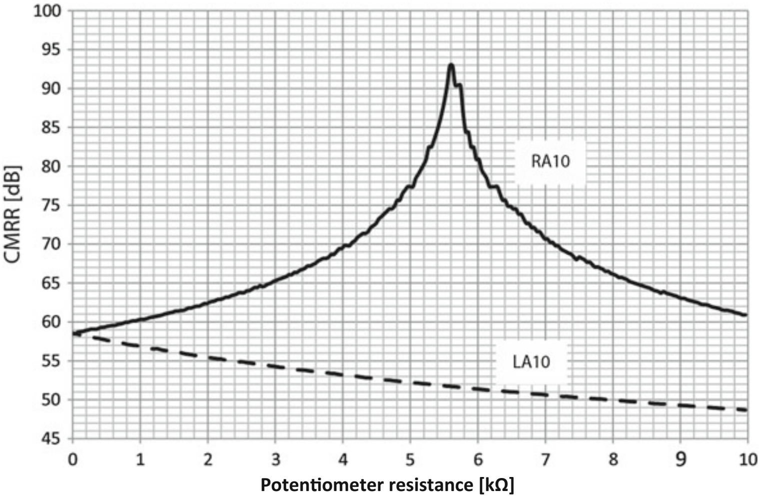

Fig. 2 CMRR versus 10 kΩ potentiometer value, with ECG filter inserted

that was 58 dB, increase up to 93 dB (Fig. 2). This means that inserting that value of resistance, in the RA lead, the system works at the best possible condition.

Typically, a good skin-electrode contact shows a resistance of few kΩ, but the difference between two contacts remains below 1 kΩ. So, without this compensation, the system would not work in optimal conditions. When the contact is poor, instead, the resistance difference between two electrodes can become even several tens of kΩ and, in the case of dry electrodes, it can exceed 100 kΩ, leading to a significant degradation of CMRR [14].

Having compensated the input circuit asymmetries, the system was used to compensate skin-electrode impedance mismatch. The first test was to set the resistor on one lead and measure the CMRR varying the impedance (100 kΩ potentiometer) on another lead. As showed in Fig. 3, an impedance difference of 10 kΩ lead to a CMRR value of 50 dB, more than 40 dB down respect the maximum CMRR in the system without compensation, otherwise, changing the value of the potentiometer, the decrease is reduced to 68 dB.

The increment of the obtained CMRR for the compensated ECG system is constant and above 18 dB, except for very little values of impedance difference (Fig. 4).

To understand how the compensator works, it can be useful to observe the chart of the CMRR versus the variation of the potentiometers on two channel, shown in Fig. 5.

Supposing a contact resistance of 6.3 kΩ in the RA lead, the system shows a CMMR of 46 dB (round dots in figure).

By choosing as an example an emulated impedance of 12.5 kΩ in the LA lead, the CMRR increases to 67 dB (square dots in figure). The compensation allows moving the working point along its curve and till the local maximum.

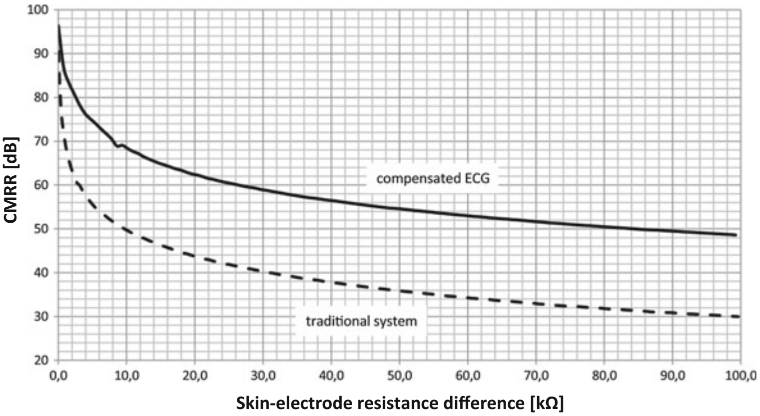

Fig. 3 CMRR for the compensated system (*solid*) and for traditional system (*dashed*) versus the resistance inserted in one of the channel branches

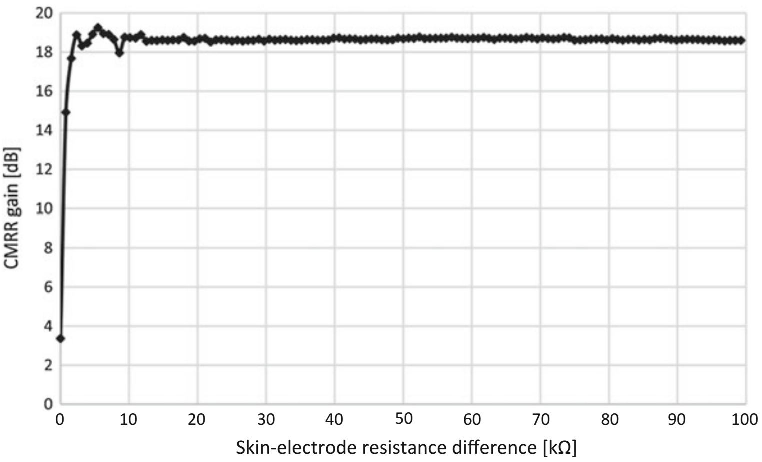

Fig. 4 CMRR gain versus difference contact resistance, (with negligible contact resistance on one electrode)

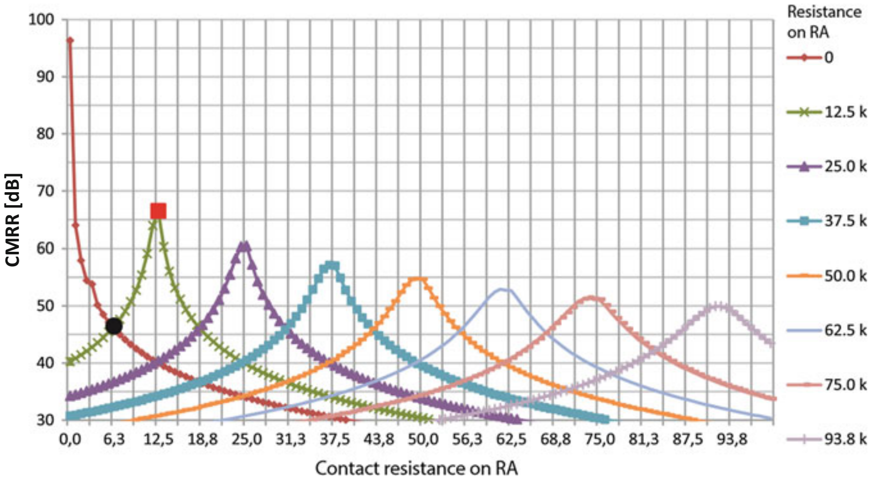

Fig. 5 CMRR varying resistances on two differentials branches

5 Conclusion

We implemented a system that prevents the degradation of the ECG signals by maintaining a high CMRR. It uses digital potentiometers to dynamically compensate both the input stage and the skin-electrode asymmetries. The system exhibits a remarkable performance improvement, with a typical SNR gain of about 18 dB above the corresponding non-compensated CMRR value. We successfully apply this method on bipolar leads; on the other hand, to apply it to unipolar leads further studies are needed.

Now, the system can be used to compensate the skin-electrode differences at the beginning of an ECG exam. Real-time compensation could be realized using an AC impedance measurement, at a frequency above the range of the ECG signal.

References

1. Xie, L., Yang, G., Xu, L., Seoane, F., Chen, Q., Zheng, L.: Characterization of dry biopotential electrodes. In: Engineering in Medicine and Biology Society (EMBC), 2013 35th Annual International Conference of the IEEE, pp. 1478–1481 (2013)
2. Kim, H.L., Kim, M.G., Lee, C., Lee, J.H., Kim, Y.J.: Miniaturized one-point detectable electrocardiography sensor for portable physiological monitoring systems. Sens. J. IEEE **12**(7), 2423–2424 (2012)
3. Gandhi, N., Khe, C., Chung, D., Chi, Y., Cauwenberghs, G.: Properties of dry and non-contact electrodes for wearable physiological sensors. In: Body Sensor Networks (BSN), 2011 International Conference on, pp. 107–112 (2011)
4. Tautan, A.M., Serdijn, W., Mihajlovic, V., Grundlehner, B., Penders, J.: Framework for evaluating eeg signal quality of dry electrode recordings. In: Biomedical Circuits and Systems Conference (BioCAS), 2013 IEEE. pp. 186–189 (2013)
5. Acharya, V.: Improving common-mode rejection using the right-leg drive amplifier. Application Report SBAA188, Texas Instruments (2011)
6. Lockhart, R.: Why use isolated signal conditioners? Application Note AN116, Dataforth Corporation
7. Winter, B.B., Webster, J.: Driven-right-leg circuit design. Biomed. Eng. IEEE Trans. BME **30**(1), 62–66 (1983)
8. Analog Devices: AD5254 Datasheet Rev. C (2012)
9. Texas Instruments: ADS1198 Datasheet (2010)
10. Zhang, Y., Sun, G., Yang, Y.: 12-lead ECG data acquisition system based on ADS1298. Procedia Eng. **29**(0), 2103–2108 (2012). International Workshop on Information and Electronics Engineering
11. Texas Instruments: INA337 Datasheet (2002)
12. Analog Devices: AD8694 Datasheet Rev. F (2013)
13. Atmel: AT32UC3C Datasheet (2012)
14. Di Buono, P., Mistretta, L.: Front-end elettronici per applicazioni biomedicali. EAI (2015)

An Optimization Device for Series Parallel Connected PV Plants

**Eleonora Riva Sanseverino, G. Costantino Giaconia,
Vincenzo Li Vigni, Pietro Di Buono, Pietro Romano,
Marco Iannello and Vincenzo Tirrasi**

Abstract In this paper it is presented a testing prototype of a reconfiguration system for photovoltaic (PV) plants. The system enables to increase the total energy output by reducing the electrical mismatch between the PV array modules. The architecture of the implemented switching matrix, performing the dynamic electrical interconnections of the PV panels, enables to reconfigure nine solar modules in a series-parallel (SP) configuration. The contribution is organized as follows. A brief state of the art is first presented, followed by a comparison between the SP and Total-Cross-Tied (TCT) connections. The prototype then is thoroughly described as well as the main design choices. Finally some tests and an extrapolation of its performance over a real size PV field are reported.

1 Introduction

The increasing energy demand of the far east growing countries as well as the improved performance of solid state relays technologies that will be soon available at reasonable prices, let us imagine that the Photovoltaic generation plants reconfiguration will soon be a realistic perspective. This will be true both for existing and new installations. The improvements that can be attained as an effect of the partial

---

E. Riva Sanseverino (✉) · G. Costantino Giaconia · V. Li Vigni · P. Di Buono · P. Romano · M. Iannello · V. Tirrasi
Department of Energy, Information Engineering and Mathematical Models, DEIM,
University of Palermo, Viale delle Scienze (Bldg. 9), 90128 Palermo, Italy
e-mail: eleonora.rivasanseverino@unipa.it

G. Costantino Giaconia
e-mail: costantino.giaconia@unipa.it

V. Li Vigni
Prysmian Electronics S.r.l., piazza principe di camporeale 27, 90138 Palermo, Italy
e-mail: vincenzo.livigni@unipa.it

P. Romano
e-mail: pietro.romano@unipa.it

A. De Gloria (ed.), *Applications in Electronics Pervading Industry,
Environment and Society*, Lecture Notes in Electrical Engineering 409,
DOI 10.1007/978-3-319-47913-2_26

correction of the mismatch effect are a touchable benefit that is difficult to quantify, especially for new installations. Roofs showing one or more obstacles will probably become a possible installation site, as well as third generation technologies and Building Integrated PV systems, allowing in places installations, where partial shading will be a quite common operating condition. They will probably (but not for sure as proved by some recent studies on the topic, [1]) require some kind of conditioning system to control the mismatch effect.

Dynamic reconfiguration to efficiently change the connection layout of PV modules into PV arrays is one of the leading edge technologies to improve power output under electrical mismatch conditions caused by partial shading or other issues. An extensive review can be found in [2] and the number of papers cited proves the interest of the scientific and industrial community around the technology.

When one or more, belonging to a set of series-connected, PV modules are shaded, the maximum generated current gets reduced, thus decreasing the output power [3]. Besides, module or modules that are shaded or faulty can reach a too high temperature, connected to the hotspot phenomenon [4] and eventually to the module breakdown. Hotspot and mismatch events can be controlled through bypass diodes although they give rise to losses and local maxima in the PV curve [5], the MPPT algorithm controlling the converter operation can be misled and local maximum operating points can be taken as absolute maximums.

In this paper a prototype based on the SP connection is presented. The design layout is provided as well as some measurements proving the efficiency of the proposed implementation to cope the mismatch effect. The key issues to be solved are also pointed out in the concluding remarks section.

2 The Series Parallel Versus Total Cross Tied in PV Plants Reconfiguration

Many basic topologies can be considered to perform reconfiguration. The most common topologies are: Series Parallel and Total Cross Tied. The first is the standard configuration used in Photovoltaic plants, see Fig. 1a.

Using this topology, reconfiguration aims to build strings of series-connected modules showing similar irradiance levels, that are then connected in parallel. As a result, well-irradiated solar panels will not be limited in current by a low irradiated panel of the same string. Total-cross-tied (TCT) configuration (see Fig. 1b) ties modules first in parallel, so that voltages are equal and currents are summed up and then these groups are connected in series. Although under uniform conditions SP and TCT modules connection provide the same power value, TCT topology reduces the overall effect of mismatch. However, in existing PV generation plants, the SP is the most common connection.

Fig. 1 **a** Series parallel connection **b** Total cross tied connection

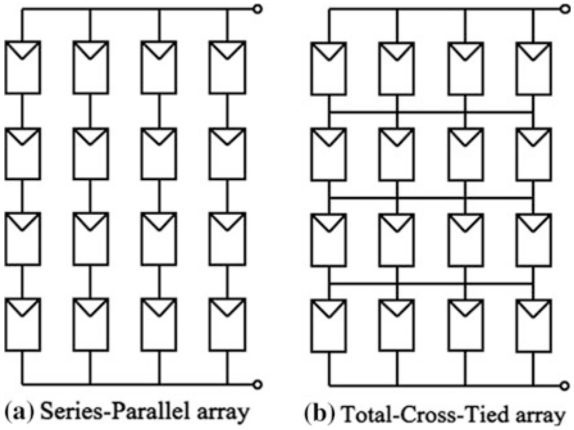

3 The Prototype

In order to test the effectiveness of a reconfigurable approach on a Series-Parallel solar array, a custom electronic system has been designed and implemented (see Fig. 2). The Reconfigurable Solar Array System (RSAS) consists of four different circuit blocks, each one performing respectively:

- Measuring
- Control logic
- Switching matrix
- Supply and Load.

In a PV module the irradiance level can be estimated by measuring the open circuit voltage V_{oc} and the temperature of the module T_c, using also the parameters related to the specific solar module [6]:

$$G = G_{STC} e^{\frac{V_{oc} - V_{oc_{STC}} - \mu_{V_{oc}} \left(T_c - T_{c_{STC}}\right)}{N_s A k \frac{T_c}{q}}} \tag{1}$$

where G is the solar radiation measured in $\frac{W}{m^2}$, G_{STC} the solar radiation in standard conditions, STC $\left(1000\ \frac{W}{m^2}\right)$, $\mu_{V_{oc}}$ is the open-circuit voltage temperature coefficient, $T_{C_{STC}}$ the temperature at STC (298.15 K), N_s the number of cells series-connected, A the ideality factor, k the Boltzmann's constant and q the electron charge. V_{oc} is the open-circuit voltage of the solar module. These parameters can be obtained from the datasheet of the module or measured directly. In (1) the only variables are V_{oc} and T_c, while the other parameters can be assumed, for our purposes, approximatively constant [7, 8]. For our purposes, it is supposed that the temperature variations between different modules connected to the RSAS are small. This means that in (1) the only variable is V_{oc}, i.e. it is possible to see the open circuit voltage of each PV panel as a quantity growing with the irradiance level, even if not strictly

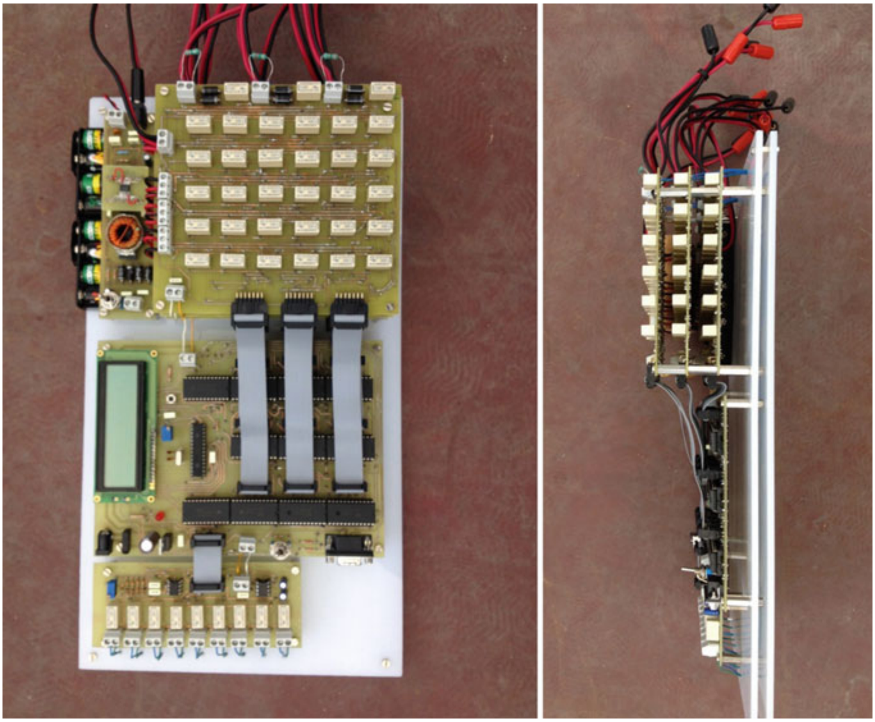

Fig. 2 RSAS Hardware Board (*front* and *cross* view)

proportional. This assumption simplifies the architecture of the electronics and control algorithm, with the downside that the optimization algorithm become less effective when the temperatures spread between PV modules is large.

The optimization algorithm implemented by the RSAS is very simple. The measuring board consists of nine non-latching relays, each connecting a PV module to the input of the analog front-end. This is formed by a voltage divider, a difference amplifier and the analog-to-digital converter of the microcontroller in the control board. When an updated measure of the modules voltage is required, the measuring board performs a scanning of the nine modules such as only one relay is active per time. A complete scanning is performed within one second.

When the RSAS is switched on, all the solar modules are disconnected by each other. A measuring is performed in open-circuit configuration, so that all the nine PV module open-circuit voltages are acquired and ordered from the highest (element 1) to the smallest one (element 9). This list is divided in groups of three modules, starting from the one with the biggest voltage:

GROUP 1—modules 1, 2, 3
GROUP 2—modules 4, 5, 6
GROUP 3—modules 7, 8, 9

Fig. 3 Working flow diagram

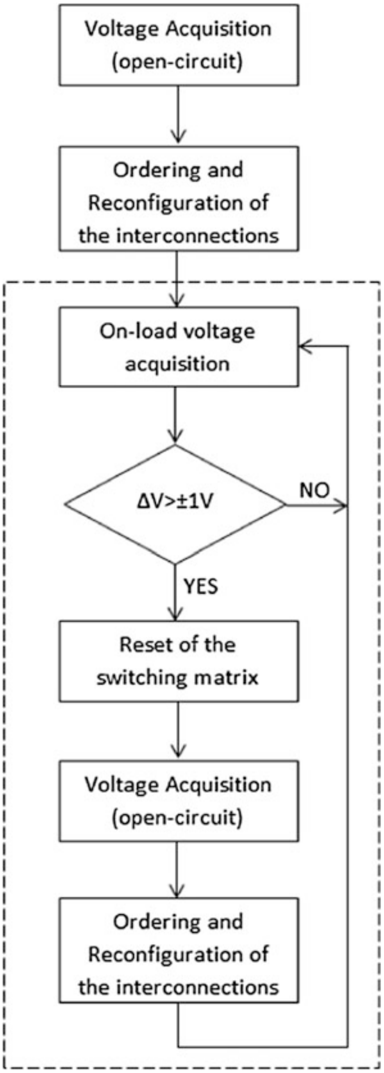

When the control logic has performed the ordering algorithm, the switching matrix implements the optimum connection of the modules, building three strings each with one of the previous groups. These three strings are then parallel connected to build the resulting optimized PV array.

In the normal working activity, the measuring is performed on-load, that is without setting in open-circuit the modules. In this condition, the control logic checks if the voltage of every module has changed for more than ±1 V respect to the previous iteration. If this happens, the switching matrix resets the PV array and the measuring is performed again in open-circuit configuration. The downside of

Table 1 BP solar module characteristics

Parameter	Value
Power	10 [W]
MPP voltage	16.8 [V]
MPP current	0.59 [A]
Short-circuit current	0.65 [A]
Open-circuit voltage	21 [V]

this approach is that, when the switching matrix is reset (all the modules are disconnected) and a voltage acquisition is performed, no power is delivered to the load, since the measuring relays temporarily put each module in open circuit, see Fig. 3.

The control logic board mainly consists of a microcontroller, implementing the so far discussed functionalities, and the multiplexers, needed to address the relays. An LCD display is also used to show the current PV array configuration.

The switching matrix is composed by 99 relays supporting currents up to 2A:

- 72 latching relays are used for implementing the series connection between modules, that is connecting the positive terminal of one module to the negative terminal of another module;
- 9 latching relays connect the positive terminal of the module to the positive output terminal of the array;
- 9 latching relays connect the negative terminal of the module to the negative output terminal or to the positive terminal of another module (series connection);
- 9 non-latching relays for completely disconnecting the 9 PV modules from the others.

The nine solar modules being used in our tests are made by “BP Solar”, with characteristics described in Table 1. Bypass and block diodes are also used. The architecture of the switching matrix allows connecting one of the nine solar modules to whatever of the other remaining eight, organizing them in three strings formed by three modules each. These strings are then connected in parallel. The final configuration is a 3 × 3 SP solar array.

The power board hosts a group of batteries able to supply the whole system. The interesting point is that the batteries can be recharged by the RSAS itself so that the system is self-sustaining.

4 Applications and Results

Some tests have been carried out during daytime on the roof of the DEIM Department. The PV plant is composed of nine panels with rated power of 10 W (Table 1).

A first test was considering the circuit in open circuit condition. It was noticed that, starting from the configuration with all panels working correctly and shading one panel per string, the reconfiguration was putting the shaded panels in one series string.

Table 2 Results under shaded and unshaded conditions

Trial	Output power w/o reconfiguration [W]	Output power with reconfiguration [W]
#1	46.92	47.47
#2	19.07	44.27
#3	14.34	24.82
#4	14.89	24.21
#5	12.25	13.38
#6	20.45	43.7
#7	22.23	42.27

After that, a suitable load was chosen; such load was allowing the whole system to work in the zone of the characteristic where the system acted as a voltage generator, hence showing a substancial difference between the case with shaded panels (unefficient) and the case with reconfigurated panels. Again, the panels were organized in a series string. The results are shown in Table 2.

In order to desume the increase of the output power deriving from the use of a reconfiguration system over an extended PV field, the following experiment has been carried out. The panels have been positioned at a certain distance *d*, as depicted in Fig. 4, and a monitoring campaign has been carried out.

The reduction in terms of energy is due instead to the time interval when the shading stays over the PV field and this depends on the wind speed. Figure 5 shows a real circumstance.

As the clouds pass by, the partial shading condition gets modified as shown above and the reconfiguration system must adapt the connections. The way and the extent to which these changes are influencing the productivity of the field, depends on the arrangement of the PV field.

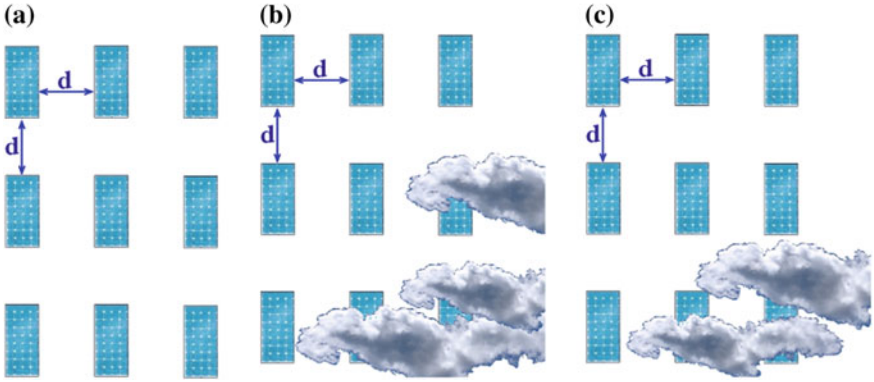

Fig. 4 **a** Layout for tests over larger PV generation systems, **b** clouds causing a 15 % reduction of output power, **c** clouds causing a 35 % reduction of output power

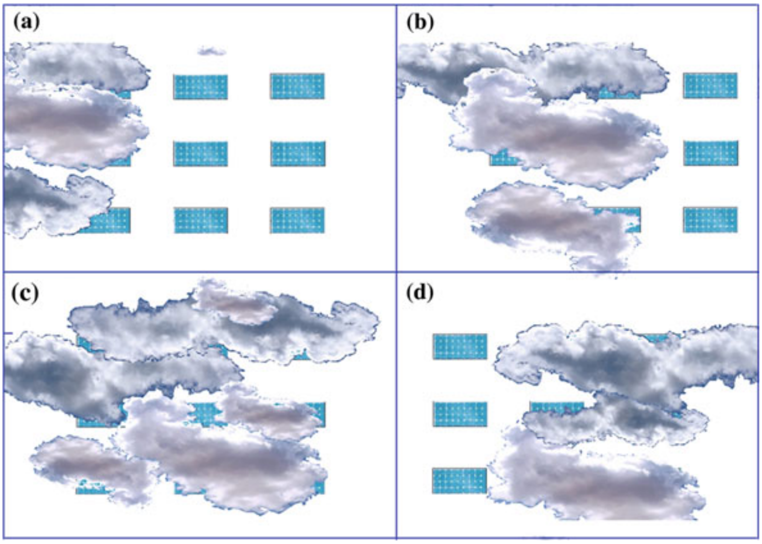

Fig. 5 Clouds passing over a PV field

Taken the data from the Weather Monitoring station of Palermo, based on data averaged over 30 years by the Weather World Organisation, the wind shows an average speed of 5.4 m/sec, with a maximum of 6.4 m/sec in december. Considering a PV generation plant with rated power of 1 MWp and large 2 ha arranged as in Fig. 6, with the shortest side being 100 m, considering that clouds are pushed all at maximum velocity, we can assume that the time required to a cloud to go from one side of the PV field to the other, is around 10 s. It is this required to monitor the situation every 4–5 s, in order to check whether the cloud is really causing a change which would require a reconfiguration.

Current versus time (I-t) characteristics along a whole day can be used to extract a yearly evaluation. A typical course taken for evaluations in this paper shows 6 episodes of shading between 10 a.m. and 11:50 a.m., therefore at least 6 reconfigurations are needed, with an energy saving of 5 %.

As far as the ageing of components is concerned, considering the monostable relays with an acquisition time of 4 s, we would have around 9000 acquisitions per day and thus around 3 million acquisitions per year, considering that the chosen relays can execute 10 million switchings, the relays would last at most 3 years.

An open issue is indeed to investigate about the triggering event for reconfiguration. Is it worth performing it just every given amount of time, or is it wiser to connect it to some triggering event? The bi-stable relays used in the control card are instead not considered in this study about ageing because the number of switching operations is considerably smaller. Another drawback of the proposed architecture

Fig. 6 Possible arrangement of a PV field with shading

is related to the voltage monitoring which, in the proposed configuration, requires an open circuit registration of the voltage value. The latter condition would not be acceptable in real world applications. Further investigations must be carried out to see whether the voltage measurement even in 'under load' condition is reliable for the purpose of reconfiguration.

5 Conclusions

In this paper a prototype for dynamic reconfiguration of PV plants is proposed. The design and operating issues as well as the performance characteristics of the system are outlined and discussed. The application shows the potential of the technology to cope with the mismatch effects caused by shading effects, ageing or weather conditions. As pointed out and detailed in application section, the issues to be addressed in the industrial development of the technology are basically: the lifetime of switching devices and the monitoring and measurement technologies.

Acknowledgments This work has been partially supported by "Energetic" a National research program (PON02_00355_3391233).

References

1. Pan, B., Weng, J., Chen, S., Huang, Y., Dai, S.: The effect of partial shading on dye-sensitized solar cell module characteristics. J. Appl. phys. D **47**(47) (2014)
2. La Manna, D., Vigni, V. L., Sanseverino, E.R., Di Dio, V., Romano, P.: Reconfigurable electrical interconnection strategies for photovoltaic arrays: a review. Renew. Sustain. Energy Rev. (2014) (Elsevier)
3. Deline, C., Dobos, A., Janzou, S., Meydbray, J., Donovan, M.: A simplified model of uniform shading in large photovoltaic arrays. Sol. Energy **96**, 274–282 (2013)
4. García, M.C., Herrmann, W., Böhmer, W., Proisy, B.: Thermal and electrical effects caused by outdoor hot-spot testing in associations of photovoltaic cells. Prog. Photovoltaics Res. Appl. **11** (5), 293–307 (2003)
5. Gokmen, N., Karatepe, E., Ugranli, F., Silvestre, S.: Voltage band based global MPPT controller for photovoltaic systems. Sol. Energy **98**, 322–334 (2013)
6. Celik, A.N., Nasir, A.: Modelling and experimental verification of the operating current of mono-crystalline photovoltaic modules using four-and five-parameter models. Appl. Energy **84** (1) (2007)
7. Skoplaki, E., Palyvos, J.: On the temperature dependence of photovoltaic module electrical performance: a review of efficiency/power correlations. Sol. Energy **83**(5), 614–624 (2009)
8. Calò, P., Fiscelli, G., Lo Bue, F., Di Stefano, A., Giaconia, C.: An electronic emulator of combined photovoltaic and solar thermal systems. In: Ecological Vehicles and Renewable Energies (EVER), 2010 Fifth International Conference (2010)